

# **Laser Powder Bed Fusion of Dispersion Strengthened Alloy 400**

Von der Fakultät für Georessourcen und Materialtechnik der  
Rheinisch-Westfälischen Technischen Hochschule Aachen

zur Erlangung des akademischen Grades eines

**Doktors der Ingenieurwissenschaften**

genehmigte Dissertation

vorgelegt von

**Jan-Philipp Roth, M.Sc.**

**Berichtende:**     **Herr Univ.-Prof. Dr.-Ing. habil. Ulrich Krupp**  
                         **Frau Prof. Dr.-Ing. Katrin Jahns**  
                         **Herr Prof. Mgr. Tomáš Kruml, CSc.**

Tag der mündlichen Prüfung: 13.03.2025

Diese Dissertation ist auf den Internetseiten der Universitätsbibliothek online verfügbar

The International Journal of Advanced Manufacturing Technology  
134, 3433–3452, DOI 10.1007/s00170-024-14328-7

Materials Science and Engineering: A  
893, 146129, DOI 10.1016/j.msea.2024.146129

Journal of Manufacturing and Materials Processing  
8, 223, DOI 10.3390/jmmp8050223

Materials Science Forum  
1082, 171–176, DOI 10.4028/p-884q32

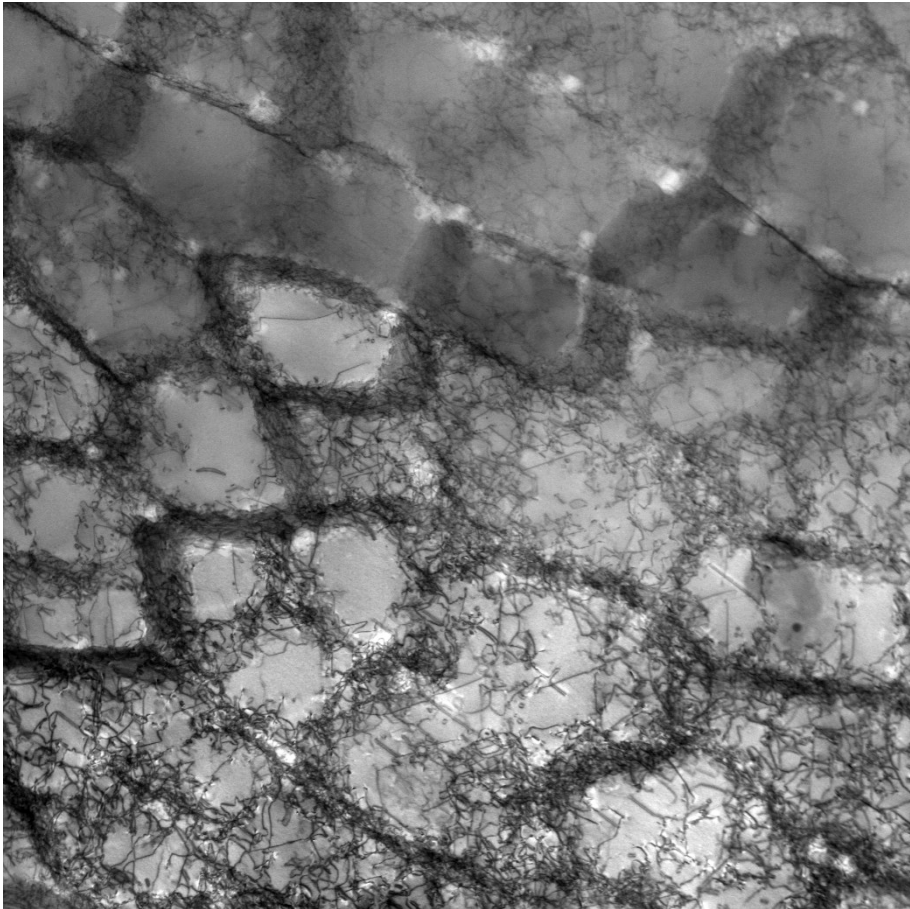
Procedia Structural Integrity  
52, 143–153, DOI 10.1016/j.prostr.2023.12.015

Solid Freeform Fabrication 2023  
574–575

D 82 (Diss. RWTH Aachen University, 2025)



## *Dots and Lines*



or

*Sub-grain, micro dendritic cell structure of PBF-LB/M manufactured Alloy 400,  
revealing a multitude of cell-wall-near dislocations (black lines)  
and dispersed TiN nanoparticles (white dots)*



## ACKNOWLEDGEMENTS

I would like to take this opportunity to thank all the people and institutions that have made this work possible and who accompanied me on my journey to my doctorate.

In the first place, I would like to thank **Prof. Krupp**, head of the steel institute IEHK at the RWTH Aachen University, for the chance to enroll as an external doctorate at his institute. The scientific exchange we have had on a multitude of topics and the associated time investment in my person over the last few years is very much appreciated. In particular, I would like to thank him for expressing his confidence in me to lead the 3D Materials Tech Campus Osnabrück and thus, to conduct hands-on science with my team. Even though working in another city, I got to know a large number of colleagues at the IEHK and want to thank them for the many interesting Aachen-Osnabrück projects completed together and the exchange of expertise.

Speaking of Osnabrück, I want to express my deep gratitude towards **Prof. Jahns** of the Laboratory for Material Design and Structural Integrity at the Osnabrück University of Applied Sciences. Our frequent exchange of academic and administrative nature truly enabled an effective development of our research campus. We came a long way in designing a wide variety of material classes for additive manufacturing. Working at a facility covering all aspects of the value chain, from bulk material, over gas atomization and laser powder bed fusion, to full characterization, was a gift to me and made possible by your efforts. I want to further thank the whole team of the laboratory, my closest colleagues at the 3D Materials Tech Campus, and our esteemed partners from KME Germany GmbH and cunova GmbH, allowing me to carry out research in an industry-related environment.

Over the last few years, I was lucky to work on a multinational project, funded by the European Union's Horizon 2020 research and innovation program under grant agreement No. 958192. I would like to thank all the partners of our topAM project for the joint efforts in pushing boundaries of additively manufactured, dispersion strengthened alloy systems for use in the energy sector. Our successful collaboration demonstrated the true spirit of Europe and once again underlines the enormous potential and innovative power when people from all backgrounds come together across national borders. I would like to thank the Research Institutes of Sweden RISE and the Institute of Physics of Materials IPM, which enabled me to carry out joint experiments on site as a visiting scientist. Also, the in-depth exchange with the colleagues at RISE, La Rochelle University and Indutherm on various powder modification techniques is very much appreciated. In particular, I am grateful for the successful collaboration between the 3D Materials Tech Campus and the IPM under the lead of **Prof. Kruml** that led to all publications included within this dissertation. This was made possible not least by dozens of joint experiments and discussions with my dear colleague **Dr. Šulák** of the IPM. Thank you.

And finally, my great thanks go to my family, my friends, and most of all, my wife. Due to your support, your interest, your encouragement, and countless conversations, I have come one step closer to my goal every day.



ABSTRACT

Additive manufacturing (AM) evolved rapidly during the last decades. Other than conventional manufacturing (CM), this technology allows for near-net-shape components, barely being limited by geometrical constraints. Revealing very fine grains, that, in turn, consist of cellular nanostructures, the resulting performance of such components differentiates significantly from CM. Continuous research is thus required to fully understand this comparably young manufacturing technology. Hence, the first pillar of this work is considering *the manufacturing*.

Besides AM, the modification of base alloy systems via the concept of dispersion strengthening (DS) has attracted great attention in recent years. The implementation of nanoscaled ceramics into the lattice of the alloy results in so-called metal matrix nanocomposites (MMNC). This material class shows clearly improved mechanical properties, mainly being linked to the successful suppression of dislocation movements. Being dependent on a complex multitude of factors, efficient DS requires considerably more fundamental studies to generate a complete picture. Therefore, this thesis also deals with *the mechanism*.

Thirdly, among the wide variety of material classes used in high-performance industries, NiCu-based alloys enable essential products like heat exchangers, pumps, and valves in key sectors like maritime, energy, and chemistry. A prominent representant of this material category is Alloy 400. However, barely any knowledge is available on this alloy when manufactured additively, restricting its potential application. Consequently, *the material* is covered in this thesis as well.

Combining these subject areas, this thesis establishes holistic process routes for *Laser Powder Bed Fusion of Dispersion Strengthened Alloy 400* variants. It is documented how to generate powder feedstocks for laser beam powder bed fusion of metals (PBF-LB/M) via gas atomization of Alloy 400 and the peculiarities of powders and parts are disclosed. Copper segregations on both grain boundaries and cell walls such as high dislocation densities throughout the micro dendritic structure were found. Due to the overall finer grain structure of the AM variant, tensile properties increased, and elongation lowered compared to CM. Based on the findings of unmodified standard Alloy 400, two successful DS modification routes were elaborated for the present alloy. The first one is based on a gas atomization reaction synthesis (GARS) principle. The feasibility of nanoparticle formation *in situ* during atomization due to reaction of the atomization gas with the melt was demonstrated. The ceramics were identified as TiN and they successfully limited dislocation movement throughout the matrix via pinning. This resulted in considerably improved mechanical properties compared to the standard PBF-LB/M variant. The second modification approach applied an *ex situ* powder modification in a fluidized bed reactor (FBR). Enabled by nitrogen diffusion, a high number of TiN was generated in powders which was again significantly increased after AM, allowing for outstanding tensile, creep, and fatigue performance.

Therefore, several alloy systems have been developed and qualified for use in AM while enabling outstanding properties.



ZUSAMMENFASSUNG

Die additive Fertigung hat sich in den letzten Jahrzehnten rasant entwickelt. Im Gegensatz zur konventionellen Fertigung ermöglicht diese Technologie die endkonturnahe Herstellung von Bauteilen, die kaum durch geometrische Restriktionen eingeschränkt sind. Da sie eine feinkörnige Mikrostruktur aufweist, die wiederum aus zellulären Nanostrukturen besteht, unterscheiden sich die resultierenden Bauteileigenschaften erheblich von denjenigen konventioneller Verfahren. Um diese vergleichsweise junge Fertigungstechnologie somit vollständig zu verstehen, bedarf es fortlaufender Forschung. Entsprechend beschäftigt sich die erste Säule dieser Arbeit mit *der Fertigung*.

Neben AM hat die Modifizierung von Legierungssystemen mittels Dispersionsverstärkung in den letzten Jahren große Aufmerksamkeit erregt. Die Implementierung nanoskaliger Keramiken in das Kristallgitter erzeugt sogenannte Metallmatrix-Nanokomposite. Diese Werkstoffklasse weist deutlich verbesserte mechanische Eigenschaften auf, was primär auf die erfolgreiche Unterdrückung von Versetzungsbewegungen zurückzuführen ist. Da eine effiziente Dispersionsverstärkung von vielen, komplexen Faktoren abhängt, sind weitaus mehr grundlegende Studien notwendig, um ein vollständiges Bild hierüber zu erhalten. Somit befasst sich diese Arbeit auch mit *dem Mechanismus*.

An dritter Stelle, neben einer Vielzahl an Werkstoffklassen, die in leistungsintensiven Industrien eingesetzt werden, ermöglichen NiCu-Basislegierungen essenzielle Produkte wie Wärmetauscher, Pumpen und Ventile in Schlüsselbranchen wie der Schifffahrt, der Energie und der Chemie. Eine prominente Vertreterin dieser Werkstoffklasse ist das Alloy 400. Allerdings gibt es kaum Erkenntnisse über diese Legierung im additiv gefertigten Zustand, was ihre Anwendungsmöglichkeiten einschränkt. Aus diesem Grund wird *der Werkstoff* ebenfalls in dieser Arbeit behandelt.

Durch die Kombination dieser Themenbereiche werden in dieser Arbeit ganzheitliche Prozessrouten für das *pulverbettbasierte Laserstrahlschmelzen von dispersionsverfestigten Alloy 400* Varianten erarbeitet. Es wird gezeigt, wie Pulver mittels Gasverdüsung von Alloy 400 für das Laserstrahlschmelzen erzeugt werden kann und welche Besonderheiten Pulver und Bauteile aufweisen. Kupfer Segierungen an Korngrenzen und Zellwänden sowie hohe Versetzungsdichten in der mikrodendritischen Struktur konnten festgestellt werden. Aufgrund des feineren Kornes der AM-Variante nahm die Zugfestigkeit zu, während die Dehnung im Vergleich zum konventionellen Bauteil abnahm. Auf Basis des unmodifizierten Standard Alloy 400 wurden zwei erfolgreiche Dispersionsverstärkungen für die vorliegende Legierung entwickelt. Die erste basiert auf dem Prinzip der Gasverdüsung mit Reaktivgas. Eine *in situ* Bildung von Nanopartikeln während der Verdüsung aufgrund der Reaktivität mit der Schmelze wurde erarbeitet. Die Keramiken wurden als TiN identifiziert und schränkten die Versetzungsbewegung in der Matrix erfolgreich ein. Dies führte zu erheblich verbesserten mechanischen Eigenschaften im Vergleich zur Standard PBF-LB/M Variante. Beim zweiten Modifizierungsansatz wurde eine *ex situ* Pulvermodifikation in einem Wirbelschichtreaktor durchgeführt. Durch Stickstoffdiffusion wurde eine hohe Anzahl von TiN in den Pulvern erzeugt, die im Zuge der additiven Fertigung nochmals deutlich erhöht wurde, was wiederum hervorragende Zug-, Kriech- und Ermüdungseigenschaften ermöglichte.

Es wurden somit verschiedene Legierungssysteme mit herausragenden Eigenschaften entwickelt und für den Einsatz in der additiven Fertigung qualifiziert.



## DECLARATION ON PUBLICATIONS



This dissertation includes the following articles that have been published in international peer-reviewed journals within the field of materials science and engineering.

Publication 1

**Jan-Philipp Roth**, Ivo Šulák, Tomáš Kruml, Wojciech Polkowski, Tomasz Dudziak, Peter Böhlke, Ulrich Krupp, Katrin Jahns, *Establishing a process route for additive manufacturing of NiCu-based Alloy 400: an alignment of gas atomization, laser powder bed fusion, and design of experiments*, The International Journal of Advanced Manufacturing Technology 134 (2024) 3433–3452. DOI 10.1007/s00170-024-14328-7.

See reference [1] in chapter 7.1 for the whole publication.

Publication 2

**Jan-Philipp Roth**, Ivo Šulák, Zdeněk Chlup, Jörg Fischer-Bühner, Ulrich Krupp, Katrin Jahns, *The dispersion-strengthening effect of TiN evoked by in situ nitridation of NiCu-based Alloy 400 during gas atomization for laser powder bed fusion*, Materials Science and Engineering: A 893 (2024) 146129. DOI 10.1016/j.msea.2024.146129.

See reference [2] in chapter 7.2 for the whole publication.

Publication 3

**Jan-Philipp Roth**, Ivo Šulák, Markéta Gálíková, Antoine Duval, Germain Boissonnet, Fernando Pedraza, Ulrich Krupp, Katrin Jahns, *The Dispersion-Strengthening Effect of TiN Nanoparticles Evoked by Ex Situ Nitridation of Gas-Atomized, NiCu-Based Alloy 400 in Fluidized Bed Reactor for Laser Powder Bed Fusion*, Journal of Manufacturing and Materials Processing 8 (2024) 223. DOI 10.3390/jmmp8050223.

See reference [3] in chapter 7.3 for the whole publication.

Additionally, the following supplementary peer-reviewed international journal articles have been published with a contribution of the candidate.

#### Appendix 1

Alice Chlupová, Ivo Šulák, Ivo Kuběna, Tomáš Kruml, **Jan-Philipp Roth**, Katrin Jahns, *Comparison of Microstructure and Properties of Nickel-Copper Alloy Prepared by Casting and Laser Powder Bed Fusion Process*, Materials Science Forum 1082 (2023) 171–176. DOI 10.4028/p-884q32.

See reference [4] in chapter 8.1 for the whole publication.

#### Appendix 2

Ivo Šulák, Alice Chlupová, Tomáš Zálezák, Ivo Kuběna, **Jan-Philipp Roth**, Katrin Jahns, Ulrich Krupp, Tomáš Kruml, *High-temperature Fatigue and Creep Performance of Additively Manufactured NiCu-based Alloy*, Procedia Structural Integrity 52 (2024) 143–153. DOI 10.1016/j.prostr.2023.12.015.

See reference [5] in chapter 8.2 for the whole publication.

Moreover, the following long abstract has been published in the conference proceedings of the 34<sup>th</sup> Annual International Solid Freeform Fabrication Symposium.

#### Appendix 3

**Jan-Philipp Roth**, Ivo Šulák, Zdeněk Chlup, Jörg Fischer-Bühner, Ulrich Krupp, Katrin Jahns, *Nanoparticle-Modification of NiCu-Based Alloy 400 for Laser Powder Bed Fusion*, in Solid Freeform Fabrication 2023: Proceedings of the 34<sup>th</sup> Annual International Solid Freeform Fabrication Symposium – An Additive Manufacturing Conference (2023) 574–575, Austin, Texas, USA.

See reference [6] in chapter 8.3 for the whole abstract.

The candidate has assumed primary responsibility for his first-authored publications 1–3 and appendix 3. This included the general design of the studies, their operational processing, the compilation of all data and results as well as further considerations, findings, conclusions, the overall explanation of the metal-physical interrelationships, and ultimately, the complete preparation and writing of all manuscripts under his own direction. He was the corresponding author and incorporated all suggestions from both the co-authors, and the reviewers and editors of the publishers. Within the scope of publications 1 and 3, the candidate conducted gas atomization of raw material to powder, including the compilation of the bulk material, optimal tuning of the atomization process parameters and powder post-processing. For all three studies, holistic PBF-LB/M parameter studies were performed by him, including the entire pre-, in- and post-processing along the AM process chain. A multitude of light optical microscopy and scanning electron microscopy characterization of powders and parts was conducted solely by the candidate, including the preliminary metallographic work, the application of the instruments and detectors of electron backscattered diffraction, energy-dispersive X-ray spectroscopy, and focused ion beam, as well as the subsequent data analysis. Also, joint scanning transmission electron microscopy was conducted with colleagues at the Institute of Physics of Materials, including specimen preparation and lamella extraction, and utilization of the bright-field detector as well as energy-dispersive X-ray spectroscopy on the nanoscale.

Within the framework of the two co-authored publications in appendix 1 and 2, the candidate took over various roles. He provided the first authors with samples which included gas atomization of bulk material to powder, powder post-processing, computer aided design (CAD) of the test geometries, execution of multiple PBF-LB/M build jobs for specimen manufacturing, and component post-processing. This was followed by scientific discussions on the component behavior during testing and the characterization results obtained. The candidate provided the first authors with further information and text passages on the work he carried out, and he reviewed and edited the manuscript drafts.

The entire long abstract was prepared exclusively by the candidate.



## ABBREVIATIONS

---

<b>2D</b>	two-dimensional	<b>LPBF</b>	laser powder bed fusion (equivalent to PBF-LB/M)
<b>3D</b>	three-dimensional		
		<b>MA</b>	mechanical alloying
<b>AM</b>	additive manufacturing	<b>MMNC</b>	metal matrix nanocomposite
<b>CAD</b>	computer aided design		
<b>CCA</b>	closed-coupled atomization	<b>MPEA</b>	multi-principal element alloy
<b>CM</b>	conventional manufacturing	<b>NAB</b>	nickel aluminum bronze
<b>CTE</b>	coefficients of thermal expansion	<b>NP</b>	nanoparticle
<b>DED</b>	directed energy deposition	<b>ODS</b>	oxide dispersion strengthening
		<b>PA</b>	plasma atomization
<b>DfAM</b>	design for additive manufacturing	<b>PBF-EB/M</b>	electron beam powder bed fusion of metals
<b>DS</b>	dispersion strengthening	<b>PBF-LB/M</b>	laser beam powder bed fusion of metals
<b>EIGA</b>	electrode induction gas atomization	<b>PREP</b>	plasma rotating electrode process
<b>FBR</b>	fluidized bed reactor	<b>PSD</b>	particle size distribution
<b>fcc</b>	face-centered cubic		
<b>FFA</b>	free-fall atomization	<b>PSPP</b>	process-property-structure-performance
<b>FGD</b>	freeze granulation and drying	<b>TRL</b>	technology readiness level
<b>GARS</b>	gas atomization reaction synthesis	<b>UTS</b>	ultimate tensile strength
<b>GND</b>	geometrically necessary dislocations	<b>VIGA</b>	vacuum inert gas atomization
<b>GRCop</b>	Glenn Research Copper	<b>WA</b>	water atomization
<b>HEA</b>	high entropy alloy		

---



SYMBOLS

<b>A</b>	aspect ratio of $l_p$ and $t_p$	<b>V<sub>p</sub></b>	volume fraction of nanoparticles
<b>b</b>	Burgers vector	<b>wt.-%</b>	weight percent
<b>c</b>	specific heat capacity		
<b>d</b>	nanoparticle diameter		
<b>d<sub>H</sub></b>	hatch distance	<b>Δα</b>	CTE mismatch of matrix and nanoparticles
<b>D</b>	initial average grain size	<b>β</b>	dislocation strengthening coefficient
<b>D<sub>ds</sub></b>	average grain size after dispersion strengthening	<b>γ'/ γ''</b>	gamma (double) prime strengthening phase
<b>ev</b>	volume energy density		
<b>G</b>	shear modulus	<b>κ</b>	thermal conductivity
<b>G</b>	temperature gradient	<b>λ</b>	space between nanoparticles
<b>HV</b>	Vickers hardness		
<b>k<sub>y</sub></b>	resistance towards crystal boundary slip	<b>ρ<sub>cte</sub></b>	CTE-caused dislocation density
<b>l<sub>p</sub></b>	nanoparticle size parallel to load	<b>σ<sub>0</sub></b>	initial strength of alloy
		<b>σ<sub>cte</sub></b>	CTE strengthening
<b>M</b>	Taylor factor	<b>σ<sub>ds</sub></b>	resulting dispersion strengthening
<b>p<sub>L</sub></b>	laser power		
<b>R</b>	electrical resistance	<b>σ<sub>gr</sub></b>	grain refinement strengthening caused by nanoparticles
<b>R</b>	solidification rate		
<b>ss</b>	scanning speed	<b>σ<sub>hp</sub></b>	Hall-Patch strengthening
<b>ΔT</b>	temperature shift during thermal expansion	<b>σ<sub>load</sub></b>	load transfer strengthening
<b>t<sub>L</sub></b>	layer thickness	<b>σ<sub>m</sub></b>	initial strength of matrix
<b>t<sub>p</sub></b>	nanoparticle size perpendicular to load	<b>σ<sub>oro</sub></b>	Orowan strengthening
<b>v</b>	Poisson's ratio		



## TABLE OF CONTENTS



---

Acknowledgements .....	IV
Abstract .....	VI
Zusammenfassung .....	VIII
Declaration on Publications .....	X
Abbreviations .....	XIV
Symbols.....	XVI
Table of Contents .....	XVIII
1 Introduction .....	1
2 Fundamentals .....	6
2.1 The manufacturing .....	7
2.1.1 Additive manufacturing.....	7
2.1.2 Laser powder bed fusion process chain .....	8
2.2 The mechanism .....	13
2.2.1 Strengthening mechanisms .....	13
2.2.2 Dispersion strengthening procedures.....	17
2.3 The material .....	20
2.3.1 Non-NiCu-based materials .....	20
2.3.2 NiCu-based materials and Alloy 400.....	22
3 Objectives and scope.....	26
4 Contribution to original knowledge .....	30
4.1 Applying laser powder bed fusion to Alloy 400 .....	31
4.2 Paving the way for dispersion strengthening of Alloy 400.....	33
4.3 Exploiting dispersion strengthening of Alloy 400 .....	36
5 Conclusion and outlook.....	40
6 References .....	44
7 Publications .....	64
7.1 Establishing a process route for additive manufacturing of NiCu-based Alloy 400: an alignment of gas atomization, laser powder bed fusion, and design of experiments .....	65
7.2 The dispersion-strengthening effect of TiN evoked by in situ nitridation of NiCu-based Alloy 400 during gas atomization for laser powder bed fusion.....	86
7.3 The dispersion-strengthening effect of TiN nanoparticles evoked by ex situ nitridation of gas-atomized, NiCu-based Alloy 400 in fluidized bed reactor for laser powder bed fusion.....	98
8 Appendix .....	128
8.1 Comparison of Microstructure and Properties of Nickel-Copper Alloy Prepared by Casting and Laser Powder Bed Fusion Process .....	129
8.2 High-temperature Fatigue and Creep Performance of Additively Manufactured NiCu-based Alloy .....	136
8.3 Nanoparticle-Modification of NiCu-Based Alloy 400 for Laser Powder Bed Fusion.....	148

---



## ***Laser Powder Bed Fusion of Dispersion Strengthened Alloy 400***

# Chapter 1

INTRODUCTION

Laser Powder Bed Fusion of Dispersion Strengthened Alloy 400 – an additive manufacturing process, a strengthening mechanism and an alloy system. This work is based on the three pillars of *the manufacturing*, *the mechanism*, and *the material*, respectively. These subareas contribute in equal measure to the superordinate question on how to additively manufacture Alloy 400 and to apply dispersion strengthening throughout this process (Figure 1). As barely any research is available on additively manufactured NiCu-based alloys on the one hand and no known attempt of DS with this alloy system is documented on the other one, the establishment of holistic AM process routes for both the standard variant and the dispersion strengthened version of

Alloy 400 are considered the key aim and novelty of this work.

### *The manufacturing*

Additive manufacturing has evolved immensely throughout the past decades. First known under the terms of rapid prototyping, three-dimensional (3D) printing or solid freeform fabrication in the 1980's, primal use cases of AM have been limited to visual aids and demonstrators in art and research [7–10]. However, having grown steadily in market capitalization, with a compound annual growth rate of nearly 14 % throughout the upcoming years, and an evolving number of patents registered and process variants established, its suitability for industrial use followed accordingly [9–11]. By 2028, the complete AM

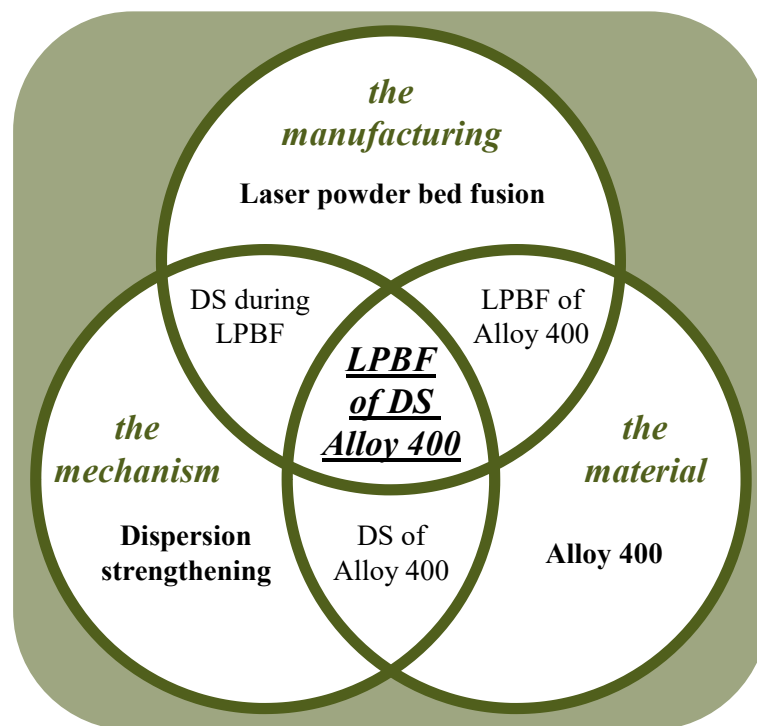


**Figure 1** Laser powder bed fusion of dispersion strengthened Alloy 400 as the intersection of the manufacturing, the mechanism, and the material.

market, consisting of the equipment, the material and the manufacturing service, is projected to be worth approx. 20 bn. €, which almost marks a duplication to 2023 [11]. Consequently, single part production emerged to small batch lot sizes and eventually, especially in highly customized markets for the end user, AM created an enormous competitive advantage and thus, almost completely replaced conventional manufacturing [11–14]. This applies in particular to the dental and medical sector, where patient-tailored implants can be realized in a single process step [12–14]. Further sectors demonstrating a wide range of applications for AM are aerospace, engineering, energy, transportation and automotive industries, where integration of functions into one originally assembled part (e.g. heat exchanger with internal cooling channels) reveals enormous potential for both lightweight construction and cost savings [15–17]. The underlying key advantage of all AM technologies is that complex, conventionally non-manufacturable structures are divided into easy-to-print two-dimensional (2D) layers, resulting in almost no geometrical restrictions in the fabrication of AM parts, as often encountered throughout CM [14,18–20]. Still, within this comparatively young manufacturing branch, a continuous development of processes and materials in order to achieve industrial maturity and scalability is an urgent need. Alike, this applies for the laser beam powder bed fusion of metals, one of the most established AM processes [11,15]. Even though defined as PBF-LB/M in DIN EN

ISO/ASTM 52900:2022-03, this AM process is still frequently referred to as laser powder bed fusion (LPBF) [21]. The terms PBF-LB/M and LPBF can therefore be regarded as equivalent; they refer to the same manufacturing process.

### *The mechanism*

It is a well-known principle in materials science that the final performance of a component is strongly determined by the way it has been produced, the resulting microstructure and the properties associated with it. This correlation is commonly referred to as the process-structure-property-performance (PSPP) relationship and a slight variance in the input variable, the process, may evoke a tremendous change in the output variable, the behavior of the component in use [22–25]. Hence, only an entire control of the manufacturing sequence and a fundamental understanding of the resulting strengthening mechanisms ensures the outcome of the desired material performance. While most of the mechanisms are caused by the nature of the applied process or the chemical composition of the alloy at hand and thus, are difficult to adjust or circumvent for, the dispersion strengthening effect of nanoparticles (NP) can be evoked as per a wide variety of modification processes [26–31]. Besides application in CM, DS is attracting particular interest in the advancement of additively processed materials. Due to cooling rates several orders of magnitude higher for AM than for CM, and the evoked high internal stresses that result from the heterogeneity

in between cooling and heating cycles during layer-wise PBF-LB/M, AM parts exhibit a considerably more pronounced dislocation formation in combination with a cellular sub-grain structure [32–35]. As a result, intense nanoparticle-dislocation-interaction is evoked, e.g. in the form of dislocation movement suppression, leading to a profound strengthening of the additively manufactured component [26,27,36,37]. Consequently, there is great interest in both academia and industry in gaining deeper insights into successful dispersion strengthening methods.

### *The material*

Humankind has tailored materials for their intended use since millennia. Starting from the Bronze Age, raw materials were combined to form new, superior alloys. To date, a fundamental understanding of the different classes of materials and their continuous improvement through intelligent design has evolved. Achievements in this field unlock new applications in both everyday life and industry on an ongoing basis. Still, as much as is known about the most popular material systems, especially about steels, as little is yet understood about both, the less common material classes, such as refractory alloys, and the recently established ones, like multi-principal element and high entropy alloys (MPEA/HEA), respectively [38–42]. Accordingly, there are plenty of materials well studied and tailored for their use in additive manufacturing, in particular titanium-, aluminum-, nickel-, copper- and cobalt-based alloys as well as steels

[11,15,22,43]. However, even though Alloy 400 has been conventionally manufactured for over a century already, little is known in terms of its applicability for AM [44]. The NiCu-based alloy, also referred to as NiCu30Fe or Monel 400, is an important material in multiple demanding industries like the energy business, the chemical processing, and the maritime sector [45–48]. It is a single-phased, face-centered cubic (fcc) crystallizing solid solution that possesses excellent resistance to corrosion, which evokes a multitude of application cases, e.g. as pump systems, heat exchangers and valves [45–48]. Therefore, in order to unlock the full potential of Alloy 400, it is necessary to create a holistic picture of the peculiarities of this alloy system when manufactured additively, apart from the CM fundamentals well known.

# Chapter 2

FUNDAMENTALS



In order to generate a deep understanding of *the manufacturing, the mechanism*, and *the material*, respectively, PBF-LB/M, DS, and Alloy 400 have to be classified into their superordinate thematic fields. Simultaneously, a differentiation to related topics within these fields must be carried out. Hence, AM is portrayed against CM and PBF-LB/M located as a subordinate component, the uniqueness of DS gets highlighted among the strengthening mechanisms in their entirety while the applicability of multiple DS approaches for PBF-LB/M is being evaluated, and finally, NiCu-based alloys, including Alloy 400, are compared to further, common material classes.

## 2.1 The manufacturing

*The manufacturing* provides an overview about the distinction between additive

manufacturing and conventional manufacturing (2.1.1), and the complete process cycle for laser powder bed fusion (2.1.2).

### 2.1.1 Additive manufacturing

According to DIN 8580:2022-12, manufacturing processes are classified into six categories, where primary shaping, defined as the production of a workpiece from shapeless raw material, is considered the initial procedure in the life cycle of every product [49,50]. In turn, primary shaping as the creation of cohesion, consists of nine groups, which differ in terms of the (aggregate) state of the material, and with additive manufacturing being a separate one among them (Figure 2) [49,50]. This is due to the fact that AM and CM are fundamentally different from each other

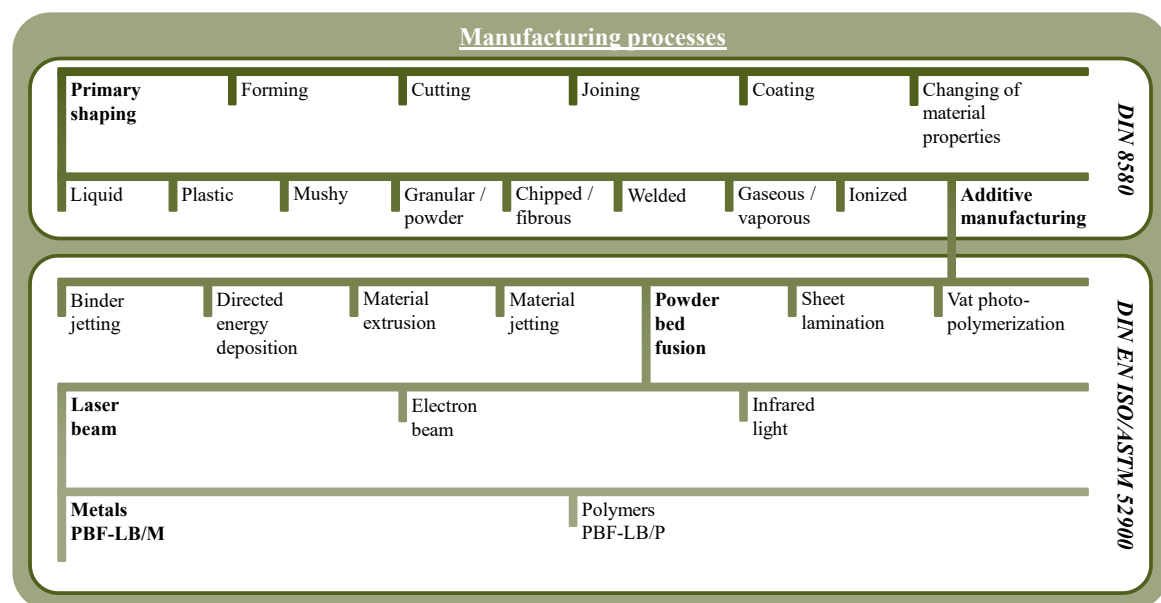


**Figure 2** Classification of AM and PBF-LB/M into standards DIN 8580 and DIN EN ISO/ASTM 52900 within the framework of the manufacturing processes.

as the former one creates the final geometry according to a layer-by-layer structure and procedure [14,18–20,51]. Compared to CM, AM reveals some specific challenges and drawbacks:

- The surface finish of as-printed parts is rather poor for most AM processes, being linked to a reduced dimensional accuracy and the need for post-processing [18,52],
- The build volume of most 3D printers (esp. for PBF-LB/M) is limited, only enabling comparably small components [52,53],
- The resulting productivity is lower than in CM, not allowing mass production [18,52,53].

However, the advantages of AM are substantial. For instance, additive technologies allow for a very high level of geometrical freedom during the design phase, enabling complex components non-manufacturable via formative or subtractive manufacturing processes, and a cost-independent “complexity for free” business model [9,18–20,52–54]. Alike, “customization for free” in AM products describes the possibility to iteratively adjust these designs in order to generate further product variants or to customize parts for the specific requirements of the end user at virtually no costs [12–14,18,20,52,55]. Resulting from these two principles, low-quantity but high-customization applications define the target markets where an exploitation of the AM capabilities is most expedient [18,20,55,56].

Further benefits in conjunction with AM are:

- No need for individual tools and a direct access to spare parts, enabling efficient production and fast supply of tools for CM [9,20,52,53],
- Function integration of properties and topology optimization of geometries that do not require any further assembly [52–54],
- Resource savings, as only the material needed for the final part is processed and most metallic feedstock materials can be recycled [9,18,54].

In the end, there are multiple AM production methods, varying in the applied principle for the creation of cohesion (based on laser, electron, ultraviolet/light-curing, binder), the material state (liquids, powders, solids), the material class (metals, polymers, ceramics, composites), and they all differ considerably from each other [9,25,57]. Here, and besides directed energy deposition (DED), PBF-LB/M stands out among the metal AM methods as it is the most technologically mature and industrialized process to allow for near-net-shape fabrication [9,11].

### **2.1.2 Laser powder bed fusion process chain**

Laser beam powder bed fusion of metals, as defined in DIN EN ISO/ASTM 52900:2022-03, is the central component of a complex metal AM process flow, consisting of pre-, in- and post-processing

(Figure 3) [9,21]. Before the actual PBF-LB/M print job, two major tasks have to be addressed: A suitable powder feedstock must be provided and a digital file of the geometry to be produced needs to be designed. Resulting from this input, the final component is generated layer-wise as per the iterative PBF-LB/M process. The post-processing may then include support structure removal, surface finish, heat-treatments, characterization and testing, all before the actual use of the part.

### Pre-process

As PBF-LB/M is a metal-powder-based process, the powder must be present in a spherical shape and with a particle size distribution (PSD) of approx. 15–63  $\mu\text{m}$ , where it shows the highest flowability [58–60]. For the generation of the respective powder feedstock, several

atomization methods exist and among further ones, the most frequently used are:

- Vacuum inert gas atomization (VIGA),
  - Plasma atomization (PA),
  - Plasma rotating electrode process (PREP),
  - Water atomization (WA),
  - Electrode induction gas atomization (EIGA).
- [61,62]

The decisive advantages of VIGA are, that there is no restriction with regard to the alloy type to be atomized under a controlled inert atmosphere, and, that a high flowability of the resulting powder is attainable due to its spherical appearance [59,61]. In principle, the VIGA setup consists of a melting chamber on top of a spray tower. The bulk material is filled into a crucible and the melting is applied

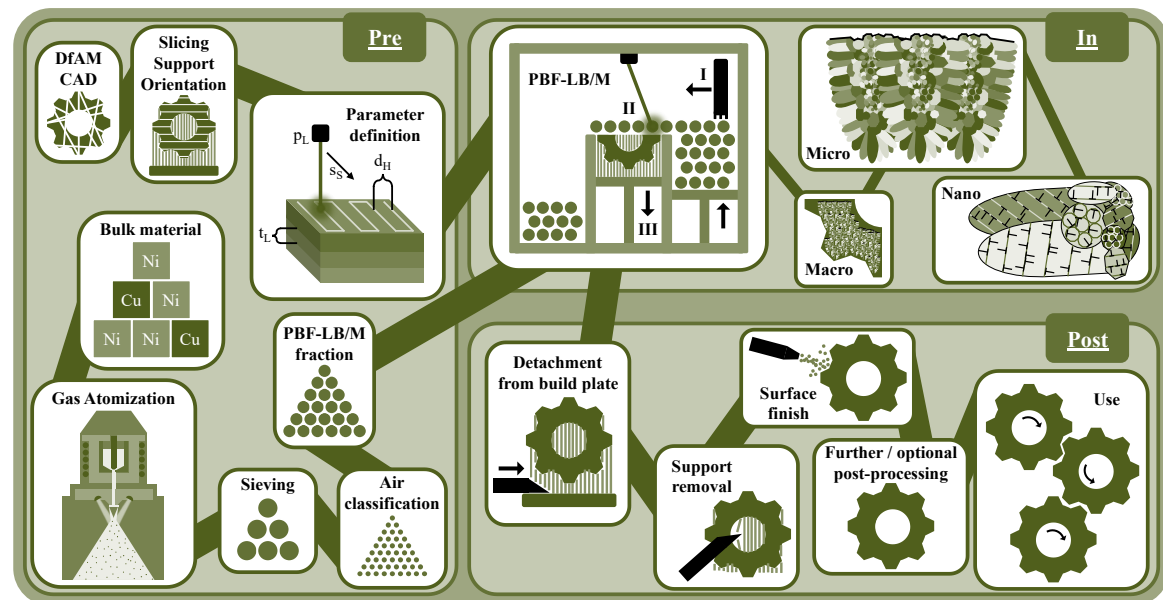


**Figure 3** The PBF-LB/M process chain, consisting of the pre-process (digital part, parameters, atomization, and powders), the in-process of powder bed fusion, and the post-process (finalization of the component and use).

via an induction coil, while overheating beyond the liquidus temperature of the alloy ensures proper viscosity and homogenization of the melt, respectively [63,64]. With the initiation of the atomization process, the melt enters the process chamber and gets atomized via a gas stream, either after a short falling distance (free-fall atomization; FFA) or directly at the nozzle outlet (closed-coupled atomization; CCA) [65,66]. As the latter approach results in a finer PSD, it is generally used for the PBF-LB/M process. During atomization, the melt-to-particle breakup process is split into a primary (film to ligament to droplet formation) and a secondary (droplet to particle formation) sequence [63,65]. During this procedure, the liquid-solid transition occurs almost immediately at a rate of  $10^3$ – $10^4$  K/s, which evokes equiaxed grains in the particles without any preferred growth direction and marginal texture only [58,60]. The resulting powders need to be further processed by means of sieving and air-classification. This way, the desired PSD can be obtained and separated from the coarse splash fraction as well as the fine, non-flowable particles. The usable powder then has to reveal proper flowability and bulk density to ensure sufficient powder distribution via the recoater and a high packing density of the powder bed during PBF-LB/M, being the first prerequisites for a successful print job, respectively. Values for flowability determined as per the standard funnel should be in the range of 10–20 s/50g for highly spherical powders [67,68]. The optimal bulk density can be accurately

determined as per the Hausner ratio and must not exceed a 1.25 maximum value of tapped density to bulk density [67,69]. Fine particles sticking on the surface of coarser particles, called satellites, are detrimental for both key figures and thus, must be avoided as per a well-defined atomization process [70,71]. This is achieved by adjusting the metal mass flow as a function of the applied temperature and resulting viscosity of the melt, the gas pressure, and the outlet diameter of the crucible nozzle.

The digital part is created as per a computer aided design software. However, in contrast to CM, design constraints concerning e.g. varying wall thicknesses or internal cooling channels do not exist for PBF-LB/M, which entails the necessity for an adapted design for additive manufacturing (DfAM) approach [18,72]. As per a consistent DfAM, 3D geometrical issues can be converted into 2D feasible solutions. Therefore, the file is sliced along its z-axis (build direction) by a respective build job preparation software according to the final layer height. A layer thickness of approx. 20–40  $\mu\text{m}$  allows for an optimal trade-off between productivity rate and a detailed resolution, which is why it is used for most applications [32,73]. A further important aspect during the design phase is the creation of the support structure, which connects the final part with the build plate, and enables both heat transfer in avoidance for internal, process-induced stresses, and proper part removal from the build plate. In general, the more pronounced the support structure, the more efficient the

part can be manufactured. However, every support arm adjoining to the part complicates the process of surface finish. Hence, a well-adjusted compromise of ensured manufacturability and as few links as possible must be found. Afterwards, the orientation of the sliced and supported part in the build space, and the definition of the process parameters for support and part manufacturing follow. Here, the parameters of main interest are the power of the laser  $p_L$  in [W], the hatch distance in between single laser scan lines  $d_H$  in [ $\mu\text{m}$ ], the thickness of a layer  $t_L$  in [ $\mu\text{m}$ ] and the scanning speed of the laser travel  $s_S$  in [mm/s]. These key figures sum up to the volume energy density  $e_V$ , defined as per:

$$e_V = \frac{p_L}{s_S \cdot d_H \cdot t_L} \quad (\text{Eq. 1})$$

Optimum tuning of these parameters throughout preceding studies is crucial for the avoidance of failures during printing, and thus, the creation of a highly dense component. With application of the powder to the 3D printer and the transfer of the digital part, the actual PBF-LB/M process may be initiated.

### *In-process*

Before the exposure of the first layer, manufacturing conditions have to be met. This includes both pressuring the build chamber with shielding gas and the consequent reduction of the oxygen level to prevent reaction with the material during the liquid state inside the melt pool. Moreover, if the build platform is heatable, to further counteract the accumulation of internal stresses, the target temperature must be reached.

Subsequently, the iterative sequence of powder recoating (I), laser fusion (II), and lowering of the build plate (III) starts (c.f. Figure 3).

During (I), a recoater shifts fresh powder from the powder reservoir to the build plate and on top of the last processed, solidified layer, respectively. Multiple types of recoaters exist, among others, metallic and ceramic profiles, rubber lips, rollers, and brushes [74,75]. Thus, a perfect fit of the recoater to the respective powder properties has to be found in advance to ensure an evenly structured powder bed. Also, it has to be noted that not only powder that corresponds to the applied layer height can be processed; as the melt pool of the previous layer evoked deep cavities in the powder bed, these can be filled with coarse particles exceeding the layer height as well. As a result, the entire share of the 15–63  $\mu\text{m}$  particles of the final PSD is evenly distributed over the powder bed.

Afterwards, via the absorption of the laser power in the powder bed (II), local micro-welding to a consistent structure occurs in the melt pool. Due to cooling rates of up to  $10^6$  K/s (thus, even exceeding the ones during VIGA), and a direction-dependent input of energy, a clearly preferred grain growth along the build direction results [25,32,33,76–79]. These columnar grains, in turn, reveal a micro dendritic cell structure that is rich in dislocations, whereas in CM, grains are comparably coarse for many processes and alloys, respectively [33,76]. As the cooling rate is directly dependent on the applied process parameters, a variation of these

results in a change of the microstructure, allowing for a wide variance of grain sizes, even within a single build layer [51,77,80]. Also, the metal-physical mechanisms occurring here are highly dependent on the temperature gradient ( $G$ ) and the respective solidification rate of the crystal ( $R$ ), hence the  $G/R$  ratio [33]. Therefore, the cell formation and the number of resulting geometrically necessary dislocations (GND) are directly dependent on  $G/R$  [76]. In general, the faster the cooling of the melt pool occurs, the finer the microstructure and thus, the higher the amount of differently oriented grains and the associated local misorientation [76,81]. The internal stresses evoked by the interplay of iterative cooling and heating during PBF-LB/M are then compensated by a multitude of GND, especially along cell walls where the solidification occurs latest, and the different orientation of the crystal lattices must be aligned [33,34]. They are accompanied by further segregations and precipitates, all benefitting the component strengthening [33,76]. However, the formation of the columnar grains within the superordinate, solidified melt pools along build direction comes with a drawback as well: anisotropy, that has to be bypassed by e.g. subsequent heat treatment [32,77,78]. Also, the presence of porosity in PBF-LB/M manufactured parts is strongly counteracting the strengthening effect of the microstructure. During repetitive melting and solidifying, density issues may occur, with the following porosity types being the most likely ones to evolve:

- *Balling*, which is mainly caused by high scanning speeds, that evoke the collapse of elongated melt pools to spherical cavities,
- *Keyholes*, as the result of extensive energy insertion, forming a deep, vertical, and gas-containing void,
- *Powder feedstock*, resulting from porosity in powders that introduce ambient air or process gas to the part when melted,
- *Lack of fusion*, insufficient energy input, leading to partly molten areas, even including unmolten particles of the powder feedstock. [15,82,83]

These porosity issues, in turn, are circumvented by a well-defined process parameter setup [32,84]. After the part is fully exposed, one loop of the PBF-LB/M sequence closes with the lowering of the build platform in accordance with the applied layer height (III). A new powder bed can be built up for the successive layer and the iteration is carried out again. With the completion of the top layer, the build job ends. The build platform may then be detached from the machine and taken out of the process chamber.

### *Post-process*

The first operation after PBF-LB/M is the separation of the part from the build plate it was manufactured on. Here, band-sawing and wire-EDM are the commonly used processes. This way, some of the support structure is already removed while most of it, especially in difficult-to-access areas, has to be machined afterwards. While some recent attempts



enable for self-dissolving support structures, nearly all PBF-LB/M processes still rely on the manual cut off with pliers, making this procedure a time- and labor-intensive one [85]. After support removal, a variety of further post-processing routines may be carried out, among others surface finish. While PBF-LB/M is capable of manufacturing parts with high dimensional accuracy, some surfaces might require a precise finish [18,52]. Especially functional areas, that demand a perfect fit to assemblies, must be flattened and reduced in roughness, often by CM methods like milling. Also, powder particles that sintered to the surface must be removed by e.g. sandblasting. Remaining, loose powder entrapped in cavities and channels is blown out via compressed air. Further surface finish, e.g. by pickling for optimal appearance, might follow. Like in CM, and depending on the intended use case, post-processing includes microstructural characterization, heat treatments, mechanical testing, and further property determination that contribute to a holistic understanding of the processed material. Ultimately, after post-processing is completed, the actual use of the part follows, closing the PBF-LB/M manufacturing process chain.

## 2.2 The mechanism

*The mechanism* provides an overview about strengthening mechanisms in general, including dispersion strengthening (2.2.1), and introduces common DS approaches for PBF-LB/M (2.2.2).

### 2.2.1 Strengthening mechanisms

Metal materials primarily derive their strength from a multitude of defects that may evolve throughout their crystal lattice structure (Figure 4) [86,87]. These defect types are grouped according to their dimensional appearance:

- *0-dimensional points*, like vacancies and substitutional atoms in the lattice, or interstitial atoms between the lattice,
- *1-dimensional lines*, like edge and screw dislocations of the lattice,
- *2-dimensional planes*, like grain and twin boundaries, or stacking faults,
- *3-dimensional volumes*, like precipitates in the lattice, or macroscopic defects like pores, inclusions, void clusters, and cracks.

[86,87]

Macroscopic defects are non-beneficial for mechanical performance as they weaken the lattice, and thus facilitate failure initiation and crack growth. Simultaneously, they are likely to evolve as a result of poorly optimized PBF-LB/M process parameters as described previously [32,84]. They can therefore be avoided while all other, lower-dimensional defect types, including three-dimensional precipitates, contribute to various strengthening effects, and eventually influence or evoke each other. The common strengthening mechanisms are (i) solid solution strengthening, (ii) work hardening / dislocation strengthening, (iii) grain refinement / grain boundary strengthening, (iv)

precipitation hardening, and (v) dispersion strengthening. They all eventually evolve in NiCu alloys as well, with Alloy 400 in particular not forming precipitates [88]. Strengthening as per a solid solution (i) causes a hardening of the crystal lattice as the result of an implementation of point defects. They can be either classified as interstitials, comparably small atoms that may diffuse through the lattice like C, H, or N, or substitutionals, that reveal similar nuclear radii to the host atoms and are thus incorporated into the lattice. Solute atoms may then pin dislocations when under load and thereby strengthen the component [89,90]. Precipitates instead, and the resulting hardening (iv), are the outcome of solute atoms reacting to a secondary phase, when the solubility of the respective alloy component in the solid solution is exceeded (corresponds to

the hypereutectic state in eutectic systems), which enables dislocation looping and shearing [89,91]. With respect to metal AM and PBF-LB/M, however, the design of an application-adjustable microstructure attracts specific interest. As a result of the very high cooling rates during PBF-LB/M, an ultra-fine-grained microstructure forms that consists of subordinate cells and is rich in dislocations, which is why the strengthening mechanisms of grain refinement (iii) and dislocation strengthening (ii) are a direct outcome of the process [33,77–79]. Such grain refinement, called Hall-Petch strengthening, is exceptionally beneficial for improving the mechanical properties, since the dislocations encounter considerably more grain boundaries as they move through the lattice [33,77–79].

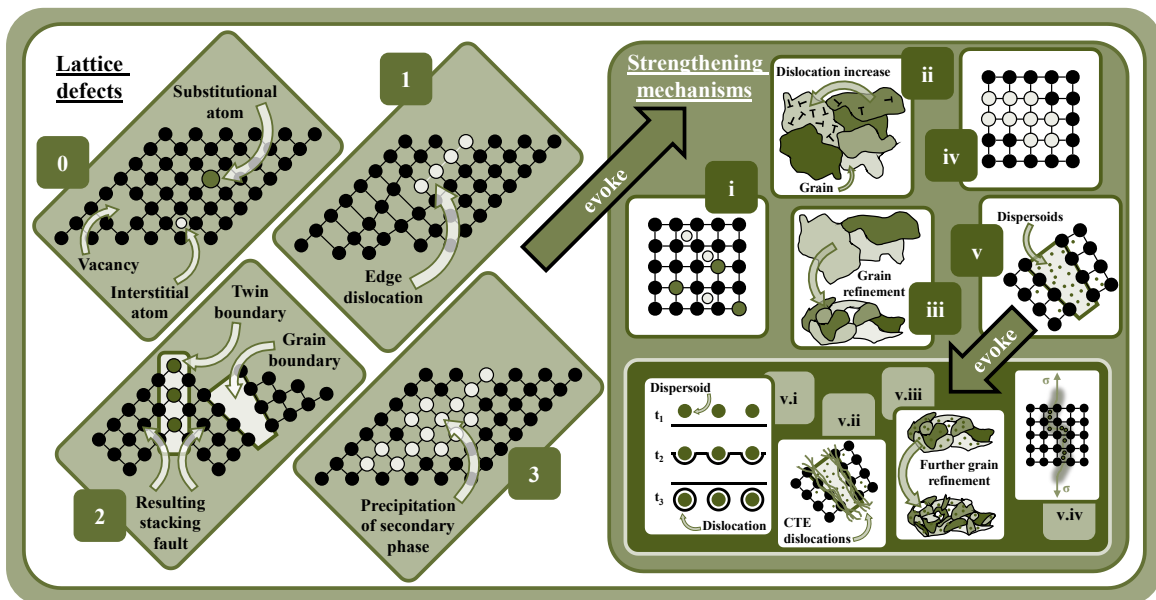


**Figure 4** Lattice defects in metal materials as the source for strengthening mechanisms, including dispersion strengthening, with its dispersoids evoking further sub-strengthening mechanisms.



The fifth strengthening mechanism, dispersion strengthening (v), is evoked by a homogeneous implementation of nanosized ceramics throughout the metallic microstructure, along grain boundaries and cell walls, respectively [27,30,92]. Such modified materials are commonly referred to as metal matrix nanocomposites [92–95]. In the majority of applications, the ceramics implemented can be classified as oxides, which gave rise to the term of oxide dispersion strengthening (ODS) [27,28,30]. However, nitrides, carbides, borides, and further ceramics or even nanosized intermetallics are common DS candidates as well. Some of the most relevant ones are TiN, TiC, TiB<sub>2</sub>, Al<sub>2</sub>O<sub>3</sub>, WC, Al<sub>3</sub>Zr, and SiC, with further DS systems being constantly developed for MMNC [26,96–99]. They successfully hinder dislocation and grain boundary movement when under load, which attracts special interest at elevated temperatures, where the DS particles reveal their particular thermodynamic stability in comparison to the metal matrix and thus restrict grain coarsening [27,36,37]. As a result, mechanical properties in terms of tensile, creep or fatigue may be enhanced significantly, eventually by several orders of magnitude [26,29,100–104]. The respective increase in strengthening evoked by climbing and/or pinning of dislocations along the dispersoids is described by the Orowan mechanism (v.i):

$$\Delta\sigma_{oro} = M \frac{0.4Gb}{\pi\sqrt{1-\nu}} \frac{\ln\left(\frac{\bar{d}}{b}\right)}{\lambda} \quad (Eq. 2)$$

$$\text{with } \lambda = \bar{d} \left( \sqrt{\frac{\pi}{4V_p}} - 1 \right) \quad (Eq. 3)$$

$$\text{with } \bar{d} = \sqrt{\frac{2}{3}} d \quad (Eq. 4)$$

with M being the Taylor factor, G being the shear modulus within the matrix, b being the Burgers vector of the lattice distortion,  $\nu$  being the Poisson's ratio,  $\lambda$  being the space between nanoparticles,  $V_p$  being the volume fraction of the reinforcing nanoparticles, and  $\bar{d}$  being the mean nanoparticle diameter [92,94,105,106]. Thus, a higher energy required for a dislocation to bypass the respective nanoparticle in the MMNC evokes an increased strength [93]. There is no exact limit for the size of nanoparticles. Still, also considering Eq. 2–4, mean values well below 100 nm in diameter are common, with even finer particles below 10 nm allowing for both a pronounced strengthening and a more homogeneous distribution over the metal matrix [28,30,92,95]. In theory and considering  $V_p$  in Eq. 2–3, the higher the volume fraction of nanoparticles, the more effective the resulting Orowan strengthening. However, fractions clearly above 5.0 % (depending on the alloy system and the dispersoids used) negatively influence the strengthening effect as the nanoparticles start to form agglomerates and thus, experience an overall coarsening [95,107–109]. These NP clusters rather act as the previously described 3D defect type, negatively affecting final part performance as they facilitate failure initiation.

While  $\sigma_{oro}$  (v.i) is considered the main contributor to the overall dispersion strengthening effect (v), further component strengthening is evoked as per a mismatch in thermal expansion (v.ii), grain refinement / Hall-Patch (v.iii) and load transfer (v.iv) [92,95,110]. Other than the primary evolution of dislocations due to rapid cooling during PBF-LB/M (ii), further dislocations form when nanoparticles are present throughout MMNC microstructures (v.ii). Due to a mismatch in between the coefficients of thermal expansion (CTE) of the base alloy matrix and the nanoparticles, internal strain is evoked throughout the component and circumvented by the formation of additional dislocations along the NP [94,109]. Therefore, dislocations resulting from the CTE mismatch are a direct outcome and constituent part of dispersion strengthening. The share of CTE strengthening is calculated as per:

$$\Delta\sigma_{cte} = M\beta Gb\sqrt{\rho_{cte}} \quad (Eq. 5)$$

$$\text{with } \rho_{cte} = \frac{12V_p\Delta\alpha\Delta T}{bd(1-V_p)} \quad (Eq. 6)$$

with  $\beta$  being the dislocation strengthening coefficient,  $\rho_{cte}$  being the dislocation density resulting from CTE mismatch, 12 being the geometric constant for equiaxed NP,  $\Delta\alpha$  being the difference in CTE of matrix and NP, and  $\Delta T$  being the temperature shift during the thermal expansion [94,95,105]. In the same manner as dislocations are not solely caused by the high cooling rates (ii) but also due to varying CTE (v.ii), grain refinement is not only evoked by cooling during PBF-LB/M (iii) but also because of the presence of the dispersoids (v.iii).

The reason is that NP act as both pinning points of growing grain boundaries, called Zener pinning, and nucleation sites for further grains [26,109,111]. Thus, the Hall-Patch effect of hindering dislocation movement due to a variety of fine, heterogeneously orientated grains is intensified according to:

$$\sigma_{hp} = \sigma_0 + \frac{k_y}{\sqrt{D}} \quad (Eq. 7)$$

$$\text{and } \Delta\sigma_{gr} = k_y \left( \frac{1}{\sqrt{D_{ds}}} - \frac{1}{\sqrt{D}} \right) \quad (Eq. 8)$$

with  $\sigma_0$  being the basic strength of the alloy, including solid solution strengthening,  $k_y$  being the material-dependent resistance to a crystal boundary slip,  $D$  being the initial average grain size,  $\Delta\sigma_{gr}$  being the resulting strength increase due to grain refinement, and  $D_{ds}$  being the resulting average grain size after dispersion strengthening [94,105,109]. The final sub-strengthening mechanism evoked by dispersion strengthening is the load transfer effect (v.iv). It describes the shift of the applied load from the comparably soft metal matrix to the hard ceramic particles, even at coarser diameters of 500–1000 nm [109,110,112]. The higher the NP volume fraction and the more pronounced the wettability of NP and matrix, the higher the resulting strengthening [93]. The delta of load transfer strengthening is denoted as per:

$$\Delta\sigma_{load} = V_p \cdot \sigma_m \left[ \frac{(l_p + t_p)A}{4l_p} \right] \quad (Eq. 9)$$

with  $\sigma_m$  being the initial strength of the matrix only,  $l_p$  being the NP size parallel to the direction of the load,  $t_p$  being the perpendicularly oriented thickness of the

NP, and A being the resulting aspect ratio of  $l_p$  and  $t_p$  [94,109].

Hence, for NiCu alloys, solid solution strengthening (i) and precipitation hardening (iv) occur as a result of the chemistry, while PBF-LB/M evokes dislocation strengthening (ii) in combination with grain refinement and grain boundary strengthening (iii). Ultimately, the fifth mechanism of dispersion strengthening (v), enables a further improvement of the mechanical properties as per four sub-strengthening mechanisms: Orowan strengthening  $\Delta\sigma_{oro}$  (dislocation pinning, v.i), CTE mismatch strengthening  $\Delta\sigma_{cte}$  (increase in dislocation density, v.ii), grain refinement strengthening  $\Delta\sigma_{gr}$  (increase in Hall-Patch, v.iii), and load transfer strengthening  $\Delta\sigma_{load}$  (load shift from matrix to NP, v.iv). Thus, the additional increase in material strength of a dispersion strengthened MMNC can be denoted as per:

$$\Delta\sigma_{ds} = \sqrt{(\Delta\sigma_{oro})^2 + (\Delta\sigma_{cte})^2 + (\Delta\sigma_{gr})^2 + (\Delta\sigma_{load})^2} \text{ (Eq. 10)}$$

where the root and the quadratic terms consider reciprocal interactions of the sub-strengthening mechanisms [92,109].

### 2.2.2 Dispersion strengthening procedures

There is not only one DS technique used for laser powder bed fusion of metals. Apart from fundamental differences according to the ceramic and metal material used, there exists a wide variety

of preparation routines for dispersion strengthened materials. They can be classified into DS of powder (A), either during powder generation (A1) or after powder generation (A2), and DS of parts during PBF-LB/M (B), as illustrated in Figure 5.

DS powder modification during the atomization process (A1) was originally introduced as gas atomization reaction synthesis [31]. As the name suggests, and other than during standard atomization, no shielding gas is used (or only to a small extent) and the melt would get in contact with a reactive gas inside the atomization tower instead [28,31,104,113]. For instance, depending on the intended nanoparticles to be formed, a nitrogen-based process gas may be used for nitride formation inside the powder, and oxygen-ambient-air mixtures evoke the formation of oxides in the material. As a result, the nanosized ceramics may deposit both on the surface and inside the base alloy powder particle [28,114]. The crucial variable here is the Gibbs free energy of formation. The lower the respective Gibbs energy for a compound, the more likely it will form during the reaction, as the joint state of single atoms to a ceramic molecule is thermodynamically favored [101,115]. As the dispersoids are evoked during the liquid-solid phase transition of the melt to powder particles, this approach may also be denoted as an *in situ* atomization. The outstanding advantage of GARS is that it is a well-known process that is suitable for big batch production of powders as demanded by industry. Its technology readiness level (TRL) can be quantified as

TRL 6 since its functionality has successfully been demonstrated in relevant environments. However, the elemental reactivity to nanoparticles during atomization can barely be influenced, eventually leading to an insufficiently low  $V_p$  within the powders.

This, in turn, can be considered the benefit of DS techniques that alter the powder after standard shielding gas atomization, and therefore, allow for a reaction under controlled conditions (A2). For instance, a very common DS modification procedure is the mechanical alloying (MA) of the base alloy powder and the added nanoparticles by steel balls. Loaded to high-energy ball mills, local micro-welding of the NP onto the surface of the base alloy occurs, providing an easy and cost-efficient way for DS powder feedstock generation [27,116]. However, the clear drawback of this

method is the deformation of originally spherical particles due to the high impact forces occurring, and the associated decrease of appropriate flowability of the powder bed [100,116]. Altering of particle morphology can be avoided when strengthening particles are only decorated onto gas-atomized powders but no alloying occurs, e.g. via electrostatic reaction / electrostatic self-assembly [26,117]. A further effective technique is called acoustic mixing; evoked by a vibrating low-amplitude, high-frequency spring-damper-system, base alloy powders can be fully and homogeneously coated with a nanoparticle film in relatively short time [29,118]. A similar result can be achieved via electromagnetic 3D vibration, where the NP film is generated as a result of a combined vibration in vertical direction and an accompanying oscillation

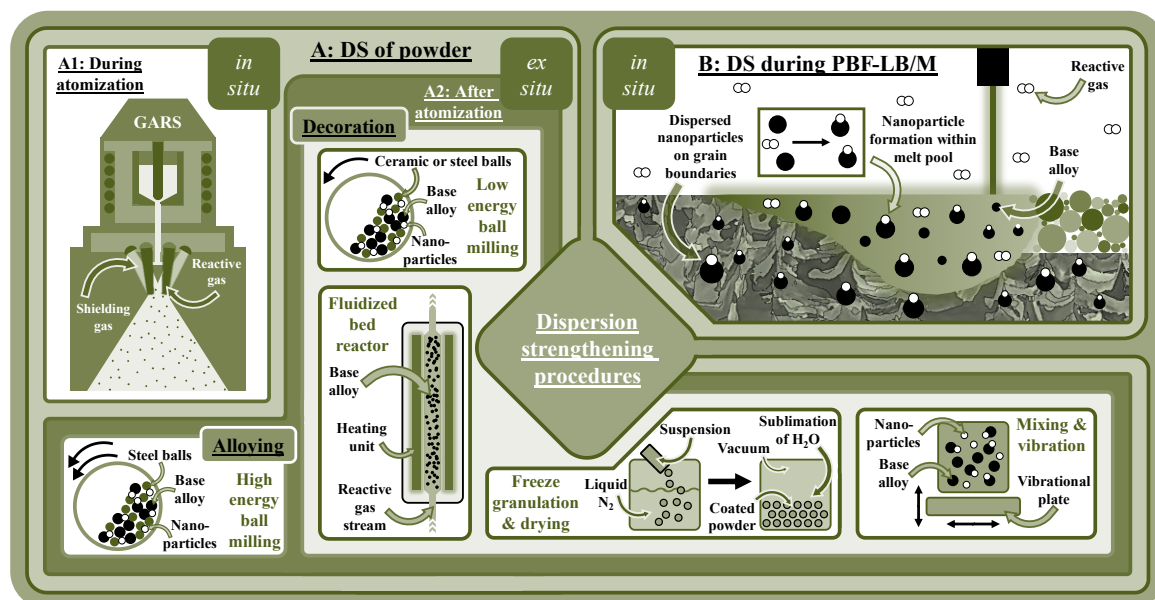


**Figure 5** A selection of dispersion strengthening procedures, split into A (DS of powder) and B (DS during PBF-LB/M), with A being further classified to A1 (during atomization) and A2 (after atomization).

mechanism [119]. Agglomerates of NP are avoided during both these methods due to a constant momentum of the particles [118,119]. Further decoration methods are low-energy ball milling [120] or ultrasonic vibration [121]. Freeze granulation and drying (FGD) might be considered as another process [122,123]. Here, the base alloy is first mixed to a suspension with water, an organic binder, and nanoparticles, and exposed to liquid nitrogen at -196 °C. Afterwards, via application of sublimation in a vacuum atmosphere, the water gets extracted from the particles without destroying their morphology, and the binder is removed. Powders homogeneously coated with nanoparticles result. Also, new approaches based on further operating principles are constantly being developed. For instance, pulsed laser fragmentation/irradiation of a suspension consisting of water and NP clusters results in the formation of nanosized, dispersed particles [124,125]. From this, in combination with a pH-balanced, electrostatic attraction in between base material and NP, MMNC feedstock material can be generated for application in AM [126,127]. Furthermore, diffusion during heated exposure of the base powder in a reactive gas atmosphere allows for the formation of new ceramic molecules and NP, respectively [36]. This may be carried out in a common furnace. However, the fluidized bed reactor makes use of a stream of the respective gas that enables a uniform flow onto the entire surface of the particles as they are rotating constantly. Besides the reactive gas, this process is further influenced by the

applied temperature and time, allowing for controlled diffusion and reaction processes within the powder. Thus, homogeneous nanoparticle formation, initiated all over the particle surface, is enabled.

To summarize, a multitude of powder modification routines for the subsequent additive manufacturing of MMNC exists with further techniques evolving steadily. The common drawback of most of the above decoration and alloying techniques is that they are laboratory scale, small batch processes, which results in a lower TRL than for GARS (TRL 4 or lower since most of the technologies are validated in laboratory-like environments only). Accordingly, their industrial applicability is still limited. However, it is not necessarily required to alter powder to fabricate a dispersion strengthened AM part. In changing the gas atmosphere of the process chamber, DS may also occur directly during PBF-LB/M of powders to parts (B). This way, common, non-modified, and process-stable powder can be used for AM. Like GARS, this approach occurs *in situ* during the phase transitions from solid powder to liquid melt to solid part. As mentioned before, the free energy of formation determines which type of ceramic molecule is most likely to evolve in an alloy. Thus, a process chamber revealing a reactive gas, like oxygen or nitrogen, or a gas mixture of reactive and shielding gas, allows NP to form in the moment of liquid aggregate state of the alloy, which itself has to reveal minor additions of highly reactive elements like Y, Mn or Ti, for instance [101,115,128,129]. During the respective

NP formation, marginal residues of reactive gases inside the build chamber are already sufficient to form a remarkable share of nanoparticles within the part [115]. Efforts are also undertaken to combine the beforementioned DS effects. More precisely, powders revealing nanoparticles, either dispersed throughout their microstructure, or in form of a surface shell, are further conditioned with a tailored process gas during PBF-LB/M [28,130]. This leads to an increase of the NP quantity that was present in the powder already, and/or creates further ceramics on the nanoscale due to chemical reaction in between melt pool and chamber atmosphere. Therefore, via DS during both, powder and part manufacturing, the respective nanoparticle share within the alloy can be increased even more, eventually further reinforcing its mechanical properties.

## 2.3 The material

*The material* provides an overview about common, non-NiCu-based materials (2.3.1), and NiCu-based materials, including Alloy 400 (2.3.2), both with an emphasis on materials in the field of additive manufacturing.

### 2.3.1 Non-NiCu-based materials

Even though new materials are constantly being qualified for application in AM, a comparatively small number of alloys is considered to hold the main share of materials used in metal-based 3D printing industry, both in general and in specific concerning PBF-LB/M (Figure 6) [11,15]. These alloys are:

- *Titanium-based*, esp. Ti-6Al-4V,
- *Cobalt-based*, esp. CoCr alloys,
- *Nickel-based*, esp. superalloy IN718,

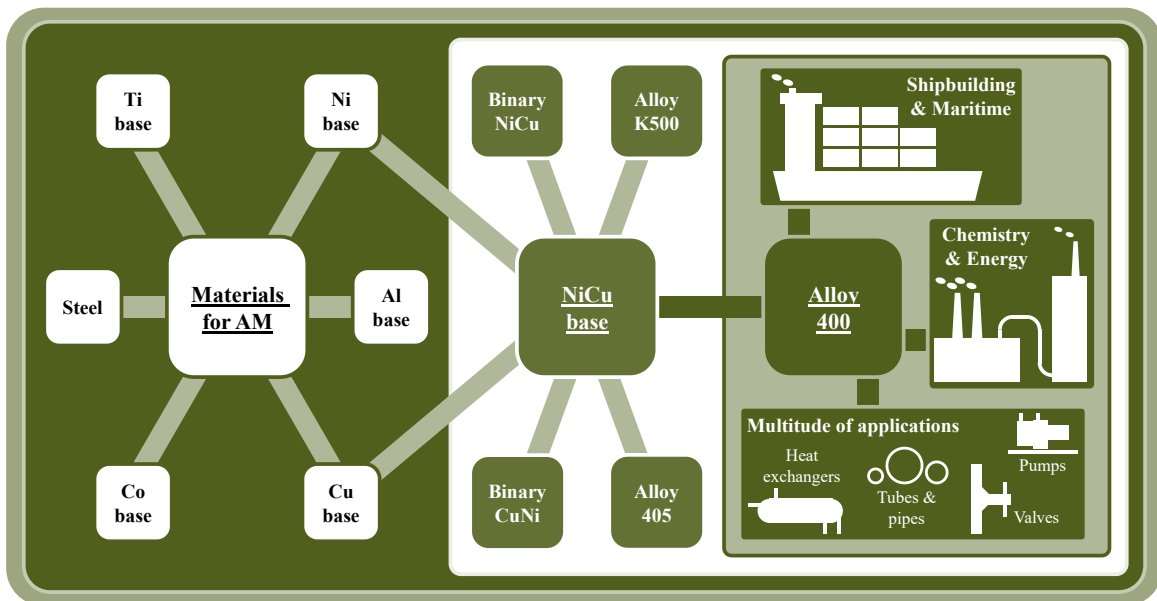


**Figure 6** Common materials in metal additive manufacturing and NiCu-based alloys, including Alloy 400 and a selection of its applications.



- *Copper-based*, esp. pure Cu, CuCrZr, bronzes like CuSnNi and NiAl bronze (NAB), and CuCrNb,
  - *Aluminum-based*, esp. AlSi10Mg,
  - *Steels*, esp. stainless steel and tool steel.
- [11,15,22,26,43]

Among the Ti-based alloys, additively manufactured Ti-6Al-4V stands out with an immense industrial interest, especially in automotive, aerospace, and biomedicine [15,131–133]. This is mainly due to the combination of two outstanding advantages: exceptional strength while still allowing lightweight design, and a high corrosion and wear resistance [131,132,134].

Cobalt-based alloys instead, and especially its CoCr-variant (Cr for improved strength and corrosion resistance, respectively), are especially used in dentistry as prosthetics, implants, or crown frames, where it represents a more convenient alternative for nickel-allergic patients [135–137]. For these highly patient-individual products, AM of CoCr can be considered the most effective manufacturing method [12,137].

Nickel superalloys find their main application in turbines for both power generation and airplanes, with near-net-shape AM providing a significant advantage over the machining difficulties faced during CM, that are evoked by the pronounced hardness of this alloy type [43,133,138]. Among the Ni-based superalloys,  $\gamma'$  and  $\gamma''$  forming IN718 is frequently used as it allows for use cases at elevated temperatures beyond 700 °C,

as required in gas turbines or during rocket operation, for instance [138,139].

A fundamentally different group of materials is formed by the Cu-based alloys, which are known for their excellent electrical and thermal conductivity, and their corrosion resistance [140,141]. This qualifies them for a wide range of applications, like induction coils, heat exchangers or even components of combustion chambers, as frequently required in industries like aerospace, electronics and automotive [140–143]. While pure Cu reveals the highest conductivity, a multitude of further Cu-based alloy systems are additively manufactured as well. Its most important representatives for the industry are CuCrZr (high conductivity combined with increased strength due to precipitation formation when age-hardened), Glenn Research Copper (GRCop; a CuCrNb alloy with exceptional high-temperature and oxidation properties, tailored for space applications), and bronze (high strength, toughness, ductility, and corrosion resistance) [141–144]. Bronze, in turn, can be further split up into its most common, additively manufactured variants of CuSn/CuSnNi (used in bearings) and NAB (used for propeller repairing in maritime) [141,145,146].

AlSi10Mg must be mentioned among the Al-based alloys that find their application in AM. Forming Mg<sub>2</sub>Si precipitates when age-hardened, this alloy offers an excellent ratio of strength to weight, which, in combination with DfAM, offers a multitude of use cases esp. in aerospace

and automotive [98,147]. Moreover, this alloy type especially qualifies as a MMNC via the formation of potential nano ceramics and intermetallics like  $\text{TiB}_2$ ,  $\text{TiN}$  or  $\text{Al}_3\text{Zr}$  throughout the metal matrix [26,97,98].

Ultimately, and alongside the beforementioned Ti-based alloys, steels form one of the two biggest groups of materials in AM (approx. 35 % each) [11,43]. Stainless steel and tool steel are required in both medical and tooling [43,148]. The stainless 361L for instance provides high corrosion resistance and a good tradeoff between ductility and strength, qualifying it for multiple AM use cases [15,43,148]. This tradeoff can also be found in maraging steel, an age-hardened martensitic steel with high nickel ( $\sim 18$  %) and low carbon ( $< 0.03$  %) shares [149]. Tool steels however, like H11 or H13, reveal excellent hardness and toughness, and allow for pronounced temperature fluctuations, qualifying them for dies and molds [150,151].

To summarize, even though a comparably small number of materials are yet qualified for AM, many applications can be realized in nearly all sectors. However, some important use cases are missing, especially in the maritime and chemical industries. NiCu-based alloys provide a remedy here, also in contrast to the purely Cu- or Ni-based alloys.

### **2.3.2 NiCu-based materials and Alloy 400**

NiCu-based alloys are of particular interest to the industry as they offer a wide range of benefits that occur simultaneously: high toughness and strength, outstanding resistance to corrosion, and good wear properties [45,88]. Accordingly, as chemical, electrical and maritime industry rely heavily on these peculiarities, it is used frequently throughout these sectors for valves, pumps, or propellers [44–46,88,152]. This alloy type is also referred to as the Monel family. First introduced by the International Nickel Company in 1906, the name of the new alloy system was set in accordance with the former company president, Ambrose Monell [44,88]. A common characteristic of these Monel alloys is that they are generally fcc solid solutions. Since the two main ingredients, Ni and Cu, both reveal this crystal structure, they allow for a wide range of alloying elements to be added while still remaining in solid solution [45,88,152–154]. However, even though being one-phased, the noticeable gap in between nickel and copper melting temperatures of nearly  $400^\circ\text{C}$  evokes segregations of the low-melting Cu in the interdendritic region during solidification [48,88,153]. Consequently, dendrite cores experience a higher Ni concentration as the solidus of this element is reached earlier during cooling and grain nucleation, respectively [88]. When slow cooling rates are present, as during casting or hot-extrusion for instance, NiCu-based alloys generate dendritic microstructures, while during



rapid solidification, as occurring during AM processes, considerably finer, more equiaxed cells start to form [88].

Within this fascinating material family, the most important representatives are alloys K500, R405, 400, and the binary NiCu/CuNi variants. Interestingly, even though (high) copper additions to pure nickel do not significantly enhance mechanical properties of the resulting binary NiCu alloy, this alloy type is still frequently used [88]. Mechanical properties are slightly improved as per both solid solution strengthening and grain refinement, while Cu also provides the alloy with an increased corrosion resistance and electrical conductivity [88,155]. Consequently, fasteners for the chemical industry or series resistors in electrical components are fabricated from this material type.

The counterpart of binary NiCu, the binary CuNi alloy, includes up to 30 % of Ni and shows excellent corrosion resistance while also providing thermal stability [141,156]. Due to copper being the primary element, its electrical conductivity is higher than of the NiCu-based materials which is why it is preferably used for electric components [154,156]. This alloy type finds its application in maritime, water treatment or the oil and gas sector with AM of CuNi being used for reparation of worn parts [141,156].

Monel type K500 is of particular interest as it is an age-hardenable alloy that forms  $\gamma'$  precipitates around 750 °C, significantly increasing both mechanical properties and operation temperature due

to dislocation mobility restriction [88,152,153]. These  $\text{Ni}_3(\text{Ti},\text{Al})$  compounds evolve throughout the microstructure due to considerable additions of up to 1.0 wt.-% titanium and 3.5 wt.-% aluminum to the NiCu base (Ni balance, Cu 27.0–34.0 wt.-%, all values approximate). Within K500,  $\gamma'$  is accompanied by further solid solution strengthening, evoked by  $\leq 2.0$  wt.-% iron,  $\leq 1.5$  wt.-% manganese,  $\leq 0.5$  wt.-% silicon, and  $\leq 0.2$  wt.-% carbon. (Offshore-) maritime and (petro-) chemistry make frequent use of this alloy type as it reveals high corrosion resistance and durability in (sea) water, alkalis, and salt solutions. Propeller shafts and reinforcements/coatings at water splash zones are resulting, common products [88,157]. Nowadays, AM of K500 is rather utilized for repairing and maintenance purposes than for original printing of such high-volume parts [157,158].

A comparable alloy with significantly smaller technical application is Alloy R405. Due to an increased sulfur share, NiCu sulfides are evoked, acting as chip breakers, and thus, allow for excellent machinability [44]. Apart from that, the properties and applications of R405 are very much in line with the remaining NiCu-based alloys [46].

Ultimately, the NiCu family harbors Alloy 400. In comparison to K500, the 400 type requires a narrower chemical intervention limit: While the alloy barely includes aluminum and titanium, manganese is added. Thus, and in accordance with material no. 2.4360 of

DIN 17743:2002-09, the composition can be narrowed down to:  $\geq 63.0$  wt.-% nickel (including  $\leq 1.0$  wt.-% cobalt), 28.0–34.0 wt.-% copper, 1.0–2.5 wt.-% iron,  $\leq 2.0$  wt.-% manganese,  $\leq 0.5$  wt.-% silicon,  $\leq 0.5$  wt.-% aluminum,  $\leq 0.3$  wt.-% titanium,  $\leq 0.15$  wt.-% carbon, and traces of sulfur. However, in industry, slight deviations from this standard are tolerated to achieve customer-specific material properties. Like the other Monel alloys, high corrosive resistance against several media qualifies Alloy 400 for the use in maritime (shipbuilding, offshore platforms, marine technology, etc.) and chemistry/energy (crude petroleum, oil, fuel, and gas production, food processing, distillation and alkylation plants, etc.) [47,48]. In syngas power plants for instance, a temperature range of approx. 450–650 °C, a strongly carburizing atmosphere, and a low oxygen partial pressure evoke metal dusting [159,160]. Alloy 400 can withstand this severe type of corrosion to a certain extent only, but when the Cu content is increased further (inhibiting effect of Cu on CO dissociation), and the carbide and oxide formers are reduced, an effective use in this environment is possible as well [160]. In terms of aqueous corrosion, the single-phased solid-solution shows excellent resistance against phosphoric, organic, hydrofluoric, and sulfuric acid, as well as alkalis, salts and sea water [161]. Enabled by these characteristics, the most common products made of Alloy 400 are (c.f. Figure 6):

- Pumps / pump shafts and impellers,

- Maritime fixtures, valves, and fasteners,
  - Condenser and heater tubes of heat exchangers,
  - Containers and tanks,
  - Pipes in power plants (feed water, steam generation, etc.),
  - Evaporators and heaters for brines in salt works,
  - Electrical components.
- [46,48,161,162]

The Alloy 400 E-modulus for tension and compression is 179 GPa and the one for torsion amounts to 65 GPa [162]. The nominal density can be determined with 8.80 g/cm<sup>3</sup> and the ultimate tensile strength (UTS) and yield strength account for 552 MPa and 276 MPa, respectively, revealing an elongation at break of approx. 45 % [161,162]. The material has a Vickers hardness around 100–250 HV, with all mechanical properties very much depending on the finishing process and the form of the material [47,48,162]. Thus, an exceptional UTS of up to 1241 MPa is feasible for cold drawn, full hard spring tempered wires (correspondingly, elongation would lower to max. 5 %), while for hot rolled and annealed sheets, it would be limited to 482 MPa (revealing an elongation of ~ 50 %) [162]. The Poisson's ratio accounts for 0.32 and its melting range is from 1300 °C (solidus) to 1350 °C (liquidus), while with a Curie temperature in between 21 °C and 49 °C, minor ferromagnetic behavior may occur at room temperature [162]. Its fracture type is always ductile, meaning that it does not undergo a ductile to brittle transition in CM and even shows ductile fracture

mechanisms near the absolute zero [47]. With a thermal conductivity  $\kappa$  of approx. 22 W/mK, a specific heat capacity  $c$  of 427 J/kgK, an electrical resistance  $R$  of  $0.511 \Omega\text{mm}^2/\text{m}$  (all at room temperature), and a pronounced reflectivity, the overall energy absorptivity of the alloy is limited [47,48,162]. This is especially detrimental in PBF-LB/M of Alloy 400 since an effective incorporation of the laser energy into the powder bed is decisive for the generation of a highly dense part. Thus, the 3D printing process window of this alloy type is rather narrow, even increasing the need for a consistent Alloy 400 AM process route.

# Chapter 3

OBJECTIVES AND SCOPE

Up to the present time, no holistic process route has existed for additive manufacturing of Alloy 400 and thus, also not for its applicability to PBF-LB/M. Consequently, in order to close this research gap, this work establishes such production sequences for both unmodified and DS-modified Alloy 400 material systems. The desired outcome is that technological maturity is reached and that the respective increased TRL leads to the adoption of this material in an additively manufactured state in both academia and industry. First, unmodified standard Alloy 400 has to be portrait against its conventionally manufactured counterpart and the peculiarities, resulting from the PBF-LB/M process, elaborated. Based on these findings, further modification of the material and the process can then be undertaken. Ultimately, a clear statement on how to 3D-fabricate this alloy and to what extent the creation of a dispersion strengthened Alloy 400 is feasible must be available.

#### *PBF-LB/M of unmodified Alloy 400*

Following the general outline of AM workflows, a pre-, in-, and post-process is conducted for the standard variant of Alloy 400. This sequence essentially consists of:

- Alloy composition and bulk material selection,
- Atomization, powder post-processing, and characterization,
- DfAM adjusted CAD and build job preparation,
- PBF-LB/M optimization of parameters and component manufacturing,

- Part post-processing, mechanical testing, and characterization.

The alloy composition must be kept in line with the standard during the complete process chain. Hence, the tolerances of the respective alloy elements have to be met precisely before bulk material loading to the VIGA atomizer. Chemical consistency must be ensured and thus is being checked after each process step. Tailoring of a well-defined atomization process is following. The interplay of the most important process parameters of target temperature, outlet diameter, and applied pressure, summing up to an optimum metal mass flow and resulting in a high yield of powder particles within the target range, must be well set. Sieving and air-classification are then used to precisely adjust the final particle size distribution. Powders are characterized afterwards, allowing to conclude for an effective powder generation process with particles meeting the morphology requirements of high sphericity, density, and resulting flowability. Meanwhile, components to be printed have to be designed via CAD software, taking into account the decisive DfAM rules to generate components that meet the relevant criteria of manufacturability and function integration likewise. A unique support structure design for every component, their orientation in the build space, and most importantly, the definition of ideal process parameters to obtain near-net-shape components requiring as little post-processing as possible, follows. To complete the image, extensive material characterization on the micro- and nanoscale, and mechanical

testing needs to be carried out. Following this approach, the discovery of fundamental novelties on additively manufactured Alloy 400 of the standard chemical composition is targeted. This allows to answer the following questions:

- Is it possible to generate powders from bulk material via the VIGA process?
- Are the resulting powders usable for the PBF-LB/M process?
- What peculiarities can be revealed concerning the powder microstructure?
- Is there a PBF-LB/M process parameter window for dense sample manufacturing?
- Which special features can be detected for the parts and how do they differ from the powders?
- What are the differences between AM and CM of Alloy 400?

Moreover, only on the basis of a holistic understanding of the AM process chain for this material type, further modification of its chemistry can be undertaken. Thus, in chronological order, the standard variant must be qualified first, and the modification routes can be evaluated in the following.

#### *PBF-LB/M of MMNC Alloy 400*

In order to apply an assessment of the various dispersion strengthening techniques, and to evaluate their suitability for PBF-LB/M of Alloy 400, five criteria of general feasibility along a modification flow (Figure 7) have to be taken into consideration:

- *C1 atomization*, bulk material can be atomized to powder,
- *C2 powder NP*, nanoparticles are evoked within powders,
- *C3 printability*, powders can be printed to dense parts,

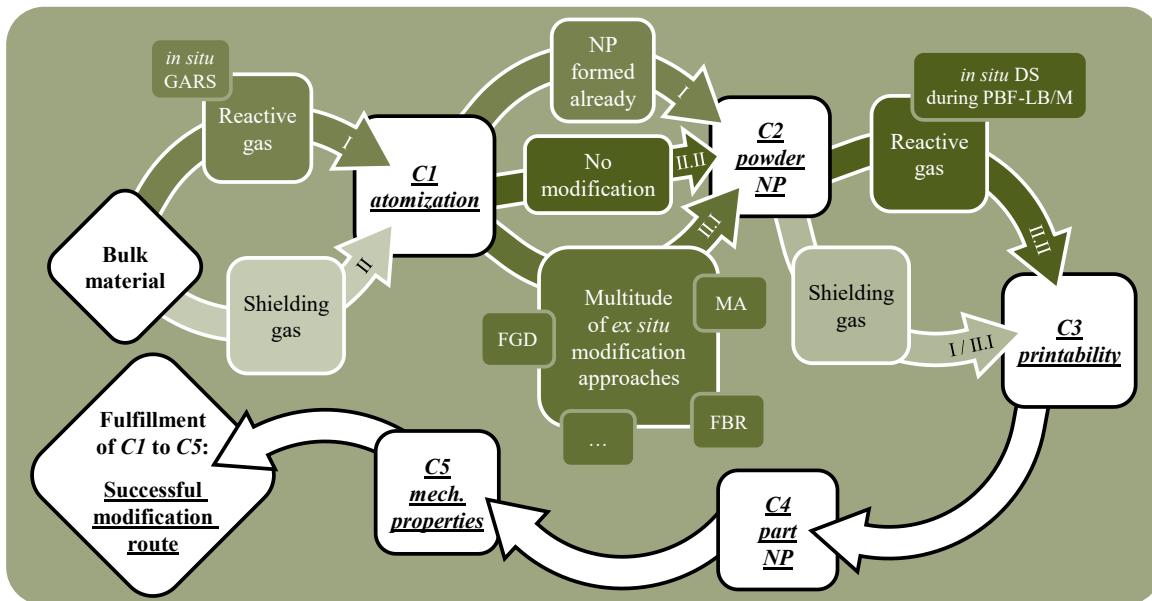


**Figure 7** Modification flow along the entire process chain, indicating multiple DS approaches during and after powder atomization, and during PBF-LB/M.

- *C4 part NP*, nanoparticles are evoked within parts,
- *C5 mech. properties*, the NP implementation causes enhanced mechanical properties.

In addressing the questions raised for unmodified and modified material, a final, complete statement on *Laser Powder Bed Fusion of Dispersion Strengthened Alloy 400* can be made.

Depending on the modification applied, the five criteria might be considered in a varying sequence. In the context of this work, four different modification routes were considered: mechanical alloying, freeze granulation and drying, gas atomization reaction synthesis, and fluidized bed reactor. As displayed, the *in situ* GARS approach follows the “I”-path whereas MA, FGD, and FBR are located along the “II/II.I”-way. An *in situ* DS modification approach during PBF-LB/M as per “II.II”, however, was originally not considered in this work. The outcome of the modification flow is a rating, allowing to conclude for successful modification routes to be pursued further, and unsuccessful ones, that should be discontinued as they failed to pass one or any of the five criteria issued. This allows to make a statement about the following:

- Are there any modification routes to alter Alloy 400 powder with ceramic nanoparticles?
- Which modifications do further qualify for dense sample printing?
- To what extent does the appearance of nanoparticles change within printed MMNC (compared to the one in powders)?
- Do the nanoparticles evoke an improvement in mechanical properties of printed components as per the DS mechanism?

# Chapter 4

CONTRIBUTION TO  
ORIGINAL KNOWLEDGE



In the context of this work, three first-authored publications were published on PBF-LB/M of Alloy 400; the first one on unmodified material, the second and the third one on modified material. Within this framework, the following original knowledge was generated.

#### **4.1 Applying laser powder bed fusion to Alloy 400**

The first publication on *Establishing a process route for additive manufacturing of NiCu-based Alloy 400: an alignment of gas atomization, laser powder bed fusion, and design of experiments* [1] set up a complete AM process chain for the alloy type at hand (c.f. chapter 7.1). It reached over the entire scope, beginning with the alloy composition and the targeted applications and concluding with mech. testing. In between, powder production and characterization such as PBF-LB/M parameter optimization were carried out and the microstructure evolution was analyzed. Throughout this study, the following novelties were found:

- *Powder production*, powders were generated via a CCA VIGA method that can be optimally adjusted to the desired PSD,
- *Powder characterization macro-scale*, powders were found to be highly spherical, dense, non-agglomerated, and mostly satellite-free, allowing for optimum flowability and the formation of a densely packed powder bed during PBF-LB/M,
- *Powder characterization micro-scale*, besides revealing a consistent chemistry with the initial bulk material, single particles consisted of fine grains (mean diameter approx. 5  $\mu\text{m}$ ), and the characteristic copper-segregation phenomena of NiCu-based alloys at grain boundaries could be verified for the present powder state as well,
- *PBF-LB/M parameter optimization*, the design of experiments revealed a single, optimum parameter set of  $p_L = 85 \text{ W}$ ,  $s_s = 1050 \text{ mm/s}$ , and  $d_H = 50 \mu\text{m}$  at a layer thickness of 20  $\mu\text{m}$ , while simultaneously, it was found that the volume energy density, as a frequently used key figure in PBF-LB/M process parameter optimization, is susceptible to being misleading and thus, should be neglected,
- *Part characterization macro-scale*, again being consistent in chemistry, almost completely dense parts (optical relative density approx. 99.9 %) were manufactured via PBF-LB/M, while process-related, minor gas inclusions, evoking keyhole porosity, could not be completely avoided,
- *Part characterization microscale*, AM-typical columnar grain growth along the build direction was confirmed, and an overall finer grain size in comparison to conventionally fabricated material (approx. 16  $\mu\text{m}$  and

- 200  $\mu\text{m}$ , respectively) and a weak [101] texture were found,
- *Part characterization nanoscale*, grains consisted of a micro-dendritic structure with pronounced dislocation formation along cell walls, while Cu segregations were less pronounced than in powders,
  - *Part mech. testing orientations*, printed tensile specimens showed a directional dependence with high strength and low ductility for horizontally fabricated parts and vice versa for upright geometries, being correlated with the build direction dependent anisotropy evolving during layer-wise AM processes,
  - *Part mech. testing AM vs CM*, additively manufactured material revealed higher strength but lower ductility along the whole tested temperature range, being correlated with the overall finer grain structure.

In the course of this publication and based on the above findings, further metal-physical mechanisms could be narrowed down. For instance, the reason for Alloy 400 revealing a [101] grain orientation, even though a [001] texture would be expected from a fcc NiCu-based alloy, is that the evolving dendrites yield into both the build plane and the build direction. This can be traced back to the product of the vertical growth along the melt pool boundary ( $\triangleq$  onset of cooling from heat affected zone towards the melt pool core, x-plane, [100]) and the growth towards the energy input ( $\triangleq$  cooling resulting

from the direction of the laser, z-plane, [001]). The resulting texture is [101]. The description of the texture being slightly pronounced only originates from the nature of the layer-by-layer manufacturing sequence. It was found that a melt pool reaches approx. 80  $\mu\text{m}$  deep, while the applied layer height was set to 20  $\mu\text{m}$  only. Thus, by a factor of 4, respective layers experience a multiple remelting, ultimately decomposing the ideal melt pool that would generate a pronounced [101] texture. This also gave reason for the difference in strong Cu segregations in powders and considerably weaker ones in parts. During atomization, rapid cooling occurs once. During PBF-LB/M instead, cooling occurs several times with heat affected zones reaching deep into the material. This causes diffusion processes within the solidified part, counteracting the chemical imbalances in between copper and nickel. As a result, Cu from the Cu segregation area dissolves into the inner grain matrix and correspondingly reversed, Ni is being transferred from the grain cores to the segregations, ultimately lowering the Cu segregation effect.

To summarize, and concerning the three pillars of this work, *the manufacturing* and *the material* were accurately addressed in defining a PBF-LB/M process route for Alloy 400, while *the mechanism* has not yet been dealt with as no dispersion strengthening was applied throughout this procedure. Further findings concerning fractography [4], and creep and fatigue [5] of standard Alloy 400 are documented in co-authored publications (c.f. appendix 8.1 and 8.2).

## 4.2 Paving the way for dispersion strengthening of Alloy 400

In accordance with the previously described modification flow, it was found that two of the four modification routes (mechanical alloying, freeze granulation and drying) did not qualify for a robust process chain, as they failed to pass one or more of the five criteria. Consequently, no publications resulted on these modifications. Still, it is an important part of the original knowledge to report on them and to explain the respective sources of failure. Only this way, future attempts may consider these conclusions to avoid similar error patterns. The other two techniques (gas atomization reaction synthesis, fluidized bed reactor), however, showed tremendous potential and thus, were investigated in greater detail that led to publications 2 and 3. In the following, all four attempts to create a MMNC Alloy 400 system are documented. They are also classified into a modification matrix, that is building up on the modification flow and portrays the five criteria against each modification route conducted (Figure 8).

### *Mechanical alloying*

Initial trials were conducted in high and low energy ball mills to follow the concept of mechanical alloying. Besides the standard variant of Alloy 400 powders,  $Y_2O_3$  was used as the ceramic component. The intention was to micro-weld the nanoparticles into the surface of the base alloy system to be used as feedstock material for PBF-LB/M. These oxides should then get homogeneously distributed within the melt pool, leading

to the formation of a MMNC component. However, due to the usage of steel balls during milling, the original, spherical shape of the comparably soft Alloy 400 particles got destroyed. A flake-shaped powder resulted, not meeting the criteria of flowability and absorptivity during AM. Therefore, even though *C1* and *C2* were met, *C3* critically failed, which is why this modification had to be terminated. On this basis, a similar attempt was carried out for low energy ball milling, but instead of using steel balls, ceramic spheres were loaded into the mill and the rotational speed was reduced. As desired, no severe deformation of the particles occurred and a processable composite of base alloy and nanoparticles resulted (c.f. MA line of the modification matrix). Also, these nanoparticles were detected within the solid metal matrix after printing. Thus, *C3* and *C4* could now be reached. Unfortunately, immense clustering of  $Y_2O_3$  occurred within the melt pool, also revealing bad wettability with the matrix. Thus, despite dispersed oxides that contributed to the DS effect, Ytria pores on the macroscale facilitated crack initiation and growth when exposed to mechanical load. Thus, *C5* failed as the performance of the reference material could not be met, and the concept of mechanical alloying of Alloy 400 was not pursued any further.

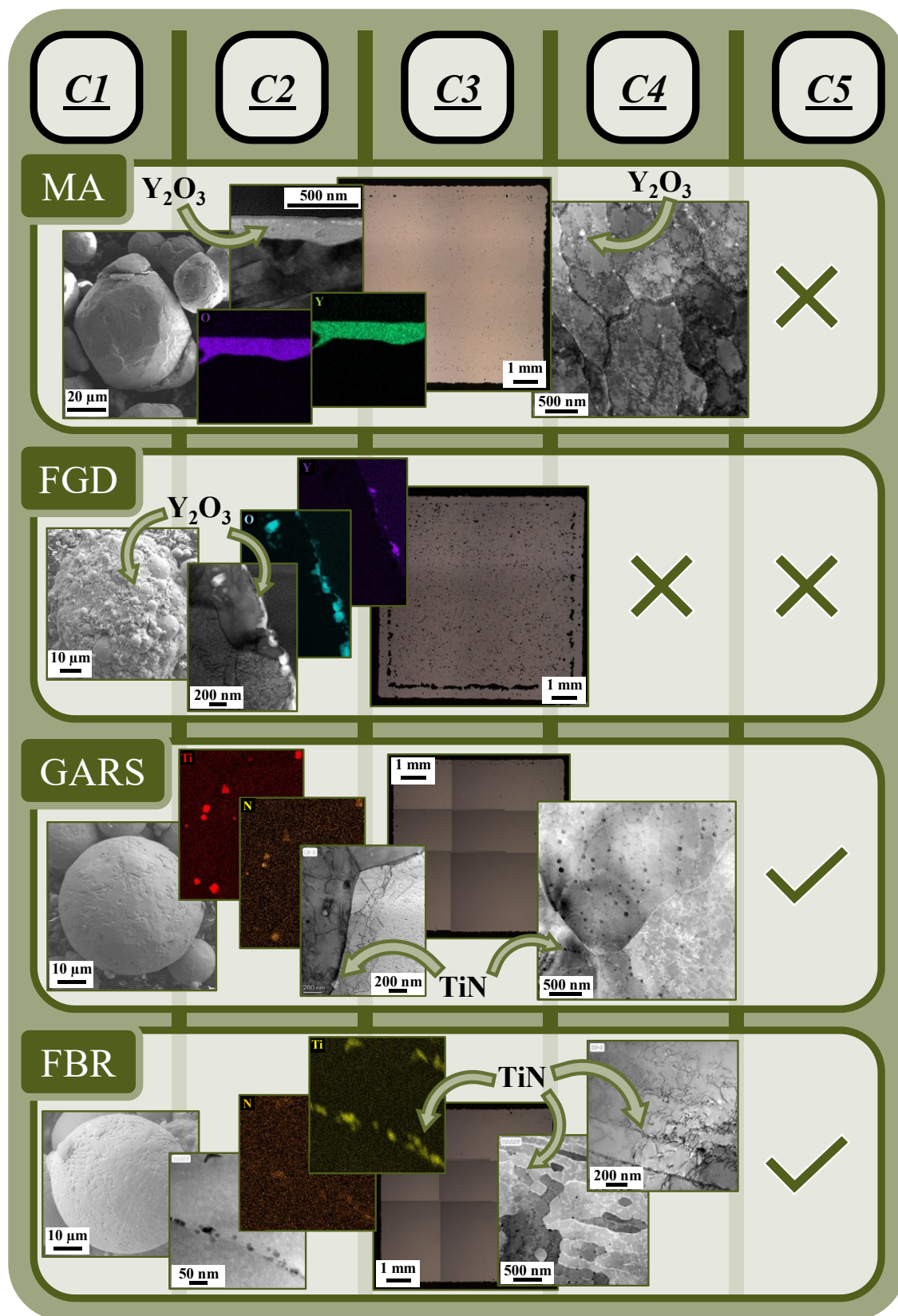


**Figure 8** Criteria evaluation for mechanical alloying, freeze granulation and drying, gas atomization reaction synthesis, and fluidized bed reactor along the modification flow, resulting in a modification matrix.

### *Freeze granulation and drying*

A freeze granulation and drying approach was carried out as well. The air-classified, fine powder fraction below 15  $\mu\text{m}$  was used to generate a compound of the base alloy and the nano Yttria. Fully coated particles resulted, then revealing the desired PSD (c.f. FGD line of the modification matrix). Therefore, it is generally possible to generate a nearly spherical powder feedstock from Alloy 400 via this routine (fulfillment of C2). However, since the outer shell of the particles now consisted of a ceramic primarily, and not of a metal anymore, the laser absorption during PBF-LB/M decreased substantially, which is why insufficient energy was introduced into the powder bed. Highly porous parts resulted. This issue could not be circumvented by an adjustment of the process parameters, which is why the freeze granulation and drying concept was aborted at C3.

### *Gas atomization reaction synthesis*

Following a GARS design, two attempts were made to form nanoparticles *in situ* during atomization: atomization in synthetic air, evoking  $\text{ZrO}_2$  in a zirconium enriched Alloy 400 version, and atomization with pure nitrogen, resulting in  $\text{TiN}$  nanoparticles in a titanium enriched Alloy 400 variant. Thus, the ceramics were not added to the process as solid particles as with MA or FGD but evoked via a reaction of the gas and a reactive element of the alloy. The zirconia variant revealed a limited success concerning the formation of nanoparticles in powders since a few oxides only were

detected within atomized particles. Printing these powders was feasible but no dispersoids could be detected on the nanoscale of the resulting components. Instead,  $\text{ZrO}_2$  appeared to agglomerate, forming voids of several hundreds of nanometers. These cavities were classified as detrimental porosity and did not act as a strengthening phase. Therefore, multiple criteria were only met partially with C5 not being achieved in its entirety. In contrast, the nitrogen-based GARS attempt revealed high potential and was investigated in detail (description in chapter 4.3). The new alloy could be printed densely, revealed a high number of nanoparticles, and performed better than unmodified material in terms of strength, elongation, creep, and fatigue (c.f. GARS line of the modification matrix). These findings were first published in a long abstract (appendix 8.3), that served as the basis for the second publication (c.f. chapter 7.2).

### *Fluidized bed reactor*

A novel concept for powder conditioning was carried out by exposure to the fluidized bed reactor of Alloy 400 in chemically modified states. Comparable to the GARS approach, a Zr- and a Ti-enriched material were used to form the respective nanoparticles. The process is mainly influenced by the process variables of applied temperature and time exposed. To allow diffusion processes of the reactive gas into the powder particles, an alloy-dependent minimum of time and temperature must be applied. This interplay did not work out for the Alloy 400 variant including Zr in order to form



ZrO<sub>2</sub> when exposed to synthetic air. Diffusion occurred throughout the entire powder and thus, excessive oxidation of all elements occurred. It was not possible to adjust the process in such a way that diffusion only occurred with regard to the zirconium. Printing of this powder feedstock evoked massive pore formation, not allowing any continuation along the modification flow. The FBR approach for Alloy 400 + Zr therefore had to be aborted at C2 and C3, respectively. As already determined for the nitrogen GARS attempt, the nitride forming FBR variant performed significantly better than its oxide counterpart. A very high number of nanoparticles in both powders and parts was detected, and the mechanical properties, especially in terms of creep and fatigue, were significantly increased again compared to the GARS approach (c.f. FBR line of the modification matrix, description in chapter 4.3). It served as the basis for the third publication (c.f. chapter 7.3).

To summarize, all modification approaches utilizing a kind of oxide did not qualify for a robust process chain. It was found that these oxides eventually evolved to macroscaled pores during PBF-LB/M, and/or were susceptible to nanoparticle coarsening and agglomeration. The two attempts forming nitrides, however, allowed for an optimal integration of the nanoparticles into the base alloy matrix. Highly dense and reinforced components resulted. This differentiation between oxides and nitrides in Alloy 400 is seen as another valuable result.

### 4.3 Exploiting dispersion strengthening of Alloy 400

As stated, the two nitrogen attempts of *in situ* GARS and *ex situ* FBR were considered for holistic Alloy 400 MMNC PBF-LB/M modification routes. In the following, the gas atomization reaction synthesis approach is paraphrased first, followed by the fluidized bed reactor method.

The second publication on *The dispersion-strengthening effect of TiN evoked by in situ nitridation of NiCu-based Alloy 400 during gas atomization for laser powder bed fusion* [2] documents the first time attempt on GARS of Alloy 400 in order to create a novel MMNC during atomization (c.f. chapter 7.2). The findings below were obtained in the course of this work:

- *Powder production*, via a CCA GARS method, and respective sieving and air-classification, Ti-enriched Alloy 400 bulk material can be atomized to well-processable powder,
- *Powder characterization micro-scale*, TiN nanoparticle formation was proven to have occurred during atomization, mainly being localized on grain boundaries and within the interdendritic region of the particle surface,
- *Powder characterization nano-scale*, both dislocation formation and Cu segregation could be verified for the grain boundary regions within powders, and cuboidal TiN was detected along the grain boundaries as well,

- *PBF-LB/M parameter optimization*, up to 99.84 % dense components can be manufactured by application of the process parameters  $p_L = 85 \text{ W}$ ,  $s_s = 1050 \text{ mm/s}$ ,  $d_H = 70 \text{ }\mu\text{m}$ , and  $t_L = 20 \text{ }\mu\text{m}$ ,
- *Part characterization microscale*, columnar grain evolution towards the direction of introduced energy was detected, barely revealing any texture, which was justified with the iterative remelting sequence of the PBF-LB/M process,
- *Part characterization nanoscale*, a highly refined, dislocation- and segregation-rich cellular network evolved during additive manufacturing, revealing a multitude of TiN nanoparticles and, to a much lesser extent, alumina,
- *Part mech. testing tensile*, the GARS processed material reveals superior UTS compared to both unmodified PBF-LB/M Alloy 400 and the CM counterpart along the whole temperature range, and it also shows enhanced ductility as a result of DS,
- *Part mech. testing creep*, a substantial improvement of creep lifetime from unmodified to MMNC Alloy 400 of an order of magnitude was found, which still lags behind the time to fracture of CM material, but at an identical creep rate.

Despite the extensive capabilities of the nitrogen GARS process route, the FBR one revealed an even higher potential for

this alloy type. The resulting third publication thus deals with *The Dispersion-Strengthening Effect of TiN Nanoparticles Evoked by Ex Situ Nitridation of Gas-Atomized, NiCu-Based Alloy 400 in Fluidized Bed Reactor for Laser Powder Bed Fusion* [3] (c.f. chapter 7.3). This publication does not only document the advancements of the respective modification route but also portrays the FBR approach against the GARS one, so that concrete differences are directly revealed. The following advancements in material science of the alloy at hand can be stated:

- *Powder production*, CCA VIGA of the Ti-enriched Alloy 400 was conducted and resulted in appropriate powder morphology,
- *Powder characterization before FBR microscale*, the remaining nitrogen during VIGA was already sufficient to form first nanoparticles, both on the surface and the inside of particles, mainly on grain boundaries,
- *Powder characterization before FBR nanoscale*, the nanoparticles were proven to be TiN,
- *Powder modification*, exposed to a nitrogen gas stream over 4 h at  $800 \text{ }^\circ\text{C}$  in the fluidized bed reactor, a controlled diffusion process in solid state was activated, allowing for the formation of further TiN dispersoids inside the powder,
- *Powder characterization after FBR microscale*, the nanoparticle quantity rose due to the FBR

- exposure, being also considerably higher than in GARS powders,
- *Powder characterization after FBR nanoscale*, a bimodal size distribution of nanoparticles was detected and its type of origin correlated with either VIGA (coarse) or FBR (fine),
- *PBF-LB/M parameter optimization*, at  $p_L = 115 \text{ W}$ ,  $s_s = 900 \text{ mm/s}$ ,  $d_H = 60 \text{ }\mu\text{m}$ , and  $t_L = 20 \text{ }\mu\text{m}$ , highly dense components of approx. 99.9 % were manufactured, only revealing residual keyhole porosity,
- *Part characterization microscale*, with an average grain size of  $7.4 \text{ }\mu\text{m}$ , a GND mean of  $4.86 \times 10^{14} / \text{m}^2$  was reached throughout the microstructure, representing a significant increase to the  $3.58 \times 10^{14} / \text{m}^2$  in parts resulting from GARS powders,
- *Part characterization nanoscale*, the share of TiN nanoparticles was clearly increased to 6.5 % and caused by the interaction of the reactive elements within the melt pool, while to a small extent, alumina was detected as well, both allowing for effective dislocation pinning and shearing,
- *Part mech. testing tensile*, UTS and elongation at potential application temperatures above  $400 \text{ }^\circ\text{C}$  were increased compared to GARS material, showing ductile to brittle transition,
- *Part mech. testing fatigue*, a substantial improvement in endured cycles was achieved,

clearly higher than for both unmodified and GARS Alloy 400,

- *Part mech. testing creep*, an immense shift of creep lifetime can be denoted, being linked to the presence of NPs that successfully hinder dislocation movement and counteract the creep loss due to PBF-LB/M grain refinement.

Beyond these findings, concrete nanoparticle and segregation formation mechanisms were elaborated for both FBR powder and the resulting printed components. The presence of TiN nanoparticles primarily along powder grain boundaries was correlated with the presence of Cu segregations. During rapid solidification of VIGA, a considerable share of the copper tends to crystallize staggered compared to the remaining solid solution matrix. Thus, the Cu rich melt is forced to the grain boundary region by the constantly growing grain cores, where nucleation occurred first. Likewise, the TiN NPs are moved to the grain boundaries, as they are incorporated in the remaining melt. Therefore, Cu segregations in NiCu alloys and nanoparticles can be found in the same locations. During the fluidized bed reactor powder conditioning, elemental titanium from the matrix then reacts with the nitrogen that diffused into the particles. Further TiN is thus evoked along grain boundaries. A distinction can be made between the size of the nanoparticles as rather coarse ones of 50–100 nm result from VIGA and comparably fine NPs of some 10 nm are the outcome of the FBR process.



Nanoparticle bimodality can be denoted and detected after PBF-LB/M again. During additive manufacturing, elemental titanium reacted with the nitrogen of the printer atmosphere inside the melt pool and so, the TiN share rose significantly. Besides, alumina, that has not been present in powders, formed as well as a product of the aluminum of the base alloy and the oxygen in the build chamber atmosphere. This multitude of various nanoparticles dispersed homogeneously over the entire microstructure.

To conclude, the previously introduced process route for standard Alloy 400 was extended to MMNC variants of this material. Therefore, besides *the manufacturing* and *the material*, the third pillar of *the mechanism* was addressed in detail as well.

# Chapter 5

CONCLUSION AND OUTLOOK

Until today, there have been no attempts on holistic AM process routes for Alloy 400. Neither any knowledge was available on its applicability to PBF-LB/M, nor were any studies concerning its potential for dispersion strengthening. Touching the three thematic fields of *the manufacturing, the mechanism and the material*, the present work of *Laser Powder Bed Fusion of Dispersion Strengthened Alloy 400* was located in their midst and closed this pending research gap. First, standard Alloy 400 was qualified for the laser powder bed fusion procedure and afterwards, modified Alloy 400 variants were generated to design novel MMNC materials. Throughout the baseline study on *Establishing a process route for additive manufacturing of NiCu-based Alloy 400: an alignment of gas atomization, laser powder bed fusion, and design of experiments* [1], the VIGA process was well adjusted for the NiCu-based alloy, resulting in highly spherical powder being very well usable for subsequent AM. Cu segregation phenomena were verified for both powders and parts with the latter ones revealing an ultrafine, cellular nanostructure accompanied by a high number of geometrically necessary dislocations. The importance of single process parameter interdependencies was elaborated, and AM components showed enhanced strength, but reduced ductility compared to CM material, both being linked to a substantially finer grain structure. On this basis, the gas atomization reaction synthesis approach in *The dispersion-strengthening effect of*

*TiN evoked by in situ nitridation of NiCu-based Alloy 400 during gas atomization for laser powder bed fusion* [2] demonstrated general feasibility of an *in situ* modification during atomization. A titanium enriched Alloy 400 variant was used for this purpose, following the highest probability of nanoparticle formation according to the free energy of formation of the reactants. Strengthening of the NiCu alloy via nanoscaled oxides on yttrium or zirconium basis did not prove to be effective while the dispersion of titanium nitrides on grain boundaries of powders and cell walls of parts, respectively, revealed tremendous potential. A significant, positive shift in mechanical properties compared to unmodified PBF-LB/M Alloy 400 was achieved. Ultimately, via the *ex situ* powder modification approach as per the fluidized bed reactor in *The Dispersion-Strengthening Effect of TiN Nanoparticles Evoked by Ex Situ Nitridation of Gas-Atomized, NiCu-Based Alloy 400 in Fluidized Bed Reactor for Laser Powder Bed Fusion* [3], the TiN share in powder and parts could be clearly increased further, allowing for exceptional mechanical performance in comparison to both the unmodified and the GARS version. Thus, a superior, additively manufactured material system resulted and based on this fundamental work, a consolidation in relation to the three sub-areas can now be considered.

### *The manufacturing*

Besides PBF-LB/M, further AM processes are of immense industrial relevance. Especially considering the

target markets for Alloy 400 of maritime, chemistry and energy, directed energy deposition is of great interest. This high-throughput AM technology allows for repairs of large format components like impellers or pipes, which are not primary use cases of PBF-LB/M. Hence, an extension of the findings of this work to this technique promises great potential. Moreover, the related electron beam powder bed fusion of metals (PBF-EB/M) can be considered for AM of a MMNC Alloy 400.

#### *The mechanism*

The dispersion strengthening effect was the focus of this work. However, incorporating further strengthening mechanisms besides DS in modified Alloy 400 versions might be of interest. Exceeding the solubility of elements in the solid solution to evoke precipitation formation for instance could further improve the material properties. Also, by application of high-power laser systems, even higher cooling rates might be achieved, leading to further grain refinement and Hall-Petch strengthening. However, it will be important to ensure that the individual mechanisms do not act contrary to each other and thus weaken themselves. The combination of the modification routes applied throughout this work might also reveal further potential. For instance, further modification of the GARS atomized powder in the fluidized bed reactor may lead to even higher quantities of TiN nanoparticles forming throughout the entire process chain. The effect of powder recycling during the GARS approach also

has to be studied further: In re-using the sieved-out splash and the air-classified fine fractions in a second atomization that formed nanoparticles during the first atomization already, a constantly evolving NP formation mechanism could be enabled over the recurring process steps.

#### *The material*

Alloy 400, mainly consisting of Ni and Cu with low additions of iron, manganese, silicon, aluminum, titanium, carbon, and sulfur, was further modified with titanium in this work. However, a variance of the standard chemical composition of Alloy 400 beyond Ti additions might be considered as well. Other and/or further strengthening elements and reactants might be included in the alloy system to allow for multiple nanoparticle formation. A theoretically perfect chemical composition of Alloy 400 for maximum strengthening possible might be targeted. Also, an exploitation of these insights to related NiCu alloys should be addressed.



# Chapter 6

REFERENCES

- 
- [1] **J.-P. Roth**, I. Šulák, T. Kruml, W. Polkowski, T. Dudziak, P. Böhlke, U. Krupp, K. Jahns, Establishing a process route for additive manufacturing of NiCu-based Alloy 400: an alignment of gas atomization, laser powder bed fusion, and design of experiments, *Int J Adv Manuf Technol* 134 (2024) 3433–3452. <https://doi.org/10.1007/s00170-024-14328-7>.
- [2] **J.-P. Roth**, I. Šulák, Z. Chlup, J. Fischer-Bühner, U. Krupp, K. Jahns, The dispersion-strengthening effect of TiN evoked by in situ nitridation of NiCu-based Alloy 400 during gas atomization for laser powder bed fusion, *Materials Science and Engineering: A* 893 (2024) 146129. <https://doi.org/10.1016/j.msea.2024.146129>.
- [3] **J.-P. Roth**, I. Šulák, M. Gálíková, A. Duval, G. Boissonnet, F. Pedraza, U. Krupp, K. Jahns, The Dispersion-Strengthening Effect of TiN Nanoparticles Evoked by Ex Situ Nitridation of Gas-Atomized, NiCu-Based Alloy 400 in Fluidized Bed Reactor for Laser Powder Bed Fusion, *JMMP* 8 (2024) 223. <https://doi.org/10.3390/jmmp8050223>.
- [4] A. Chlupová, I. Šulák, I. Kuběna, T. Kruml, **J.-P. Roth**, K. Jahns, Comparison of Microstructure and Properties of Nickel-Copper Alloy Prepared by Casting and Laser Powder Bed Fusion Process, *MSF* 1082 (2023) 171–176. <https://doi.org/10.4028/p-884q32>.
- [5] I. Šulák, A. Chlupová, T. Záležák, I. Kuběna, **J.-P. Roth**, K. Jahns, U. Krupp, T. Kruml, High-temperature Fatigue and Creep Performance of Additively Manufactured NiCu-based Alloy, *Procedia Structural Integrity* 52 (2024) 143–153. <https://doi.org/10.1016/j.prostr.2023.12.015>.
- [6] **J.-P. Roth**, I. Šulák, Z. Chlup, J. Fischer-Bühner, U. Krupp, K. Jahns, Nanoparticle-Modification of NiCu-Based Alloy 400 for Laser Powder Bed Fusion, *Solid Freeform Fabrication 2023: Proceedings of the 34th Annual International Solid Freeform Fabrication Symposium – An Additive Manufacturing Conference* (2023) 574–575. <https://utw10945.utweb.utexas.edu/2023-table-contents>.
- [7] K.V. Wong, A. Hernandez, A Review of Additive Manufacturing, *ISRN Mechanical Engineering* 2012 (2012) 1–10. <https://doi.org/10.5402/2012/208760>.
- [8] R.H. Crawford, J.J. Beaman, Solid freeform fabrication, *IEEE Spectr.* 36 (1999) 34–43. <https://doi.org/10.1109/6.744874>.
-

- 
- [9] O. Abdulhameed, A. Al-Ahmari, W. Ameen, S.H. Mian, Additive manufacturing: Challenges, trends, and applications, *Advances in Mechanical Engineering* 11 (2019) 168781401882288. <https://doi.org/10.1177/1687814018822880>.
- [10] J.-P. Kruth, M.C. Leu, T. Nakagawa, Progress in Additive Manufacturing and Rapid Prototyping, *CIRP Annals* 47 (1998) 525–540. [https://doi.org/10.1016/S0007-8506\(07\)63240-5](https://doi.org/10.1016/S0007-8506(07)63240-5).
- [11] AMPOWER Report on Additive Manufacturing, Ampower Additive Manufacturing Report, 2024. <https://additive-manufacturing-report.com/>.
- [12] A. Bhargav, V. Sanjairaj, V. Rosa, L.W. Feng, J. Fuh Yh, Applications of additive manufacturing in dentistry: A review, *J. Biomed. Mater. Res. B Appl. Biomater.* 106 (2018) 2058–2064. <https://doi.org/10.1002/jbm.b.33961>.
- [13] R. Galante, C.G. Figueiredo-Pina, A.P. Serro, Additive manufacturing of ceramics for dental applications: A review, *Dent. Mater.* 35 (2019) 825–846. <https://doi.org/10.1016/j.dental.2019.02.026>.
- [14] H. Hassanin, L. Finet, S.C. Cox, P. Jamshidi, L.M. Grover, D.E. Shepherd, O. Addison, M.M. Attallah, Tailoring selective laser melting process for titanium drug-delivering implants with releasing micro-channels, *Additive Manufacturing* 20 (2018) 144–155. <https://doi.org/10.1016/j.addma.2018.01.005>.
- [15] W. Abd-Elaziem, S. Elkatatny, A.-E. Abd-Elaziem, M. Khedr, M.A. Abd El-baky, M.A. Hassan, M. Abu-Okail, M. Mohammed, A. Järvenpää, T. Allam, A. Hamada, On the current research progress of metallic materials fabricated by laser powder bed fusion process: a review, *Journal of Materials Research and Technology* 20 (2022) 681–707. <https://doi.org/10.1016/j.jmrt.2022.07.085>.
- [16] A. Uriondo, M. Esperon-Miguez, S. Perinpanayagam, The present and future of additive manufacturing in the aerospace sector: A review of important aspects, *Proceedings of the Institution of Mechanical Engineers, Part G: Journal of Aerospace Engineering* 229 (2015) 2132–2147. <https://doi.org/10.1177/0954410014568797>.
- [17] N. Guo, M.C. Leu, Additive manufacturing: technology, applications and research needs, *Front. Mech. Eng.* 8 (2013) 215–243. <https://doi.org/10.1007/s11465-013-0248-8>.
-



- 
- [18] T. Pereira, J.V. Kennedy, J. Potgieter, A comparison of traditional manufacturing vs additive manufacturing, the best method for the job, *Procedia Manufacturing* 30 (2019) 11–18. <https://doi.org/10.1016/j.promfg.2019.02.003>.
- [19] N. Hopkinson, P. Dicknes, Analysis of rapid manufacturing—using layer manufacturing processes for production, *Proceedings of the Institution of Mechanical Engineers, Part C: Journal of Mechanical Engineering Science* 217 (2003) 31–39. <https://doi.org/10.1243/095440603762554596>.
- [20] I. Gibson, D.W. Rosen, B. Stucker, *Direct Digital Manufacturing, Additive manufacturing technologies* (2015) 375–397. [https://doi.org/10.1007/978-1-4939-2113-3\\_16](https://doi.org/10.1007/978-1-4939-2113-3_16).
- [21] DIN EN ISO/ASTM 52900:2022-03, *Additive manufacturing - General principles - Fundamentals and vocabulary* (2022). <https://doi.org/10.31030/3290011>.
- [22] S.M. Hashemi, S. Parvizi, H. Baghbanijavid, A.T.L. Tan, M. Nematollahi, A. Ramazani, N.X. Fang, M. Elahinia, Computational modelling of process–structure–property–performance relationships in metal additive manufacturing: a review, *International Materials Reviews* 67 (2022) 1–46. <https://doi.org/10.1080/09506608.2020.1868889>.
- [23] S. Li, S. Yuan, J. Zhu, W. Zhang, H. Zhang, J. Li, Multidisciplinary topology optimization incorporating process-structure-property-performance relationship of additive manufacturing, *Struct Multidisc Optim* 63 (2021) 2141–2157. <https://doi.org/10.1007/s00158-021-02856-9>.
- [24] T. Pinomaa, I. Yashchuk, M. Lindroos, T. Andersson, N. Provatas, A. Laukkanen, Process-Structure-Properties-Performance Modeling for Selective Laser Melting, *Metals* 9 (2019) 1138. <https://doi.org/10.3390/met9111138>.
- [25] J. Smith, W. Xiong, W. Yan, S. Lin, P. Cheng, O.L. Kafka, G.J. Wagner, J. Cao, W.K. Liu, Linking process, structure, property, and performance for metal-based additive manufacturing: computational approaches with experimental support, *Comput Mech* 57 (2016) 583–610. <https://doi.org/10.1007/s00466-015-1240-4>.
- [26] J.H. Martin, B.D. Yahata, J.M. Hundley, J.A. Mayer, T.A. Schaedler, T.M. Pollock, 3D printing of high-strength aluminium alloys, *Nature* 549 (2017) 365–369. <https://doi.org/10.1038/nature23894>.
-

- 
- [27] H. Hadraba, Z. Chlup, A. Dlouhy, F. Dobes, P. Roupčova, M. Vilemova, J. Matejíček, Oxide dispersion strengthened CoCrFeNiMn high-entropy alloy, *Materials Science and Engineering: A* 689 (2017) 252–256. <https://doi.org/10.1016/j.msea.2017.02.068>.
- [28] T. Horn, C. Rock, D. Kaoumi, I. Anderson, E. White, T. Prost, J. Rieken, S. Saptarshi, R. Schoell, M. DeJong, S. Timmins, J. Forrester, S. Lapidus, R. Napolitano, D. Zhang, J. Darsell, Laser powder bed fusion additive manufacturing of oxide dispersion strengthened steel using gas atomized reaction synthesis powder, *Materials & Design* 216 (2022) 110574. <https://doi.org/10.1016/j.matdes.2022.110574>.
- [29] T.M. Smith, A.C. Thompson, T.P. Gabb, C.L. Bowman, C.A. Kantzos, Efficient production of a high-performance dispersion strengthened, multi-principal element alloy, *Sci Rep* 10 (2020) 9663. <https://doi.org/10.1038/s41598-020-66436-5>.
- [30] J. Wang, S. Liu, B. Xu, J. Zhang, M. Sun, D. Li, Research progress on preparation technology of oxide dispersion strengthened steel for nuclear energy, *Int. J. Extrem. Manuf.* 3 (2021) 32001. <https://doi.org/10.1088/2631-7990/abff1a>.
- [31] I.E. Anderson, J.C. Foley, Determining the role of surfaces and interfaces in the powder metallurgy processing of aluminum alloy powders, *Surface & Interface Analysis* 31 (2001) 599–608. <https://doi.org/10.1002/sia.1087>.
- [32] Y. Huang, T.G. Fleming, S.J. Clark, S. Marussi, K. Fezzaa, J. Thiayagalingam, C.L.A. Leung, P.D. Lee, Keyhole fluctuation and pore formation mechanisms during laser powder bed fusion additive manufacturing, *Nat Commun* 13 (2022) 1170. <https://doi.org/10.1038/s41467-022-28694-x>.
- [33] D. Kong, C. Dong, S. Wei, X. Ni, L. Zhang, R. Li, L. Wang, C. Man, X. Li, About metastable cellular structure in additively manufactured austenitic stainless steels, *Additive Manufacturing* 38 (2021) 101804. <https://doi.org/10.1016/j.addma.2020.101804>.
- [34] G. Wang, H. Ouyang, C. Fan, Q. Guo, Z. Li, W. Yan, Z. Li, The origin of high-density dislocations in additively manufactured metals, *Materials Research Letters* 8 (2020) 283–290. <https://doi.org/10.1080/21663831.2020.1751739>.
-

- 
- [35] T.G. Gallmeyer, S. Moorthy, B.B. Kappes, M.J. Mills, B. Amin-Ahmadi, A.P. Stebner, Knowledge of process-structure-property relationships to engineer better heat treatments for laser powder bed fusion additive manufactured Inconel 718, *Additive Manufacturing* 31 (2020) 100977. <https://doi.org/10.1016/j.addma.2019.100977>.
- [36] J. Boes, A. Röttger, L. Becker, W. Theisen, Processing of gas-nitrided AISI 316L steel powder by laser powder bed fusion – Microstructure and properties, *Additive Manufacturing* 30 (2019) 100836. <https://doi.org/10.1016/j.addma.2019.100836>.
- [37] V.G. Gavriljuk, V.N. Shivanyuk, B.D. Shanina, Change in the electron structure caused by C, N and H atoms in iron and its effect on their interaction with dislocations, *Acta Materialia* 53 (2005) 5017–5024. <https://doi.org/10.1016/j.actamat.2005.07.028>.
- [38] L.L. Snead, D.T. Hoelzer, M. Rieth, A.A. Nemith, Chapter 13 - Refractory Alloys: Vanadium, Niobium, Molybdenum, Tungsten, in: R. Odette, S.J. Zinkle (Eds.), *Structural alloys for nuclear energy applications*, Elsevier, Amsterdam, 2019, pp. 585–640.
- [39] T. DebRoy, H.L. Wei, J.S. Zuback, T. Mukherjee, J.W. Elmer, J.O. Milewski, A.M. Beese, A. Wilson-Heid, A. De, W. Zhang, Additive manufacturing of metallic components – Process, structure and properties, *Progress in Materials Science* 92 (2018) 112–224. <https://doi.org/10.1016/j.pmatsci.2017.10.001>.
- [40] J.-W. Yeh, S.-K. Chen, S.-J. Lin, J.-Y. Gan, T.-S. Chin, T.-T. Shun, C.-H. Tsau, S.-Y. Chang, Nanostructured High-Entropy Alloys with Multiple Principal Elements: Novel Alloy Design Concepts and Outcomes, *Advanced Engineering Materials* 6 (2004) 299–303. <https://doi.org/10.1002/adem.200300567>.
- [41] P. Sharma, V.K. Dwivedi, S.P. Dwivedi, Development of high entropy alloys: A review, *Materials Today: Proceedings* 43 (2021) 502–509. <https://doi.org/10.1016/j.matpr.2020.12.023>.
- [42] N. Birbilis, S. Choudhary, J.R. Scully, M.L. Taheri, A perspective on corrosion of multi-principal element alloys, *npj Mater Degrad* 5 (2021) 1–8. <https://doi.org/10.1038/s41529-021-00163-8>.
- [43] D. Zhang, S. Sun, D. Qiu, M.A. Gibson, M.S. Dargusch, M. Brandt, M. Qian, M. Easton, Metal Alloys for Fusion-Based Additive Manufacturing, *Advanced Engineering Materials* 20 (2018) 1700952. <https://doi.org/10.1002/adem.201700952>.
-

- 
- [44] L.E. Shoemaker, G.D. Smith, A century of monel metal: 1906–2006, *JOM* 58 (2006) 22–26. <https://doi.org/10.1007/s11837-006-0077-x>.
- [45] I. Raffeis, F. Adjei-Kyeremeh, U. Vroomen, E. Westhoff, S. Bremen, A. Hohoi, A. Bührig-Polaczek, Qualification of a Ni–Cu Alloy for the Laser Powder Bed Fusion Process (LPBF): Its Microstructure and Mechanical Properties, *Applied Sciences* 10 (2020) 3401. <https://doi.org/10.3390/app10103401>.
- [46] U. Esgin, D. Özyürek, H. Kaya, An investigation of wear behaviors of different Monel alloys produced by powder metallurgy, *AIP Conf. Proc.* 1727 (2016) 20008. <https://doi.org/10.1063/1.4945963>.
- [47] C.-H. Zhang, C.-L. Wu, S. Zhang, Y.-F. Jia, M. Guan, J.-Z. Tan, B. Lin, Laser cladding of NiCrSiB on Monel 400 to enhance cavitation erosion and corrosion resistance, *Rare Met.* 41 (2022) 4257–4265. <https://doi.org/10.1007/s12598-016-0814-4>.
- [48] M. Kukliński, A. Bartkowska, D. Przestacki, Microstructure and selected properties of Monel 400 alloy after laser heat treatment and laser boriding using diode laser, *Int J Adv Manuf Technol* 98 (2018) 3005–3017. <https://doi.org/10.1007/s00170-018-2343-9>.
- [49] DIN 8580:2022-12, Manufacturing processes - Terms and definitions, division (2022). <https://doi.org/10.31030/3217872>.
- [50] K.-H. Grote, H. Hefazi, Springer Handbook of Mechanical Engineering, Springer International Publishing (2021). <https://doi.org/10.1007/978-3-030-47035-7>.
- [51] C. Körner, M. Markl, J.A. Koepf, Modeling and Simulation of Microstructure Evolution for Additive Manufacturing of Metals: A Critical Review, *Metall Mater Trans A* 51 (2020) 4970–4983. <https://doi.org/10.1007/s11661-020-05946-3>.
- [52] S. Singh, S. Mehla, S.K. Bhargava, S. Ramakrishna, History and Evolution of Additive Manufacturing, *Additive manufacturing for chemical science and engineering* (2022) 19–51. [https://doi.org/10.1007/978-981-19-2293-0\\_2](https://doi.org/10.1007/978-981-19-2293-0_2).
- [53] B.P. Conner, G.P. Manogharan, A.N. Martof, L.M. Rodomsky, C.M. Rodomsky, D.C. Jordan, J.W. Limperos, Making sense of 3-D printing: Creating a map of additive manufacturing products and services, *Additive Manufacturing* 1-4 (2014) 64–76. <https://doi.org/10.1016/j.addma.2014.08.005>.
-

- 
- [54] G.-J. Tüzün, D. Roth, M. Kreimeyer, FUNCTION INTEGRATION IN ADDITIVE MANUFACTURING: A REVIEW OF APPROACHES, *Proc. Des. Soc.* 3 (2023) 2005–2014. <https://doi.org/10.1017/pds.2023.201>.
- [55] R. Handal, An implementation framework for additive manufacturing in supply chains, *JOSCM* 10 (2017) 18–31. <https://doi.org/10.12660/joscmv10n2p18-31>.
- [56] D.L. Bourell, Perspectives on Additive Manufacturing, *Annu. Rev. Mater. Res.* 46 (2016) 1–18. <https://doi.org/10.1146/annurev-matsci-070115-031606>.
- [57] D. Bourell, J.P. Kruth, M. Leu, G. Levy, D. Rosen, A.M. Beese, A. Clare, Materials for additive manufacturing, *CIRP Annals* 66 (2017) 659–681. <https://doi.org/10.1016/j.cirp.2017.05.009>.
- [58] N. Ciftci, N. Ellendt, G. Coulthard, E. Soares Barreto, L. Mädler, V. Uhlenwinkel, Novel Cooling Rate Correlations in Molten Metal Gas Atomization, *Metall Mater Trans B* 50 (2019) 666–677. <https://doi.org/10.1007/s11663-019-01508-0>.
- [59] J.J. Dunkley, Metal Powder Atomisation Methods for Modern Manufacturing, *Johnson Matthey Technology Review* 63 (2019) 226–232. <https://doi.org/10.1595/205651319X15583434137356>.
- [60] E. Soares Barreto, M. Frey, J. Wegner, A. Jose, N. Neuber, R. Busch, S. Kleszczynski, L. Mädler, V. Uhlenwinkel, Properties of gas-atomized Cu-Ti-based metallic glass powders for additive manufacturing, *Materials & Design* 215 (2022) 110519. <https://doi.org/10.1016/j.matdes.2022.110519>.
- [61] X. Sun, M. Chen, T. Liu, K. Zhang, H. Wei, Z. Zhu, W. Liao, Characterization, preparation, and reuse of metallic powders for laser powder bed fusion: a review, *Int. J. Extrem. Manuf.* 6 (2024) 12003. <https://doi.org/10.1088/2631-7990/acfb3>.
- [62] A. Popovich, V. Sufiarov, Metal Powder Additive Manufacturing, in: G. Biglino (Ed.), *3D Printing Cardiovascular Anatomy: A Single-Centre Experience*, IntechOpen, [s.l.], 2016.
- [63] H. OUYANG, X. CHEN, B. HUANG, Influence of melt superheat on breakup process of close-coupled gas atomization, *Transactions of Nonferrous Metals Society of China* 17 (2007) 967–973. [https://doi.org/10.1016/S1003-6326\(07\)60209-X](https://doi.org/10.1016/S1003-6326(07)60209-X).
-

- 
- [64] D. Schwenck, N. Ellendt, J. Fischer-Bühner, P. Hofmann, V. Uhlenwinkel, A novel convergent–divergent annular nozzle design for close-coupled atomisation, *Powder Metallurgy* 60 (2017) 198–207. <https://doi.org/10.1080/00325899.2017.1291098>.
- [65] N. Zeoli, H. Tabbara, S. Gu, Three-dimensional simulation of primary break-up in a close-coupled atomizer, *Appl. Phys. A* 108 (2012) 783–792. <https://doi.org/10.1007/s00339-012-6966-7>.
- [66] I.E. Anderson, R.L. Terpstra, Progress toward gas atomization processing with increased uniformity and control, *Materials Science and Engineering: A* 326 (2002) 101–109. [https://doi.org/10.1016/S0921-5093\(01\)01427-7](https://doi.org/10.1016/S0921-5093(01)01427-7).
- [67] S. Sendino, S. Martinez, A. Lamikiz, Characterization of IN718 recycling powder and its effect on LPBF manufactured parts, *Procedia CIRP* 94 (2020) 227–232. <https://doi.org/10.1016/j.procir.2020.09.043>.
- [68] J. Zegzulka, D. Gelnar, L. Jezerska, R. Prokes, J. Rozbroj, Characterization and flowability methods for metal powders, *Sci Rep* 10 (2020) 21004. <https://doi.org/10.1038/s41598-020-77974-3>.
- [69] H.Y. Saw, C.E. Davies, A.H. Paterson, J.R. Jones, Correlation between Powder Flow Properties Measured by Shear Testing and Hausner Ratio, *Procedia Engineering* 102 (2015) 218–225. <https://doi.org/10.1016/j.proeng.2015.01.132>.
- [70] J.A. Slotwinski, E.J. Garboczi, P.E. Stutzman, C.F. Ferraris, S.S. Watson, M.A. Peltz, Characterization of Metal Powders Used for Additive Manufacturing, *Journal of Research of the National Institute of Standards and Technology* 119 (2014) 460–493. <https://doi.org/10.6028/jres.119.018>.
- [71] R. Cohn, I. Anderson, T. Prost, J. Tiarks, E. White, E. Holm, Instance Segmentation for Direct Measurements of Satellites in Metal Powders and Automated Microstructural Characterization from Image Data, *JOM* 73 (2021) 2159–2172. <https://doi.org/10.1007/s11837-021-04713-y>.
- [72] M. Kumke, H. Watschke, P. Hartogh, A.-K. Bavendiek, T. Vietor, Methods and tools for identifying and leveraging additive manufacturing design potentials, *Int J Interact Des Manuf* 12 (2018) 481–493. <https://doi.org/10.1007/s12008-017-0399-7>.
-

- 
- [73] Y. Mahmoodkhani, U. Ali, S. Imani Shahabad, A. Rani Kasinathan, R. Esmaeilizadeh, A. Keshavarzkermani, E. Marzbanrad, E. Toyserkani, On the measurement of effective powder layer thickness in laser powder-bed fusion additive manufacturing of metals, *Prog Addit Manuf* 4 (2019) 109–116. <https://doi.org/10.1007/s40964-018-0064-0>.
- [74] E. Li, Z. Zhou, L. Wang, R. Zou, A. Yu, Particle scale modelling of powder recoating and melt pool dynamics in laser powder bed fusion additive manufacturing: A review, *Powder Technology* 409 (2022) 117789. <https://doi.org/10.1016/j.powtec.2022.117789>.
- [75] M.H. Sehhat, A. Mahdianikhotbesara, Powder spreading in laser-powder bed fusion process, *Granular Matter* 23 (2021) 1–18. <https://doi.org/10.1007/s10035-021-01162-x>.
- [76] T. Voisin, J.-B. Forien, A. Perron, S. Aubry, N. Bertin, A. Samanta, A. Baker, Y.M. Wang, New insights on cellular structures strengthening mechanisms and thermal stability of an austenitic stainless steel fabricated by laser powder-bed-fusion, *Acta Materialia* 203 (2021) 116476. <https://doi.org/10.1016/j.actamat.2020.11.018>.
- [77] P. Bajaj, A. Hariharan, A. Kini, P. Kürnsteiner, D. Raabe, E.A. Jägle, Steels in additive manufacturing: A review of their microstructure and properties, *Materials Science and Engineering: A* 772 (2020) 138633. <https://doi.org/10.1016/j.msea.2019.138633>.
- [78] Y. Kok, X.P. Tan, P. Wang, M. Nai, N.H. Loh, E. Liu, S.B. Tor, Anisotropy and heterogeneity of microstructure and mechanical properties in metal additive manufacturing: A critical review, *Materials & Design* 139 (2018) 565–586. <https://doi.org/10.1016/j.matdes.2017.11.021>.
- [79] K.M. Bertsch, G. Meric de Bellefon, B. Kuehl, D.J. Thoma, Origin of dislocation structures in an additively manufactured austenitic stainless steel 316L, *Acta Materialia* 199 (2020) 19–33. <https://doi.org/10.1016/j.actamat.2020.07.063>.
- [80] J.H.K. Tan, S.L. Sing, W.Y. Yeong, Microstructure modelling for metallic additive manufacturing: a review, *Virtual and Physical Prototyping* 15 (2020) 87–105. <https://doi.org/10.1080/17452759.2019.1677345>.
-



- 
- [81] T. Pinomaa, M. Lindroos, M. Walbrühl, N. Provatas, A. Laukkanen, The significance of spatial length scales and solute segregation in strengthening rapid solidification microstructures of 316L stainless steel, *Acta Materialia* 184 (2020) 1–16. <https://doi.org/10.1016/j.actamat.2019.10.044>.
- [82] C. Du, Y. Zhao, J. Jiang, Q. Wang, H. Wang, N. Li, J. Sun, Pore defects in Laser Powder Bed Fusion: Formation mechanism, control method, and perspectives, *Journal of Alloys and Compounds* 944 (2023) 169215. <https://doi.org/10.1016/j.jallcom.2023.169215>.
- [83] V. Lindström, G. Lupo, J. Yang, V. Turlo, C. Leinenbach, A simple scaling model for balling defect formation during laser powder bed fusion, *Additive Manufacturing* 63 (2023) 103431. <https://doi.org/10.1016/j.addma.2023.103431>.
- [84] M. Higashi, T. Ozaki, Selective laser melting of pure molybdenum: Evolution of defect and crystallographic texture with process parameters, *Materials & Design* 191 (2020) 108588. <https://doi.org/10.1016/j.matdes.2020.108588>.
- [85] C.S. Lefky, T.G. Gallmeyer, S. Moorthy, A. Stebner, O.J. Hildreth, Microstructure and corrosion properties of sensitized laser powder bed fusion printed Inconel 718 to dissolve support structures in a self-terminating manner, *Additive Manufacturing* 27 (2019) 526–532. <https://doi.org/10.1016/j.addma.2019.03.020>.
- [86] J. Čížek, Characterization of lattice defects in metallic materials by positron annihilation spectroscopy: A review, *Journal of Materials Science & Technology* 34 (2018) 577–598. <https://doi.org/10.1016/j.jmst.2017.11.050>.
- [87] R. Freitas, Y. Cao, Machine-learning potentials for crystal defects, *MRS Communications* 12 (2022) 510–520. <https://doi.org/10.1557/s43579-022-00221-5>.
- [88] O. Marenych, A. Kostyryhev, Strengthening Mechanisms in Nickel-Copper Alloys: A Review, *Metals* 10 (2020) 1358. <https://doi.org/10.3390/met10101358>.
- [89] H.A. Roth, C.L. Davis, R.C. Thomson, Modeling solid solution strengthening in nickel alloys, *Metall Mater Trans A* 28 (1997) 1329–1335. <https://doi.org/10.1007/s11661-997-0268-2>.
-



- 
- [90] Z. Wu, M.C. Tropsky, Y.F. Gao, J.R. Morris, G.M. Stocks, H. Bei, Phase stability, physical properties and strengthening mechanisms of concentrated solid solution alloys, *Current Opinion in Solid State and Materials Science* 21 (2017) 267–284.  
<https://doi.org/10.1016/j.cossms.2017.07.001>.
- [91] G.K. Dey, R. Tewari, P. Rao, S.L. Wadekar, P. Mukhopadhyay, Precipitation hardening in nickel-copper base alloy monel K 500, *Metall Trans A* 24 (1993) 2709–2719.  
<https://doi.org/10.1007/BF02659495>.
- [92] R. Casati, M. Vedani, Metal Matrix Composites Reinforced by Nano-Particles—A Review, *Metals* 4 (2014) 65–83.  
<https://doi.org/10.3390/met4010065>.
- [93] W. Chen, T. Yang, L. Dong, A. Elmasry, J. Song, N. Deng, A. Elmarakbi, T. Liu, H.B. Lv, Y.Q. Fu, Advances in graphene reinforced metal matrix nanocomposites: Mechanisms, processing, modelling, properties and applications, *Nanotechnol. Precis. Eng.* 3 (2020) 189–210.  
<https://doi.org/10.1016/j.npe.2020.12.003>.
- [94] A. Sanaty-Zadeh, Comparison between current models for the strength of particulate-reinforced metal matrix nanocomposites with emphasis on consideration of Hall–Petch effect, *Materials Science and Engineering: A* 531 (2012) 112–118.  
<https://doi.org/10.1016/j.msea.2011.10.043>.
- [95] Z. Zhang, D.L. Chen, Contribution of Orowan strengthening effect in particulate-reinforced metal matrix nanocomposites, *Materials Science and Engineering: A* 483–484 (2008) 148–152.  
<https://doi.org/10.1016/j.msea.2006.10.184>.
- [96] C. Gao, W. Wu, J. Shi, Z. Xiao, A.H. Akbarzadeh, Simultaneous enhancement of strength, ductility, and hardness of TiN/AlSi10Mg nanocomposites via selective laser melting, *Additive Manufacturing* 34 (2020) 101378.  
<https://doi.org/10.1016/j.addma.2020.101378>.
- [97] Y.K. Xiao, H. Chen, Z.Y. Bian, T.T. Sun, H. Ding, Q. Yang, Y. Wu, Q. Lian, Z. Chen, H.W. Wang, Enhancing strength and ductility of AlSi10Mg fabricated by selective laser melting by TiB<sub>2</sub> nanoparticles, *Journal of Materials Science & Technology* 109 (2022) 254–266.  
<https://doi.org/10.1016/j.jmst.2021.08.030>.
-

- 
- [98] X. Wang, X. Nan, C. Ma, T. Shi, M. Guo, J. Hu, Y. Wang, Strain rate dependence of mechanical behavior in an AlSi10Mg alloy with different states fabricated by laser powder bed fusion, *Journal of Materials Research and Technology* 32 (2024) 1354–1367.  
<https://doi.org/10.1016/j.jmrt.2024.08.006>.
- [99] T. Rong, D. Gu, Formation of novel graded interface and its function on mechanical properties of WC1-x reinforced Inconel 718 composites processed by selective laser melting, *Journal of Alloys and Compounds* 680 (2016) 333–342.  
<https://doi.org/10.1016/j.jallcom.2016.04.107>.
- [100] T.M. Smith, C.A. Kantzos, N.A. Zarkevich, B.J. Harder, M. Heczko, P.R. Gradl, A.C. Thompson, M.J. Mills, T.P. Gabb, J.W. Lawson, A 3D printable alloy designed for extreme environments, *Nature* 617 (2023) 513–518.  
<https://doi.org/10.1038/s41586-023-05893-0>.
- [101] R. Xu, Z. Geng, Y. Wu, C. Chen, M. Ni, D. Li, T. Zhang, H. Huang, F. Liu, R. Li, K. Zhou, Microstructure and mechanical properties of in-situ oxide-dispersion-strengthened NiCrFeY alloy produced by laser powder bed fusion, *Advanced Powder Materials* 1 (2022) 100056.  
<https://doi.org/10.1016/j.apmate.2022.100056>.
- [102] J. Jang, T.K. Kim, C.H. Han, H.-K. Min, S.-H. Jeong, D.H. Kim, A Preliminary Development and Characterization of Ni-based ODS Alloys, *Procedia Engineering* 55 (2013) 284–288.  
<https://doi.org/10.1016/j.proeng.2013.03.255>.
- [103] L. Yu, Z. Lu, J. Xian, X. Chen, S. Peng, X. Li, H. Li, Effects of Al content on microstructure and tensile properties of Ni-based ODS superalloys, *Journal of Alloys and Compounds* 941 (2023) 168965.  
<https://doi.org/10.1016/j.jallcom.2023.168965>.
- [104] D. Zhang, J.T. Darsell, J. Wang, X. Ma, G.J. Grant, I.E. Anderson, J.R. Rieken, D.J. Edwards, W. Setyawan, T.J. Horn, G.R. Odette, No ball milling needed: Alternative ODS steel manufacturing with gas atomization reaction synthesis (GARS) and friction-based processing, *Journal of Nuclear Materials* 566 (2022) 153768.  
<https://doi.org/10.1016/j.jnucmat.2022.153768>.
- [105] C.-S. Kim, I. Sohn, M. Nezafati, J.B. Ferguson, B.F. Schultz, Z. Bajestani-Gohari, P.K. Rohatgi, K. Cho, Prediction models for the yield strength of particle-reinforced unimodal pure magnesium (Mg) metal matrix nanocomposites (MMNCs), *J Mater Sci* 48 (2013) 4191–4204.  
<https://doi.org/10.1007/s10853-013-7232-x>.
-

- 
- [106] J. Ye, B.Q. Han, Z. Lee, B. Ahn, S.R. Nutt, J.M. Schoenung, A tri-modal aluminum based composite with super-high strength, *Scripta Materialia* 53 (2005) 481–486. <https://doi.org/10.1016/j.scriptamat.2005.05.004>.
- [107] L. Carroll, M. Sternitzke, B. Derby, Silicon carbide particle size effects in alumina-based nanocomposites, *Acta Materialia* 44 (1996) 4543–4552. [https://doi.org/10.1016/1359-6454\(96\)00074-2](https://doi.org/10.1016/1359-6454(96)00074-2).
- [108] S.F. Hassan, M. Gupta, Development of high performance magnesium nanocomposites using solidification processing route, *Materials Science and Technology* 20 (2004) 1383–1388. <https://doi.org/10.1179/026708304X3980>.
- [109] W.H. Yu, S.L. Sing, C.K. Chua, C.N. Kuo, X.L. Tian, Particle-reinforced metal matrix nanocomposites fabricated by selective laser melting: A state of the art review, *Progress in Materials Science* 104 (2019) 330–379. <https://doi.org/10.1016/j.pmatsci.2019.04.006>.
- [110] C.-S. Kim, K. Cho, M.H. Manjili, M. Nezafati, Mechanical performance of particulate-reinforced Al metal-matrix composites (MMCs) and Al metal-matrix nano-composites (MMNCs), *J Mater Sci* 52 (2017) 13319–13349. <https://doi.org/10.1007/s10853-017-1378-x>.
- [111] B.F. Schultz, J.B. Ferguson, P.K. Rohatgi, Microstructure and hardness of Al<sub>2</sub>O<sub>3</sub> nanoparticle reinforced Al–Mg composites fabricated by reactive wetting and stir mixing, *Materials Science and Engineering: A* 530 (2011) 87–97. <https://doi.org/10.1016/j.msea.2011.09.042>.
- [112] S. Pasebani, A.K. Dutt, J. Burns, I. Charit, R.S. Mishra, Oxide dispersion strengthened nickel based alloys via spark plasma sintering, *Materials Science and Engineering: A* 630 (2015) 155–169. <https://doi.org/10.1016/j.msea.2015.01.066>.
- [113] S. Saptarshi, M. deJong, C. Rock, I. Anderson, R. Napolitano, J. Forrester, S. Lapidus, D. Kaoumi, T. Horn, Laser Powder Bed Fusion of ODS 14YWT from Gas Atomization Reaction Synthesis Precursor Powders, *JOM* 74 (2022) 3303–3315. <https://doi.org/10.1007/s11837-022-05418-6>.
- [114] J.R. Rieken, I.E. Anderson, M.J. Kramer, G.R. Odette, E. Stergar, E. Haney, Reactive gas atomization processing for Fe-based ODS alloys, *Journal of Nuclear Materials* 428 (2012) 65–75. <https://doi.org/10.1016/j.jnucmat.2011.08.015>.
-

- 
- [115] S. Mirzababaei, M. Ghayoor, R.P. Doyle, S. Pasebani, In-situ manufacturing of ODS FeCrAlY alloy via laser powder bed fusion, *Materials Letters* 284 (2021) 129046. <https://doi.org/10.1016/j.matlet.2020.129046>.
- [116] M. Li, Y. Guo, W. Li, Y. Zhang, Y. Chang, Property enhancement of CoCrNi medium-entropy alloy by introducing nano-scale features, *Materials Science and Engineering: A* 817 (2021) 141368. <https://doi.org/10.1016/j.msea.2021.141368>.
- [117] J. Yi, C. Chang, X. Yan, Y. Xie, Y. Liu, M. Liu, K. Zhou, A novel hierarchical manufacturing method of the selective laser melted Al 7075 alloy, *Materials Characterization* 191 (2022) 112124. <https://doi.org/10.1016/j.matchar.2022.112124>.
- [118] M. Soulier, A. Benayad, L. Teulon, Y. Oudart, S. Senol, K. Vanmeensel, Nanocomposite powder for powder-bed-based additive manufacturing obtained by dry particle coating, *Powder Technology* 404 (2022) 117474. <https://doi.org/10.1016/j.powtec.2022.117474>.
- [119] A. Elsayed, C. Haase, U. Krupp, Additive manufacturing of metal matrix nanocomposites: Novel approach for nanoparticles dispersion by electromagnetic three-dimensional vibration, *Materials Letters* 344 (2023) 134399. <https://doi.org/10.1016/j.matlet.2023.134399>.
- [120] Z. Wang, L. Zhuo, E. Yin, Z. Zhao, Microstructure evolution and properties of nanoparticulate SiC modified AlSi10Mg alloys, *Materials Science and Engineering: A* 808 (2021) 140864. <https://doi.org/10.1016/j.msea.2021.140864>.
- [121] C. Gao, Z. Xiao, Z. Liu, Q. Zhu, W. Zhang, Selective laser melting of nano-TiN modified AlSi10Mg composite powder with low laser reflectivity, *Materials Letters* 236 (2019) 362–365. <https://doi.org/10.1016/j.matlet.2018.10.126>.
- [122] S. Guo, W. Zhou, Z. Zhou, Y. Fan, W. Luo, N. Nomura, In-Situ Reduction of Mo-Based Composite Particles during Laser Powder Bed Fusion, *Crystals* 11 (2021) 702. <https://doi.org/10.3390/cryst11060702>.
- [123] M. Stuer, Z. Zhao, P. Bowen, Freeze granulation: Powder processing for transparent alumina applications, *Journal of the European Ceramic Society* 32 (2012) 2899–2908. <https://doi.org/10.1016/j.jeurceramsoc.2012.02.038>.
-

- 
- [124] H. Wang, M. Lau, T. Sannomiya, B. Gökce, S. Barcikowski, O. Odawara, H. Wada, Laser-induced growth of  $\text{YVO}_4:\text{Eu}^{3+}$  nanoparticles from sequential flowing aqueous suspension, *RSC Adv.* 7 (2017) 9002–9008. <https://doi.org/10.1039/C6RA28118D>.
- [125] M. Lau, S. Barcikowski, Quantification of mass-specific laser energy input converted into particle properties during picosecond pulsed laser fragmentation of zinc oxide and boron carbide in liquids, *Applied Surface Science* 348 (2015) 22–29. <https://doi.org/10.1016/j.apsusc.2014.07.053>.
- [126] C. Doñate-Buendía, F. Frömel, M.B. Wilms, R. Streubel, J. Tenkamp, T. Hupfeld, M. Nachev, E. Gökce, A. Weisheit, S. Barcikowski, F. Walther, J.H. Schleifenbaum, B. Gökce, Oxide dispersion-strengthened alloys generated by laser metal deposition of laser-generated nanoparticle-metal powder composites, *Materials & Design* 154 (2018) 360–369. <https://doi.org/10.1016/j.matdes.2018.05.044>.
- [127] C. Doñate-Buendia, P. Kürnsteiner, F. Stern, M.B. Wilms, R. Streubel, I.M. Kusoglu, J. Tenkamp, E. Bruder, N. Pirch, S. Barcikowski, K. Durst, J.H. Schleifenbaum, F. Walther, B. Gault, B. Gökce, Microstructure formation and mechanical properties of ODS steels built by laser additive manufacturing of nanoparticle coated iron-chromium powders, *Acta Materialia* 206 (2021) 116566. <https://doi.org/10.1016/j.actamat.2020.116566>.
- [128] H. Yin, B. Wei, A. Shmatok, J. Yang, M.F. Salek, L. Beckingham, B. Prorok, J. Wang, X. Lou, On the nanoscale oxide dispersion via in-situ atmospheric oxidation during laser powder bed fusion, *Journal of Materials Processing Technology* 322 (2023) 118191. <https://doi.org/10.1016/j.jmatprotec.2023.118191>.
- [129] M.P. Haines, N.J. Peter, S.S. Babu, E.A. Jägle, In-situ synthesis of oxides by reactive process atmospheres during L-PBF of stainless steel, *Additive Manufacturing* 33 (2020) 101178. <https://doi.org/10.1016/j.addma.2020.101178>.
- [130] P. Chen, C. Yang, S. Li, M.M. Attallah, M. Yan, In-situ alloyed, oxide-dispersion-strengthened CoCrFeMnNi high entropy alloy fabricated via laser powder bed fusion, *Materials & Design* 194 (2020) 108966. <https://doi.org/10.1016/j.matdes.2020.108966>.
- [131] H. Gu, H. Gong, J. Dilip, D. Pal, Effects of Powder Variation on the Microstructure and Tensile Strength of Ti6Al4V Parts Fabricated by Selective Laser Melting, University of Texas at Austin, 2014.
-

- 
- [132] B. Dutta, F.H. Froes, The Additive Manufacturing (AM) of titanium alloys, *Metal Powder Report* 72 (2017) 96–106. <https://doi.org/10.1016/j.mprp.2016.12.062>.
- [133] N. Li, S. Huang, G. Zhang, R. Qin, W. Liu, H. Xiong, G. Shi, J. Blackburn, Progress in additive manufacturing on new materials: A review, *Journal of Materials Science & Technology* 35 (2019) 242–269. <https://doi.org/10.1016/j.jmst.2018.09.002>.
- [134] L.-C. Zhang, H. Attar, Selective Laser Melting of Titanium Alloys and Titanium Matrix Composites for Biomedical Applications: A Review, *Advanced Engineering Materials* 18 (2016) 463–475. <https://doi.org/10.1002/adem.201500419>.
- [135] H.W. Roberts, D.W. Berzins, B.K. Moore, D.G. Charlton, Metal-ceramic alloys in dentistry: a review, *Journal of Prosthodontics* 18 (2009) 188–194. <https://doi.org/10.1111/j.1532-849X.2008.00377.x>.
- [136] H. Wang, J.Y. Lim, Metal-ceramic bond strength of a cobalt chromium alloy for dental prosthetic restorations with a porous structure using metal 3D printing, *Computers in Biology and Medicine* 112 (2019) 103364. <https://doi.org/10.1016/j.compbiomed.2019.103364>.
- [137] B. Ganbold, S.-J. Heo, J.-Y. Koak, S.-K. Kim, J. Cho, Human Stem Cell Responses and Surface Characteristics of 3D Printing Co-Cr Dental Material, *Materials* 12 (2019) 3419. <https://doi.org/10.3390/ma12203419>.
- [138] A. Mostafaei, R. Ghiaasiaan, I.-T. Ho, S. Strayer, K.-C. Chang, N. Shamsaei, S. Shao, S. Paul, A.-C. Yeh, S. Tin, A.C. To, Additive manufacturing of nickel-based superalloys: A state-of-the-art review on process-structure-defect-property relationship, *Progress in Materials Science* 136 (2023) 101108. <https://doi.org/10.1016/j.pmatsci.2023.101108>.
- [139] Y. Lu, S. Wu, Y. Gan, T. Huang, C. Yang, L. Junjie, J. Lin, Study on the microstructure, mechanical property and residual stress of SLM Inconel-718 alloy manufactured by differing island scanning strategy, *Optics & Laser Technology* 75 (2015) 197–206. <https://doi.org/10.1016/j.optlastec.2015.07.009>.
- [140] Q. Jiang, P. Zhang, Z. Yu, H. Shi, Di Wu, H. Yan, X. Ye, Q. Lu, Y. Tian, A Review on Additive Manufacturing of Pure Copper, *Coatings* 11 (2021) 740. <https://doi.org/10.3390/coatings11060740>.
-

- 
- [141] A. Vahedi Nemani, M. Ghaffari, K. Sabet Bokati, N. Valizade, E. Afshari, A. Nasiri, Advancements in Additive Manufacturing for Copper-Based Alloys and Composites: A Comprehensive Review, *JMMP* 8 (2024) 54. <https://doi.org/10.3390/jmmp8020054>.
- [142] K. Artzt, M. Siggel, J. Kleinert, J. Riccius, G. Requena, J. Haubrich, Pyrometric-Based Melt Pool Monitoring Study of CuCr1Zr Processed Using L-PBF, *Materials* 13 (2020) 4626. <https://doi.org/10.3390/ma13204626>.
- [143] K. Morshed-Behbahani, A. Aliyu, D.P. Bishop, A. Nasiri, Additive manufacturing of copper-based alloys for high-temperature aerospace applications: A review, *Materials Today Communications* 38 (2024) 108395. <https://doi.org/10.1016/j.mtcomm.2024.108395>.
- [144] K. Morshed-Behbahani, A.J. Rayner, D.P. Bishop, A. Nasiri, Perspectives on the unusual electrochemical corrosion of Nickel Aluminum Bronze (NAB) alloy fabricated through laser-powder bed fusion additive manufacturing, *Corrosion Science* 228 (2024) 111846. <https://doi.org/10.1016/j.corsci.2024.111846>.
- [145] S. Scudino, C. Unterdörfer, K.G. Prashanth, H. Attar, N. Ellendt, V. Uhlenwinkel, J. Eckert, Additive manufacturing of Cu–10Sn bronze, *Materials Letters* 156 (2015) 202–204. <https://doi.org/10.1016/j.matlet.2015.05.076>.
- [146] S.M. Orzolek, J.K. Semple, C.R. Fisher, Influence of processing on the microstructure of nickel aluminum bronze (NAB), *Additive Manufacturing* 56 (2022) 102859. <https://doi.org/10.1016/j.addma.2022.102859>.
- [147] Le Zhou, A. Mehta, E. Schulz, B. McWilliams, K. Cho, Y. Sohn, Microstructure, precipitates and hardness of selectively laser melted AlSi10Mg alloy before and after heat treatment, *Materials Characterization* 143 (2018) 5–17. <https://doi.org/10.1016/j.matchar.2018.04.022>.
- [148] G. Ko, W. Kim, K. Kwon, T.-K. Lee, The Corrosion of Stainless Steel Made by Additive Manufacturing: A Review, *Metals* 11 (2021) 516. <https://doi.org/10.3390/met11030516>.
- [149] L. Guo, L. Zhang, J. Andersson, O. Ojo, Additive manufacturing of 18% nickel maraging steels: Defect, structure and mechanical properties: A review, *Journal of Materials Science & Technology* 120 (2022) 227–252. <https://doi.org/10.1016/j.jmst.2021.10.056>.
-



- 
- [150] R. Casati, M. Coduri, N. Lecis, C. Andrianopoli, M. Vedani, Microstructure and mechanical behavior of hot-work tool steels processed by Selective Laser Melting, *Materials Characterization* 137 (2018) 50–57. <https://doi.org/10.1016/j.matchar.2018.01.015>.
- [151] F. Deirmina, N. Peghini, B. AlMangour, D. Grzesiak, M. Pellizzari, Heat treatment and properties of a hot work tool steel fabricated by additive manufacturing, *Materials Science and Engineering: A* 753 (2019) 109–121. <https://doi.org/10.1016/j.msea.2019.03.027>.
- [152] O.O. Marenych, A.G. Kostryzhev, Z. Pan, H. Li, S. van Duin, Comparative effect of Mn/Ti solute atoms and TiC/Ni<sub>3</sub>(Al,Ti) nanoparticles on work hardening behaviour in NiCu alloys fabricated by wire arc additive manufacturing, *Materials Science and Engineering: A* 753 (2019) 262–275. <https://doi.org/10.1016/j.msea.2019.03.040>.
- [153] O. Marenych, A. Kostryzhev, C. Shen, Z. Pan, H. Li, S. van Duin, Precipitation Strengthening in Ni–Cu Alloys Fabricated Using Wire Arc Additive Manufacturing Technology, *Metals* 9 (2019) 105. <https://doi.org/10.3390/met9010105>.
- [154] S. Bhattacharya, G.P. Dinda, A.K. Dasgupta, J. Mazumder, A comparative study of microstructure and mechanical behavior of CO<sub>2</sub> and diode laser deposited Cu–38Ni alloy, *J Mater Sci* 49 (2014) 2415–2429. <https://doi.org/10.1007/s10853-013-7883-7>.
- [155] P.Q. Dai, C. Zhang, J.C. Wen, H.C. Rao, Q.T. Wang, Tensile Properties of Electrodeposited Nanocrystalline Ni–Cu Alloys, *J. of Materi Eng and Perform* 25 (2016) 594–600. <https://doi.org/10.1007/s11665-016-1881-2>.
- [156] S. Bhattacharya, G.P. Dinda, A.K. Dasgupta, H. Natsu, B. Dutta, J. Mazumder, Microstructural evolution and mechanical, and corrosion property evaluation of Cu–30Ni alloy formed by Direct Metal Deposition process, *Journal of Alloys and Compounds* 509 (2011) 6364–6373. <https://doi.org/10.1016/j.jallcom.2011.03.091>.
- [157] M. Marya, V. Singh, Y. Lu, J.-Y. Hascoet, S. Marya, Transition Microstructures and Properties in the Laser Additive Manufacturing Repair of Monel K-500 (UNS N05500) and Toughmet 3AT (UNS C72900), in: M.&M.S. The Minerals (Ed.), TMS 2015 144th Annual Meeting & Exhibition, Annual Meeting Supplemental Proceedings, firstst ed., Springer International Publishing, Cham, 2016, pp. 413–420.
-



- [158] O.O. Marenych, A.G. Kostryzhev, Z. Pan, H. Li, S. van Duin, Application of wire arc additive manufacturing for repair of Monel alloy components, *Australian Journal of Mechanical Engineering* 19 (2021) 609–617. <https://doi.org/10.1080/14484846.2021.1981528>.
- [159] D.J. Young, J. Zhang, C. Geers, M. Schütze, Recent advances in understanding metal dusting: A review, *Materials & Corrosion* 62 (2011) 7–28. <https://doi.org/10.1002/maco.201005675>.
- [160] K. Jahns, A.S. Ulrich, C. Schlereth, L. Reiff, U. Krupp, M.C. Galetz, The Effect of Cu Content and Surface Finish on the Metal Dusting Resistance of Additively Manufactured NiCu Alloys, *Oxid Met* 96 (2021) 241–256. <https://doi.org/10.1007/s11085-021-10037-8>.
- [161] Special Metals Corporation, Publication number SMC-026: High-performance alloys for resistance to aqueous corrosion, 2000. <https://www.specialmetals.com/documents/guides-and-handbooks/>.
- [162] Special Metals Corporation, Publication Number SMC-053: Monel Alloy 400, 2005. <https://www.specialmetals.com/documents/technical-bulletins/>.
-

# Chapter 7

PUBLICATIONS

**7.1     Establishing a process route  
for additive manufacturing of  
NiCu-based Alloy 400: an  
alignment of gas atomization,  
laser powder bed fusion, and  
design of experiments**

**Jan-Philipp Roth**, Ivo Šulák, Tomáš  
Kruml, Wojciech Polkowski, Tomasz  
Dudziak, Peter Böhlke, Ulrich Krupp,  
Katrin Jahns

The International Journal of Advanced  
Manufacturing Technology 134 (2024)  
3433–3452

DOI 10.1007/s00170-024-14328-7

Reference [1]



# Establishing a process route for additive manufacturing of NiCu-based Alloy 400: an alignment of gas atomization, laser powder bed fusion, and design of experiments

Jan-Philipp Roth<sup>1</sup> · Ivo Šulák<sup>2</sup> · Tomáš Kruml<sup>2</sup> · Wojciech Polkowski<sup>3</sup> · Tomasz Dudziak<sup>3</sup> · Peter Böhlke<sup>4</sup> · Ulrich Krupp<sup>5</sup> · Katrin Jahns<sup>1</sup>

Received: 25 March 2024 / Accepted: 22 August 2024 / Published online: 3 September 2024  
© The Author(s) 2024

## Abstract

Alloy 400 is a corrosion-resistant, NiCu-based material which is used in numerous industrial applications, especially in marine environments and the high-temperature chemical industry. As conventional manufacturing limits geometrical complexity, additive manufacturing (AM) of the present alloy system promises great potential. For this purpose, a robust process chain, consisting of powder production via gas atomization and a design of experiment (DoE) approach for laser powder bed fusion (LPBF), was developed. With a narrow particle size distribution, powders were found to be spherical, flowable, consistent in chemical composition, and, hence, generally applicable to the LPBF process. Copper segregations at grain boundaries were clearly detected in powders. For printed parts instead, low-intensity micro-segregations at cell walls were discovered, being correlated with the iterative thermal stress applied to solidified melt-pool-near grains during layer-by-layer manufacturing. For the production of nearly defect-free LPBF structures, DoE suggested a single optimum parameter set instead of a broad energy density range. The latter key figure was found to be misleading in terms of part densities, making it an outdated tool in modern, software-based process parameter optimization. On the microscale, printed parts showed an orientation of melt pools along the build direction with a slight crystallographic [101] texture. Micro-dendritic structures were detected on the nanoscale being intersected by a high number of dislocations. Checked against hot-extruded reference material, the LPBF variant performed better in terms of strength while lacking in ductility, being attributed to a finer grain structure and residual porosity, respectively.

**Keywords** Alloy 400 · Monel · Gas atomization · Additive manufacturing · Laser powder bed fusion · Design of experiments

## 1 Introduction

Alloy 400 is a NiCu-based alloy, consisting mainly of two-thirds nickel and one-third copper, respectively. Both, nickel and copper, crystallize in a face-centered cubic (fcc) structure and form a solid solution [1–3]. Thus, Alloy 400, also known as Monel 400, consists of one phase only and shows isomorphic characteristics [2, 4, 5]. Further alloying elements with marginal proportions are iron, silicon, manganese, aluminum, and carbon.

The alloy shows excellent corrosion resistance in various media, such as acids, bases, and sea water [1, 4, 6–8]. It finds its application in steam generator tubes as well as in gas- and liquid-carrying pipelines for power plants. In the field of shipbuilding and marine technology, impellers, pump shafts, and splash zone claddings on offshore

---

✉ Jan-Philipp Roth  
j.roth@hs-osnabrueck.de

<sup>1</sup> Faculty of Engineering and Computer Science, Osnabrück University of Applied Sciences, 49076 Osnabrück, Germany

<sup>2</sup> Institute of Physics of Materials, Czech Academy of Sciences, 61600 Brno, Czech Republic

<sup>3</sup> Krakow Institute of Technology, Łukasiewicz Research Network, 30-418, Kraków, Poland

<sup>4</sup> KME Germany GmbH, Klosterstraße 29, 49074 Osnabrück, Germany

<sup>5</sup> Steel Institute IEHK, RWTH Aachen University, 52072 Aachen, Germany

platforms are made of Alloy 400. In pump construction, components are facing a combined stress resulting from abrasion, erosion, corrosion, and chemical resistance, which is why Alloy 400 can be considered indispensable within this field [9]. Generally speaking, products being manufactured out of Monel alloys are very long-lasting due to their long-term resistance to the environment [8]. Further benefits of Alloy 400 are its good ductility and easy cold formability, which opens up a wide variety of engineering systems [10]. It behaves ductile at temperatures below 0 °C, meaning that it does not show brittle properties in a cold state [5].

With nickel being the base material, the alloy has great potential in high-temperature environments as well [11]. Also, due to the high copper content within Alloy 400, heat exchangers for combustion engines can be considered a further area of application [12]. Most importantly, critical component failure due to metal dusting, as present in the aggressive environments of power plants, can be addressed by NiCu-based alloys. Caused by a combination of temperatures around 450–800 °C, a high carbon activity  $a_c > 1$ , and a low oxygen partial pressure  $p_{O_2}$ , coke deposits both at the surface and inside the structure, eventually leading to the destruction of the entire component [13, 14]. Monel alloys can counter this effect as a Cu content of at least 30% catalytically inhibits the sedimentation of C, and thus, no coke layer is formed [13, 15].

Monel alloys have already been manufactured via conventional fabrication processes for more than a century [8]. But besides tool-bound technologies, additive manufacturing paves the way for products that cannot be manufactured in a classical manner and that allow complex undercuts as in extremely fine ribbed heat exchangers for instance. In contrast to conventional manufacturing processes, AM shows good applicability when it comes to low quantity but high complexity issues. Considering the physical state of the input material, AM technologies can generally be split up into the three different categories of powders, liquids, and solids, and against the background of metal materials, powder-based applications are of main interest [16, 17]. According to DIN EN ISO/ASTM 52900, as one of seven process categories for additive manufacturing, powder bed fusion processes locally introduce thermal energy in order to fully melt loose powder particles. Thus, after rapid solidification of the melt, highly dense structures are created. Since a wide range of metal alloys show repeatable good processability, laser powder bed fusion, also known as selective laser melting (SLM), can be considered a promising technology for AM of Alloy 400 [18]. In this iterative process, a layer of powder is applied to a build plate and partly melted by a laser beam, resulting in complex structures with a higher degree of geometrical freedom than in conventional manufacturing.

For LPBF to be a powder bed-based process, suitable material has to be provided. Here, the atomization of bulk Alloy 400 to fine powder plays an essential part in the process route. There are existing several atomization processes within the field of metal additive manufacturing such as water atomization, electrode induction gas atomization (EIGA), the plasma rotating electrode process (PREP), plasma atomization (PA), and vacuum inert gas atomization (VIGA). Among these processes, VIGA leads to a high homogeneity of the melt and the alloying system, respectively. Vacuum and inert gas, such as argon, both prevent the melt from forming oxides with the ambient air, leading to very low oxygen contents of only a few ppm in the alloy. Moreover, an ideal particle size distribution (PSD) for LPBF such as high flowabilities and bulk densities of the powder can be achieved. Also, VIGA is well known for the processing of nonreactive metal alloys which is why, in summary, this atomization process is suited best for the production of Alloy 400 powders [19, 20].

During atomization, when it comes to the exact place of the inert gas introduction, two different set-ups may be applied: free-fall atomization (FFA) or close-coupled atomization (CCA). The former method gives the melt a chance of falling out of the crucible nozzle into the atomization chamber. After a defined distance, the gas stream hits the melt stream, atomizing the alloy to spherical powder that reveals a log-normal PSD [21]. During the latter method, the powder is atomized just as it exits the crucible nozzle. The gas stream rapidly cools down the melt, resulting in a local low-pressure area that further increases the melt volume rate (MVR;  $MVR = \text{cm}^3/10 \text{ min}$ ). High homogeneities and purities can be reached by application of CCA [21, 22].

When setting up an experiment, there are several methods that can be applied. A classic approach would be the one-factor-at-a-time (OFAT) strategy. This approach, which dates back more than a century, is still used frequently in modern science although not being the most promising one as it is very time-consuming and only varies one parameter at a time. In contrast, a design of experiments approach has the ability to vary several parameters simultaneously, resulting in a more detailed overview of parameter interdependencies in less time. Here, on the basis of multiple input variables, a prediction of the system response can be carried out [23]. In general, DoE requires fewer resources, the prediction for a single parameter is more accurate, interconnections in between parameters cannot be determined with OFAT, and the optimal response of a system is located more precisely [24]. There are many DoE techniques that can be applied to different optimization cases, but they all require a design space as an input, which indicates the spectrum of the variability of one parameter. Conclusions from this input may explain alterations in the output data [25]. The full factorial method is a widely known one with the big advantage

that it can clearly differentiate between single parameters, and therefore, clear conclusions of the respective effect of a parameter on the whole system can be drawn [25–27].

Developing usable material for AM in general and for LPBF in particular comes with some difficulties; the desired state and shape of the feedstock material have to be producible, key properties such as sufficient flowability and bulk density need to be ensured, and the chemical composition must be consistent and free of any impurities [28]. Moreover, defect formation of powders, e.g., in terms of satellite formation or lack of sphericity, has to be avoided as it negatively affects absorptivity and recoatability during printing [29]. Hence, finding a consistent procedure in powder and material development for any alloy to be used for LPBF is essential for the adaptation of the technology. Although numerous processes for gas atomization and laser powder bed fusion of metals are already known, there is no holistic approach for Alloy 400 at this point. The complexity of the atomization of high-melting alloys and the challenges associated with LPBF processing of conductive materials are the main reasons for this. Hence, this study aims to establish such an AM process routine to serve as a standard reference for the present alloy system. This includes material supply via gas atomization, parameter definition according to a design of experiments, and LPBF production of components. Throughout the whole process, powders and parts were analyzed on their micro-scale, including grain structure and chemical composition. Mechanical properties in terms of indentation hardness and tensile strength were quantified. Not least due to its wide applicability in industrial applications, there is an exigent need to qualify this alloy for the LPBF process. By putting a special focus on reproducibility and unambiguous comparability to hot-extruded reference material (provided by Cunova GmbH), this demand is intended to be satisfied. In order to reach this goal, an emphasis was put on the following novelties:

- Development of a well-adjusted atomization routine, including extensive powder investigations for Alloy 400
- Elaboration of a DoE approach tailored to the Alloy 400 LPBF process, reaching for the highest densities possible
- First-time identification of material characteristics of the additively manufactured Alloy 400 and comparison to conventional fabrication

## 2 Experimental procedure

### 2.1 Gas atomization

For the production of metal powder prior to the AM process, an Indutherm Blue Power AU3000 gas atomizer was utilized. Due to its high atomization temperature of  $\sim 1600$  °C

(liquidus temperature:  $\sim 1350$  °C), Alloy 400 can only be atomized using a high-temperature (HT) equipment setup; the bulk material got loaded into a ceramic crucible which itself was applied to a graphite susceptor as displayed in Fig. 1. The heating was done via induction, and a close-coupled atomization setup was used with argon as inert gas. The CCA setup causes the formation of a low-pressure area beneath the nozzle and in combination with the low viscosity of the melt, achieved by considerable overheating, and high gas stream velocity; this leads to the formation of relatively fine particles [30]. During atomization, the Ar pressure was set to  $\sim 8$  bar, and the gas flow was  $\sim 215$  m<sup>3</sup>/h. In literature, the hereby resulting cooling rates vary from  $10^2$  to  $10^8$  K/s [30, 31]. For a powder fraction from 20 to 63  $\mu\text{m}$ , which matches approximately the desired range in this work, more precise cooling rates of  $10^3$  to  $10^4$  K/s are stated [32, 33]. In order not to freeze the nozzle with Ar gas and to ensure a sufficient discharge of the liquid, the gas stream was activated with a delay of 1.5 s post to the release of the melt. To further homogenize the material, the liquid Alloy 400 was held at its atomization temperature for 15 min before releasing the melt into the atomization tower. Moreover, low viscosity and, thus, more effective mixing of the melt were ensured by overheating the system by  $\sim 250$  °C above its liquidus temperature. This way, 10 kg of bulk material was atomized to powder during approx. 2 min.

Considering LPBF fabrication capability, the powder being too coarse was sieved out, and particles being too fine were air-separated from the final fraction of 15–63  $\mu\text{m}$  by using an automated sieve (EOS/Russell) and an AC1000 air

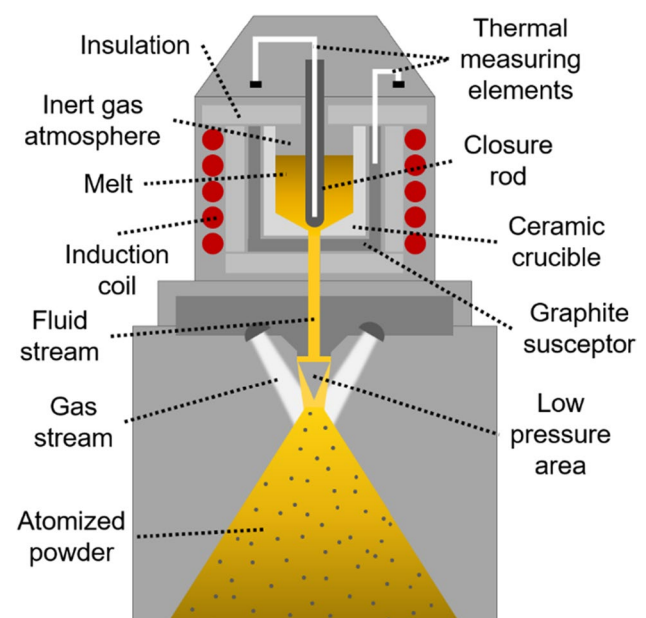


**Fig. 1** High-temperature close-coupled atomization setup according to [34]

classifier (Indutherm Blue Power), respectively. The final powder was analyzed by a Zeiss Auriga scanning electron microscope (SEM) in terms of particle size, microstructure, and porosity. By application of a focused ion beam (FIB), cross-sections of particles were analyzed for their grain structure, utilizing  $\text{Ga}^+$  as the respective liquid metal ion source. Moreover, the existing elements were classified in greater detail via the application of energy-dispersive X-ray spectroscopy (EDS), using Aztec software (Oxford Instruments) for evaluation. The chemical composition of the powder used for LPBF was double-checked by wet chemical analysis (WCA, Agilent 5800 ICP-OES) and compared to the initial composition of the bulk material. Hall flow testing was performed in order to verify the flowability (DIN EN ISO 4490) and bulk density (DIN EN ISO 3923–1) of the powder. The measurements were extended by powder rheology investigations using a FT4 universal powder rheometer (Freeman Technology) according to ASTM D 7981 at the Research Institutes of Sweden (RISE). These shear cell investigations consisted of flow function, cohesion, Hausner ratio, and surface area. To quantify the particle size distribution with dynamic image analysis (ISO 13322–2), a CamSizer X2 (Retsch) was used.

## 2.2 Laser powder bed fusion

Throughout the whole laser powder bed fusion fabrication and optimization process, an EOS AMCM M290 customized machine was used. Special features of this machine are a heatable build plate (up to 500 °C), a reduced build space (diameter 100 mm, height 100 mm) for small batch investigations, and a green laser source (wavelength 532 nm). A brush was used as a recoater, and the build chamber was pressured with Ar inert gas. One layer had a thickness of 20  $\mu\text{m}$ , the build plate was pre-heated at 80 °C, and a rotating scanning strategy of 67° was applied. Moreover, the travel of the laser was always directed against the inert gas stream. This way, ejections from the melt pool onto the unmolten powder bed, due to acceleration caused by the gas flow, were prevented. As a test geometry, cubes with an edge length of  $8 \times 8 \times 8 \text{ mm}^3$  (1.5 mm of support beneath) were examined. In total, 24 cubes were fabricated within one build job. Support structures beneath the cubes allowed heat transferability from the part to the build plate and vice versa, as well as easy removal from the build plate by either band sawing or wire electrical discharge machining. The build plate was made of 1.0050 (E295) plain carbon steel and had a round shape with a diameter of 100 mm.

The resulting relative densities were obtained via buoyancy according to Archimedes and optically via light optical microscopy (LOM), respectively, as per VDI 3405–2. As stated in this standard, the first method leads to a quite accurate overview of the overall density of a part, while optical

investigations provide more meaningful insights into the arrangement and form of pores in one specific layer. For this reason, densities measured according to both procedures were considered: buoyancy for a fast, approximate value and optical microscopy evaluations for the more accurate final value. Five areas of a single layer of DoE cubes were considered for the calculation of the average relative density within one specimen. Images of cross-sections parallel and perpendicular to the build plane were taken and compared. They showed no significant difference in terms of density in between each other, and thus, parallel preparation was chosen for the evaluation of optical density due to faster preparation. LOM images were taken by a digital microscope (Keyence), and the ImageJ software was used for the determination of density. Also, specimens were etched with ferric chloride in order to make visible the melt pool propagation in the build direction under the LOM.

For examinations via SEM, cubes were cut in half perpendicular to the build plane by a linear precision saw IsoMet 4000 (Buehler) and fixed in a conductive-filled phenolic mounting compound, using a warm embedding device SimpliMet 1000 (Buehler). Afterwards, parts were ground (down to 2500 grit SiC paper) and polished (down to 0.02  $\mu\text{m}$  colloidal silica suspension) by an EcoMet 300 (Buehler). Chemical analysis was carried out by wet chemical analysis and double-checked by application of EDS. The grain structure was investigated by electron backscattered diffraction (EBSD). For more in-depth characterization of the nanoscale, a transmission electron microscope (TEM) JEOL JEM-2100F working at 200 kV was used. It was operated at the Institute of Physics of Materials, Brno, and it is equipped with a bright-field detector allowing observation in scanning mode (STEM) as well as an Oxford XMAX80 EDS detector for analysis of the local chemical composition.

## 2.3 Material properties

In order to obtain the mechanical properties of the LPBF-fabricated alloy, tensile tests according to VDI 3405–2 were performed. A universal electromechanical Zwick Z050 tensile testing machine was used with a strain rate of  $8.0 \times 10^{-3}/\text{s}$ . The elongation was detected via sensor arm extensometers. Cylinders for tensile testing had a diameter of 10 mm and were reworked by machining, resulting in type B specimens as per DIN 50125 (diameter 6 mm, gauge length 30 mm). As recommended in the standard, blanks were built in three different orientations:

- In a polar angle  $\Theta$  of 90° to the build direction (horizontal orientation in build space)
- In a polar angle  $\Theta$  of 45° to the build direction (diagonal orientation in build space)



- In a polar angle  $\Theta$  of  $0^\circ$  to the build direction (vertical orientation in build space)

All blanks revealed an azimuth angle  $\varphi$  of  $45^\circ$  to the coater brush. This angle was chosen in order to ensure proper coverage of the melt pool with every new layer of powder. For hardness measurements,  $8 \times 8 \times 8 \text{ mm}^3$  cubes were manufactured and ground on the test surfaces (parallel as well as perpendicular to the building plane). Hardness was then obtained according to Vickers as per DIN EN ISO 6507–1.

Tensile tests were also carried out at elevated temperatures at the Institute of Physics of Materials, Brno, in order to further investigate the behavior of the alloy in possible high-temperature fields of application. For this purpose, small cylindrical specimens (3 mm in diameter, 9 mm in gauge length) were used. The specimens were fabricated from a material block prepared by additive manufacturing; the specimen axis was perpendicular to the building direction ( $\Theta = 90^\circ$ ). A universal electromechanical Zwick Z050 system was used in the regime of constant traverse speed (1 mm/min, which corresponds to a strain rate of  $1.6 \times 10^{-3}/\text{s}$ ). The ductility was measured by a clip-on extensometer with ceramic rods (MayTec), touching the specimen. The furnace was equipped with 3 thermocouples for controlling the temperature stability and keeping a low thermal gradient. Tests were performed in laboratory air.

## 2.4 Design of experiments

To be able to find a LPBF parameter set that exceeds high densities of 99.5%, a DoE approach using Minitab software was carried out and applied to the optical density data taken from cross-sections of specimens. As parameters, laser power  $p_L$  in (W), scanning speed  $s_s$  in (mm/s), and hatch distance  $d_H$  in ( $\mu\text{m}$ ) were investigated. They all affect the final density of the part in a significant way, and their interdependency can be described by a cube, consisting of a dark blue center point, orange corner points, and light blue star points (Fig. 2). The center point describes the input data, taken from previous studies and/or iterations. With the help of corner points, a space is built up around the center point which is likely to contain a better response in terms of density. Several combinations of input variables fluctuate in a positive and negative manner around the starting values of the center point. Ultimately, star points are reaching out of the cube, representing extreme values of one parameter only, while the other two stay at their center point levels. Single-parameter influences can be derived from this.

Three DoE iterations were carried out to narrow down further the parameter ranges needed to reach the goal of high density. However, before processing the first DoE iteration, the program needed initial information about the

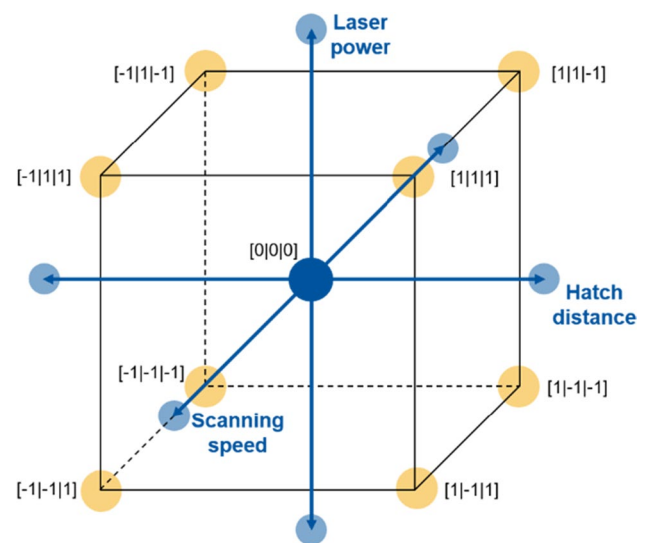


**Fig. 2** Laser power, scanning speed, and hatch distance within the design space

input–output interdependence. Therefore, the very first print job was carried out without the use of software but based on parameter sets that showed good processability for different yet comparable alloys, such as Alloy K500. By finding the correlations between parameter combinations and resulting densities, the computational simulation was filled with data. As a result, new parameter settings were calculated and interpreted, leading to higher densities throughout the first DoE iteration. The maximum attainable density rose from one iteration to another, but ultimately, the optimization would stagnate, revealing no significant improvement of a new parameter set when compared to the previous one. This indicated the end of the procedure.

## 3 Results

### 3.1 Powder production and characterization

The chemical composition was determined for gas-atomized powders, LPBF-fabricated parts, and hot-extruded reference samples by wet chemical analysis and EDS, respectively. Results and face values according to DIN 17743 (material no. 2.4360, NiCu30Fe) are given in Table 1. For carbon being a light element with a very low proportion in the present alloy, measurements were excluded due to unreliable detectability.

With respect to the chemical requirements of Alloy 400, no significant deviations were detected for LPBF-fabricated parts throughout the whole process. Moreover, when comparing powders and LPBF specimens, only small variations were measured. Due to this analytical evidence, the



**Table 1** Intervention limits of Alloy 400 and measured compositions according to application of wet chemical analysis and energy-dispersive X-ray spectroscopy in different states (in wt. %)

Chem. element	Ni	Cu	Fe	Si	Mn	Al
Nominal composition	≥ 63.0	28.0–34.0	1.0–2.5	≤ 0.5	≤ 2.0	≤ 0.5
Reference (WCA)	62.5	31.4	2.2	0.2	1.3	0.1
Reference (EDS)	62.3	29.7	2.0	0.3	1.1	0.2
Powder (WCA)	63.2	31.6	1.9	0.2	1.0	0.2
Powder (EDS)	63.2	28.6	2.1	0.3	1.1	0.3
LPBF (WCA)	64.1	31.0	2.4	0.2	1.3	0.2
LPBF (EDS)	63.4	30.1	2.1	0.4	1.1	0.3

processing of gas-atomized powder was considered to fulfill the specification. Analyses on reference samples were to a great extent in line with the standard as well.

Further SEM investigations of the powder were carried out with a secondary electrons secondary ions (SESI) detector, and results are displayed in Fig. 3a. Gas-atomized Alloy 400 reveals mostly spherical particles with only sporadic occurrence of satellites or coarse agglomerates, which would negatively influence powder processing properties, in particular its flowability [35, 36]. The images clearly indicate the rapid cooling of the particles during atomization, resulting in very fine, dendritic grain growth and grain sizes of approx. 1 to 9  $\mu\text{m}$  (mean  $5.2 \pm 3.2 \mu\text{m}$ ). Small powder particles tend to evolve small grains of a few micrometers only, and larger particles show coarser grains of up to 15  $\mu\text{m}$ . Figure 3b shows a single powder particle that was cut with a focused Gallium ion beam. Having a more detailed look at single grains and grain boundaries with the in-lens detector, no precipitates of the associated elements were detected, being in line with the assumption of this alloy being a solid solution [1]. Nevertheless, having a closer look at EDS data,

a special property of Alloy 400 was detected; the concentration of copper is higher at the grain boundaries than within the grains and vice versa, and the concentration of nickel is lower at the grain boundaries than within the grains. These local differences in concentration were classified as segregations, which are typical for NiCu-based alloys [37–39]. Segregations concerning the remaining five elements were not detected. Furthermore, no gas porosity or impurity was detected within the particles. Such defect-free particles with fine grains are considered favorable for production as stated in [31, 40]. In general, the chemical distribution of elements can be described as homogeneous, both on the surface of and inside the particles, respectively.

On average, the volumetric sphericity measured by dynamic image analysis reached a normalized value of  $\text{sph}_3 = 0.766$  (1.000 being perfectly spherical). Even though most particles appear spherical in SEM, a lower  $\text{sph}_3$  was attributed to the few attached satellites, as documented in [41]. Volumetric symmetry ( $\text{symm}_3 = 0.916$ ) and volumetric aspect ratio of width to length ( $w/l_3 = 0.821$ ) correspond to this observation. This indicates that the powder is probably

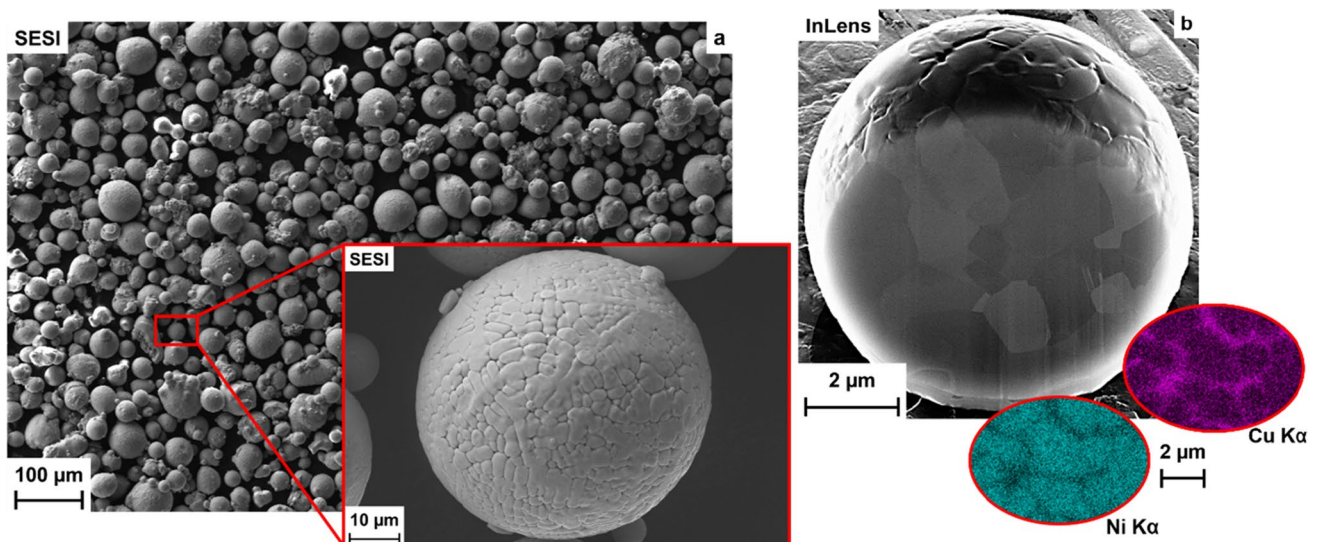


**Fig. 3** **a** SEM micrograph of gas-atomized powder (overview and detail); **b** a FIB cross-section of a single particle, illustrating grain growth and, via application of EDS, Cu segregations at grain boundaries

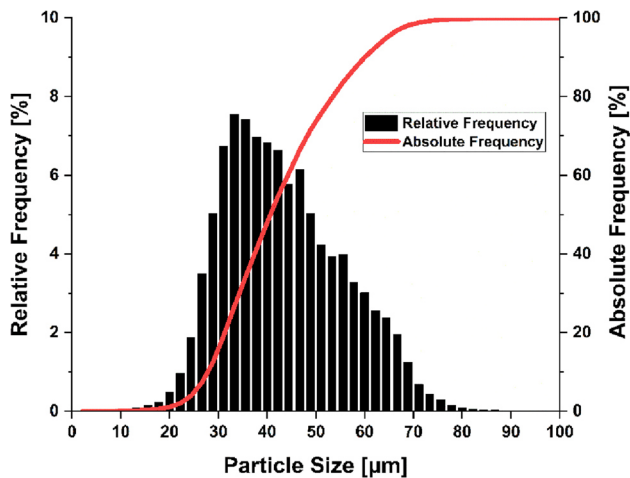


**Fig. 4** Particle size distribution of the final powder fraction used for LPBF printing

processable as key values close to 1.000 are linked to a high flowability of the powder and great energy absorption of the laser into the particles [42, 43]. Powder being too coarse was sieved out by a sieve with a mesh size of 63  $\mu\text{m}$ . The remaining fraction was then air-separated in order to remove particles being finer than 15  $\mu\text{m}$ . This way and as displayed in Fig. 4, the particle size distribution could be narrowed down to a  $Q_3$  (10%) of 28.9  $\mu\text{m}$  and a  $Q_3$  (90%) of 61.5  $\mu\text{m}$ ; the  $Q_3$  (50%) was 42.3  $\mu\text{m}$  and in line with the qualitative findings via SEM. The bulk density of the final powder fraction was  $\rho_b = 4.38 \text{ g/cm}^3$ , indicating a relative density of  $\rho_{\text{rel}} = \sim 50\%$  when compared to the nominal density of Alloy 400 ( $\rho_n = 8.80 \text{ g/cm}^3$ ) [7]. With a Hall flowability of 15.22 s per 50 g powder, the particles showed a good mass flow; rat-holing phenomena were not observed, and the standard funnel did not have to be knocked at in order to initiate the flow. A good flowability was attributed to the high sphericity of the particles [44]. Shear cell investigations were performed after conditioning the powder with a pressure of 9 kPa. By twisting one layer of powder relative to another one, a flow function  $\text{FF} = \sigma_M / \sigma_C$  was calculated with  $\sigma_M$  being the major principal stress and  $\sigma_C$  the unconfined yield strength. A normalized flow function value of approx. 15 was detected, with values above 10 being considered as flowing well according to the specifications of the device manufacturer (Freeman Technology, 2023). This is underlined by the low degree of cohesion of  $\sim 0.25 \text{ kPa}$  of the powder when being sheared. Moreover, the Hausner ratio as an indicator for the attrition in between particles was 1.09 for the present Alloy 400, which is desired in terms of processability [45–47]. On average, the surface area of the coarse powder measured  $0.034 \text{ m}^2/\text{g}$ .

The above results led to the conclusion that the powder should behave as expected during LPBF, which meant that

it could be applied properly to the powder bed and that processability was generally ensured.

## 3.2 Laser powder bed fusion and design of experiments

### 3.2.1 Parameter optimization

Throughout the LPBF process parameter optimization, the parameters were varied as follows:

- Laser power  $p_L$ : 60–120 W.
- Scanning speed  $s_S$ : 250–1350 mm/s.
- Hatch distance  $d_H$ : 30–120  $\mu\text{m}$ .

Considering a single DoE iteration, the simulation needed to be interpreted against the background of input–output correlations, exemplary as displayed in Fig. 5. This figure can be considered as a two-dimensional cut through the cube presented in Fig. 2. The parameter setting revealed a constant value for the hatching distance (80  $\mu\text{m}$ ) and variations in the other two: scanning speed (600–1300 mm/s) and laser power (60–110 W), respectively. On the basis of density measurements and allocation to the set parameters (black dots), calculations were performed that predicted the occurrence of different, pre-defined density ranges (shades of green). In this particular case, no densities above 99.5% were predicted for a constant hatch distance of 80  $\mu\text{m}$ , regardless of how much the other two parameters were adjusted. A hatching of 80  $\mu\text{m}$  is therefore generally considered unsuitable in order to reach high densities. Hence, the investigated process window did not show sufficient measuring points at this stage and needed to be investigated for other hatch distances.

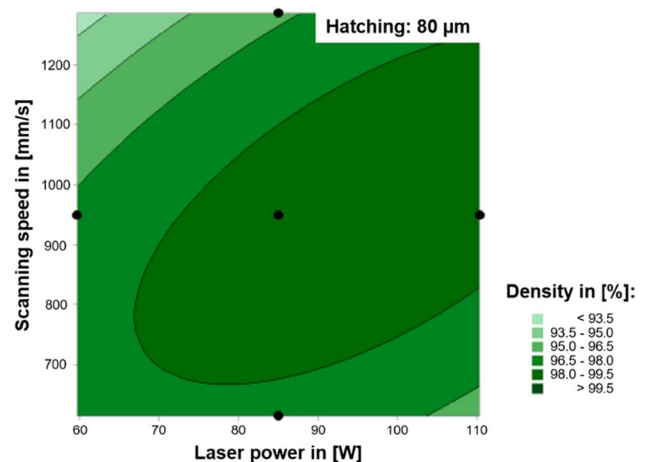


**Fig. 5** DoE contour diagram for varying laser powers and scanning speeds at a constant hatching distance of 80  $\mu\text{m}$ , expected density ranges in shades of green

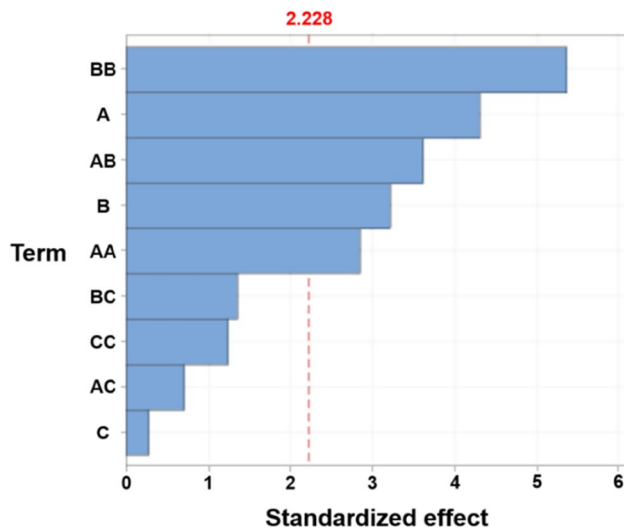


**Fig. 6** Pareto diagram of standardized effects revealing the statistical significance of the parameters laser power (A), scanning speed (B), hatch distance (C), and their combinations

With density being the output variable of the regression equation, a Pareto diagram of standardized effects as in Fig. 6 was drawn from the parameters. For A being the laser power, B being the scanning speed, and C being the hatch distance, the diagram clearly indicates statistical significance for A and B as they cross the reference line of 2.228 in whatever combination (A, B, AA, AB, BB). The reference value varies from one iteration to another as it results from the respective regression equation of one iteration. The value is affected by the linear term, the quadratic term, the two-factor interaction, and the error term. The linear term illustrates the effect of a single parameter only, while the quadratic term acts as a balancing calculation (a more accurate replica of the answer term). For variable C, hatching, no statistically significant term was found with respect to the parameter combinations displayed in Fig. 5. This underlines the need for further testing and evaluation of the influence of the hatch distance. The factors are statistically significant at the  $\alpha=0.05$  level, which meant that the probability of the displayed results being not due to the investigated relationships is below 5%.

According to [48, 49], the nominal energy introduced into the part (neglecting reflection) can be described by

$$e_V = p_L / (s_S * d_H * t_L)$$

with  $e_V$  being the volume energy density in ( $\text{J}/\text{mm}^3$ ) and  $t_L$  the thickness of a layer in ( $\mu\text{m}$ ) with a constant value of  $20 \mu\text{m}$ . In total, 72 parameter combinations were examined during three DoE iterations. Figure 7 gives an overview of the absolute positioning in the design space consisting of laser power, scanning speed, and hatch distance as well

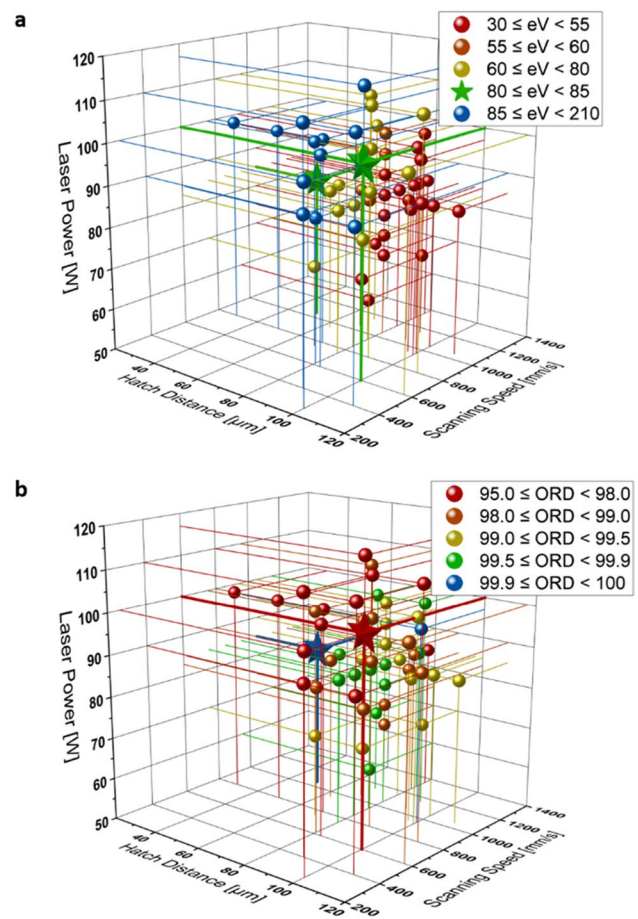


**Fig. 7** **a** Parameter combinations within the design space, color-coded according to their resulting volume energy density in ( $\text{J}/\text{mm}^3$ ); **b** same parameter combinations but in turn, color-coded according to their resulting optical relative density in (%)

as relative positioning in between various parameter sets. While Fig 7a indicates the resulting volume energy density, Fig 7b shows the resulting optical relative density (ORD). Parameters leading to similar volume energy densities are colored equally with an  $e_V$  of  $210 \text{ J}/\text{mm}^3$  being the maximum tested one. It can clearly be observed that border areas like 0 to  $55 \text{ J}/\text{mm}^3$  and  $85$  to  $210 \text{ J}/\text{mm}^3$  are distributed widely throughout the design space, while an energy density of 60 to  $80 \text{ J}/\text{mm}^3$  leads to a rather marginal distribution around the common core of the examined parameter sets. There are only two parameter combinations belonging to the category of 80 to  $85 \text{ J}/\text{mm}^3$ , indicated by two green stars. The lower left star represents an  $e_V$  of  $80.95 \text{ J}/\text{mm}^3$ , originating from  $p_L=85 \text{ W}$ ,  $s_S=1050 \text{ mm/s}$ , and  $d_H=50 \mu\text{m}$ . For the upper right star,  $p_L=100 \text{ W}$ ,  $s_S=600 \text{ mm/s}$ , and  $d_H=100 \mu\text{m}$  were the parameters, resulting in an  $e_V$  of  $83.33 \text{ J}/\text{mm}^3$ . Both stars are highlighted concerning their ORD as well, once as a blue star with an ORD of 99.94% and once as a red star with an ORD of 97.26%.



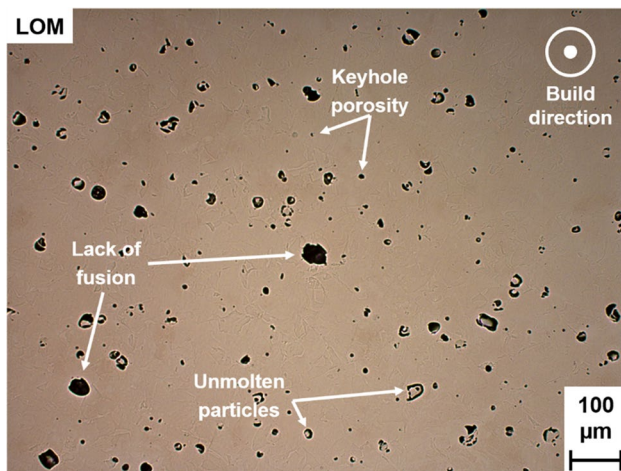


**Fig. 8** Non-adjusted parameter set “red star,” leading to pronounced pore formation

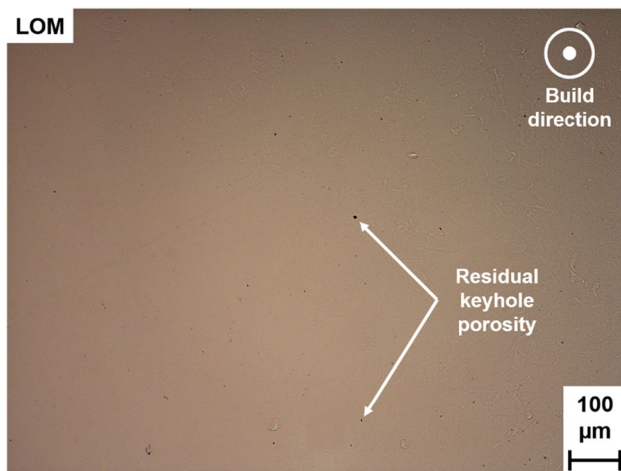


**Fig. 9** DoE-adjusted parameter set “blue star,” revealing a significant increase in part density

### 3.2.2 Optical density

Representing the above-mentioned “red star,” Fig. 8 shows a cross-section perpendicular to the build direction. Since the parameters were not coordinated with each other, high porosity occurred, leading to multiple defect formation. According to [50, 51], present defects were described as a profound lack of fusion and unmolten powder particles, both originating from low energy density, and fine keyhole formation, originating from high energy density.

For Fig. 9 instead, representing the “blue star,” very little pore formation occurred during LPBF. The existing pores were considered keyholes, resulting from fine shielding gas inclusions during re-solidification of the material and vaporization of the melt [50–52]. Comparing both the “red

star” and the “blue star,” it was observed that highly similar volume energy densities led to highly different optical relative densities.

## 3.3 Part characterization

### 3.3.1 Microstructural analysis

Following the parameter optimization process, samples with the highest achievable densities were selected to be investigated for their microstructure, and comparisons to conventional materials were drawn. Having a look at the polished *xy*-plane of the LPBF specimen (view from the top, perpendicularly to the build direction) by operation of a back-scattered electron detector (BSD), as displayed in Fig. 10a, small cellular grains with a maximum length of 50 μm were detected, while most of the grains were even finer (~16.5 μm on average). This particular layer revealed an orientation of the laser travel paths (yellow lines) of ~35° tilted against the nominal of the plane. Nevertheless, as a rotating scanning strategy was applied to other layers, different rotation angles have been found. The orientation within one single *xy*-layer varies along the *z*-axis throughout the whole part. When investigating the parts in parallel to the build direction (Fig. 10b), fan-shell-shaped melt pools directed along the *z*-axis became observable, resulting from the iterative (re-) melting and solidification during LPBF in between layers, as described in [53]. An orientation along the build direction is a common phenomenon of LPBF-built parts that can be explained by the extreme temperature gradients occurring during fabrication and the resulting directed solidification [54, 55]. Moreover, the width of the laser beam focus of approx. 50 μm was detected (yellow lines). The shell shape of single melt pools and the solidification orientated in the build direction were confirmed by an EBSD mapping (Fig. 10c). It also revealed a slight crystallographic  $\langle 101 \rangle$  texture of the fcc unit cell parallel to the build direction. The corresponding inverse pole figure for the build direction (IPF Z) underlines this finding as the [101]-orientation is highlighted in red with a standardized maximum of 1.77. IPF Z was retrieved in the associated  $\langle 100 \rangle$  pole figure (PF), highlighting the respective [101] texture uniformly around the [100] center at approximately 45°. In contrast to this, the texture of grains perpendicular to the build direction is randomly and evenly distributed; a clearly preferred orientation for IPF Z was not observed in the IPF X (Fig. 10d) and IPF Y (Fig. 10e) mappings.

In comparison, the grain structure of the hot-extruded, recrystallized material was substantially coarser and reached grain sizes of up to 200 μm (Fig. 11). No directed solidification could be observed, and grains appeared in an equiaxed state. Hence, by a factor of approximately 10, LPBF-fabricated parts revealed a much finer grain structure.



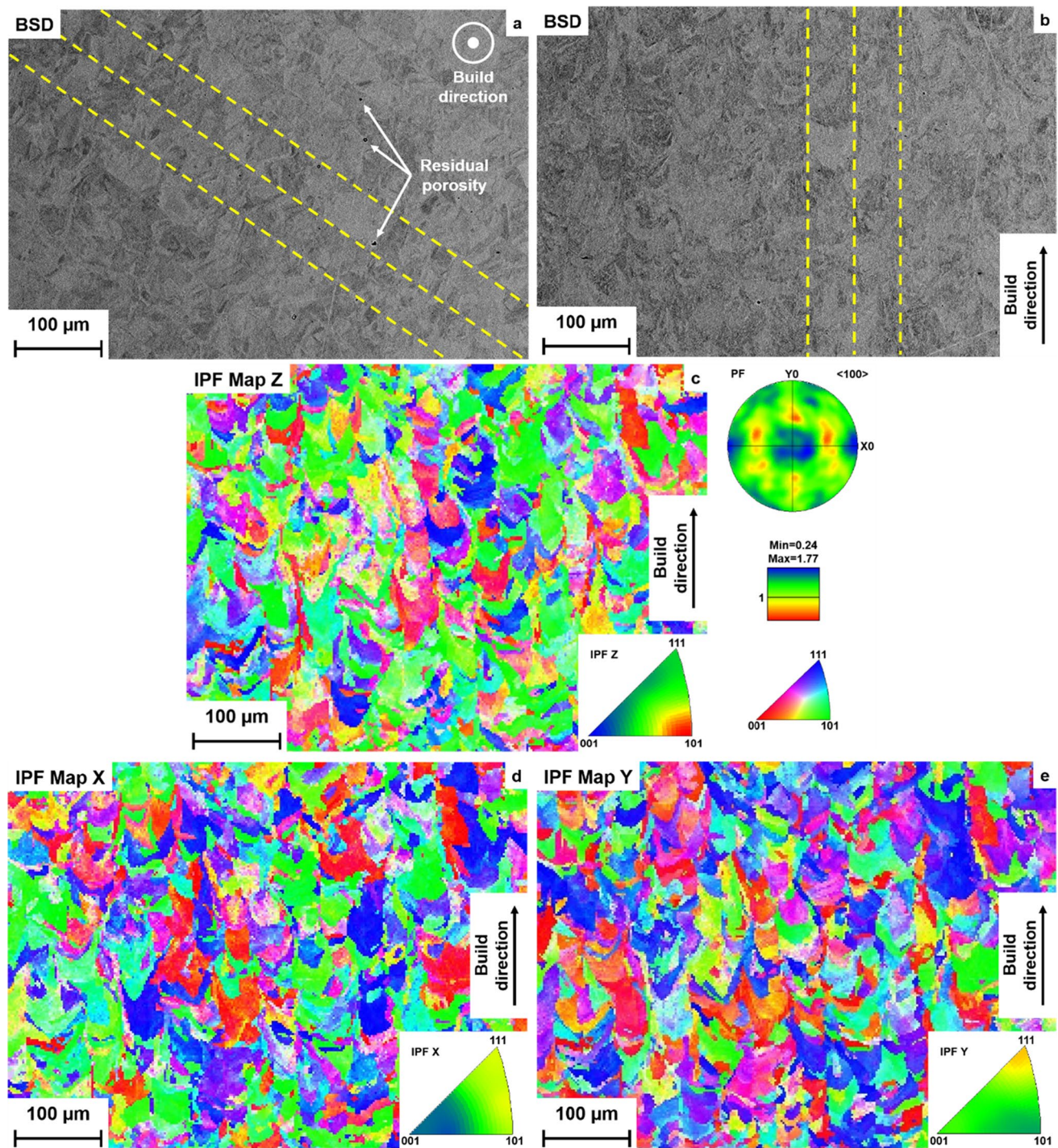


**Fig. 10** **a** BSD of LPBF-printed specimen perpendicular to the build direction; **b** BSD parallel to the build direction; **c** Z EBSD mapping, IPF Z, PF for the build direction, color intensity bar and color code triangle; **d** X EBSD mapping and IPF X; **e** Y EBSD mapping and IPF Y

Micro-dendritic structures as well as high dislocation densities are a common, well-studied phenomenon of LPBF-produced parts in as-built conditions, resulting from the high cooling-melting ratio [56–62]. Accordingly, these internal structures were also detected in this work as shown in Fig. 12. Micro-dendritic cell structures, revealing

a cell size of approx. 250–500 nm, accumulate in between grain and sub-grain boundaries and are intersected by a wide variety of dislocations. The dislocations, which to some extent compensate for the immense internal stresses due to rapid temperature changes during production, are



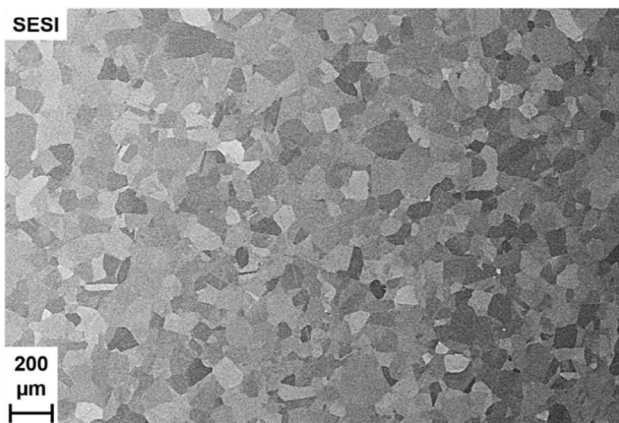


**Fig. 11** Recrystallized reference material revealing a coarse, equiaxed grain structure, detected by SESI

mainly focused on the cell walls and to a lesser extent are also present inside these cells.

### 3.3.2 Mechanical properties

In order to quantify the mechanical properties of additively manufactured Alloy 400, tensile tests at room temperature were carried out on specimens that had been printed in different polar angles according to the DoE-optimized parameter set: perpendicular (90°), diagonal (45°), and parallel

(0°) to the build direction. Tensile test specimens revealed an ORD of 99.56% on average. As displayed in Fig 13a, for parts that were printed in horizontal orientation, ultimate tensile strength  $R_m$  and yield strength  $R_{p0.2}$  showed maximum values of 615 MPa and 556 MPa, respectively. Tensile specimens with a polar angle of 0° showed minimum values instead ( $R_m = 592$  MPa and  $R_{p0.2} = 519$  MPa, respectively). Therefore, tensile strength and yield strength decreased when the specimen axis approached the build direction (upright specimens). Young's modulus  $E$  revealed a clear maximum of 159 GPa for 45° built geometries and lower values for the other two orientations (90°, 133 GPa; 0°, 135 GPa). In Fig 13b, elongation at break  $A_5$ , uniform elongation  $A_g$ , and fracture necking  $Z$  are displayed.  $A_g$  showed a certain tendency, the smaller the polar angle, the stronger the elongation (90°, 3.0%; 45°, 3.6%; 0°, 3.7%). Also,  $A_5 = 11.7\%$  and  $Z = 28.9\%$  had their minima at 90°, respectively, leading to the observation that the ductility of the alloy increased with parts being printed more upright/vertically in the build space. These findings are in line with the above-described decline of  $R_m$  and  $R_{p0.2}$  from 90 to 0° oriented parts; the smaller the polar angle (speaking the more upright the part is orientated in the build space), the lower the strength and the higher the ductility within the part.

Further tensile testing on specimens fabricated perpendicularly to the build direction was carried out at elevated temperatures, and a comparison to conventionally fabricated

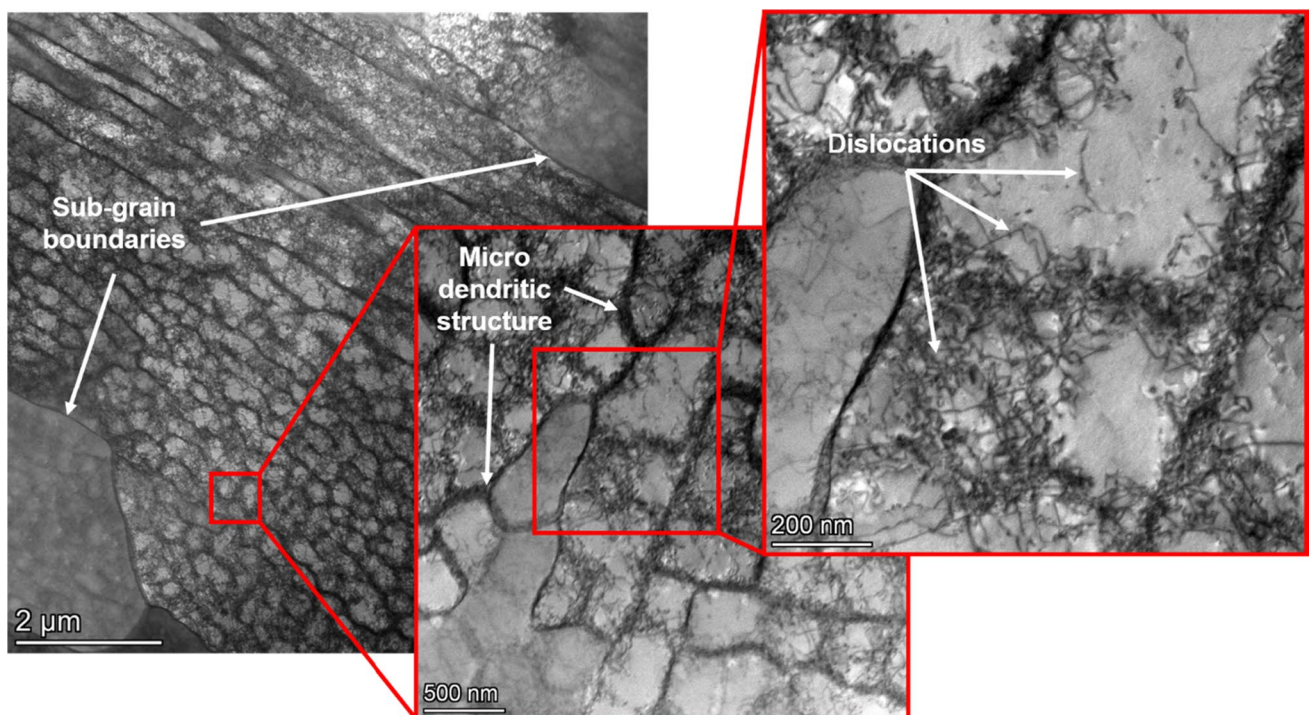


**Fig. 12** Bright-field STEM micrographs revealing grain and sub-grain boundaries and internal micro-dendritic structures with high dislocation density in wall segments and dislocation-free center

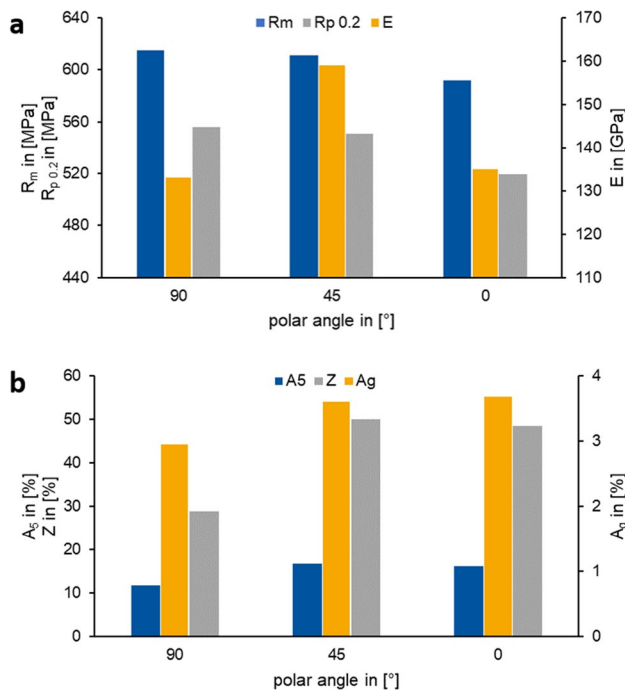


**Fig. 13** **a** Stress and Young's modulus for LPBF Alloy 400, printed in different orientations; **b** strain and necking

Alloy 400 was drawn. The resulting tensile curves are shown in Fig 14a. LPBF parts were tested at room temperature, 400 °C, 550 °C, 650 °C, and 750 °C (red lines). For the hot-extruded, bulk parts, room temperature, 530 °C, and 936 °C were applied (blue lines). Fig 14b shows the dependence of

the yield strength on the testing temperature. The tensile strength and yield strength of the LPBF part were similar or higher in comparison to the bulk variant. However, the elongation at fracture of the LPBF variant was substantially lower with a tendency to decrease with rising temperature.

Concerning hardness, cubes were evaluated in parallel and perpendicular to the build direction; no difference was observed here. Moreover, results for micro- and macro-hardness were identical. On average, the samples showed a hardness according to Vickers of 194 HV1 and HV10, respectively. For conventionally fabricated material (annealed condition), a hardness of ~107–147 HV1 was stated, while hot-rolled and hot-finished parts may reach similar hardness values as the LPBF variant [1, 7]. Hot-extruded material, as used throughout this study, shows an HBW 2.5/62.5 of 115–121. Higher hardness in the LPBF variant was traced back to the finer grain structure, as discussed in [2].

## 4 Discussion

### 4.1 Powder suitability for LPBF

The atomization process window was considered suitable in terms of an effective operation of the low-pressure area, leading to the desired rapid undercooling of the melt. Fine powders resulted, porosities and impurities were not detected which would be detrimental for the LPBF process [63, 64]. It was possible to create spherical particles showing only a small number of satellites, resulting in high flowabilities

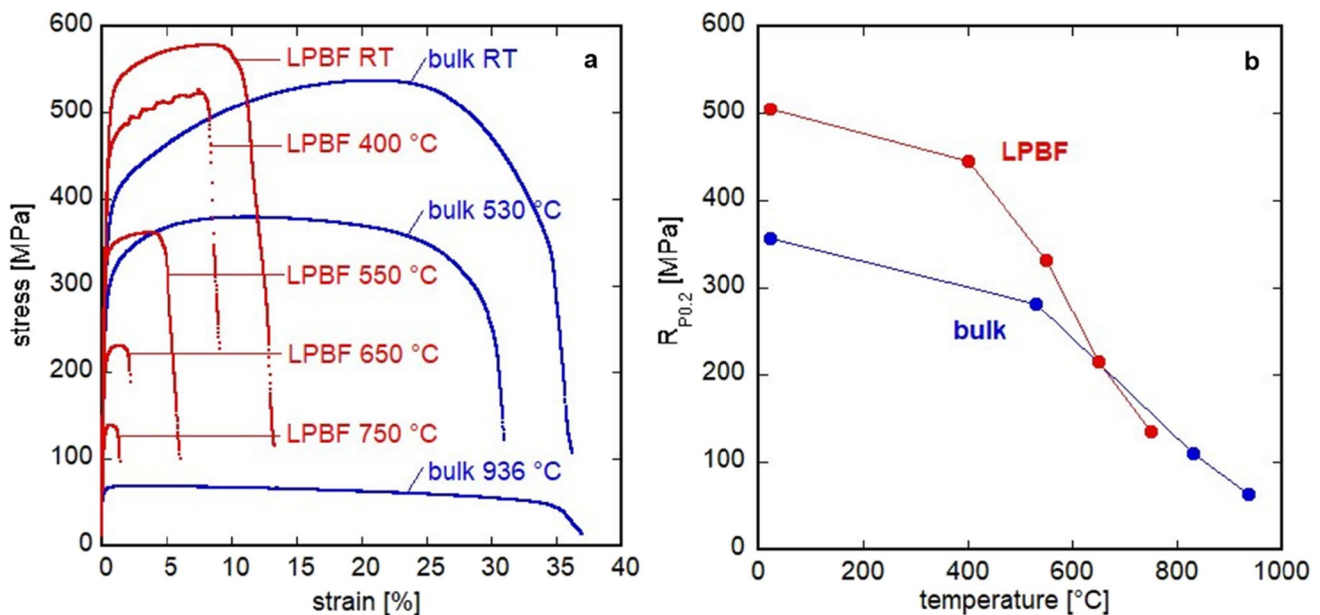


**Fig. 14** **a** Stress–strain-diagram for bulk (blue curves) and LPBF (red curves) Alloy 400 at various temperatures; **b** yield strength as a function of applied temperature

and bulk densities needed for successful AM [64, 65]. As a consequence, this eventually leads to higher build quality during LPBF [63–65]. The resulting fractal nature of the powder bed in the LPBF process was introduced by Estrada-Díaz et al., i.e., as per the fractal dimensions and lacunarity, accurately correlating both homogeneity and morphology with a sustainable, low-defect LPBF process [66, 67]. No precipitates were found within the particles, which is in line with the assumption of this alloy being a one-phase solid solution [1–3]. Besides, Cu segregations were expected and also detected on grain boundaries [37–39]. A consistent chemical composition was found in both, powders and parts, and thus, the generated powder was generally considered appropriate for LPBF.

## 4.2 Melt pool geometry and resulting microstructure

NiCu-based Alloy 400 is a fcc alloy, and thus, it is expected that the preferred dendrite growth direction is along the [001] crystal direction [68–71]. In the case of LPBF, the thermal gradients are pointed normally to the melt pool boundary, and thus, grains with [001] directions parallel to the thermal gradients will preferentially grow from the melt pool boundary. Attributed to the Gaussian profile of the laser source, the core of the melt pool eventually exhibits higher temperatures than the border areas [68, 71–73]. As frequently observed in other works like [55, 71, 74, 75], due to the geometry of the melt pool, boundary-near grains grow transversely to the direction of the introduced laser power and build direction, respectively. In turn, nucleation near the melt pool core experiences undirected undercooling, leading to the formation of more equiaxed grains. Figure 15 shows the ideal melt pool that would result under these circumstances, consisting of dendrites near the melt pool boundary and of cross-sections of elongated grains resulting from the laser beam travel (here, out of the figure plane). The resulting growth mechanism gives reason for the [101] orientation with respect to the build direction that has been found for the present alloy and manufacturing routine, respectively; dendrites do not only grow along the build direction but deviate into the build plane as well. This type of process-induced deflection of grain growth toward  $\langle 011 \rangle$  orientations was also found for a Ni-based IN718 by Pant et al. and for a NiTi-based alloy by Safaei et al. [71, 76].

Nevertheless, the texture was described as marginal only (Fig. 10). This was found to be due to a wide variety of geometries, sizes, and growth directions of the grains, resulting in a very heterogeneous microstructure. In other words, the above-described ideal melt pool was hardly detected within the present LPBF manufactured parts as illustrated in Fig. 16. Melt pool boundaries could be tracked down partially only, and equiaxed and columnar grains appeared

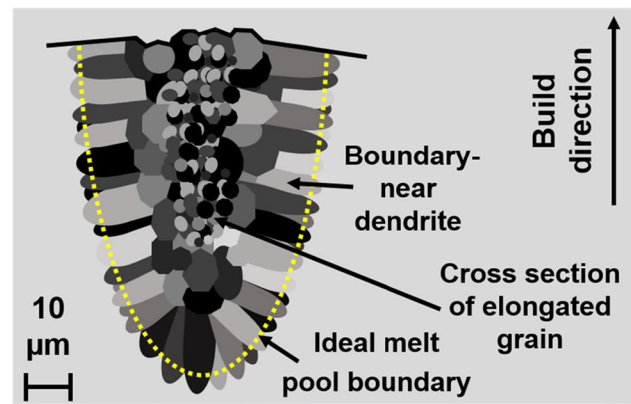


Fig. 15 Schematic of an ideal melt pool, denoting different types of directed grain nucleation

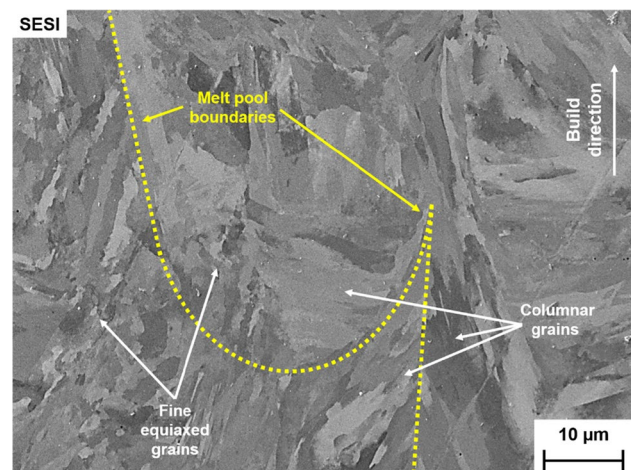


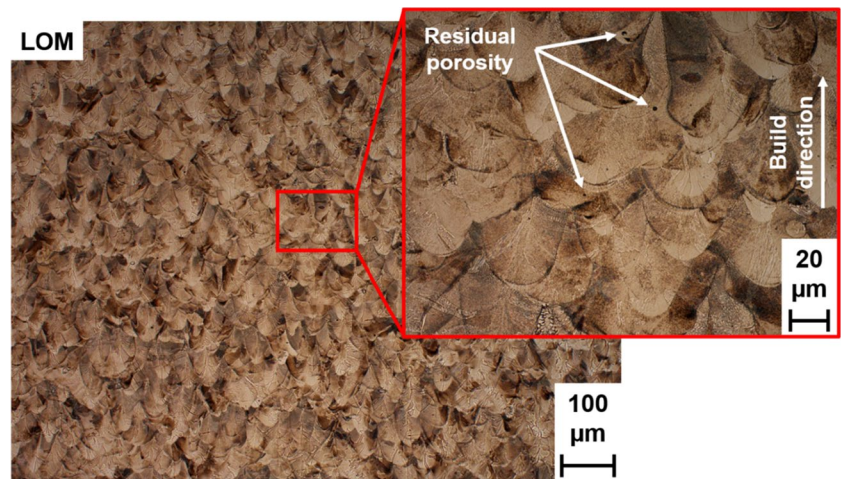
Fig. 16 SEM closeup of the melt pool intersections in between several layers

randomly distributed over the cross-section. This can be related to the rotating scanning strategy; as stated by Serrano-Munoz et al., a rotation of  $67^\circ$  in between layers allows for the formation of both elongated grains along build direction and epitaxial growth [77]. According to Qin et al., this type of rotation lowers the overall texture [55].

Etched with ferric chloride, the melt pool propagation in the build direction ( $z$ -axis) was revealed in greater detail (Fig. 17). The pre-described fan-shell shape became even more observable, resulting from an overlapping of melt pools from one layer to another. The ratio of melt pool depth and layer height shows an effect here; with a width of  $50\ \mu\text{m}$ , approximately  $80\ \mu\text{m}$  was found to be the maximum melt pool depth, while the applied layer height measured  $20\ \mu\text{m}$  only. Hence, a melt pool of a considered level reached four layers deep into the part, meaning that the original melt pool geometry of one respective layer was dissolved by the



**Fig. 17** Light optical image of an etched slice parallel to the build direction, illustrating overlapping melt pools



impacts of further melt pools from overlying layers. This, in turn, results in a quadruple (re-)melting and solidification of the material with the heat-affected zone (HAZ) reaching even deeper. The HAZ may further significantly alter the microstructure [78, 79]. These findings serve as another explanation for the above-found very different grain structures and nucleation mechanisms. Apart from that, a few remaining pores were observed on the etched samples, being classified as keyholes.

Copper segregations on grain boundaries were clearly visible for the as-atomized powders (Fig. 3). In contrast, using TEM for as-built LPBF parts, chemical micro-Cu-segregations became visible on the nanoscale, revealing a very low intensity at cell walls (Fig. 18). According to Bertsch et al., the occurrence of these micro-segregations can, in some cases, be correlated with the previously mentioned dislocations as these can act as traps for some elements [80]. Sabzi et al. showed that high cell-wall-near dislocation densities significantly enhance the strength performance of the respective alloy, while Kong et al. stated that

high dislocation densities go along with nanosized cellular structures which, in turn, enable superior performance in comparison to conventional manufacturing [59, 60]. These nanocell structures, revealing high dislocation occurrence, have been found for the present LPBF Alloy 400 as well as previously displayed in Fig. 12.

Compared to the one-time rapid undercooling of the melt during powder atomization, the thermal impact on LPBF parts is more complex and caused by an entire sequence of iterative laser melting and subsequent very high cooling rates [68, 81]. As illustrated above (Fig. 18), the respective part layers experience several iterations of melting and solidifying before being additionally exposed to the HAZ during the fabrication of further layers. Also, non-molten powders aside may keep the heat locally concentrated near the melt pool [82]. Hence, an in situ, process-related heat treatment during manufacturing caused by the succession of several layers can be noted, inevitably benefitting diffusion processes based on a temperature gradient. From one layer to another, this eventually results in a decrease of locally

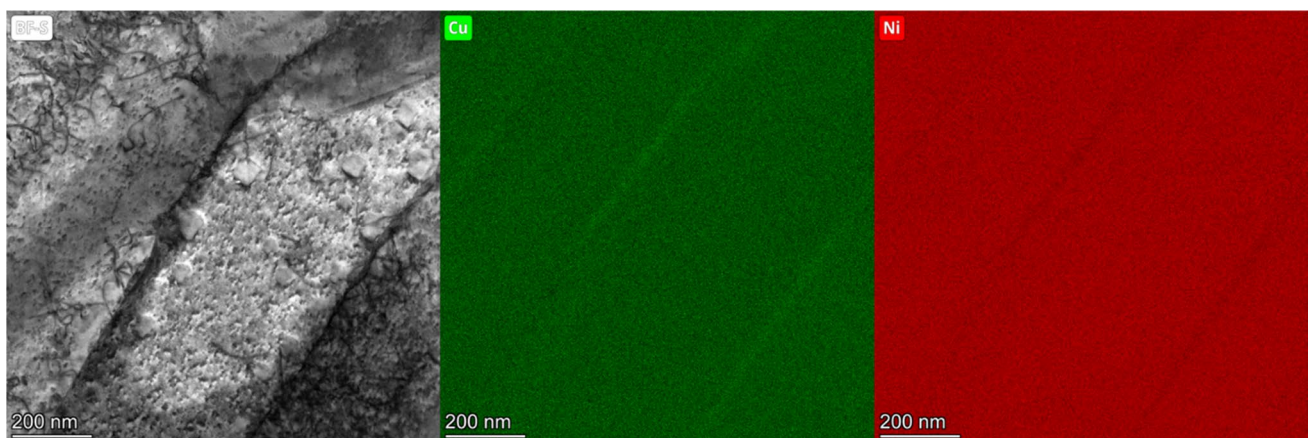


**Fig. 18** Bright-field STEM micrograph and micro-segregation of Cu and Ni on the nanoscale as detected by EDS analysis in STEM

different chemical concentrations, and ultimately, inhomogeneities almost dissolve completely into the preferred homogeneous solid solution. This serves as a further explanation for the copper segregations being only detectable on the nanoscale via TEM within LPBF parts compared to the strongly pronounced segregations in powders.

### 4.3 Building strategy and consequential material properties

Even though chemical imbalances are eliminated within the parts, structural irregularities do remain. Not only that no significant texture was found for the  $xy$ -plane but solely along the build direction, but there are also differences in mechanical properties concerning the orientations of fabricated specimens. As observed, the ultimate tensile strength and yield strength of tensile test specimens decrease with a falling polar angle from 90 to 0° to the build direction (Fig 13a). In other words, the more upright the cylinders were manufactured during LPBF, the less strength they showed. Keeping in mind the directed grain growth along the build direction, this leads to the assumption that the lateral overlap of melt pools (horizontally in the build space, primarily present in 90° oriented samples) results in a higher strength performance than the overlap of melt pools on top of each other (vertically in the build space, primarily present in 0° oriented samples). Here, the 45° oriented samples are equivalent to a combination of both, vertical and horizontal overlap, resulting in mechanical properties between them. The samples that were tested perpendicular to the build direction showed the lowest levels of elongation (Fig 13b). Accordingly, higher ductility in the build direction was found by Wilson-Heid et al. for a Ti-6Al-4 V alloy, being correlated to the columnar grain growth along the  $z$ -axis and a consequent damage accumulation in the horizontal direction [83]. Also, Yu et al. found a higher ductility for upright-oriented Hastelloy X samples, mainly attributed to a considerable extent of texture and grain rotation in this direction [84]. These results are consistent with those shown here that the strength is inversely correlated with ductility. This is further underlined by the low fracture necking for 90° oriented samples. Thus, strength and ductility are evolving contrarily with the Young's modulus being the highest for the diagonally oriented specimens. This anisotropic behavior of Young's modulus in LPBF with accompanying varying stiffness values depending on the orientation of the specimen has been frequently discussed in literature like [84–86]. Ultimately, anisotropy along the  $z$ -axis was found, while for single  $xy$ -planes, isotropic behavior is present since it is not possible to differentiate between directions  $x$  and  $y$ . Still, due to the application of the rotating scanning strategy, anisotropy in build direction was kept at a comparably low level; for an IN718 alloy, Serrano-Munoz

et al. demonstrated that the texture index can approx. be reduced by half when a 67° rotation is applied instead of a 90° alternating  $xy$ -scanning scheme as a columnar grain growth with preferred  $\langle 001 \rangle$  orientation over several layers is inhibited [77]. Accordingly, as stated by Safaei et al. for NiTi alloys, suppressing the grain orientation leads to a decline in anisotropy [71].

Further mechanical testing revealed differences in between bulk and LPBF material. An in situ heat treatment was assumed for the LPBF parts above. Still, the resulting microstructure did not reveal coarse and equiaxed grains as in hot-extruded parts but a finer, ten times smaller, and elongated shaping. The fact that LPBF produces a finer and non-equiaxed grain structure as present in conventional manufacturing processes has already been shown frequently in the literature for many alloy systems, including several Ni-based ones [2, 87–89]. This grain refinement in AM parts leads inevitably to a hardening of the structure, resulting in the superior mechanical properties found for yield strength and ultimate tensile strength up to 530 °C. Still, slight residual keyhole porosity was found for the additively manufactured parts by Chlupová et al., facilitating crack initiation and resulting in a more brittle material failure type than in the reference parts [90]. This gives reason for the overall lower ductility.

### 4.4 Reconsideration of the volume energy density as key performance indicator

As identified throughout the DoE studies, hatching of 80  $\mu\text{m}$  was generally found to be unsuitable in order to reach high densities (Fig. 5). With a laser focus of approximately 50  $\mu\text{m}$ , the resulting porosity can be correlated to residual lack of fusion in between scanning lines. This evidence exemplifies precisely the problem of utilizing the volume energy density as the main target figure of parameter optimizations in laser powder bed fusion processes; no matter how the residual parameters (among others, laser power, scanning speed, layer height, etc.) are adapted for a constant hatch distance, the resulting part density may not be raised to a satisfactory high value. Complete melting of the entire powder bed is not achievable for hatch distances being too broad, independently from an energy increase through, e.g., a higher laser power or a slower scanning velocity. Anyway, in modern LPBF parameter development, it is considered a general agreement to search for the optimum  $e_v$  range. Although similar volume energy densities may consist of completely different parameter combinations, this approach is widely used as applied and discussed in [48, 91, 92]. In other words, as stated in the results section, equal volume energy densities are likely to result in very different optical relative densities, which is why the  $e_v$  can only be consulted as an approximate orientation (Fig 7a). This issue has been

addressed by Scipioni Bertoli et al. in stating that  $e_v$  does not adequately describe the melt pool dynamics and must therefore be used very cautiously in LPBF parameter optimization [49]. Estrada-Díaz et al. further supported this finding by stating that the LPBF process can only be described partially with the help of VED as it lacks information on powder ejection and sublimation [93]. Single process parameters must be interpreted against the background of their interaction with other process parameters. DoE instead consists of smooth continuous parameter functions which map single parameters adequately. As the regression equation consists of the three target values of laser power, scanning speed, and hatch distance, the found parameter set fits accurately into this system. Moreover, as identified above for uncoordinated parameter sets, several kinds of defects can be found for a single layer (Fig. 8). High energy input would result in keyhole porosity, while lack of fusion and unmolten particles can be correlated with low energy introduced into the layer [51, 94]. Hence, the energy density is not distributed equally over one layer, further proof that optimum fabrication is attributable to process parameters instead of  $e_v$ . The approach of focusing on the process parameters revealed a high potential for the present Alloy 400 as high densities were achievable. While this work focused on the correlation of  $p_L$ ,  $s_s$ , and  $d_H$  (input variables) with the resulting density (output variable) reduced by keyhole porosity, unmolten particles, and lack of fusion, further potential outputs such as distortion, balling, or cracking as a function of several input parameters could be investigated as well to overcome the uncoordinated nature of single process parameters. Here, applying Buckingham's  $\pi$ -theorem, setting the focus on the most significant physical interactions occurring, and dimensional analysis, describing a process as the sum of dimensionless products, counteract poorly adjusted parameter sets as well [95].

## 5 Conclusion

In this study, a holistic AM process route for Alloy 400 was established, reaching from application and alloy design according to standard specifications over in-house powder generation and characterization to a DoE-assisted laser powder bed fusion process, resulting in part microstructure analysis and comparison to conventionally fabricated material. The concrete results were then discussed and put into perspective, resulting in the following notable findings and overall conclusions of this work:

- The usable powder can be generated via the application of a close-coupled gas atomization setup using a high-temperature ceramic crucible. The final particle size distribution of 15 to 63  $\mu\text{m}$  was adjusted by sieving and air-separation post-processing, resulting in spherical and

flowable particles which provided the basis for successful LPBF fabrication.

- The standard target chemical composition was in line with powders, LPBF parts, and hot-extruded reference Alloy 400, allowing us to conclude the chemical purity and consistency of the applied processes. Hence, a comparison in between the various states was enabled and carried out.
- At grain boundaries in powders, Cu segregations were clearly detectable and verified via SEM on the micro-scale as expected for this alloy type. Still, within printed parts, only slight micro-segregations were detected via TEM. Heat-induced diffusion processes, resulting from the iterative sequence of the LPBF process, give reason for this phenomenon as chemical imbalances may almost dissolve completely into the solid solution.
- As typical for LPBF-produced parts, a wide range of dislocations was found to be present, primarily along cell walls and occasionally inside cells. These cells were classified as micro-dendritic structures within the super-ordinate grains.
- The design of experiments approach for LPBF parameter development led to a final parameter set that enabled the fabrication of highly dense parts, consisting of  $p_L=85\text{ W}$ ,  $s_s=1050\text{ mm/s}$ ,  $d_H=50\text{ }\mu\text{m}$ , and  $t_L=20\text{ }\mu\text{m}$ , resulting in an  $e_v=80.95\text{ J/mm}^3$ . A rotating scanning strategy of  $67^\circ$  in between layers, a green laser with a wavelength of 532 nm, and a pre-heating of the build plate of  $80\text{ }^\circ\text{C}$  completed the parameter setup. In any case and beforehand, the basic requirement for AM material development is the identification of key parameters and resulting defect formation that prevent the production of high-density parts.
- The DoE-based approach revealed the high importance of the interdependency of single process parameters. Based on the finding that similar or even the same volume energy densities may result in very different part densities, the search for a single parameter set was found to be most expedient. Hence, for process parameter development of LPBF processes, this work greatly encourages to shift in the focus from a broad energy density range to a more integrated course of action of identifying a single optimum parameter combination. DoE does not only increase the efficiency of AM process parameter development, but the smaller number of parameter sets that need to be tested also results in overall fewer resources such as the number of build jobs, energy consumption, powder demand, and man hours.
- Mechanical properties of LPBF parts being manufactured in an upright orientation within the build space showed lower strength but higher ductility than parts being manufactured perpendicularly to the build direction. This finding was correlated with changing melt



pool formation, preferred texture, and varying anisotropy along building direction for different specimen orientations.

- At room temperature and at 530 °C, the fine-grained LPBF variant of Alloy 400 performed equally or better in terms of strength when compared to the hot-extruded, bulk reference material, revealing comparably coarse grains. At higher temperatures instead, the conventional material performed better as slight residual keyhole porosity in AM parts amplified crack initiation, compensating its beneficial microstructure.
- For elongation, the AM parts did not reach the performance of the conventional ones, which is also due to porosity acting as a fracture trigger and causing a more brittle failure mode. Moreover, this is connected to the inverted relationship between strength (which is higher in AM parts) and elongation.
- The hardness of LPBF-built parts was significantly higher compared to conventionally fabricated material being correlated to the coarser grain size of the hot-extruded material.

**Acknowledgements** The authors would like to acknowledge Sepehr Hatami, Ph.D.; Erik Adolfsson, Ph.D.; and Anton Dahl-Jendelin for the chance to perform joint investigations on powder particle rheology at the RISE Research Institutes of Sweden laboratories in Mölndal, Sweden. The authors would further like to acknowledge Zdeněk Chlup, Ph.D. of the Institute of Physics of Materials at the Czech Academy of Sciences for his investigations on tensile testing in Brno, Czech Republic. Moreover, the authors would like to acknowledge Dr. Jörg Fischer-Bühner of Indutherm Erwärmungsanlagen GmbH, Walzbachtal, Germany, for the information exchange on gas atomizations. Also, the authors would like to acknowledge Thomas Volkery of KME Germany GmbH, Osnabrück, Germany, for his great support in specimen preparation and light optical microscopy. This work has received funding from the European Union's Horizon 2020 research and innovation program under grant agreement No. 958192 which is gratefully acknowledged.

**Author contribution** Jan-Philipp Roth: conceptualization, data curation, formal analysis, investigation, methodology, software, supervision, validation, visualization, and writing—original draft and review and editing. Ivo Šulák: investigation and writing—review and editing. Tomáš Kruml: supervision and writing—review and editing. Wojciech Polkowski: supervision and writing—review and editing. Tomasz Dudziak: supervision and writing—review and editing. Peter Böhlke: resources, supervision, and writing—review and editing. Ulrich Krupp: conceptualization, funding acquisition, project administration, resources, supervision, and writing—review and editing. Katrin Jahns: conceptualization, funding acquisition, project administration, resources, supervision, validation, and writing—review and editing.

**Funding** Open Access funding enabled and organized by Projekt DEAL. This work has received funding from the European Union's Horizon 2020 research and innovation program under grant agreement No. 958192 which is gratefully acknowledged.

## Declarations

**Competing Interests** The authors declare no competing interests.

**Open Access** This article is licensed under a Creative Commons Attribution 4.0 International License, which permits use, sharing, adaptation, distribution and reproduction in any medium or format, as long as you give appropriate credit to the original author(s) and the source, provide a link to the Creative Commons licence, and indicate if changes were made. The images or other third party material in this article are included in the article's Creative Commons licence, unless indicated otherwise in a credit line to the material. If material is not included in the article's Creative Commons licence and your intended use is not permitted by statutory regulation or exceeds the permitted use, you will need to obtain permission directly from the copyright holder. To view a copy of this licence, visit <http://creativecommons.org/licenses/by/4.0/>.

## References

1. Special Metals Corporation (2005) Monel Alloy 400. <https://www.specialmetals.com/documents/technical-bulletins/monel-alloy-400.pdf>
2. Raffei I, Adjei-Kyeremeh F, Vroomen U et al (2020) Qualification of a Ni–Cu alloy for the laser powder bed fusion process (LPBF): its microstructure and mechanical properties. *Appl Sci* 10:3401. <https://doi.org/10.3390/app10103401>
3. Zhang C-H, Wu C-L, Zhang S et al (2022) Laser cladding of NiCrSiB on Monel 400 to enhance cavitation erosion and corrosion resistance. *Rare Met* 41:4257–4265. <https://doi.org/10.1007/s12598-016-0814-4>
4. Esgin U, Özyürek D, Kaya H (2016) An investigation of wear behaviors of different Monel alloys produced by powder metallurgy. *AIP Conf Proc* 1727:20008. <https://doi.org/10.1063/1.4945963>
5. Kukliński M, Bartkowska A, Przestacki D (2018) Microstructure and selected properties of Monel 400 alloy after laser heat treatment and laser boriding using diode laser. *Int J Adv Manuf Technol* 98:3005–3017. <https://doi.org/10.1007/s00170-018-2343-9>
6. Devendranath RK, Arivazhagan N, Narayanan S et al (2011) Development of defect free Monel 400 welds for marine application. *AMR* 383–390:4693–4696. <https://doi.org/10.4028/www.scientific.net/AMR.383-390.4693>
7. Special Metals Corporation (2000) High-performance alloys for resistance to aqueous corrosion. <https://www.specialmetals.com/documents/aqueous-corrosion-handbook.pdf>
8. Shoemaker LE, Smith GD (2006) A century of Monel metal: 1906–2006. *JOM* 58:22–26. <https://doi.org/10.1007/s11837-006-0077-x>
9. Zils R (2008) Werkstoffe im Pumpenbau. *Chem Ing Tec* 80:499–508. <https://doi.org/10.1002/cite.200700183>
10. Ventrella VA, Berretta JR, de Rossi W (2011) Micro welding of Ni-based alloy Monel 400 thin foil by pulsed Nd:YAG laser. *Phys Procedia* 12:347–354. <https://doi.org/10.1016/j.phpro.2011.03.143>
11. Maier HJ, Niendorf T, Bürgel R (2019) Handbuch Hochtemperatur-Werkstofftechnik. Springer Vieweg, Wiesbaden
12. Bargel H-J (2022) Werkstoffkunde. Springer, Berlin Heidelberg, Berlin, Heidelberg
13. Young DJ, Zhang J, Geers C et al (2011) Recent advances in understanding metal dusting: a review. *Mater Corros* 62:7–28. <https://doi.org/10.1002/maco.201005675>

14. Schneider R, Pippel E, Woltersdorf J et al (1997) Microprocesses of metal dusting on nickel and Ni-base alloys. *Steel Research* 68:326–332. <https://doi.org/10.1002/srin.199701796>
15. Jahns K, Ulrich AS, Schlereth C et al (2021) The effect of Cu content and surface finish on the metal dusting resistance of additively manufactured NiCu alloys. *Oxid Met* 96:241–256. <https://doi.org/10.1007/s11085-021-10037-8>
16. Abdulhameed O, Al-Ahmari A, Ameen W et al (2019) Additive manufacturing: challenges, trends, and applications. *Adv Mech Eng* 11:168781401882288. <https://doi.org/10.1177/1687814018822880>
17. Ramazani H, Kami A (2022) Metal FDM, a new extrusion-based additive manufacturing technology for manufacturing of metallic parts: a review. *Prog Addit Manuf* 7:609–626. <https://doi.org/10.1007/s40964-021-00250-x>
18. Yap CY, Chua CK, Dong ZL et al (2015) Review of selective laser melting: materials and applications. *Appl Phys Rev* 2:41101. <https://doi.org/10.1063/1.4935926>
19. Popovich A, Sufiarov V (2016) Metal powder additive manufacturing. *New Trends in 3D Printing*. <https://doi.org/10.5772/63337>
20. Dunkley JJ (2019) Metal powder atomisation methods for modern manufacturing. *Johnson Matthey Technol Rev* 63:226–232. <https://doi.org/10.1595/205651319X15583434137356>
21. Antony LVM, Reddy RG (2003) Processes for production of high-purity metal powders. *JOM* 55:14–18. <https://doi.org/10.1007/s11837-003-0153-4>
22. Hussain S, Cui C, He L et al (2020) Effect of hot gas atomization on spray forming of steel tubes using a close-coupled atomizer (CCA). *J Mater Process Technol* 282:116677. <https://doi.org/10.1016/j.jmatprotec.2020.116677>
23. Mathews PG (2005) Design of experiments with MINITAB. ASQ Quality Press, Milwaukee, WI, USA
24. Czitrom V (1999) One-factor-at-a-time versus designed experiments. *Am Stat* 53:126–131. <https://doi.org/10.1080/00031305.1999.10474445>
25. Tanco M, Viles E, Pozueta L (2008) Are all designs of experiments approaches suitable for your Company? Proceedings of the World Congress on Engineering 2008, Vol. 2 WCE. London
26. Tanco M, Viles E, Ilzarbe L et al. (2007) Manufacturing industries need design of experiments (DoE). Proceedings of the World Congress on Engineering 2007, Vol. 2 WCE. London
27. Cavazzuti M (2013) Design of experiments. In: Cavazzuti M (ed) Optimization methods. Springer, Berlin Heidelberg, Berlin, Heidelberg, pp 13–42
28. Bourell D, Kruth JP, Leu M et al (2017) Materials for additive manufacturing. *CIRP Ann* 66:659–681. <https://doi.org/10.1016/j.cirp.2017.05.009>
29. Clare AT, Reynolds WJ, Murray JW et al (2020) Laser calorimetry for assessment of melting behaviour in multi-walled carbon nanotube decorated aluminium by laser powder bed fusion. *CIRP Ann* 69:197–200. <https://doi.org/10.1016/j.cirp.2020.04.053>
30. Schwenck D, Ellendt N, Fischer-Bühner J et al (2017) A novel convergent-divergent annular nozzle design for close-coupled atomisation. *Powder Metall* 60:198–207. <https://doi.org/10.1080/00325899.2017.1291098>
31. Mullis AM, Farrell L, Cochrane RF et al (2013) Estimation of cooling rates during close-coupled gas atomization using secondary dendrite arm spacing measurement. *Metall Mater Trans B* 44:992–999. <https://doi.org/10.1007/s11663-013-9856-2>
32. Ciftci N, Ellendt N, Coulthard G et al (2019) Novel cooling rate correlations in molten metal gas atomization. *Metall Mater Trans B* 50:666–677. <https://doi.org/10.1007/s11663-019-01508-0>
33. Soares Barreto E, Frey M, Wegner J et al (2022) Properties of gas-atomized Cu-Ti-based metallic glass powders for additive manufacturing. *Mater Des* 215:110519. <https://doi.org/10.1016/j.matdes.2022.110519>
34. Blue Power Casting and Powder Production Systems (2023) AUG-Series catalogue. [https://bluepower-casting.com/media/e4/47/38/1674564361/Indutherm\\_Catalogue\\_en\\_2023\\_web\\_DS.pdf](https://bluepower-casting.com/media/e4/47/38/1674564361/Indutherm_Catalogue_en_2023_web_DS.pdf)
35. Sun P, Fang ZZ, Zhang Y et al (2017) Review of the methods for production of spherical Ti and Ti alloy powder. *JOM* 69:1853–1860. <https://doi.org/10.1007/s11837-017-2513-5>
36. Cohn R, Anderson I, Prost T et al (2021) Instance segmentation for direct measurements of satellites in metal powders and automated microstructural characterization from image data. *JOM* 73:2159–2172. <https://doi.org/10.1007/s11837-021-04713-y>
37. Erdélyi Z, Girardeaux C, Tôkei Z et al (2002) Investigation of the interplay of nickel dissolution and copper segregation in Ni/Cu(111) system. *Surf Sci* 496:129–140. [https://doi.org/10.1016/S0039-6028\(01\)01571-0](https://doi.org/10.1016/S0039-6028(01)01571-0)
38. Pellicer E, Varea A, Sivaraman KM et al (2011) Grain boundary segregation and interdiffusion effects in nickel-copper alloys: an effective means to improve the thermal stability of nanocrystalline nickel. *ACS Appl Mater Interfaces* 3:2265–2274. <https://doi.org/10.1021/am2004587>
39. Naghash AR, Etsell TH, Xu S (2006) XRD and XPS study of Cu–Ni interactions on reduced copper–nickel–aluminum oxide solid solution catalysts. *Chem Mater* 18:2480–2488. <https://doi.org/10.1021/cm051910o>
40. Kearns M (2004) Development and applications of ultrafine aluminium powders. *Mater Sci Eng, A* 375–377:120–126. <https://doi.org/10.1016/j.msea.2003.10.160>
41. Slotwinski JA, Garboczi EJ, Stutzman PE et al (2014) Characterization of metal powders used for additive manufacturing. *J Res Natl Inst Stand Technol* 119:460–493. <https://doi.org/10.6028/jres.119.018>
42. Sun J, Guo M, Shi K et al (2022) Influence of powder morphology on laser absorption behavior and printability of nanoparticle-coated 90W-Ni-Fe powder during laser powder bed fusion. *Mater Sci Add Manuf* 1. <https://doi.org/10.18063/msam.v1i2.11>
43. Sendino S, Martinez S, Lamikiz A (2020) Characterization of IN718 recycling powder and its effect on LPBF manufactured parts. *Procedia CIRP* 94:227–232. <https://doi.org/10.1016/j.procir.2020.09.043>
44. Zegzulka J, Gelnar D, Jezerska L et al (2020) Characterization and flowability methods for metal powders. *Sci Rep* 10:21004. <https://doi.org/10.1038/s41598-020-77974-3>
45. Saw HY, Davies CE, Paterson AH et al (2015) Correlation between powder flow properties measured by shear testing and Hausner ratio. *Procedia Eng* 102:218–225. <https://doi.org/10.1016/j.proeng.2015.01.132>
46. Abdullah EC, Geldart D (1999) The use of bulk density measurements as flowability indicators. *Powder Technol* 102:151–165. [https://doi.org/10.1016/s0032-5910\(98\)00208-3](https://doi.org/10.1016/s0032-5910(98)00208-3)
47. Hao T (2015) Understanding empirical powder flowability criteria scaled by Hausner ratio or Carr index with the analogous viscosity concept. *RSC Adv* 5:57212–57215. <https://doi.org/10.1039/C5RA07197F>
48. Ciurana J, Hernandez L, Delgado J (2013) Energy density analysis on single tracks formed by selective laser melting with CoCrMo powder material. *Int J Adv Manuf Technol* 68:1103–1110. <https://doi.org/10.1007/s00170-013-4902-4>
49. Scipioni Bertoli U, Wolfer AJ, Matthews MJ et al (2017) On the limitations of volumetric energy density as a design parameter for selective laser melting. *Mater Des* 113:331–340. <https://doi.org/10.1016/j.matdes.2016.10.037>
50. Kasperovich G, Haubrich J, Gussone J et al (2016) Correlation between porosity and processing parameters in TiAl6V4 produced by selective laser melting. *Mater Des* 105:160–170. <https://doi.org/10.1016/j.matdes.2016.05.070>

51. Shrestha S, Starr T, Chou K (2019) A study of keyhole porosity in selective laser melting: single-track scanning with micro-CT analysis. *J Manuf Sci Eng* 141. <https://doi.org/10.1115/1.4043622>
52. Gan Z, Kafka OL, Parab N et al (2021) Universal scaling laws of keyhole stability and porosity in 3D printing of metals. *Nat Commun* 12:2379. <https://doi.org/10.1038/s41467-021-22704-0>
53. Yu SJ, Wang P, Li HC et al (2023) Heterogeneous microstructure and mechanical behaviour of Al-8.3Fe-1.3V-1.8Si alloy produced by laser powder bed fusion. *Virtual Phys Prototyp* 18:e2155197. <https://doi.org/10.1080/17452759.2022.2155197>
54. Krakhmalev P, Fredriksson G, Svensson K et al (2018) Microstructure, solidification texture, and thermal stability of 316 L stainless steel manufactured by laser powder bed fusion. *Metals* 8:643. <https://doi.org/10.3390/met8080643>
55. Qin H, Fallah V, Dong Q et al (2018) Solidification pattern, microstructure and texture development in laser powder bed fusion (LPBF) of Al10SiMg alloy. *Mater Charact* 145:29–38. <https://doi.org/10.1016/j.matchar.2018.08.025>
56. Zhang XX, Andr  H, Harjo S et al (2021) Quantifying internal strains, stresses, and dislocation density in additively manufactured AlSi10Mg during loading-unloading-reloading deformation. *Mater Des* 198:109339. <https://doi.org/10.1016/j.matdes.2020.109339>
57. Martin N, Hor A, Copin E et al (2022) Correlation between microstructure heterogeneity and multi-scale mechanical behavior of hybrid LPBF-DED Inconel 625. *J Mater Process Technol* 303:117542. <https://doi.org/10.1016/j.jmatprotec.2022.117542>
58. Voisin T, Forien J-B, Perron A et al (2021) New insights on cellular structures strengthening mechanisms and thermal stability of an austenitic stainless steel fabricated by laser powder-bed-fusion. *Acta Mater* 203:116476. <https://doi.org/10.1016/j.actamat.2020.11.018>
59. Sabzi HE, Hernandez-Nava E, Li X-H et al (2021) Strengthening control in laser powder bed fusion of austenitic stainless steels via grain boundary engineering. *Mater Des* 212:110246. <https://doi.org/10.1016/j.matdes.2021.110246>
60. Kong D, Dong C, Wei S et al (2021) About metastable cellular structure in additively manufactured austenitic stainless steels. *Addit Manuf* 38:101804. <https://doi.org/10.1016/j.addma.2020.101804>
61. Li Z, He B, Guo Q (2020) Strengthening and hardening mechanisms of additively manufactured stainless steels: the role of cell sizes. *Scripta Mater* 177:17–21. <https://doi.org/10.1016/j.scriptamat.2019.10.005>
62. Wang YM, Voisin T, McKeown JT et al (2018) Additively manufactured hierarchical stainless steels with high strength and ductility. *Nat Mater* 17:63–71. <https://doi.org/10.1038/nmat5021>
63. Gruber K, Smolina I, Kasproicz M et al (2021) Evaluation of Inconel 718 metallic powder to optimize the reuse of powder and to improve the performance and sustainability of the laser powder bed fusion (LPBF) process. *Materials* 14:1538. <https://doi.org/10.3390/ma14061538>
64. Ardila LC, Garc andia F, Gonz lez-D az JB et al (2014) Effect of IN718 recycled powder reuse on properties of parts manufactured by means of selective laser melting. *Phys Procedia* 56:99–107. <https://doi.org/10.1016/j.phpro.2014.08.152>
65. Field AC, Carter LN, Adkins NJE et al (2020) The effect of powder characteristics on build quality of high-purity tungsten produced via laser powder bed fusion (LPBF). *Metall Mater Trans A* 51:1367–1378. <https://doi.org/10.1007/s11661-019-05601-6>
66. Estrada-D az JA, El as-Z niga A, Mart nez-Romero O et al (2024) A novel mathematical model for predicting a sustainable selective laser melting and controlled densification. *Int J Sustain Eng* 17:1–11. <https://doi.org/10.1080/19397038.2024.2327386>
67. ESTRADA-D AZ JA, MART NEZ-ROMERO O, OLVERA-TREJO D et al (2022) Elucidating the fractal nature of powder bed in selective laser melting of metallic components. *Fractals* 30. <https://doi.org/10.1142/S0218348X22500621>
68. Jodi DE, Kitashima T, Singh A et al (2023) High-temperature microstructural stability of pure Ni fabricated by laser powder bed fusion using Gaussian and flat-top beam profiles. *Mater Charact* 200:112897. <https://doi.org/10.1016/j.matchar.2023.112897>
69. Suwas S, Ray RK (2014) Crystallographic texture of materials. Engineering Materials and Processes, Springer London, London
70. Dantzig JS, Rappaz M (2016) Solidification methods microstructure and modelling. CRC Press, Boca Raton, Engineering sciences Materials
71. Safaei K, Abedi H, Nematollahi M et al (2021) Additive manufacturing of NiTi shape memory alloy for biomedical applications: review of the LPBF process ecosystem. *JOM* 73:3771–3786. <https://doi.org/10.1007/s11837-021-04937-y>
72. Pilz S, Gustmann T, G nther F et al (2022) Controlling the Young's modulus of a  $\beta$ -type Ti-Nb alloy via strong texturing by LPBF. *Mater Des* 216:110516. <https://doi.org/10.1016/j.matdes.2022.110516>
73. Hooper PA (2018) Melt pool temperature and cooling rates in laser powder bed fusion. *Addit Manuf* 22:548–559. <https://doi.org/10.1016/j.addma.2018.05.032>
74. Qin H, Dong Q, Fallah V et al (2020) Rapid solidification and non-equilibrium phase constitution in laser powder bed fusion (LPBF) of AlSi10Mg alloy: analysis of nano-precipitates, eutectic phases, and hardness evolution. *Metall Mater Trans A* 51:448–466. <https://doi.org/10.1007/s11661-019-05505-5>
75. He Y, Zhong M, Jones N et al (2021) The columnar-to-equiaxed transition in melt pools during laser powder bed fusion of M2 steel. *Metall Mater Trans A* 52:4206–4221. <https://doi.org/10.1007/s11661-021-06380-9>
76. Pant P, Salvemini F, Proper S et al (2022) A study of the influence of novel scan strategies on residual stress and microstructure of L-shaped LPBF IN718 samples. *Mater Des* 214:110386. <https://doi.org/10.1016/j.matdes.2022.110386>
77. Serrano-Munoz I, Ulbricht A, Fritsch T et al (2021) Scanning manufacturing parameters determining the residual stress state in LPBF IN718 small parts. *Adv Eng Mater* 23:2100158. <https://doi.org/10.1002/adem.202100158>
78. Solheid JS, Elkaseer A, Wunsch T et al (2022) Multiobjective optimization of laser polishing of additively manufactured Ti-6Al-4V parts for minimum surface roughness and heat-affected zone. *Materials* 15:3323. <https://doi.org/10.3390/ma15093323>
79. Hatakeyama T, Sawada K, Suzuki M et al (2023) Microstructure development of modified 9Cr-1Mo steel during laser powder bed fusion and heat treatment. *Addit Manuf* 61:103350. <https://doi.org/10.1016/j.addma.2022.103350>
80. Bertsch KM, Meric de Bellefon G, Kuehl B et al (2020) Origin of dislocation structures in an additively manufactured austenitic stainless steel 316L. *Acta Mater* 199:19–33. <https://doi.org/10.1016/j.actamat.2020.07.063>
81. Bassini E, Sivo A, Martelli PA et al (2022) Effects of the solution and first aging treatment applied to as-built and post-HIP CM247 produced via laser powder bed fusion (LPBF). *J Alloy Compd* 905:164213. <https://doi.org/10.1016/j.jallcom.2022.164213>
82. Cox B, Ghayoor M, Doyle RP et al (2022) Numerical model of heat transfer during laser powder bed fusion of 316L stainless steel. *Int J Adv Manuf Technol* 119:5715–5725. <https://doi.org/10.1007/s00170-021-08352-0>
83. Wilson-Heid AE, Wang Z, McCornac B et al (2017) Quantitative relationship between anisotropic strain to failure and grain morphology in additively manufactured Ti-6Al-4V. *Mater Sci Eng, A* 706:287–294. <https://doi.org/10.1016/j.msea.2017.09.017>
84. Yu C-H, Peng RL, Lee TL et al (2022) Anisotropic behaviours of LPBF Hastelloy X under slow strain rate tensile testing at elevated

- temperature. *Mater Sci Eng, A* 844:143174. <https://doi.org/10.1016/j.msea.2022.143174>
85. Pérez-Ruiz JD, Marin F, Martínez S et al (2022) Stiffening near-net-shape functional parts of Inconel 718 LPBF considering material anisotropy and subsequent machining issues. *Mech Syst Signal Process* 168:108675. <https://doi.org/10.1016/j.ymssp.2021.108675>
  86. Fedorenko A, Fedulov B, Kuzminova Y et al (2021) Anisotropy of mechanical properties and residual stress in additively manufactured 316L specimens. *Materials* 14:7176. <https://doi.org/10.3390/ma14237176>
  87. Avateffazeli M, Carrion PE, Shachi-Amirkhiz B et al (2022) Correlation between tensile properties, microstructure, and processing routes of an Al–Cu–Mg–Ag–TiB<sub>2</sub> (A205) alloy: additive manufacturing and casting. *Mater Sci Eng, A* 841:142989. <https://doi.org/10.1016/j.msea.2022.142989>
  88. Li C, White R, Fang XY et al (2017) Microstructure evolution characteristics of Inconel 625 alloy from selective laser melting to heat treatment. *Mater Sci Eng, A* 705:20–31. <https://doi.org/10.1016/j.msea.2017.08.058>
  89. Raghavan S, Zhang B, Wang P et al (2017) Effect of different heat treatments on the microstructure and mechanical properties in selective laser melted Inconel 718 alloy. *Mater Manuf Processes* 32:1588–1595. <https://doi.org/10.1080/10426914.2016.1257805>
  90. Chlupová A, Šulák I, Kuběna I et al (2023) Comparison of microstructure and properties of nickel-copper alloy prepared by casting and laser powder bed fusion process. *MSF* 1082:171–176. <https://doi.org/10.4028/p-884q32>
  91. Ghayoor M, Lee K, He Y et al (2020) Selective laser melting of 304L stainless steel: role of volumetric energy density on the microstructure, texture and mechanical properties. *Addit Manuf* 32:101011. <https://doi.org/10.1016/j.addma.2019.101011>
  92. Megahed S, Aniko V, Schleifenbaum JH (2022) Electron beam-melting and laser powder bed fusion of Ti6Al4V: transferability of process parameters. *Metals* 12:1332. <https://doi.org/10.3390/met12081332>
  93. Estrada-Díaz JA, Elías-Zúñiga A, Martínez-Romero O et al (2021) A mathematical dimensional model for predicting bulk density of Inconel 718 parts produced by selective laser melting. *Materials* 14:512. <https://doi.org/10.3390/ma14030512>
  94. de Terris T, Andreau O, Peyre P et al (2019) Optimization and comparison of porosity rate measurement methods of selective laser melted metallic parts. *Addit Manuf* 28:802–813. <https://doi.org/10.1016/j.addma.2019.05.035>
  95. Estrada-Díaz JA, Elías-Zúñiga A, Martínez-Romero O et al (2021) Enhanced mathematical model for producing highly dense metallic components through selective laser melting. *Materials* 14:1571. <https://doi.org/10.3390/ma14061571>

**Publisher's Note** Springer Nature remains neutral with regard to jurisdictional claims in published maps and institutional affiliations.

**7.2 The dispersion-strengthening effect of TiN evoked by in situ nitridation of NiCu-based Alloy 400 during gas atomization for laser powder bed fusion**

**Jan-Philipp Roth**, Ivo Šulák, Zdeněk Chlup, Jörg Fischer-Bühner, Ulrich Krupp, Katrin Jahns

Materials Science and Engineering: A  
893 (2024) 146129

DOI 10.1016/j.msea.2024.146129

Reference [2]





# The dispersion-strengthening effect of TiN evoked by *in situ* nitridation of NiCu-based Alloy 400 during gas atomization for laser powder bed fusion

J.-P. Roth<sup>a,\*</sup>, I. Šulák<sup>b</sup>, Z. Chlup<sup>b</sup>, J. Fischer-Bühner<sup>c</sup>, U. Krupp<sup>d</sup>, K. Jahns<sup>a</sup>

<sup>a</sup> Faculty of Engineering and Computer Science, Osnabrück University for Applied Sciences, 49076, Osnabrück, Germany

<sup>b</sup> Institute of Physics of Materials, Czech Academy of Sciences, 61600, Brno, Czech Republic

<sup>c</sup> INDUTHERM Erwärmungsanlagen GmbH, 75045, Walzbachtal, Germany

<sup>d</sup> Steel Institute IEHK, RWTH Aachen University, 52072, Aachen, Germany

## ARTICLE INFO

### Keywords:

Alloy 400

*In situ* gas atomization

Laser powder bed fusion

Internal nitridation

TiN nanoparticle

Dispersion strengthening

## ABSTRACT

Alloy 400 is a widely used material being known for its excellent corrosive resistance. Within the chemical industry and in contrast to conventional manufacturing processes, Laser Powder Bed Fusion (LPBF) of Alloy 400 opens up for functional components that withstand harsh environments. On the basis of a holistic process route, the present work focusses on modifying the chemical composition of the base material with Titanium in order to allow the formation of TiN nanoparticles during powder production and LPBF, respectively, as well as documenting their influence on the mechanical properties. Parameter optimization for gas atomization and LPBF is carried out and the microstructure of both powders and parts is examined. It was found that besides Cu segregations on grain boundaries and dislocation formation on cell walls, TiN successfully formed in both powders and parts. The Ti-enriched parts resulted in enhanced mechanical properties in terms of hardness, tensile and creep due to these homogeneously distributed dispersoids. Hence, nanoparticle integration proved to be feasible and effective for the present alloy system.

## 1. Introduction

NiCu-based Alloy 400, also being referred to as Monel 400 or NiCu30Fe, crystallizes in a fcc solid solution and is well known for its excellent corrosion properties [1–3]. Its long-lasting, durable performance in sea water, acids and bases makes it an indispensable alloy system for a wide variety of functional parts in various high-tech industries; in particular, the maritime and chemical sector make frequent use of Alloy 400, utilizing parts such as feedwater and steam generator tubes in power plants, impellers and pump shafts, heat exchangers and condenser tubes in ship building and sour gas resistant components for oil and gas production [4–7]. However, material failure of Alloy 400 at elevated temperatures of 400–800 °C in carbon-rich atmospheres with a low oxygen partial pressure is an issue [8–10]. Conditions like these can be found in syngas power plants, for instance, and lead to metal dusting (MD), a highly detrimental form of corrosion that may fully decompose Ni-based alloys due to extensive coke formation, but by increasing the Cu content this effect can be successfully counteracted [10,11]. Besides MD resistance, creep is significantly determining the lifetime of such components as well and needs to be improved for the present alloy. For

instance, for Ni-based SRR99 in the range of 700–900 °C, Yu et al. found that the higher the temperature, the weaker the creep performance [12]. A solution against such rapid creep failure at elevated temperature can be found in the combination of additive manufacturing (AM) and nanoparticle integration [13].

To fabricate near-net-shape, function-integrated parts with little post processing effort, AM shows great potential [14,15]. One of its major benefits is its geometrical freedom, which is given as parts are being manufactured in an iterative process, two-dimensional and layer by layer, resulting in a complete three-dimensional part [16,17]. Thus, AM processes are currently used to produce parts from several alloys such as Ni-based superalloys and steels including stainless steels in various industries [18–24]. Amongst many other AM processes, Laser Powder Bed Fusion is one of the most frequently used ones, in general as well as for Ni-based alloy systems; selective melting of powders results in micro welding of several particles to a consistent part [25,26]. Specimens manufactured by this technique show a completely different microstructure compared to conventional manufacturing processes; they reveal elongated and directed grains with inevitably improved mechanical properties as they are much finer than in castings, for instance

\* Corresponding author.

E-mail address: [j.roth@hs-osnabrueck.de](mailto:j.roth@hs-osnabrueck.de) (J.-P. Roth).

<https://doi.org/10.1016/j.msea.2024.146129>

Received 22 September 2023; Received in revised form 11 January 2024; Accepted 14 January 2024

Available online 17 January 2024

0921-5093/© 2024 The Authors. Published by Elsevier B.V. This is an open access article under the CC BY-NC-ND license (<http://creativecommons.org/licenses/by-nc-nd/4.0/>).

[27,28]. Also, due to the rapid solidification occurring during LPBF, the phase formation may take place in a non-equilibrium state, which leads to a cellular arrangement of micro dendrites [29–31]. Hence, via the application of LPBF, parts can be tailored to their desired needs, enabling very complex structures not being manufacturable via conventional processes and with an adjusted microstructure.

The study of the integration of nanoparticles into base alloy matrices is becoming more and more intense. Mechanical properties of such reinforced alloy systems, especially in terms of creep and fatigue, outperform unmodified base alloys, also at elevated temperatures [32–35]. The mechanism occurring here is that these nanoscaled dispersoids prevent dislocations from moving throughout the matrix (i.e. dislocation pinning on e.g. oxides) [32,35–39]. Likewise, a positive shift of tensile properties, especially in terms of ultimate tensile strength at high temperatures, can be considered as a further major benefit of nanoparticle integration into base alloys [32,40,41]. Often, the respective nanoparticles can be classified as oxides, which is why the term oxide dispersion strengthening (ODS) was introduced in particular with dispersion strengthening (DS) referring to a wider variety of nanoparticles. Nitrogen can be named as a further frequently used reactive species for DS. In general, there are two different approaches in achieving well dispersed nanoparticles: (i) formation of nanoparticles during LPBF or (ii) implementation of nanoparticles prior to the AM process in terms of modifying the initial base-alloy powder with the respective additives. The first approach makes use of the remaining reactive element (in particular oxygen or nitrogen) within the build chamber of the 3D printer. In the melt pool, prior to solidification, these elements react with further alloying elements showing the lowest free Gibbs energy [32]. Via this routine, Chen et al. successfully integrated well dispersed MnO and Mn<sub>2</sub>O<sub>3</sub> in a CoCrFeMnNi high entropy alloy, while Mirzababaei et al. strengthened a FeCrAlY alloy with Y–Al–O and Y–O nanoparticles [42,43]. Hence, nanoscaled dispersoids result throughout the base matrix. Still, in this study, the latter method of altering the feedstock powder was carried out because the build chamber showed a very small remaining number of reactive elements only as it is fully pressured with argon shielding gas. Powders can be modified prior to LPBF by a wide variety of processes such as and amongst others mechanical alloying [33,36,44], acoustic mixing [34], electrostatic assembly techniques [45], electromagnetic three-dimensional vibration [46] or during powder atomization [47–50]. The latter approach was first introduced as gas atomization reaction synthesis (GARS) by Anderson and Foley [50], a procedure, where nanoparticles, such as oxides, eventually form during powder production by introduction of a combination of both reactive and shielding gases [49,51]. DS during atomization comes with several advantages: it is suitable for large-scale production, there is no need for adding nanoparticles as they are formed *in situ* and DS occurs evenly during solidification of the melt to powder. Hence, throughout the present study, this approach of *in situ* atomization was carried out. A pure nitrogen atmosphere was generated within the atomizer as a nano-sized TiN precipitate formation was targeted. The resulting powders were then further processed via LPBF.

## 2. Experimental procedure

For the atomization of powders, an Induterm/Blue Power AUG1000HTC atomizer (generator power of 20 kW) was operated with a direct inductive heating capacity in ceramic crucibles up to 1850 °C. Considering appropriate overheating of the system in order to further homogenize the melt and to lower its viscosity, an atomization temperature of 1600 °C was set (liquidus temperature: ~1350 °C). To withstand these high temperatures, ceramic consumables were used – an Al-oxide crucible, stopper rod and outlet (outlet diameter: 2.5 mm). Hot pure nitrogen gas (200 °C) was used for close-coupled atomization and the spray tower was pre-pressured with nitrogen as well. The crucible chamber was pressured with pure argon shielding gas. The gas stream was pressured with 15 bar, adding up in a gas stream of 280 Nm<sup>3</sup>/h and

a metal mass stream of approx. 4.3 kg/min. The chemical composition of Alloy 400 (approx. 65.0 wt.-% Ni, 31.5 wt.-% Cu, 2.0 wt.-% Fe, 1.0 wt.-% Mn, 0.2 wt.-% Si, 0.2 wt.-% Al, 0.1 wt.-% C) was adjusted in such a way that titanium, which rather can be found in the related Alloy K500 (besides Ti also revealing at least 2.3 wt.-% Al), was added in order to allow for the formation of Ti-nitrides during atomization. Pre-alloyed compounds as well as raw elements were utilized when loading the atomizer crucible with bulk material, resulting in approx. 6.5 kg input per atomization. After atomization, powders were further processed under nitrogen atmosphere, first being sieved and then air-separated by an Induterm/Blue Power AC1000G air classifier. During this procedure, well processable powder with a desired particle size distribution (PSD) of 15–53 µm was targeted and measured with a Camsizer X2.

After qualifying powders for AM, the LPBF process was initiated, using an EOS AMCM M290 customized machine. Due to its reduced build platform (100 mm in diameter) and pre-heating capability, the equipment allows for the parameter optimization of small batch powder fractions. A green laser system was used under argon atmosphere and a design of experiments (DoE) approach was carried out, varying laser power ( $p_L$ ) in [W], scanning speed ( $s_s$ ) in [mm/s] and hatch distance ( $d_H$ ) in [µm]. The layer thickness ( $t_L$ ) was at a constant level of 20 µm and the resulting volume energy density ( $e_v$ ) was defined as per  $e_v = p_L / (s_s \cdot d_H \cdot t_L)$ . As an optimum parameter set for the standard Alloy 400,  $p_L = 85$  W,  $s_s = 1050$  mm/s and  $d_H = 50$  µm was found in previous studies [52]. These values served as a basis for the parameter study carried out in this work. Here, at least 99.5 % in optical density was targeted. Mechanical properties of the Ti-enriched Alloy 400 were determined in terms of tensile, creep and hardness testing. For hardness, all values are the average of five separate measurements on five cubes each (25 total measurements for the top as well as for the side surfaces). For the evaluation of optical density and for hardness measurements, cubic samples with an edge length of 8 mm were produced. For density evaluation via light optical microscopy, these were ground down to 2500 grit (SiC paper). For mechanical testing (tensile, creep) instead, a block of  $14 \times 45 \times 70$  mm<sup>3</sup> was manufactured and subtractively machined in order to generate the final test specimens. Tensile specimens were generated from M6 x 40 mm cylinders (test area: Ø 3 mm x 9 mm), creep specimens from samples with a  $14 \times 3.2$  mm<sup>2</sup> cross section and total length of 41 mm (test area:  $4 \times 3.2$  mm<sup>2</sup>, 25 mm). Stress exponents during creep experiments were obtained as per the formula  $\ln(\dot{\epsilon}) = \ln(B) + n \ln(\sigma^n)$  where  $\dot{\epsilon}$  is the true strain rate, B is a temperature-dependent pre-factor,  $\sigma$  is the applied stress and n is the stress exponent.

In order to investigate powder and part microstructure, a scanning electron microscope (SEM), equipped with energy dispersive X-ray spectroscopy (EDS) as well as electron backscattered diffraction (EBSD), was operated on the microscale. EBSD band contrast (BC) images and crystallographic orientation mappings were both taken with an EBSD Symmetry detector. For more in-depth nanoscale characterization, a transmission electron microscope (TEM) was utilized. Concerning the TEM sample preparation, a thin lamella was extracted from powder particles using a dual beam for focussed Ga<sup>+</sup> ion beam milling (FIB). In order to avoid damage of the area of the future lamella, a very thin platinum layer was deposited using electron deposition and later a thicker platinum layer was applied using ion deposition. This step was followed by gallium ion milling using 30 keV accelerating voltage over a range of currents tuned for precise control over the beam-sample interactions. For rough milling, ion currents of 1–4 nA were applied to produce craters from both sides until a 1.5 µm thick and 10 µm high wall was formed. Subsequently, this pre-lamella was cut free, extracted via a nano-manipulator and welded by platinum to an omniprobe grid. Following milling of the lamella was performed using gentler ion doses, down to electron-transparent thicknesses (<100 nm) with an ion current of 0.1–1 nA. Final polishing was performed with low energy ion milling at 5 KeV and ion current of 250 pA with ±1.5° inclination to the perpendicular direction of the FIB. High-resolution TEM investigations

of lamellae were accomplished by a Talos F200i TEM with FEG electron source in scanning TEM (STEM) mode at 200 kV. To obtain a whole view of the lamellae of powders and additively manufactured parts, the information obtained by bright field (BF) imaging were supplemented by unique EDS absorption correction enabling accurate element quantification. For tensile testing, a universal electromechanical machine was operated, and for creep measurements, a self-designed creep machine developed at the Institute of Physics of Materials as per [53] was used. Vickers-hardness was obtained according to DIN EN ISO 6507-1. Ultimately, mechanical properties were compared to LPBF standard Alloy 400 (without Ti addition) and hot-extruded bulk reference material (also free of Ti), both resulting from previous studies [52].

### 3. Results and discussion

#### 3.1. Nanoparticle integration into powders

In order to be suitable for LPBF, it is known that as-atomized powders need to be processed. After the removal of splash via sieving at 200  $\mu\text{m}$ , and of particles being either too fine (<15  $\mu\text{m}$ ) or too coarse (>53  $\mu\text{m}$ ) via air-classification, a particle size distribution that satisfactorily matches the targeted 15–53  $\mu\text{m}$  range was achieved. In Fig. 1, the PSD for the Ti-modified Alloy 400 is displayed in terms of cumulative and relative frequency. It can be clearly seen that the highest yield is between 20 and 25  $\mu\text{m}$ , indicated by the highest column as well as the strongest slope of the line. The particle size at 50 % cumulative frequency amounts to 30.69  $\mu\text{m}$  with 17.26  $\mu\text{m}$  for 10 % and 51.48  $\mu\text{m}$  for 90 %. The yield of powder after air classification within the final PSD was 57 % compared to the crucible input material.

SEM investigations revealed spherical powder particle geometries as shown for a particle of  $\sim 55 \mu\text{m}$  in diameter in Fig. 2. Only negligible satellite formation was observed, further lowering the total surface of a respective particle and thus, enhancing its flowability [54–56]. Spherical particles are generally favorable in AM as they ensure a proper build platform coverage during LPBF. This way, the recoater may supply well flowing powder from the feedstock and consequently build up a homogenous new layer iteratively. Concerning the targeted formation of Ti-nitrides, only little evidence was found at grain boundaries via the application of EDS. As can be seen from the EDS element maps, Ti and N are enriched at the exact same locations in between single grains on the microscale. In contrast, a corresponding proof of the remaining alloying elements forming a chemical bond with nitrogen was not observed. Double-checked via EDS, target values and detected compositions in powders matched. Hence, the preceding atomization process is assumed to operate appropriately; the chemical composition is not affected by any residues or slagging inside the crucible. Also, when printing powders to parts during LPBF, no significant shift in chemistry was detected neither.

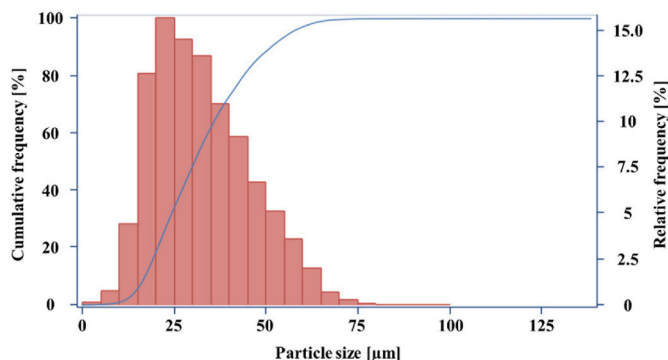


Fig. 1. Particle size distribution in cumulative (blue line) and relative (red columns) frequency. (For interpretation of the references to color in this figure legend, the reader is referred to the Web version of this article.)

In order to indicate an effect on the internal structure of the powder, a lamella was extracted from a single particle and studied by TEM as shown in Fig. 3. Bright and dark field images show dislocation formation along cell walls, resulting from rapid cooling during atomization [57]. Ni and Cu mappings indicate an interdendritic segregation of Cu on cell walls, a well-known characteristic of NiCu alloys [58–60]. Rapid solidification does not allow sufficient Ni diffusion in the dendrites leading to Cu enrichment in the remaining liquid. Besides Cu, no further elements were found to be preferably present on cell walls. Marked by orange arrows, Ti and N enriched areas could be detected near cell walls. They reveal a cuboidal shape corresponding to the characteristic morphology of TiN. Moreover, no further compounds were detected in the same region of interest, leading to the assumption that the targeted TiN formation has successfully been evoked in powders. Accordingly, this reaction has been demonstrated previously for other nanoparticles, such as Y-, Fe- or Cr-oxides, throughout powder production [49,61,62].

#### 3.2. LPBF dispersion-strengthened parts

As the powder was specified as AM-suitable and since noticeable amounts of Ti and N were not dissolved in the matrix but were rather detectable on grain boundaries and cell walls as TiN, these powders were further processed via LPBF in order to achieve TiN formation within the microstructure of the printed parts as well. Even though the LPBF process chamber is pressured with Ar shielding gas, further nitrogen uptake during the manufacturing process might occur as some residual proportions of accompanying gases, such as O or N, inevitably do remain; this was already proven for oxygen uptake in Ar atmosphere for a CoCrFeMnNi alloy and for oxygen uptake in N atmosphere for a FeCrAlY system [42,43]. Hence, the presence of TiN nanoparticles in powders might act as nuclei for an even more pronounced formation of TiN in parts.

Applying a DoE scheme enabled for dense fabrication of the Ti-modified powders into parts. Several parameter sets were evaluated on seventeen cubes as displayed in Table 1. Here, the blue-colored cubes A1 to B2 indicate a variation around the starting point (yellow-colored cubes C3 to C5, initial parameter set found previously for unmodified Alloy 400 [52]) and the orange-colored ones B3 to C2 illustrate extreme points where only one parameter value is shifted. Italic numbers indicate non-varied parameters. Furthermore, the parameter set of cube C2 is highlighted, as it shows the highest attainable optical density throughout this study of 99.84 %. Cross sections of cubes A2, A6, B6 and C2, viewed from the top, are displayed in Fig. 4. Concerning the pore formation within the filling, it can clearly be observed that a too high volume energy density of 169 J/mm<sup>3</sup> for cube A2 leads to the formation of severe defects. The pore size reduces with falling energy density as for A6, pores, resulting from a too high energy input, are still present but they now rather appear as the well-studied key hole defects caused by material evaporation in the melt pool [63,64]. Hence, a decrease of 56 J/mm<sup>3</sup> enables for an increase in density from 97.57 % to 98.65 %. Further lowering the energy density finally allowed the formation of highly dense parts such as B6 (61 J/mm<sup>3</sup> → 99.81 %) or C2 (58 J/mm<sup>3</sup> → 99.84 %). It is important to mention that the missing few per mille to 100 % completely dense parts cannot be correlated with porosities within the filling of the parts but rather have to be located at the edges of the cube as can be seen for all four cross sections. This has been demonstrated by Ertay et al. [65] and Ulbricht et al. [66], assuming that acceleration and deceleration at the end of laser tracks on part edges eventually lead to a localized energy accumulation (which in turn causes key hole porosity). Therefore, in exceeding the targeted 99.5 % in density, C2-parameters (85 W, 1050 mm/s and 70  $\mu\text{m}$ ) were considered appropriate and chosen for the further LPBF fabrication of test specimens.

After having found a parameter set for dense part fabrication, SEM and TEM characterizations were carried out. Fig. 5 shows the EBSD BC image in build direction (BD) on the left side and the crystallographic



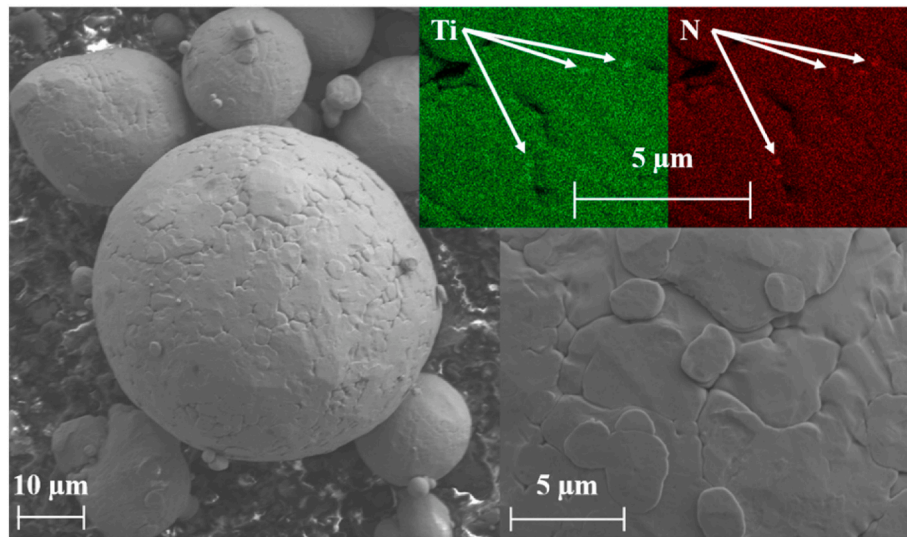


**Fig. 2.** Ti-enriched particle in the SEM – complete particle with satellites, particle surface and Ti-/N-EDS-mappings.

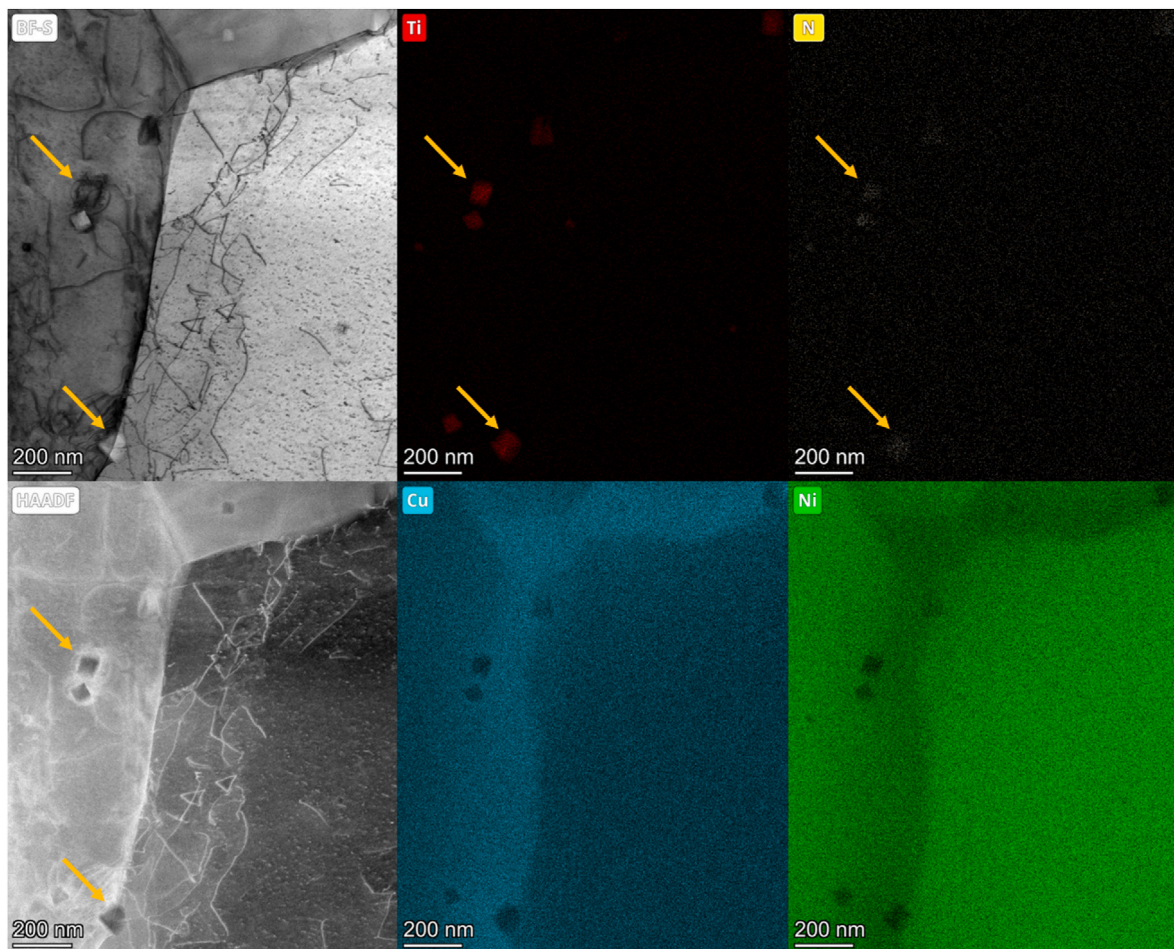


**Fig. 3.** Bright field, dark field, Ti-, N-, Cu- and Ni-mappings within the modified Alloy 400 powder.

orientation mapping along BD on the right side. The BC image allows for a clear distinguishability between several laser tracks within one respective layer of the part. As mentioned above, 70  $\mu\text{m}$  hatch distance was chosen, resulting in a scan track width of approx. 58  $\mu\text{m}$ . The resulting margin of 12  $\mu\text{m}$  did not result in a lack of fusion between scan tracks due to the iterative sequence of several part layers, all being

exposed in another orientation around the BD-axis and leading to the formation of a heat-affected zone as commonly known for LPBF [67,68]. This way, porosity eventually gets prevented as sufficient energy and material are applied to one respective layer. The EBSD image was taken from another perspective, illustrating the grain growth along the build direction when viewed from the side. A well-studied peculiarity of AM is

**Table 1**

Parameter sets for different cubes, resulting in volume energy densities and optical relative densities, respectively.

Cube	Laser power in [W]	Scanning speed in [mm/s]	Hatch distance in [ $\mu\text{m}$ ]	Volume energy density in [ $\text{J}/\text{mm}^3$ ]	Optical relative density in [%]
A1	55	850	40	81	95.18
A2	115	850	40	169	97.57
A3	55	1250	40	55	95.29
A4	115	1250	40	115	96.93
A5	55	850	60	54	98.70
A6	115	850	60	113	98.65
B1	55	1250	60	37	95.14
B2	115	1250	60	77	98.33
B3	35	1050	50	33	90.41
B4	136	1050	50	129	98.75
B5	85	714	50	119	97.47
B6	85	1386	50	61	99.81
C1	85	1050	30	135	98.51
C2	85	1050	70	58	99.84
C3	85	1050	50	81	99.64
C4	85	1050	50	81	99.80
C5	85	1050	50	81	99.57

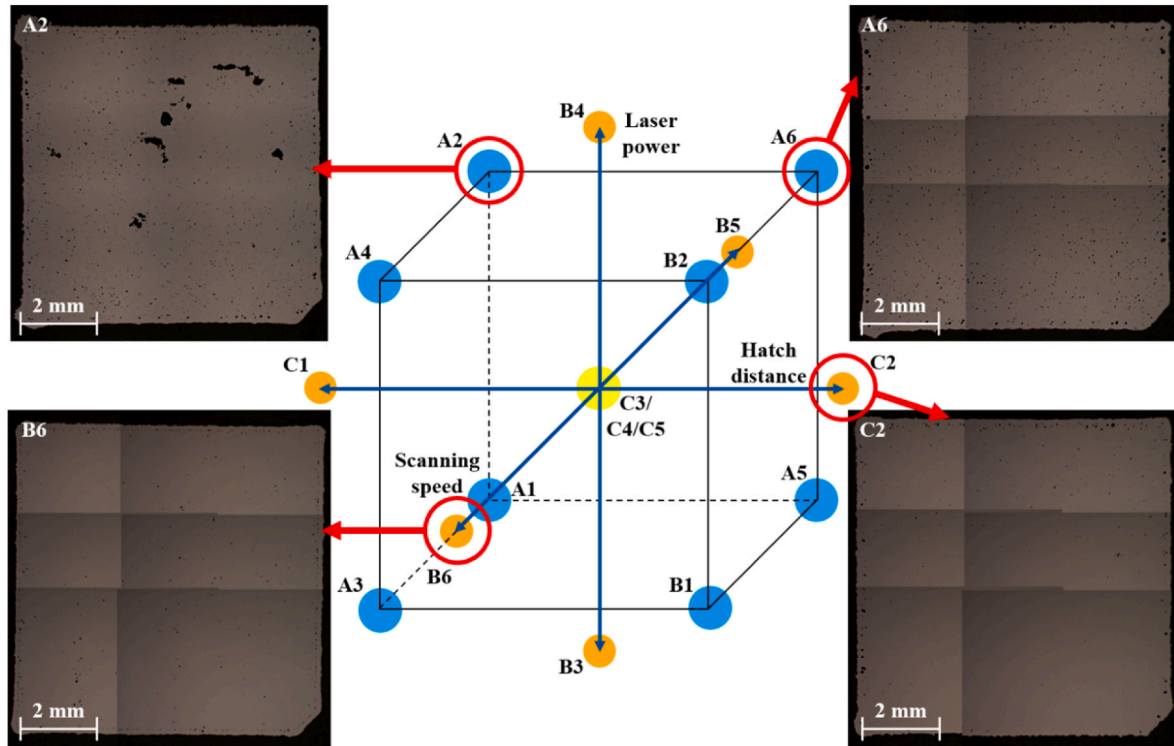


**Fig. 4.** Design of experiments cube, revealing the location of the above-mentioned parameter sets within the design space, and corresponding cross sections of cubes A2, A6, B6 and C2.

that grains show a clear tendency in growing along BD, being correlated with both the direction of energy input and the heat flow [69,70]. Regarding the respective fcc crystal structure, a wide variety of preferred orientations was detected. As indicated by the inverse pole figure, no preferred texture was verified with respect to the BD. Qin et al. showed a weakly pronounced texture for LPBF-AlSiMg as well and justified it with the rotating scanning strategy (which amounted to 67°

as in this work) [68]. As layers get re-melted several times and in varying orientations, no preference in orientation can evolve.

The Ti and N enrichments found in the powder were expected to reappear in the parts. So, TEM characterization was carried out to study the microstructure on the nanoscale. Fig. 6 illustrates the respective findings. Having a look at the dark and bright field images in the first row, a cellular structure becomes clearly visible. The micro-dendritic



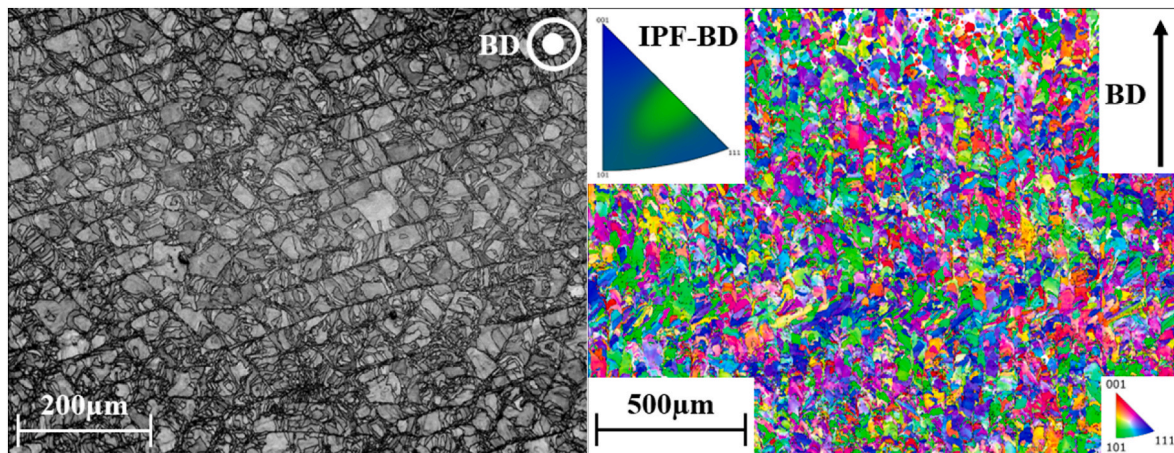


Fig. 5. EBSD band contrast for the top-down view in BD (left) and EBSD map for the side view along BD (right).

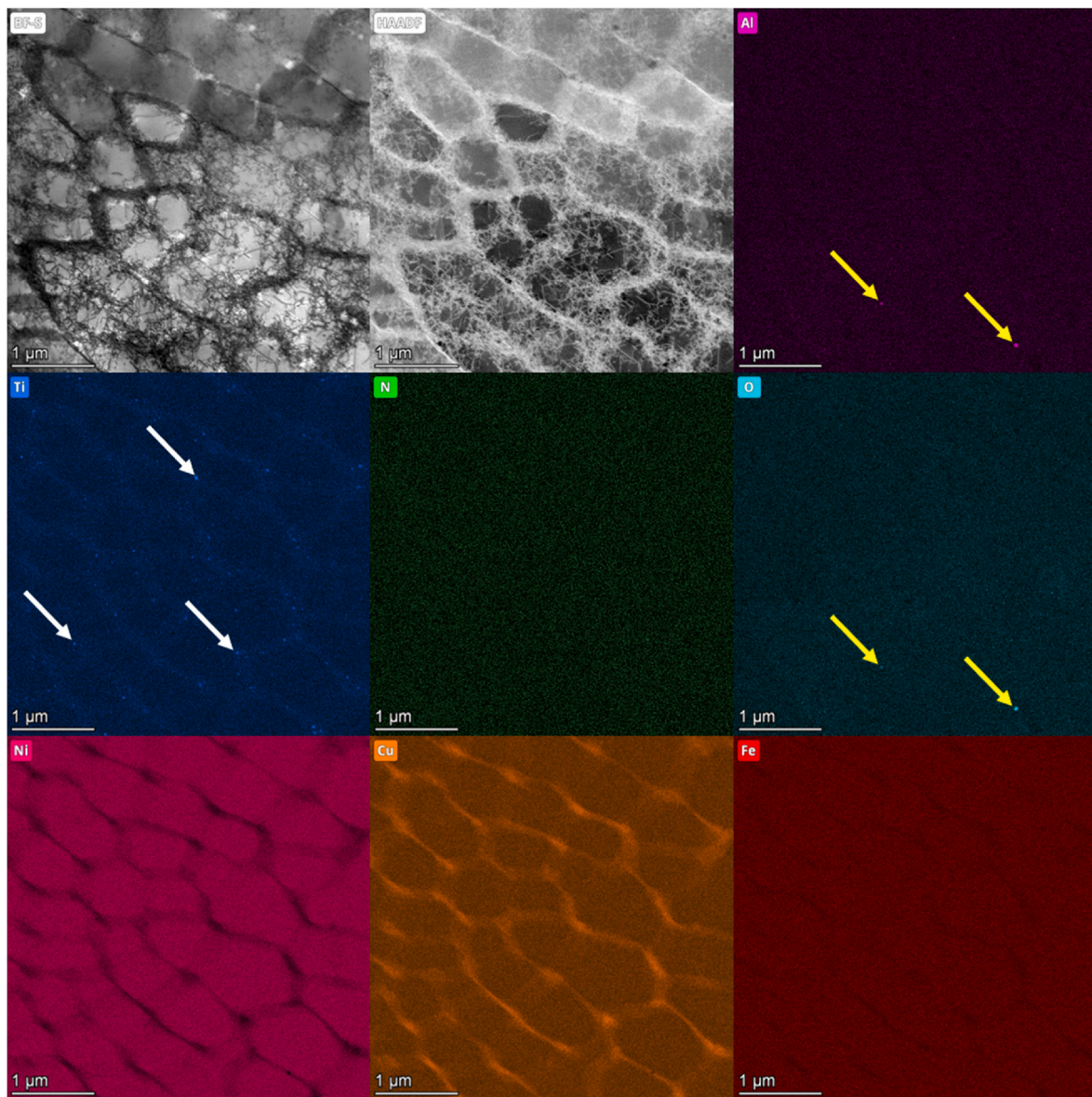


Fig. 6. Bright field, dark field, Al-, Ti-, N-, O-, Ni-, Cu-, and Fe-mappings within the modified Alloy 400 part, Ti highlighted with white arrows, Al and O highlighted with yellow arrows. (For interpretation of the references to color in this figure legend, the reader is referred to the Web version of this article.)



cell walls are comprised of a high number of dislocations, while cell cores experience a weaker intensity in dislocations. This is due to the fact that segregations at cell walls of solid solutions facilitate the nucleation of dislocations [71]. Also, compared to the powder lamella in Fig. 3, the dislocation density is significantly higher. High dislocation density and micro dendritic structures within single grains, resulting from the occurring high cooling rates, are frequently investigated phenomena in AM for a wide variety of alloys and thus, they were expected and also verified for the present alloy system as well [52,72–75]. Having a closer look at these cell walls dense in dislocations, nano-segregations can be detected for Cu and, in lower intensity, for Ti. In contrast, Ni and Fe are rather present within the cells than at their boundaries. As found in powders already, such Cu segregations are a common property of NiCu-based alloys that have been reported intensively for decades [58–60]; they are due to the insufficient interdiffusion within the solid nuclei in the two-phase regime, leading to an interdendritic Cu enrichment. For Ti, a high number of nano-scaled precipitates can be reported on cell walls, some of them being marked with white arrows. However, via application of this characterization technique, no such precipitates could be verified for N by STEM-EDS which is due to the limited quantifiability by this technique. Fig. 7 reveals the presence of precipitates in higher resolution, probably being TiN. The cuboidal nanoparticles can be clearly detected on the cell walls within single grains, and its morphology is typical for the occurrence of TiN. This characteristic shape has been reported frequently in literature already [76–79]. The formation mechanism can be traced back to a low standard free energy of TiN. The presence of Ti and N outside the preferred solid solution was targeted throughout this work and is now expected to have an influence on the mechanical properties in comparison to Alloy 400 without any Ti addition.

Besides this finding, the occasional presence of Al and O was detected and indicated by yellow arrows. Hence, Al-oxide seems to form as a secondary by-product in marginal quantity. As stated by Xu et al. and Hadraba et al. for Y-oxides, this may eventually lead to the pinning of dislocations [32,36]. Still, with the present alloy and its very low pronounced Al-oxide formation, it cannot be assumed that these nanoparticles will cause any effect on the mechanical properties; mechanical improvements can only be associated with the TiN formation.

### 3.3. Enhanced mechanical properties

As the formation of TiN (and to a significantly lesser extent of  $\text{Al}_2\text{O}_3$ ) seems to take place during LPBF, mechanical properties are expected to outperform the ones of non-modified Alloy 400. The latter key figures were elaborated in previous work [52] already. For hardness according to Vickers, HV10 was specified as listed in Table 2 and measured on as-built surfaces. While the Ti-enriched Alloy 400 shows a high hardness on the top surface, which exceeds the non-modified standard version of the alloy by approx. 15 HV10, the side surfaces reveal a lower hardness which in turn is approx. 15 HV10 below the reference value. This finding can be correlated to the pronounced pore formation below the side surfaces of the parts, as illustrated in Fig. 4 already, which occurred to a lesser extent in the reference material. During hardness measurements, such voids facilitate the penetration of the Vickers geometry. Therefore, the mean value of 207.4 HV10 of the top surface, where no such pore formation was observed, better indicates the hardness potential of the present modified alloy, outperforming the unmodified version. In conventionally manufactured, hot-extruded bulk material, only 121–127 HV10 can be reached [52]. This can be explained by the overall finer grain structure of the LPBF-manufactured parts, as discussed by Raffes et al. for a NiCu-based alloy [3]. To summarize, a clear hierarchy can be noted: Ti-enriched Alloy 400 shows a higher hardness than unmodified Alloy 400 which in turn demonstrates a higher hardness than conventionally manufactured bulk material. An increase in hardness due to DS is a well-studied characteristic throughout literature; for instance, Elsayed et al. denoted a 20 % increase in Vickers hardness after modifying an AlSi10Mg with  $\text{B}_4\text{C}$  and Gao et al. reached a 16 % increase due to TiN integration into the same base alloy [46,80].

Fig. 8 illustrates the results of tensile tests for (i) the Ti-enriched Alloy 400 ('LPBF + Ti'), (ii) hot-extruded bulk Alloy 400 ('bulk'), taken from previous work [52], and (iii) the standard LPBF version of

**Table 2**  
Hardness for Ti-enriched and unmodified LPBF Alloy 400.

Hardness	HV10
<b>Ti-enriched Alloy 400</b>	207.4 ± 4.2 (top surface) 179.8 ± 5.4 (side surface)
<b>Standard Alloy 400</b>	192.9 ± 3.1 (top surface) 194.9 ± 3.2 (side surface)

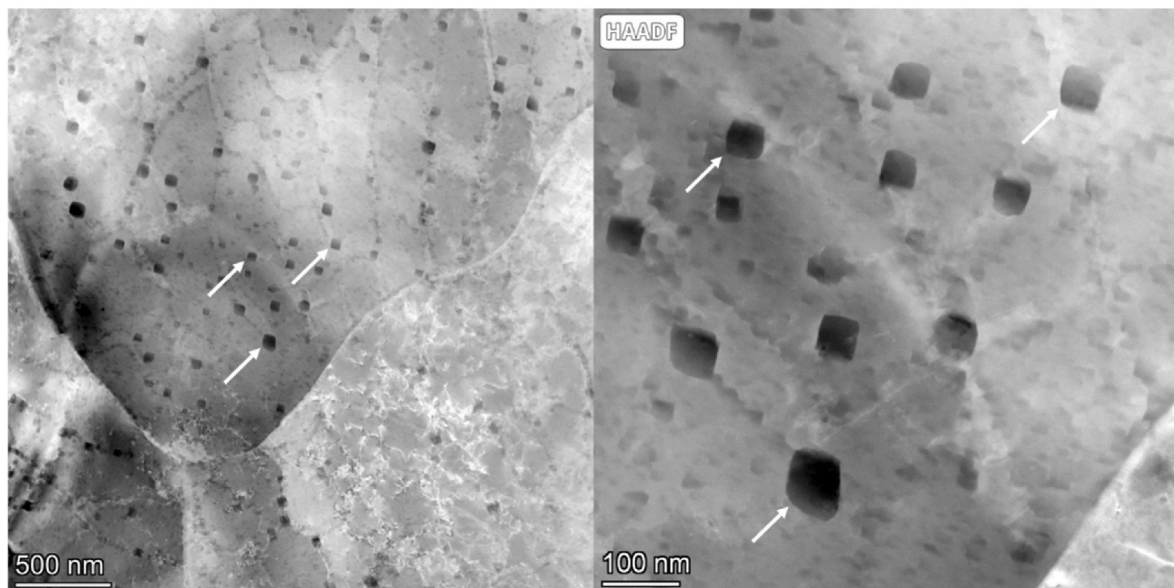


**Fig. 7.** Dark-field TEM of cuboidal TiN nanoparticles on sub-grain cell walls.

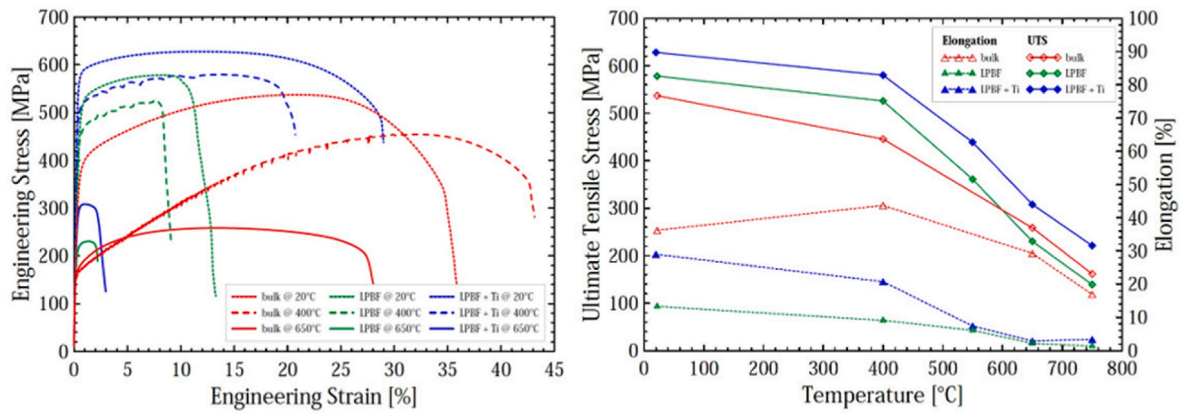


Fig. 8. Stress-strain curves at several temperatures and UTS & elongation over temperature for the three variants of Alloy 400.

Alloy 400 containing no Ti ('LPBF'). When comparing the tensile curves for the three different material types at temperatures of 20 °C, 400 °C and 650 °C (potential application temperatures of Alloy 400 heat exchangers), they all show the highest attainable stress for room temperature and lowest for 650 °C, respectively. Also, the Ti-enriched Alloy 400 shows higher strength levels for all temperatures than the other two versions (with 'LPBF' being slightly higher or equal to 'bulk'). Higher strength is attributed to the finer grain size of the AM variants [3,27,28]. Moreover, TiN particles on cell boundaries seem to positively affect the ultimate tensile strength (UTS) of 'LPBF + Ti' even further as it lies at least  $\sim 50$  MPa above the 'LPBF' values for all tested temperatures (20 °C, 400 °C, 550 °C, 650 °C and 750 °C). When comparing the strains at fracture (elongations) as a measure of ductility, the bulk variant outperforms both LPBF variants throughout the whole temperature range. The remaining porosity and the high dislocation densities at the cell boundaries in the LPBF versions serve as an explanation here. The 'LPBF + Ti' version reveals better strain performance than the 'LPBF' variant. However, this effect becomes negligible at temperatures  $\geq 550$  °C. At room temperature, the strain of the Ti-modified LPBF version almost reaches bulk performance. An overall positive effect of the TiN nano precipitates can be noted at this stage; especially contributing to a better strength performance. Improved tensile properties due to DS are a well-studied phenomenon. Yu et al. correlated an increase in tensile strength for a Ni-based superalloy with the presence of several oxides on the nanoscale [40]. Accordingly, Jang et al. reported that ODS Ni-based alloys outperform the non-modified versions in terms of mechanical properties at elevated temperatures due to suppression of dislocation movement; e.g. a 84 % increase at 700 °C for alloy 617 was reported [41]. For a NiCrFeY alloy enriched with  $Y_2O_3$ , Xu et al. revealed a high ultimate tensile strength around 563 MPa at 600 °C, traced back

to the interplay of a high dislocation density and the nanoparticles [32].

Shifting the focus to the targeted enhanced creep properties due to TiN-precipitate-induced dislocation pinning, Fig. 9 shows the test results for 'LPBF + Ti', 'bulk' and 'LPBF'. The image on the left-hand side illustrates the correlation between the applied stress  $\sigma$  in [MPa] and the time to fracture  $t_f$  in [h]. At approx. 50, 80 and 100 MPa, a comparison between the three different alloy states is most accurate as measuring points are available for all of them. From the measured time to fracture data at various stress levels, it can be concluded that the creep properties of bulk material and Ti-enhanced LPBF material outperform the unmodified alloy, while the bulk one shows slightly higher values than 'LPBF + Ti'. It may thus be concluded that the AM variants of Alloy 400 do not show better creep performance than the conventionally fabricated material. However, comparing only the two LPBF variants, a clear shift in terms of enhanced creep properties can be attributed to the Ti-alloyed material. Therefore, the previously found TiN nanoparticles on cell walls seem to have a certain impact on dislocation pinning. Al-oxides might also slightly contribute here but occur considerably less in the nanostructure than the Ti-nitrides. Fig. 9 right illustrates the detected stress exponent  $n$  for the respective material types 'bulk', 'LPBF' and 'LPBF + Ti', resulting from the applied stress levels  $\sigma$  in [MPa] and steady creep rates  $\dot{\epsilon}$  in [%/s] at 650 °C (determined at a strain of  $\epsilon = 1$  %). Accordingly, the stress exponents are:  $n = 3.1$  for 'LPBF',  $n = 4.9$  for 'bulk' and  $n = 4.8$  for 'LPBF + Ti'. Therefore, the bulk and the Ti-enhanced LPBF variants can be described as significantly more resistant to creep with stress exponents of an order around  $n = 5$  (which corresponds to a typical value for pure metals); the unmodified LPBF version instead reveals a stress exponent around  $n = 3$ , matching the typical order for solid solutions [81]. Also, when comparing the data for 100 MPa applied stress, the steady creep rate for the standard LPBF Alloy 400

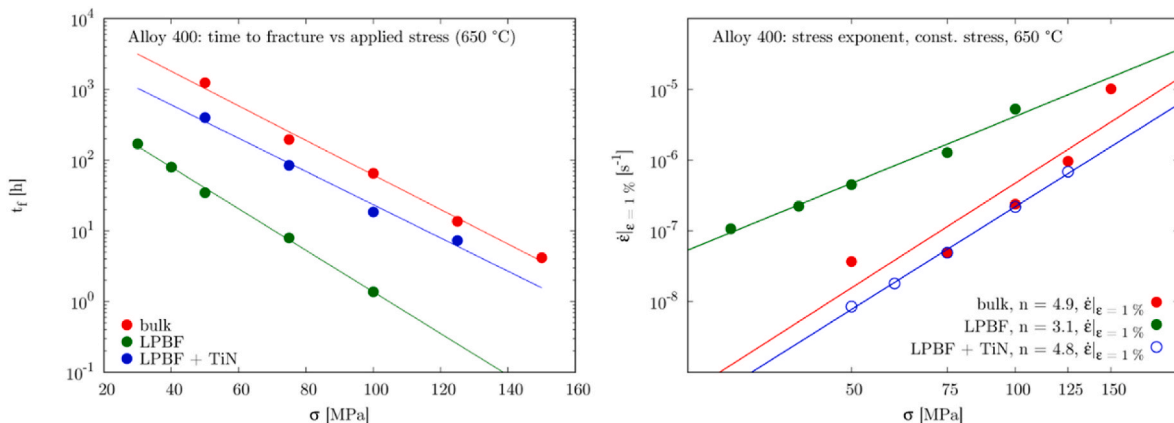


Fig. 9. Time to fracture and stress exponents, resulting from creep experiments at 650 °C for the three variants of Alloy 400.



measures approx.  $10^{-5}$ /s, while the other two reveal a rate of  $\sim 10^{-7}$ /s. Hence, creep takes place more slowly, allowing to conclude for a positive effect on the creep properties due to TiN, enabling for comparable creep properties as in bulk material. For several Fe-based, ferritic alloys, Wasilkowska et al. exemplified that, especially at elevated temperatures, there is a clear positive effect of ODS nanoparticles on creep performance, being correlated with a successful pinning of dislocations [37]. The same finding of a positive ODS-dislocation-creep connection at 950 °C was found by Rakhmonov et al. for Hastelloy X reinforced by  $Y_2O_3$  [38]. For a gas-nitrided AISI 316L steel, Boes et al. stated that both nitrides and carbonitrides, e.g. enriched in Ti, inevitably improve the creep performance of the alloy [39].

#### 4. Conclusion

In this work, a nanoparticle modification route for a Ti-enriched, NiCu-based Alloy 400 was established. The process consisted of the nitrogen atomization of raw material to powder being suitable for AM, a DoE-assisted LPBF parameter optimization for manufacturing of highly dense parts and a determination of mechanical properties in terms of hardness, tensile and creep. In between, an in-depth characterization of powders and parts was carried out. It was aimed to introduce TiN particles on the sub-grain nanoscale. Enrichments of Ti and N were detected on powder surfaces and TiN was proven to be present inside powders, resulting from the internal nitridation during atomization. TiN formation was determined on cell walls of the LPBF built parts as well. This eventually led to enhanced mechanical properties, resulting from the Ti modification of the standard Alloy 400 and the respective TiN nanoparticles. The proven improvements include:

- A positive shift in Vickers hardness of 15 HV10 to 207 HV10 in total for the Ti-enriched variant when compared to the unmodified LPBF one.
- Enhanced ultimate tensile strength of the Ti-enhanced version throughout the whole tested temperature range (room temperature up to 750 °C) when compared to bulk material and non-modified LPBF Alloy 400.
- A comparably high elongation for 'LPBF + Ti' and 'bulk' at 20 °C, while for all temperatures above the strain rates of the bulk material are substantially higher than the ones of the LPBF versions.
- Comparable creep performance of the LPBF variant including Ti to the bulk one, both being clearly higher than for the standard LPBF Alloy 400 by one order of magnitude, allowing for a substantially longer time to fracture for several applied stresses.

To conclude, a nanoparticle modification is feasible for the present Alloy 400 system enriched in Ti as TiN formed *in situ* during nitrogen atomization and in the subsequent LPBF process. This, in turn, successfully limited dislocation movement on the nanoscale and allowed for superior mechanical properties when compared to the unmodified version of the alloy system.

#### CRediT authorship contribution statement

**J.-P. Roth:** Conceptualization, Data curation, Formal analysis, Investigation, Methodology, Software, Supervision, Validation, Visualization, Writing – original draft, Writing – review & editing. **I. Šulák:** Data curation, Investigation, Software, Visualization, Writing – review & editing. **Z. Chlup:** Data curation, Investigation, Software, Visualization, Writing – review & editing. **J. Fischer-Bühner:** Investigation, Writing – review & editing. **U. Krupp:** Conceptualization, Funding acquisition, Project administration, Resources, Supervision, Writing – review & editing. **K. Jahns:** Conceptualization, Funding acquisition, Project administration, Resources, Supervision, Writing – review & editing.

#### Declaration of competing interest

The authors declare that they have no known competing financial interests or personal relationships that could have appeared to influence the work reported in this paper.

#### Data availability

Data will be made available on request.

#### Acknowledgements

The authors would like to acknowledge QuesTek Europe AB for providing the Ti-modified alloy composition. This work has received funding from the European Union's Horizon 2020 research and innovation program under grant agreement No 958192 which is gratefully acknowledged.

#### References

- [1] Special Metals Corporation, Monel alloy 400 (2005).
- [2] C.-H. Zhang, C.-L. Wu, S. Zhang, Y.-F. Jia, M. Guan, J.-Z. Tan, B. Lin, Laser cladding of NiCrSiB on Monel 400 to enhance cavitation erosion and corrosion resistance, *Rare Met.* 41 (2022) 4257–4265, <https://doi.org/10.1007/s12598-016-0814-4>.
- [3] I. Raffaele, F. Adjei-Kyeremeh, U. Vroomen, E. Westhoff, S. Bremen, A. Hohoi, A. Bührig-Polaczek, Qualification of a Ni-Cu alloy for the laser powder bed fusion process (LPBF): its microstructure and mechanical properties, *Appl. Sci.* 10 (2020) 3401, <https://doi.org/10.3390/app10103401>.
- [4] R.K. Devendranath, N. Arivazhagan, S. Narayanan, M. Narayanan, A. Mondody, R. Kashyap, Development of defect free monel 400 welds for marine application, *AMR* 383–390 (2011) 4693–4696, <https://doi.org/10.4028/www.scientific.net/AMR.383-390.4693>.
- [5] U. Esgin, D. Özyürek, H. Kaya, An investigation of wear behaviors of different Monel alloys produced by powder metallurgy, *AIP Conf. Proc.* 1727 (2016) 20008, <https://doi.org/10.1063/1.4945963>.
- [6] L.E. Shoemaker, G.D. Smith, A century of monel metal: 1906–2006, *JOM* 58 (2006) 22–26, <https://doi.org/10.1007/s11837-006-0077-x>.
- [7] Special Metals Corporation, High-Performance Alloys for Resistance to Aqueous Corrosion, 2000.
- [8] D.J. Young, J. Zhang, C. Geers, M. Schütze, Recent advances in understanding metal dusting: a review, *Mater. Corros.* 62 (2011) 7–28, <https://doi.org/10.1002/maco.201005675>.
- [9] R. Schneider, E. Pippel, J. Woltersdorf, S. Strauß, H.J. Grabke, Microprocesses of metal dusting on nickel and Ni-base alloys, *Steel Res.* 68 (1997) 326–332, <https://doi.org/10.1002/srin.199701796>.
- [10] K. Jahns, A.S. Ulrich, C. Schlereth, L. Reiff, U. Krupp, M.C. Galetz, The effect of Cu content and surface finish on the metal dusting resistance of additively manufactured NiCu alloys, *Oxid Met* 96 (2021) 241–256, <https://doi.org/10.1007/s11085-021-10037-8>.
- [11] C. Geers, Inhibition of Coking and Metal Dusting on Conventional Alloys by Using a Nickel-Tin Intermetallic Coating, 2013.
- [12] J. Yu, X. Sun, T. Jin, N. Zhao, H. Guan, Z. Hu, High temperature creep and low cycle fatigue of a nickel-base superalloy, *Mater. Sci. Eng., A* 527 (2010) 2379–2389, <https://doi.org/10.1016/j.msea.2010.01.001>.
- [13] C. Donate-Buendía, F. Frömel, M.B. Wilms, R. Streubel, J. Tenkamp, T. Hupfeld, M. Nachev, E. Gökce, A. Weisheit, S. Barcikowski, F. Walther, J.H. Schleifenbaum, B. Gökce, Oxide dispersion-strengthened alloys generated by laser metal deposition of laser-generated nanoparticle-metal powder composites, *Mater. Des.* 154 (2018) 360–369, <https://doi.org/10.1016/j.matdes.2018.05.044>.
- [14] O. Abdulhameed, A. Al-Ahmari, W. Ameen, S.H. Mian, Additive manufacturing: challenges, trends, and applications, *Adv. Mech. Eng.* 11 (2019) 168781401882288, <https://doi.org/10.1177/1687814018822880>.
- [15] B. Cox, M. Ghayoor, R.P. Doyle, S. Pasebani, J. Gess, Numerical model of heat transfer during laser powder bed fusion of 316L stainless steel, *Int. J. Adv. Manuf. Technol.* 119 (2022) 5715–5725, <https://doi.org/10.1007/s00170-021-08352-0>.
- [16] C. Klahn, B. Leuteneker, M. Meboldt, Design for additive manufacturing – supporting the substitution of components in series products, *Procedia CIRP* 21 (2014) 138–143, <https://doi.org/10.1016/j.procir.2014.03.145>.
- [17] A. Hussein, L. Hao, C. Yan, R. Everson, P. Young, Advanced lattice support structures for metal additive manufacturing, *J. Mater. Process. Technol.* 213 (2013) 1019–1026, <https://doi.org/10.1016/j.jmatprotec.2013.01.020>.
- [18] G. Çam, Prospects of producing aluminum parts by wire arc additive manufacturing (WAAM), *Mater. Today: Proc.* 62 (2022) 77–85, <https://doi.org/10.1016/j.matpr.2022.02.137>.
- [19] Ö.S. Bölükbaşı, T. Serindag, U. Gürol, A. Günen, G. Çam, Improving oxidation resistance of wire arc additive manufactured Inconel 625 Ni-based superalloy by pack aluminizing, *CIRP Journal of Manufacturing Science and Technology* 46 (2023) 89–97, <https://doi.org/10.1016/j.cirpj.2023.07.011>.
- [20] U. Gürol, Y. Altınay, A. Günen, Ö.S. Bölükbaşı, M. Koçak, G. Çam, Effect of powder-pack aluminizing on microstructure and oxidation resistance of wire arc additively

- manufactured stainless steels, *Surf. Coating. Technol.* 468 (2023) 129742, <https://doi.org/10.1016/j.surfcoat.2023.129742>.
- [21] A. Günen, U. Gürol, M. Koçak, G. Çam, A new approach to improve some properties of wire arc additively manufactured stainless steel components: simultaneous homogenization and boriding, *Surf. Coating. Technol.* 460 (2023) 129395, <https://doi.org/10.1016/j.surfcoat.2023.129395>.
- [22] A. Günen, U. Gürol, M. Koçak, G. Çam, Investigation into the influence of boronizing on the wear behavior of additively manufactured Inconel 625 alloy at elevated temperature, *Prog Addit Manuf* 8 (2023) 1281–1301, <https://doi.org/10.1007/s40964-023-00398-8>.
- [23] F. Ceritbinmez, A. Günen, U. Gürol, G. Çam, A comparative study on drillability of Inconel 625 alloy fabricated by wire arc additive manufacturing, *J. Manuf. Process.* 89 (2023) 150–169, <https://doi.org/10.1016/j.jmapro.2023.01.072>.
- [24] N. Zhao, M. Parthasarathy, S. Patil, D. Coates, K. Myers, H. Zhu, W. Li, Direct additive manufacturing of metal parts for automotive applications, *J. Manuf. Syst.* 68 (2023) 368–375, <https://doi.org/10.1016/j.jmsys.2023.04.008>.
- [25] Z. Tian, C. Zhang, D. Wang, W. Liu, X. Fang, D. Wellmann, Y. Zhao, Y. Tian, A review on laser powder bed fusion of inconel 625 nickel-based alloy, *Appl. Sci.* 10 (2020) 81, <https://doi.org/10.3390/app10010081>.
- [26] S. Sanchez, P. Smith, Z. Xu, G. Gaspard, C.J. Hyde, W.W. Wits, I.A. Ashcroft, H. Chen, A.T. Clare, Powder Bed Fusion of nickel-based superalloys: a review, *Int. J. Mach. Tool Manuf.* 165 (2021) 103729, <https://doi.org/10.1016/j.ijmachtools.2021.103729>.
- [27] M. Avateffazeli, P.E. Carrion, B. Shachi-Amirkhiz, H. Pirgazi, M. Mohammadi, N. Shamsaei, M. Haghsheenas, Correlation between tensile properties, microstructure, and processing routes of an Al–Cu–Mg–Ag–TiB<sub>2</sub> (A205) alloy: additive manufacturing and casting, *Mater. Sci. Eng., A* 841 (2022) 142989, <https://doi.org/10.1016/j.msea.2022.142989>.
- [28] P. Krakhmalev, G. Fredriksson, K. Svensson, I. Yadroitsev, I. Yadroitsava, M. Thuvander, R. Peng, Microstructure, solidification texture, and thermal stability of 316 L stainless steel manufactured by laser powder bed fusion, *Metals* 8 (2018) 643, <https://doi.org/10.3390/met8080643>.
- [29] W. Abd-Elaziem, S. Elkattatny, A.-E. Abd-Elaziem, M. Khedr, M.A. Abd El-baky, M. A. Hassan, M. Abu-Okail, M. Mohammed, A. Järvenpää, T. Allam, A. Hamada, On the current research progress of metallic materials fabricated by laser powder bed fusion process: a review, *J. Mater. Res. Technol.* 20 (2022) 681–707, <https://doi.org/10.1016/j.jmrt.2022.07.085>.
- [30] J.J. Lewandowski, M. Seifi, Metal additive manufacturing: a review of mechanical properties, *Annu. Rev. Mater. Res.* 46 (2016) 151–186, <https://doi.org/10.1146/annurev-matsci-070115-032024>.
- [31] L. Thijs, K. Kempen, J.-P. Kruth, J. van Humbeeck, Fine-structured aluminium products with controllable texture by selective laser melting of pre-alloyed AlSi10Mg powder, *Acta Mater.* 61 (2013) 1809–1819, <https://doi.org/10.1016/j.actamat.2012.11.052>.
- [32] R. Xu, Z. Geng, Y. Wu, C. Chen, M. Ni, D. Li, T. Zhang, H. Huang, F. Liu, R. Li, K. Zhou, Microstructure and mechanical properties of in-situ oxide-dispersion-strengthened NiCrFeY alloy produced by laser powder bed fusion, *Advanced Powder Materials* 1 (2022) 100056, <https://doi.org/10.1016/j.apmat.2022.100056>.
- [33] T.M. Smith, C.A. Kantzos, N.A. Zarkevich, B.J. Harder, M. Heczko, P.R. Gradl, A. C. Thompson, M.J. Mills, T.P. Gabb, J.W. Lawson, A 3D printable alloy designed for extreme environments, *Nature* 617 (2023) 513–518, <https://doi.org/10.1038/s41586-023-05893-0>.
- [34] T.M. Smith, A.C. Thompson, T.P. Gabb, C.L. Bowman, C.A. Kantzos, Efficient production of a high-performance dispersion strengthened, multi-principal element alloy, *Sci. Rep.* 10 (2020) 9663, <https://doi.org/10.1038/s41598-020-66436-5>.
- [35] J.H. Martin, B.D. Yahata, J.M. Hundley, J.A. Mayer, T.A. Schaedler, T.M. Pollock, 3D printing of high-strength aluminium alloys, *Nature* 549 (2017) 365–369, <https://doi.org/10.1038/nature23894>.
- [36] H. Hadraba, Z. Chlup, A. Dlouhy, F. Dobes, P. Roupčova, M. Vilemova, J. Matejček, Oxide dispersion strengthened CoCrFeNiMn high-entropy alloy, *Mater. Sci. Eng., A* 689 (2017) 252–256, <https://doi.org/10.1016/j.msea.2017.02.068>.
- [37] A. Wasilkowska, M. Bartsch, U. Messerschmidt, R. Herzog, A. Czyrska-Filemonowicz, Creep mechanisms of ferritic oxide dispersion strengthened alloys, *J. Mater. Process. Technol.* 133 (2003) 218–224, [https://doi.org/10.1016/S0924-0136\(02\)00237-6](https://doi.org/10.1016/S0924-0136(02)00237-6).
- [38] J.U. Rakhmonov, C. Kenel, A. de Luca, C. Leinenbach, D.C. Dunand, Effect of Y<sub>2</sub>O<sub>3</sub> dispersoids on microstructure and creep properties of Hastelloy X processed by laser powder-bed fusion, *Additive Manufacturing Letters* 3 (2022) 100069, <https://doi.org/10.1016/j.addlet.2022.100069>.
- [39] J. Boes, A. Röttger, L. Becker, W. Theisen, Processing of gas-nitrided AISI 316L steel powder by laser powder bed fusion – microstructure and properties, *Addit. Manuf.* 30 (2019) 100836, <https://doi.org/10.1016/j.addma.2019.100836>.
- [40] L. Yu, Z. Lu, J. Xian, X. Chen, S. Peng, X. Li, H. Li, Effects of Al content on microstructure and tensile properties of Ni-based ODS superalloys, *J. Alloys Compd.* 941 (2023) 168965, <https://doi.org/10.1016/j.jallcom.2023.168965>.
- [41] J. Jang, T.K. Kim, C.H. Han, H.-K. Min, S.-H. Jeong, D.H. Kim, A preliminary development and characterization of Ni-based ODS alloys, *Procedia Eng.* 55 (2013) 284–288, <https://doi.org/10.1016/j.proeng.2013.03.255>.
- [42] P. Chen, C. Yang, S. Li, M.M. Attallah, M. Yan, In-situ alloyed, oxide-dispersion-strengthened CoCrFeMnNi high entropy alloy fabricated via laser powder bed fusion, *Mater. Des.* 194 (2020) 108966, <https://doi.org/10.1016/j.matdes.2020.108966>.
- [43] S. Mirzababaei, M. Ghayoor, R.P. Doyle, S. Pasebani, In-situ manufacturing of ODS FeCrAlY alloy via laser powder bed fusion, *Mater. Lett.* 284 (2021) 129046, <https://doi.org/10.1016/j.matlet.2020.129046>.
- [44] M. Li, Y. Guo, W. Li, Y. Zhang, Y. Chang, Property enhancement of CoCrNi medium-entropy alloy by introducing nano-scale features, *Mater. Sci. Eng., A* 817 (2021) 141368, <https://doi.org/10.1016/j.msea.2021.141368>.
- [45] J.H. Martin, B.D. Yahata, J.M. Hundley, J.A. Mayer, T.A. Schaedler, T.M. Pollock, 3D printing of high-strength aluminium alloys, *Nature* 549 (2017) 365–369, <https://doi.org/10.1038/nature23894>.
- [46] A. Elsayed, C. Haase, U. Krupp, Additive manufacturing of metal matrix nanocomposites: novel approach for nanoparticles dispersion by electromagnetic three-dimensional vibration, *Mater. Lett.* 344 (2023) 134399, <https://doi.org/10.1016/j.matlet.2023.134399>.
- [47] T. Horn, C. Rock, D. Kaoumi, I. Anderson, E. White, T. Prost, J. Rieken, S. Saptarshi, R. Schoell, M. DeJong, S. Timmins, J. Forrester, S. Lapidus, R. Napolitano, D. Zhang, J. Darsell, Laser powder bed fusion additive manufacturing of oxide dispersion strengthened steel using gas atomized reaction synthesis powder, *Mater. Des.* 216 (2022) 110574, <https://doi.org/10.1016/j.matdes.2022.110574>.
- [48] S. Saptarshi, M. deJong, C. Rock, I. Anderson, R. Napolitano, J. Forrester, S. Lapidus, D. Kaoumi, T. Horn, Laser powder bed fusion of ODS 14YWT from gas atomization reaction synthesis precursor powders, *JOM* 74 (2022) 3303–3315, <https://doi.org/10.1007/s11837-022-05418-6>.
- [49] D. Zhang, J.T. Darsell, J. Wang, X. Ma, G.J. Grant, I.E. Anderson, J.R. Rieken, D. J. Edwards, W. Setyawan, T.J. Horn, G.R. Odette, No ball milling needed: alternative ODS steel manufacturing with gas atomization reaction synthesis (GARS) and friction-based processing, *J. Nucl. Mater.* 566 (2022) 153768, <https://doi.org/10.1016/j.jnucmat.2022.153768>.
- [50] I.E. Anderson, J.C. Foley, Determining the role of surfaces and interfaces in the powder metallurgy processing of aluminum alloy powders, *Surf. Interface Anal.* 31 (2001) 599–608, <https://doi.org/10.1002/sia.1087>.
- [51] J.R. Rieken, I.E. Anderson, M.J. Kramer, G.R. Odette, E. Stergar, E. Haney, Reactive gas atomization processing for Fe-based ODS alloys, *J. Nucl. Mater.* 428 (2012) 65–75, <https://doi.org/10.1016/j.jnucmat.2011.08.015>.
- [52] J.-P. Roth, I. Šulák, T. Kruml, W. Polkowski, T. Dudziak, P. Böhlke, U. Krupp, K. Jahns, establishing a novel process route for additive manufacturing of NiCu-based Alloy 400 – an alignment of gas atomization, laser powder bed fusion and design of experiments, *SSRN*, <https://doi.org/10.2139/ssrn.4537351>.
- [53] R.L. Meltzer, Y.R. Fiorini, R.T. Horstman, I.C. Moore, A.L. Batik, T. Hostinsky, J. adek, A constant tensile stress creep testing machine, *J. Test. Eval.* 4 (1976) 26, <https://doi.org/10.1520/JTE10503J>.
- [54] S. Sendino, S. Martinez, A. Lamikiz, Characterization of IN718 recycling powder and its effect on LPBF manufactured parts, *Procedia CIRP* 94 (2020) 227–232, <https://doi.org/10.1016/j.procir.2020.09.043>.
- [55] J. Sun, M. Guo, K. Shi, D. Gu, Influence of powder morphology on laser absorption behavior and printability of nanoparticle-coated 90W-Ni-Fe powder during laser powder bed fusion, *Mater Sci Add Manuf* 1 (2022), <https://doi.org/10.18063/msam.v1i2.11>.
- [56] J. Zegzulka, D. Gelnar, L. Jezerska, R. Prokes, J. Rozbroj, Characterization and flowability methods for metal powders, *Sci. Rep.* 10 (2020) 21004, <https://doi.org/10.1038/s41598-020-77974-3>.
- [57] T. Liu, J.D. Leazer, S.K. Menon, L.N. Brewer, Microstructural analysis of gas atomized Al-Cu alloy feedstock powders for cold spray deposition, *Surf. Coating. Technol.* 350 (2018) 621–632, <https://doi.org/10.1016/j.surfcoat.2018.07.006>.
- [58] Z. Erdélyi, C. Girardeaux, Z. Tökei, D.L. Beke, C. Cserhádi, A. Rolland, Investigation of the interplay of nickel dissolution and copper segregation in Ni/Cu(111) system, *Surf. Sci.* 496 (2002) 129–140, [https://doi.org/10.1016/S0039-6028\(01\)01571-0](https://doi.org/10.1016/S0039-6028(01)01571-0).
- [59] A.R. Naghash, T.H. Etsell, S. Xu, XRD and XPS study of Cu–Ni interactions on reduced Copper–Nickel–Aluminum oxide solid solution catalysts, *Chem. Mater.* 18 (2006) 2480–2488, <https://doi.org/10.1021/cm051910o>.
- [60] E. Pellicer, A. Varea, K.M. Sivaraman, S. Pané, S. Suriñach, M.D. Baró, J. Nogués, B. J. Nelson, J. Sort, Grain boundary segregation and interdiffusion effects in nickel-copper alloys: an effective means to improve the thermal stability of nanocrystalline nickel, *ACS Appl. Mater. Interfaces* 3 (2011) 2265–2274, <https://doi.org/10.1021/am2004587>.
- [61] J. Rieken, I. Anderson, M. Kramer, *Innovative Powder Processing of Oxide Dispersion Strengthened ODS Ferritic Stainless Steels*, 2011.
- [62] J. Rieken, Gas Atomized Precursor Alloy Powder for Oxide Dispersion Strengthened Ferritic Stainless Steel 2011, 2011, <https://doi.org/10.2172/1048516>.
- [63] T. de Terris, O. Andreau, P. Peyre, F. Adamski, I. Koutiri, C. Gorny, C. Dupuy, Optimization and comparison of porosity rate measurement methods of Selective Laser Melted metallic parts, *Addit. Manuf.* 28 (2019) 802–813, <https://doi.org/10.1016/j.addma.2019.05.035>.
- [64] S. Shrestha, T. Starr, K. Chou, A study of keyhole porosity in selective laser melting: single-track scanning with micro-CT analysis, *J. Manuf. Sci. Eng.* 141 (2019), <https://doi.org/10.1115/1.4043622>.
- [65] D.S. Ertay, H. Ma, M. Vlasea, *Correlative Beam Path and Pore Defect Space Analysis for Modulated Powder Bed Laser Fusion Process*, University of Texas at Austin, 2018.
- [66] A. Ulbricht, G. Mohr, S.J. Altenburg, S. Oster, C. Maierhofer, G. Bruno, Can potential defects in LPBF Be healed from the laser exposure of subsequent layers? A Quantitative Study, *Metals* 11 (2021) 1012, <https://doi.org/10.3390/met11071012>.

- [67] T. Hatakeyama, K. Sawada, M. Suzuki, M. Watanabe, Microstructure development of modified 9Cr-1Mo steel during laser powder bed fusion and heat treatment, *Addit. Manuf.* 61 (2023) 103350, <https://doi.org/10.1016/j.addma.2022.103350>.
- [68] H. Qin, V. Fallah, Q. Dong, M. Brochu, M.R. Daymond, M. Gallerneault, Solidification pattern, microstructure and texture development in Laser Powder Bed Fusion (LPBF) of Al10SiMg alloy, *Mater. Char.* 145 (2018) 29–38, <https://doi.org/10.1016/j.matchar.2018.08.025>.
- [69] C. Li, R. White, X.Y. Fang, M. Weaver, Y.B. Guo, Microstructure evolution characteristics of Inconel 625 alloy from selective laser melting to heat treatment, *Mater. Sci. Eng., A* 705 (2017) 20–31, <https://doi.org/10.1016/j.msea.2017.08.058>.
- [70] S. Pilz, T. Gustmann, F. Günther, M. Zimmermann, U. Kühn, A. Gebert, Controlling the Young's modulus of a  $\beta$ -type Ti-Nb alloy via strong texturing by LPBF, *Mater. Des.* 216 (2022) 110516, <https://doi.org/10.1016/j.matdes.2022.110516>.
- [71] L. Zou, C. Yang, Y. Lei, D. Zakharov, J.M.K. Wiezorek, D. Su, Q. Yin, J. Li, Z. Liu, E. A. Stach, J.C. Yang, L. Qi, G. Wang, G. Zhou, Dislocation nucleation facilitated by atomic segregation, *Nat. Mater.* 17 (2018) 56–63, <https://doi.org/10.1038/nmat5034>.
- [72] X.X. Zhang, H. Andrä, S. Harjo, W. Gong, T. Kawasaki, A. Lutz, M. Lahres, Quantifying internal strains, stresses, and dislocation density in additively manufactured AlSi10Mg during loading-unloading-reloading deformation, *Mater. Des.* 198 (2021) 109339, <https://doi.org/10.1016/j.matdes.2020.109339>.
- [73] T. Voisin, J.-B. Forien, A. Perron, S. Aubry, N. Bertin, A. Samanta, A. Baker, Y. M. Wang, New insights on cellular structures strengthening mechanisms and thermal stability of an austenitic stainless steel fabricated by laser powder-bed-fusion, *Acta Mater.* 203 (2021) 116476, <https://doi.org/10.1016/j.actamat.2020.11.018>.
- [74] D. Kong, C. Dong, S. Wei, X. Ni, L. Zhang, R. Li, L. Wang, C. Man, X. Li, About metastable cellular structure in additively manufactured austenitic stainless steels, *Addit. Manuf.* 38 (2021) 101804, <https://doi.org/10.1016/j.addma.2020.101804>.
- [75] K.M. Bertsch, G. Meric de Bellefon, B. Kuehl, D.J. Thoma, Origin of dislocation structures in an additively manufactured austenitic stainless steel 316L, *Acta Mater.* 199 (2020) 19–33, <https://doi.org/10.1016/j.actamat.2020.07.063>.
- [76] E.B. Clatworthy, S. Yick, A.T. Murdock, M.C. Allison, A. Bendavid, A.F. Masters, T. Maschmeyer, Enhanced photocatalytic hydrogen evolution with TiO<sub>2</sub>-TiN nanoparticle composites, *J. Phys. Chem. C* 123 (2019) 3740–3749, <https://doi.org/10.1021/acs.jpcc.8b09221>.
- [77] A. Alvarez Barragan, N.V. Ilawe, L. Zhong, B.M. Wong, L. Mangolini, A non-thermal plasma route to plasmonic TiN nanoparticles, *J. Phys. Chem. C* 121 (2017) 2316–2322, <https://doi.org/10.1021/acs.jpcc.6b08910>.
- [78] U. Guler, S. Suslov, A.V. Kildishev, A. Boltasseva, V.M. Shalaev, Colloidal plasmonic titanium nitride nanoparticles: properties and applications, *Nanophotonics* 4 (2015) 269–276, <https://doi.org/10.1515/nanoph-2015-0017>.
- [79] J. Tavares, S. Coulombe, J.-L. Meunier, Synthesis of cubic-structured monocrystalline titanium nitride nanoparticles by means of a dual plasma process, *J. Phys. D Appl. Phys.* 42 (2009) 102001, <https://doi.org/10.1088/0022-3727/42/10/102001>.
- [80] C. Gao, Z. Wang, Z. Xiao, D. You, K. Wong, A.H. Akbarzadeh, Selective laser melting of TiN nanoparticle-reinforced AlSi10Mg composite: microstructural, interfacial, and mechanical properties, *J. Mater. Process. Technol.* 281 (2020) 116618, <https://doi.org/10.1016/j.jmatprotec.2020.116618>.
- [81] J. Cadek, Creep in metallic materials, in: *Materials Science Monographs*, 1988.

**7.3 The dispersion-strengthening effect of TiN nanoparticles evoked by ex situ nitridation of gas-atomized, NiCu-based Alloy 400 in fluidized bed reactor for laser powder bed fusion**

**Jan-Philipp Roth**, Ivo Šulák, Markéta Gálíková, Antoine Duval, Germain Boissonnet, Fernando Pedraza, Ulrich Krupp, Katrin Jahns






Journal of Manufacturing and Materials Processing 8 (2024) 223

DOI 10.3390/jmmp8050223

Reference [3]

Article

# The Dispersion-Strengthening Effect of TiN Nanoparticles Evoked by Ex Situ Nitridation of Gas-Atomized, NiCu-Based Alloy 400 in Fluidized Bed Reactor for Laser Powder Bed Fusion

Jan-Philipp Roth <sup>1,\*</sup> , Ivo Šulák <sup>2</sup> , Markéta Gálíková <sup>2,3</sup> , Antoine Duval <sup>4</sup>, Germain Boissonnet <sup>4</sup> , Fernando Pedraza <sup>4</sup> , Ulrich Krupp <sup>5</sup> and Katrin Jahns <sup>1</sup>

<sup>1</sup> Faculty of Engineering and Computer Science, Osnabrück University of Applied Sciences, 49076 Osnabrück, Germany; k.jahns@hs-osnabrueck.de

<sup>2</sup> Institute of Physics of Materials, Czech Academy of Sciences, 61600 Brno, Czech Republic; sulak@ipm.cz (I.Š.); galikova@ipm.cz (M.G.)

<sup>3</sup> CEITEC—Central European Institute of Technology, Brno University of Technology, 62100 Brno, Czech Republic

<sup>4</sup> Laboratoire des Sciences de l'Ingénieur Pour l'Environnement (LaSIE), Université de La Rochelle, 17042 La Rochelle, France; antoine.duval@univ-lr.fr (A.D.); germain.boissonnet@univ-lr.fr (G.B.); fpedraza@univ-lr.fr (F.P.)

<sup>5</sup> Steel Institute IEHK, RWTH Aachen University, 52072 Aachen, Germany; krupp@iehk.rwth-aachen.de

\* Correspondence: j.roth@hs-osnabrueck.de

**Abstract:** Throughout recent years, the implementation of nanoparticles into the microstructure of additively manufactured (AM) parts has gained great attention in the material science community. The dispersion strengthening (DS) effect achieved leads to a substantial improvement in the mechanical properties of the alloy used. In this work, an ex situ approach of powder conditioning prior to the AM process as per a newly developed fluidized bed reactor (FBR) was applied to a titanium-enriched variant of the NiCu-based Alloy 400. Powders were investigated before and after FBR exposure, and it was found that the conditioning led to a significant increase in the TiN formation along grain boundaries. Manufactured to parts via laser-based powder bed fusion of metals (PBF-LB/M), the ex situ FBR approach not only revealed a superior microstructure compared to unconditioned parts but also with respect to a recently introduced in situ approach based on a gas atomization reaction synthesis (GARS). A substantially higher number of nanoparticles formed along cell walls and enabled an effective suppression of dislocation movement, resulting in excellent tensile, creep, and fatigue properties, even at elevated temperatures up to 750 °C. Such outstanding properties have never been documented for AM-processed Alloy 400, which is why the demonstrated FBR ex situ conditioning marks a promising modification route for future alloy systems.

**Keywords:** Alloy 400; fluidized bed reactor; laser powder bed fusion; internal nitridation; TiN nanoparticle; dispersion strengthening



**Citation:** Roth, J.-P.; Šulák, I.; Gálíková, M.; Duval, A.; Boissonnet, G.; Pedraza, F.; Krupp, U.; Jahns, K. The Dispersion-Strengthening Effect of TiN Nanoparticles Evoked by Ex Situ Nitridation of Gas-Atomized, NiCu-Based Alloy 400 in Fluidized Bed Reactor for Laser Powder Bed Fusion. *J. Manuf. Mater. Process.* **2024**, *8*, 223. <https://doi.org/10.3390/jmmp8050223>

Academic Editor: Hamed Asgari

Received: 4 September 2024

Revised: 27 September 2024

Accepted: 29 September 2024

Published: 2 October 2024



**Copyright:** © 2024 by the authors. Licensee MDPI, Basel, Switzerland. This article is an open access article distributed under the terms and conditions of the Creative Commons Attribution (CC BY) license (<https://creativecommons.org/licenses/by/4.0/>).

## 1. Introduction

For many industries, such as the energy, maritime, and chemistry sectors, the fcc solid solution Ni-30Cu-based Alloy 400 (Monel 400) is the material of choice [1,2]. Here, the alloy finds its application as heat exchangers, feedwater/steam-containing heater tubes, reinforcements of offshore installations, and evaporators in both oxidizing (e.g., nitric acid) and reducing (e.g., alkaline salts, phosphoric acid) environments, even at higher temperatures [2–5]. Alloy 400 consists of approximately two-thirds of Ni, one-third of Cu, and, in small and decreasing proportion, Fe, Si, Mn, Al, and C. Similar alloys used for alternative applications are the related age-hardenable K500 (rather used as a high-strength variant for freshwater- and seawater-related corrosion) and the binary Ni-50Cu (enhanced stability during metal dusting in carburizing atmospheres) [2,3,6]. Hence, incorporating



further benefits in a strengthened Alloy 400 variant to withstand the harsh environments of the various demanding sectors while not losing its characteristic properties is considered an urgent need. In utilizing the respective benefits of additive manufacturing and the dispersion-strengthening effect, such superior parts could be produced and, thus, product lifetimes extended [7,8]. This idea was elaborated in a previous work [9] based on a gas atomization reaction synthesis [10–13]. Designing a modified Alloy 400 that exceeds the good properties reached via the GARS method is the main aim of this study.

Additive manufacturing still reveals plenty of drawbacks when compared to conventional fabrication: investment costs are comparatively high, geometrical precision is often lacking, and, due to the high cooling rates during solidification, immense induced residual stresses occur [14,15]. Also, the process-related anisotropy in the build direction is difficult to avoid or compensate for [16–18]. Yet, the advantages of this manufacturing route are manifold. For instance, since there is no need for geometry-specific tools and consecutive manufacturing steps, the part costs are very low for small and medium batch sizes, allowing for many different product variants of near-net shape (customization for free) [14,16,19]. Also, as three-dimensional tasks are divided into two-dimensional layers, the costs per part are independent of its complexity (complexity for free), which is why the design can iteratively be adjusted at no extra costs [14,16,20]. Besides economic benefits, there are also specific advantages concerning the microstructural condition of the manufactured part as it can be tailored to its specific need. Here, an AM technique of special interest for the material design of Ni-based materials is the laser-based powder bed fusion of metals (PBF-LB/M as per standard DIN EN ISO/ASTM 52900), also frequently referred to as laser powder bed fusion (LPBF), an iterative and selective micro-welding process of a powder bed resulting in a layer-wise solidified part [21–24]. Via LPBF, a controlled and consistent solidification of the melt pool to fine grains throughout the whole geometry can be achieved [25]. Also, it allows for printed parts with a relatively high-resolution surface quality [21]. Most importantly, LPBF allows for the processing of nanoparticle (NP)-reinforced powder feedstocks, as intended throughout this work as well [7,25,26].

A current, very promising approach at the intersection of materials science and AM is the homogenous introduction of such nanoparticles on the sub-grain level, enabling for equiaxed grains and, thus, restricting anisotropy as normally present with production-related columnar grains [7,25]. The intention is to enhance the mechanical performance of these dispersion-strengthened alloy systems due to dislocation pinning or climbing (Orowan mechanism) at the respective NPs when under load [7,26,27]. Moreover, NP dispersion strengthening can be considered a very effective strengthening mechanism as the NPs are not only beneficial to the material performance themselves but also come with some indirect effects. For instance, they act as nuclei for a more pronounced growth of fine grains during the LPBF liquid–solid phase transformation, which in turn restricts cracking and increases mechanical performance [8,28,29]. Another result is strengthening due to a high number of grain boundaries (GB) and a more pronounced geometrically necessary dislocation (GND) formation [8,30]. As an ultimate result, NP-strengthened alloys exhibit higher static strength, such as an enhanced ultimate tensile strength associated with longer fatigue and creep lifetime, as adequately reported in the literature, even within an increased temperature regime [7,31–35]. The underlying mechanism of evoking NPs is related to the free energy of formation in reactive atmospheres [31,36–38]. Considering the components of the modified Alloy 400 and in accordance with the respective Gibbs free energy over the entire temperature range, TiN is the most likely candidate for NP emergence, with  $\text{Al}_2\text{O}_3$  being considered a possible one as well although to a much lesser extent, as the experiments were carried out in non-oxidizing argon and nitrogen atmospheres, respectively.

A preceding work [9] introduced the topic of TiN NP modification of the present Alloy 400 during nitrogen gas atomization, which is referred to as *in situ*, as the nitridation occurs during the liquid–solid phase transition of the melt to powders during atomization. It was demonstrated that Alloy 400 GARS is a feasible concept for providing a TiN-enriched, well-processible powder feedstock for laser powder bed fusion, which in turn results in

an even more pronounced nanoparticle formation in additively manufactured parts. The in situ processed alloy led to a comparable mechanical performance to conventionally fabricated reference material and outperformed the unmodified LPBF material in terms of tensile and creep properties. Still, to reduce porosity issues and increase the NP content in as-built parts even further, a new kind of TiN-enriched material could potentially surpass the performance of the conventional counterpart. For instance, Tjong demonstrated that increasing the  $\text{Al}_2\text{O}_3$  NP volume percentage in an Al composite material from 1% up to 4% would result in a steadily increasing yield and tensile strength [39]. Therefore, this research focuses on a novel treatment of Alloy 400 powders resulting from standard vacuum inert gas atomizations (VIGA) in close-coupled atomization (CCA) mode and a subsequent modification of the powders in a fluidized bed reactor. During this process, the powder is set to a nitrogen atmosphere to allow for the formation of TiN NPs at a high quantity, detached from the atomization process. Hence, as the phase transformation and the nitridation of powders are divided into successive sections, this approach is referred to as ex situ. Results of this new powder preparation approach are accompanied by a comparison between both modification routes, the in situ one and the ex situ one, and their respective peculiarities are set in relation and also against the background of unmodified LPBF-processed material. Table 1 provides an initial overview of the key distinguishing features between the in situ and the ex situ approaches. The latter is further split up into the pre (atomized but no FBR) and the post (both atomized and FBR) states.

**Table 1.** Comparison of the in situ and ex situ nitridation approaches for Alloy 400.

	In Situ Nitridation [9]	Pre-FBR Ex Situ Nitridation [This Work, Sections 3.1 and 3.3]	Post-FBR Ex Situ Nitridation [This Work, Sections 3.2–3.4]
Atomization type	GARS (nitrogen) CCA	Shielding gas (argon) CCA	-
Post-treatment	-	-	FBR (nitrogen)
Targeted NPs in powder	TiN	None	TiN
Targeted NPs in LPBF part	TiN	None	TiN

## 2. Materials and Methods

### 2.1. Gas Atomization

The LPBF powder feedstock was generated via gas atomization with an AUG1000HTC atomizer (Blue Power/Indutherm) under a full inert gas atmosphere (argon) present in both the spray tower and the melting chamber. Bulky material consisting of pure elements and binary pre-alloys was molten in an alumina crucible via induction heating of a surrounding graphite crucible. The chemical composition of standard Alloy 400 (approx. 65.0 wt.-% Ni, 31.5 wt.-% Cu, 2.0 wt.-% Fe, 1.0 wt.-% Mn, 0.2 wt.-% Si, 0.2 wt.-% Al, 0.1 wt.-% C) was enriched with titanium in the form of a CuTi30 pre-alloy. The liquidus temperature for Alloy 400 + Ti was calculated at approximately 1350 °C, and an overheating of ~300 °C was applied, adding up to an atomization temperature of 1650 °C. A close-coupled setup was applied, meaning that the melt was atomized to powder right after flowing out of the crucible nozzle, which allows for a narrow, fine particle size distribution and thus increases the yield of usable powder. Besides overheating, a 5 min holding at atomization temperature was applied to homogenize the alloy and to allow for a sufficiently low viscosity of the melt, leading to a smooth flow during atomization. Powders were further processed via sieving and air-classifying in order to adjust the intended final particle size distribution (PSD) for LPBF in the range between 15 µm and 63 µm. For this purpose, a sieving unit (Russell/EOS) and an air classifier AC1000G (Blue Power/Indutherm) were operated. Dynamic image analysis (Camsizer X2) was applied to verify the obtained PSD and to adjust the classifier parameters accordingly.

## 2.2. Fluidized Bed Reactor

The fluidized bed reactor process is a newly developed method of the LaSIE laboratory, University of La Rochelle, France (patent number: FR2311060), and it causes both surface and internal nanoparticle formation in metal matrix powders. A gas flow is introduced from the bottom of the plenum, which homogenizes and heats the gas before it contacts the micro-sized metal particles. The latter are retained by a porous filter plate through which the gas blows up the particles (Figure 1). During the exposure of the base alloy to the nitriding gas composition at high temperatures, nitridation of the more reactive elements occurs from the surface to the core of the metal particle following a diffusion-controlled mechanism. Therefore, the longer the exposure, the deeper the NP formation occurs in the metal powders. Ultimately, the efficiency of the process depends on several parameters, such as:

- The chemical composition of the powder and the gas: reactive elements with preferably low free energy of formation result in a high number of NPs,
- The initial particle size distribution of the powders: the coarser the powder, the longer it takes for the internal NP formation to fully occur throughout the whole particle,
- Their shape, sphericity and density: highly spherical and dense particles allow for homogeneous gas penetration,
- The temperature applied to the chamber: high diffusion rates correlate with increasing temperature, while disintegration of the particles due to tremendous heat exposure must be avoided.

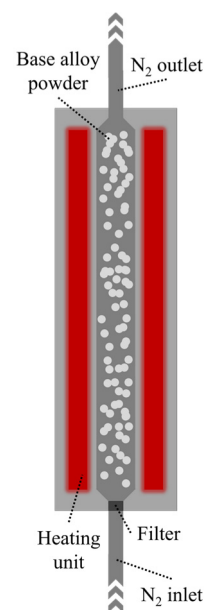


**Figure 1.** Fluidized bed reactor with nitrogen gas stream, heating unit, and exposed powder.

As a result of a preliminary feasibility study, several FBR process parameter sets were tested in the temperature range of 600 °C to 800 °C at different durations. Here, it was found to be most effective to apply a temperature of 800 °C under a pure nitrogen gas flow of 1.2 L/min over 4 h to the exposed Alloy 400 powders. The heating and cooling process steps were regulated with an argon gas flow.

## 2.3. Laser Powder Bed Fusion

After atomization and FBR exposure, the powders were used as the LPBF feedstock. For manufacturing, an EOS M290 customized by AMCM was operated, providing several peculiarities for AM material qualification. The laser system operated at a comparably low wavelength of 532 nm (green laser source) to allow for more effective energy incorporation



into the reflective material. It also had a heated build platform of 10 cm in diameter for small powder batches. During manufacturing, a constant heating of 80 °C as well as a layer height of 0.02 mm were applied. The laser traveled according to a rotating scanning strategy (67°) in between layers. The system was fully pressured with argon shielding gas. The parameters were laser power ( $p_L$ ), scanning speed ( $s_S$ ), and hatch distance ( $d_H$ ). For parameter optimization, previously found start values of  $p_L = 85$  W,  $s_S = 1050$  mm/s, and  $d_H = 50$   $\mu$ m were set and further varied to obtain highly dense parts [9]. In the M290 system, the following components were manufactured during this study:

- Cubes ( $8 \times 8 \times 8$  mm<sup>3</sup>) for optical density measurements (VDI 3405-2), hardness testing (DIN EN ISO 6507-1), and part characterization;
- Blocks ( $14 \times 45 \times 70$  mm<sup>3</sup>) for subsequent machining of tensile, fatigue, and creep specimens:
  - o Tensile and fatigue specimens resulted from  $M6 \times 40$  mm cylinders and revealed a final test area of  $\varnothing 3$  mm  $\times$  9 mm (see [40,41] for sample illustration);
  - o Creep specimens were obtained from  $41 \times 14 \times 3.2$  mm<sup>3</sup> cuboids and machined to a test area of  $25 \times 4 \times 3.2$  mm<sup>3</sup> (see [40,41] for sample illustration);
- Cylinders ( $\varnothing 10$  mm  $\times$  50 mm) for thermal diffusivity testing.

#### 2.4. Testing and Characterization

Vickers hardness measurements were performed on as-printed surfaces and averaged (Innovatest Falcon 500). Cubes for optical density determination via light optical microscopy were first ground (2500 grit SiC) and then further polished (0.02  $\mu$ m colloidal SiO<sub>2</sub> suspension) for scanning electron microscopy (SEM) investigations. For SEM characterization, a Zeiss Auriga system was operated, and chemical compositions of the various powder and part states were examined via energy dispersive x-ray spectroscopy (EDS). Electron backscattered diffraction (EBSD) was used for grain and dislocation evolution characterization. High-resolution characterization on the nanoscale was performed by utilizing a Talos F200i transmission electron microscope (TEM) at an acceleration voltage of 200 kV with a built-in bright field detector, facilitating the operation in scanning mode (STEM). TEM samples (thin lamellae) were generated via focused (Ga)<sup>+</sup> ion beam milling (FIB) in SEM and micro-welded to an omniprobe grid (see [9] for the standard lamella preparation procedure). For mechanical investigations, a universal electromechanical tensile machine Zwick Z50, a servo-hydraulic fatigue testing system MTS810 [40], and a self-designed creep machine [42] were operated. The thermal diffusivity was determined using high-temperature laser-flash measurements with a Linseis LFA1600 apparatus at low pressure ( $\sim 10^{-2}$  mbar) and at 100 °C intervals between room temperature and 900 °C. Three coupon samples ( $\varnothing 10$  mm, 2 mm thick) per modification of Alloy 400 were measured simultaneously to give the average value reported. Prior to the measurements with the laser flash, the thicknesses of the samples were accurately determined ( $\sim 10^{-3}$  mm) with a digital caliper. All samples were then coated on both sides with a 4–5  $\mu$ m graphite layer to increase the absorption of the laser pulse at the rear surface as well as the emissivity of the heat signal for the measurement by the InSb infrared detector on the front face of the sample.

### 3. Results and Discussion

#### 3.1. Pre-FBR: Inert Gas Atomization, Powder Post-Processing, and Powder Characterization

##### 3.1.1. Atomization Process

In total, three atomizations were carried out to generate a sufficient powder feedstock for subsequent fluidized bed reactor exposure. One of the atomizations is exemplarily illustrated in Figure 2; the current set temperature (orange), the actual temperatures in the closure rod (center of crucible, grey), and the crucible wall (yellow), as well as the oxygen content in the melting chamber (blue, resolution of the sensor: 1 ppm), changed constantly throughout approximately 160 min of heating. At the start of the heating procedure, the

final temperature was set to 1650 °C. For ten minutes, a gas purging and testing cycle was activated. As can be seen from the blue line, the oxygen content fell from ~20,000 ppm to a value of almost 0 ppm during this cycle and remained at this level for the rest of the heating and atomization procedure. It is important to mention that the oxygen level inside the atomization tower was constantly kept at nearly 0 ppm as well. Hence, oxide formation in the liquid state with the alloying elements was prevented. Right after the initializing cycle (green circle), the set temperature rose from 100 °C to 1650 °C after 120 min post-launch. Accordingly, the yellow line indicating the actual temperature inside the crucible wall rose. This line runs linearly as the induction is constantly incorporating heat into the crucible. For the temperature measured in the middle of the crucible (grey line, inside the closure rod), a different slope was observed. For temperatures < 1080 °C (black circle), it rose constantly (left turn), while for temperatures > 1080 °C, it fell constantly (right turn). The reason can be found in the respective melting temperatures of the elements and pre-alloys, with copper as a major ingredient of the alloy and a liquidus of approximately 1080 °C. Pure copper and copper-based pre-alloys passed through the solid–liquid phase transformation here. Hence, the induced energy was only slightly transferred to further heat the system, while a considerable portion acted as a phase converter [43]. With further high-melting elements in the alloy, the slope decreased even further until reaching the desired atomization temperature of 1650 °C (purple circle). Ultimately, when releasing the closure rod after a short holding time, thus initiating the atomization process, the pressure amounted to 9 bar with a gas stream of nearly 180 Nm<sup>3</sup>/h, resulting in a melt mass stream of approximately 2.2 kg/min. Consequently, set and actual temperatures fell to room temperature. Atomized powders were then post-processed.

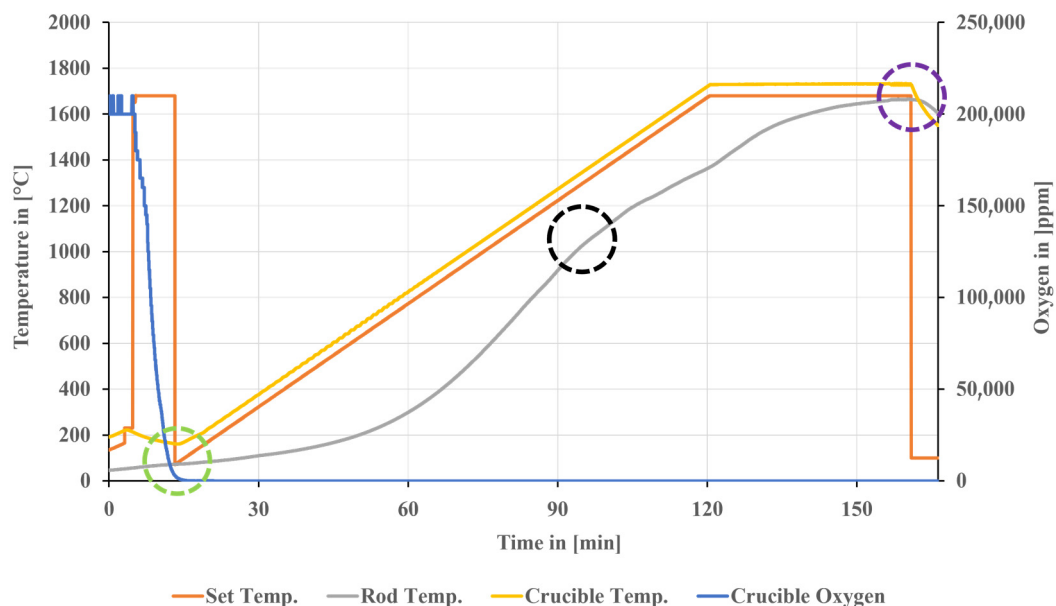


**Figure 2.** Temperature and oxygen gradients during the pre-atomization heating cycle.

### 3.1.2. Powder Post-Processing and Pre-FBR Powder Surface Characterization

After cooling down to RT, the powders were post-processed by means of removal of the coarse and fine fractions by sieving and air separation, respectively. The resulting final fraction usable for LPBF revealed both a satisfactory bulk density of ~4.3 g/cm<sup>3</sup> and a flowability of ~14.5 s/50 g. The characteristic particle size distribution was determined as per  $d_{10} = 21.3 \mu\text{m}$ ,  $d_{50} = 37.9 \mu\text{m}$ , and  $d_{90} = 58.1 \mu\text{m}$ , fitting very well into the targeted range of 15–63  $\mu\text{m}$ . This way, no particles were too fine or coarse, and thus, restricting LPBF processability was part of the powder feedstock that would be further modified by means of the fluidized bed reactor. Moreover, the sphericity of single particles was determined to be 0.816 on average and only slight satellite formation (Figure 3a), unavoidably occurring

during VIGA, was found but was acceptable for further processing [44,45]. Considerably higher sphericities could be reached via the application of ultrasonic atomization [46]. However, recoatability during PBF-LB/M is still ensured with these powders, and besides, VIGA allows for remarkably higher yields and industrial scalability than other atomization techniques. Remarkably, even though the atomization was performed under an argon atmosphere, and thus nitrogen uptake should have been suppressed, titanium nanoparticles formed on the surface of powders, as can be seen in Figure 3c,d. It is evident that the NPs primarily formed along surface grain boundaries in the interdendritic region (Figure 3b) linked to the segregation behavior of NiCu alloys (Figure 4d,e) [47–49]. Considering (i) the characteristic cuboidal shape and (ii) the results of accompanying Ti-EDS mapping (Figure 3e), the particles formed can be classified as titanium nitrides [9,50–53]. This leads to the assumption that a marginal proportion of nitrogen remained inside the atomizer even though the system was pressured with shielding gas for over ~2.5 h. Due to the very low free energy of formation/high reactivity of titanium and nitrogen, these few ppm N would be sufficient in order to form a remarkable quantity of TiN NPs in these powders per the reaction equation  $2 \text{Ti} + \text{N}_2 \rightarrow 2 \text{TiN}$ . More precisely, the NP share was determined as per 0.96% in Figure 3c. Even though unexpected, this is assumed to be only beneficial for the further processing of the powders during FBR conditioning. Furthermore, it can be concluded from the EDS mapping that elemental Ti is present all over the particle as well. Hence, most of the Ti is dissolved in the NiCu-based solid solution still and not solely within the TiN. By exposure to the nitrogen stream during FBR, a considerable part of the remaining Ti share in the solid solution can thus act as nuclei for a more pronounced TiN formation and an increase in NP quantity.

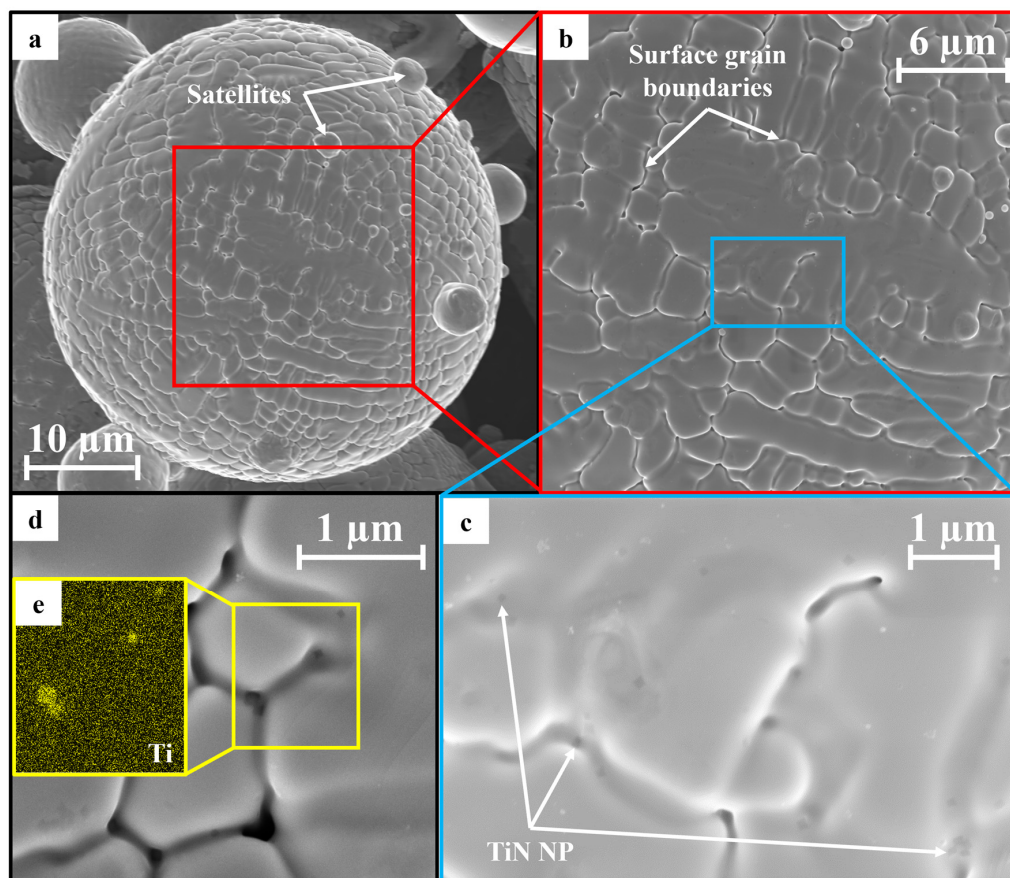


**Figure 3.** Pre-FBR particle surface SEM characterization revealing (a) satellite formation, (b) pronounced surface dendrite formation, (c) the presence of TiN NPs on GB, (d,e) a Ti-EDS-mapping on a GB intersection.



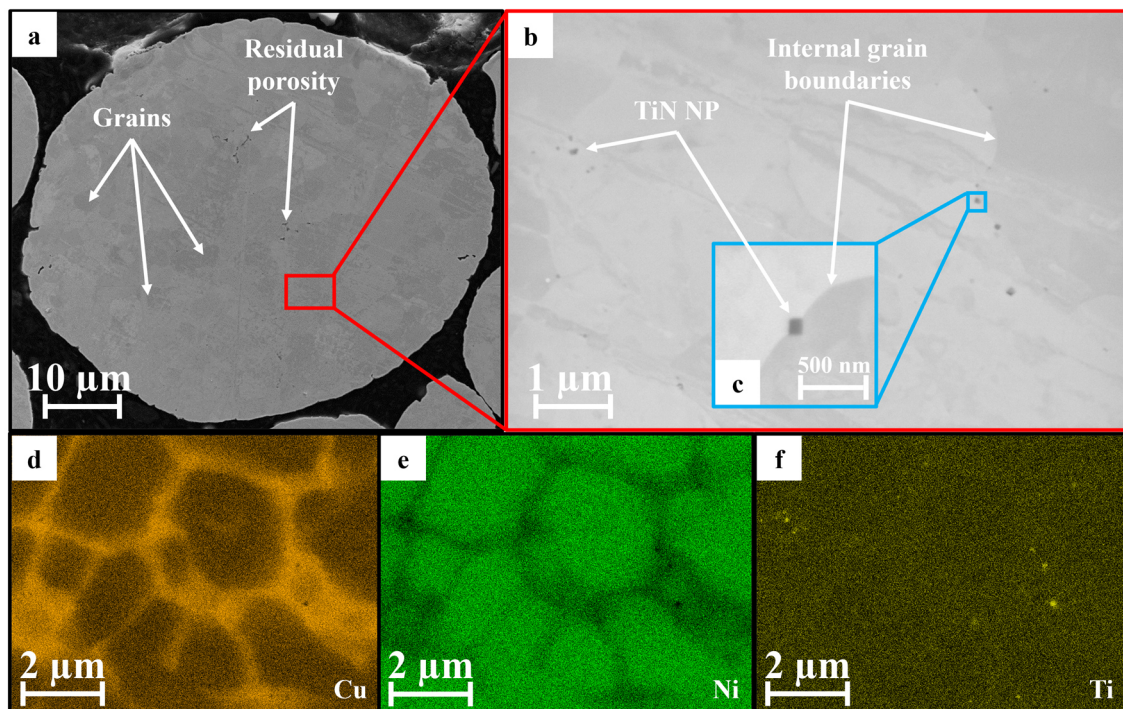


**Figure 4.** Pre-FBR particle cross-section SEM characterization revealing (a) residual porosity, (b) the presence of TiN NPs on GB, (c) a magnification of a single TiN NP, (d–f) accompanying Cu-/Ni-/Ti-EDS mappings of (b).

### 3.1.3. Pre-FBR Powder Cross-Section Characterization

From the perspective of achieving a TiN formation on the surface, the assumption arose that TiN would also have formed on the inside of these particles during atomization. By examining the cross section, porosity was detected (see Figure 4a). However, slight residual pore formation is inevitable for gas-atomized metallic powders and is not seen as critically hindering the subsequent LPBF process [54–56]. Equally distributed over the whole cross-section, TiN was detected aligning to internal grain boundaries, representing an NP share of ~0.22% on average (Figure 4b). Thus, from the pre-FBR powder SEM characterization, it can already be concluded that both the surface (pre-FBR ex situ: 0.96%; in situ: 0.12%) and the cross-section (pre-FBR ex situ: 0.22%; in situ: 0.13%) NP concentration is more pronounced than via the GARS approach [9]. At higher magnification (Figure 4c), the characteristic morphology was highlighted in greater detail for a nanoparticle of approx. 100 nm edge length. It can be observed that it is located right in the middle of two colliding grains. The corresponding Cu- and Ni-EDS mappings (Figure 4d,e) provide further information on the well-known Cu segregation phenomenon on grain boundaries of the interdendritic region [47–49]. It can be clearly seen that Cu was predominantly present at GB, while Ni was rather present within the grains. Moreover, both mappings revealed several black dots that corresponded to an increased Ti intensity within the Ti mapping (Figure 4f). Hence, in the same manner that TiN NPs form on surface grain walls, they also form on inner laying grain boundaries of as-atomized powder particles with a maximum detected size of 150 nm edge length. Via STEM characterization on the nanoscale, single NPs were detected on or near the GB as well (Figure 5a). According to both their cuboidal shape and the respective Ti- and N-EDS mappings, the preliminary assumption that the NPs detected via SEM can indeed be classified as TiN was confirmed (Figure 5b,c). These particles revealed a mean diameter of ~50–100 nm, which corresponded to the particle edge length for TiN NPs found in GARS-atomized in situ powders [9]. Further reactants such as Al or O were not found in the same location. The reason for encountering NPs on the surface and inside the powder can be found in the very high cooling rates during atomization; as

the cooling of the melt occurred at a speed of up to  $10^4$  K/s, solidification occurred nearly instantly throughout the whole particle [57–61]. Therefore, right before the liquid–solid phase transition, encapsulated nitrogen within the particle melt formed TiN to a rather low degree ( $\rightarrow 0.22\%$ ), while the outer side was exposed to a higher level of remaining elemental nitrogen within the argon atmosphere ( $\rightarrow 0.96\%$ ).

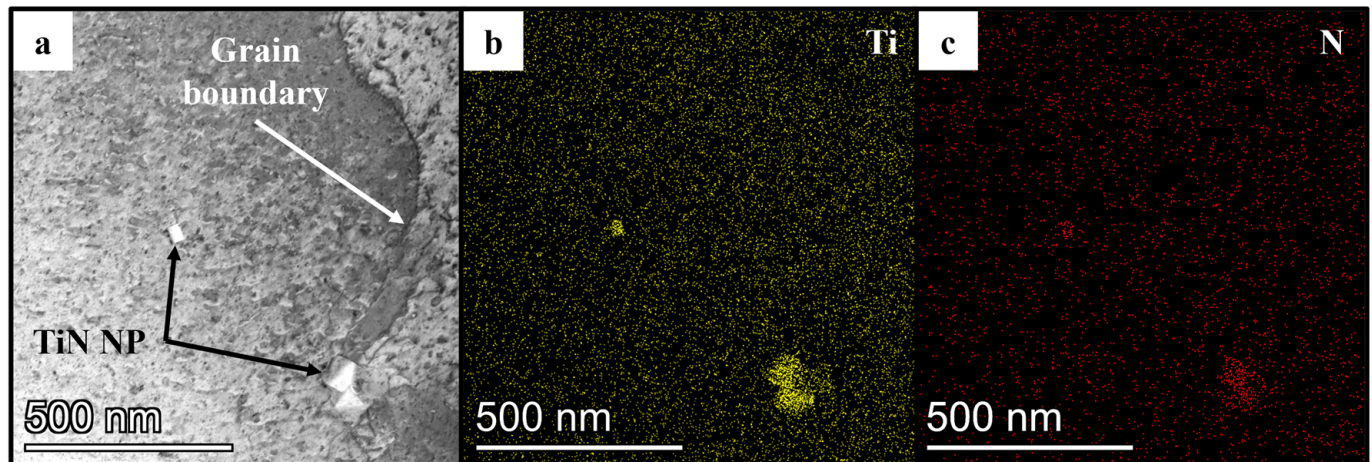


**Figure 5.** Pre-FBR particle STEM characterization revealing (a) magnification of GB area and TiN nanoparticles and (b,c) accompanying Ti-/N-EDS mappings of (a).

### 3.2. Post-FBR: Fluidized Bed Reactor and Powder Characterization

#### 3.2.1. Post-FBR Powder Surface Characterization

The intermediate powder was further processed via the fluidized bed reactor. Here, a temperature of  $800\text{ }^{\circ}\text{C}$  and a constant nitrogen gas flow of  $1.2\text{ L/min}$  (4 h) were set as FBR process parameters, as described above. The resulting final powder revealed a bulk density of  $\sim 4.7\text{ g/cm}^3$  and a flowability of  $\sim 15.2\text{ s/50 g}$ . Hence, these properties only changed marginally during FBR exposure, not leading to a substantially different behavior during LPBF. The PSD revealed key values of  $d_{10} = 20.2\text{ }\mu\text{m}$ ,  $d_{50} = 38.8\text{ }\mu\text{m}$ , and  $d_{90} = 59.8\text{ }\mu\text{m}$ , also being very much in line with the previous powders and within the desired range. Still, a slight difference became apparent when examining the post-FBR particle surface; the grain boundaries were not as pronounced/deep as for the pre-FBR counterpart (Figure 6a). The effect can be traced back to a slight, temperature-induced grain coarsening during FBR, closing these cavities [62,63]. This also serves as an explanation for the slightly higher bulk density, which is beneficial for stable LPBF manufacturing. The TiN formation can be compared to the intermediate state of the powders; NPs primarily formed along surface GB and could barely be found inside grains (Figure 6b,c). The main difference was in the NP quantity as the fraction rose from  $0.96\%$  (pre-FBR) by  $0.84\%$  to  $1.80\%$  (post-FBR) as a result of the exposure to nitrogen during FBR. This also marks a significant increase when compared to the GARS method, which revealed a surface NP fraction of  $0.12\%$  only [9]. The NP quantity in the post-FBR powders could be increased by longer exposure during FBR. However, (i) as these  $1.80\%$  act as a source for further TiN nucleation within the subsequent additively manufactured parts, thus even further increasing the share, and (ii) since a too high NP quantity leads to both a substantial loss in ductility and sudden fracture mechanism, the current share is considered optimal for further processing.



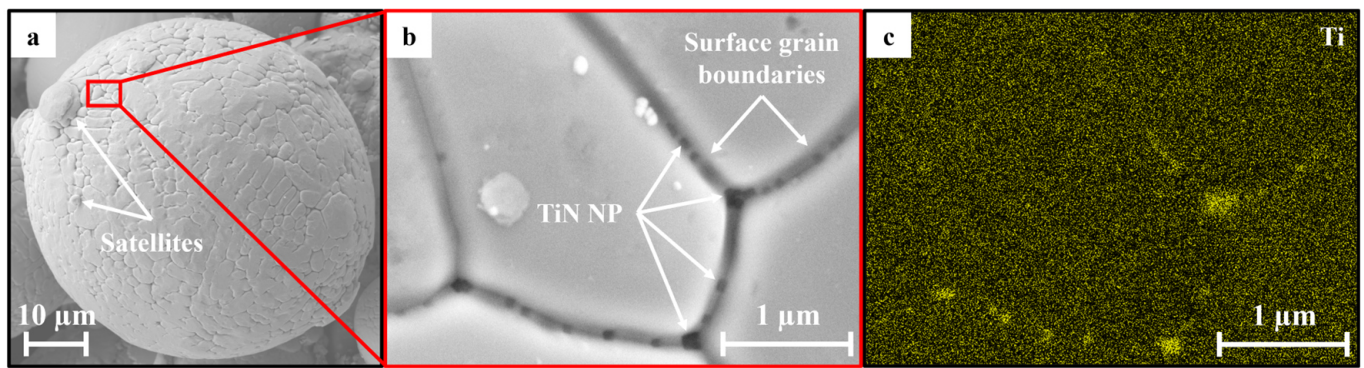


**Figure 6.** Post-FBR particle surface SEM characterization revealing (a) occasional satellite formation, (b) the presence of a high quantity of TiN NPs on surface GB, and (c) an accompanying Ti-EDS mapping of (b).

### 3.2.2. Post-FBR Powder Cross-Section Characterization

Subsequently, the cross-section of the post-FBR state was further characterized (Figure 7a). In terms of grain evolution and porosity detected, no significant difference was recorded in comparison to the pre-FBR powder (cf. Figure 4). However, the NP fraction increased by 0.66% from 0.22% (pre-FBR) to 0.88% (post-FBR) while revealing a maximum NP size of 150 nm, with the great majority being within 50–100 nm edge length as well (Figure 7b). Also, considering the NP fraction on the cross-section of GARS in situ powders, which amounted to only 0.13%, a clear improvement originating from the FBR processing can be noted [9]. To summarize, also considering the high amount of surface NPs, FBR exposure led to a substantial multiplication of TiN nanoparticles, hence fulfilling the main aim of this work. As the powders remained in the solid state during FBR, the mechanism for nitrogen uptake on the inner side of the particles was a diffusion-controlled one [64]. Over the 4 h exposure, the nitrogen diffused deeper into the particle along grain boundaries, forming TiN with elemental Ti, which detached from the solid solution due to the high temperature applied and its high reactivity with N. As the NP fraction on the surface increased by 0.84% while on the inside, only a 0.66% shift was reported, and the direction of the diffusion mechanism can be clearly traced back to “from outside to inside”. Hence, FBR exposure is more effective on the outside of powder particles (=N gas contact area) than on their inside, as expected. Comparing the EDS mappings for Cu, Ni, and Ti in Figure 7c–e, it again becomes apparent that strong Cu segregation on grain boundaries occurred and moreover, that the TiN NPs are located along these GB but almost never within the grains. This was proven to be the case via STEM-EDS as well (Figure 8b–d); most TiN nanoparticles aligned along the magnified GB while occasionally only NPs were detected approximately 150 nm apart from it. Checked against the GARS method and the pre-FBR powders, it becomes apparent that there were not only coarse NPs in the mean size of 50–100 nm but also considerably finer particles, some of which were only 10 nm (cf. Figure 8c) [9]. Hence, in post-FBR powders, the titanium nitride evolution can be described as bimodal [8,65,66]. This is assumed to be beneficial for the Orowan strengthening in parts manufactured using these powders, as there is a contrasting effect of decreasing NP size and more effective strengthening [67,68]. As the coarse NPs were already detected in pre-FBR powders, the additional fine NPs detected in post-FBR powders were considered the direct outcome of the FBR process. Also, dislocation formation occurred near grain boundaries and segregations (Figure 8a). This can be attributed to solid solution segregations eventually leading to the formation of dislocations: as the lattice constants of the Cu-rich segregation area and the neighboring NiCu-rich solid solution varied, interfacial strain was evoked, which, in turn, was circumvented by the formation of dislocations [69].



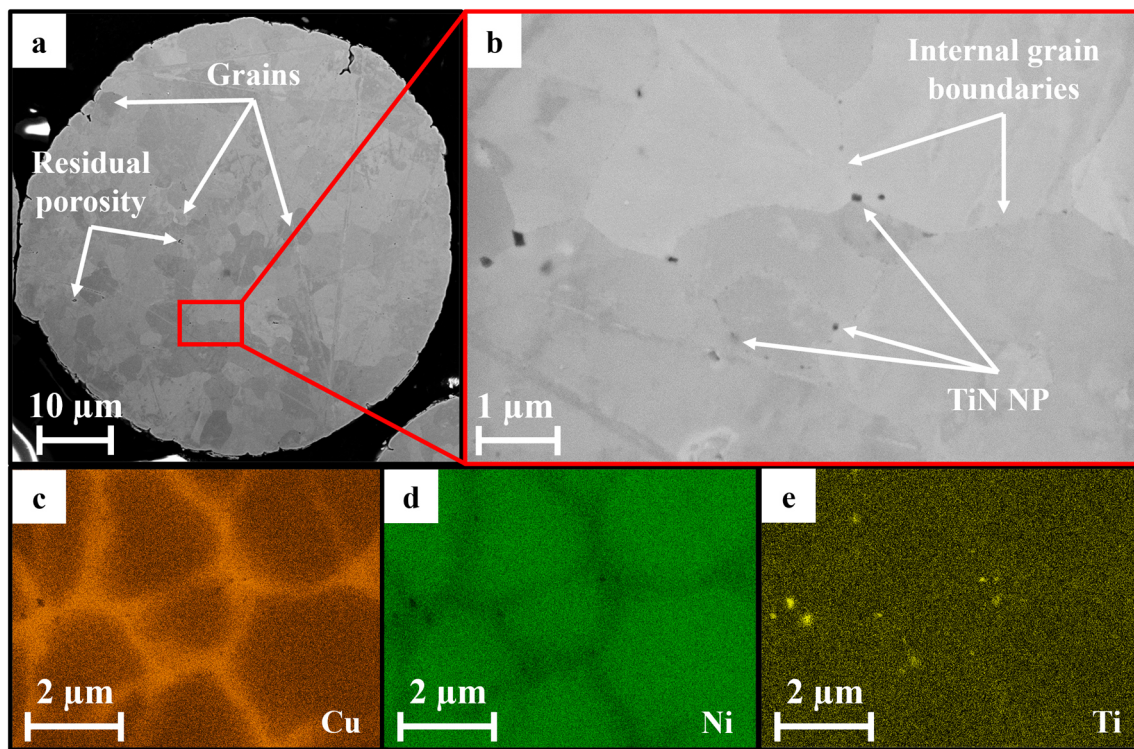


**Figure 7.** Post-FBR particle cross-section SEM characterization revealing (a) occasional porosity, (b) the presence of TiN NPs on GB, (c–e) accompanying Cu-/Ni-/Ti-EDS mappings of (b).

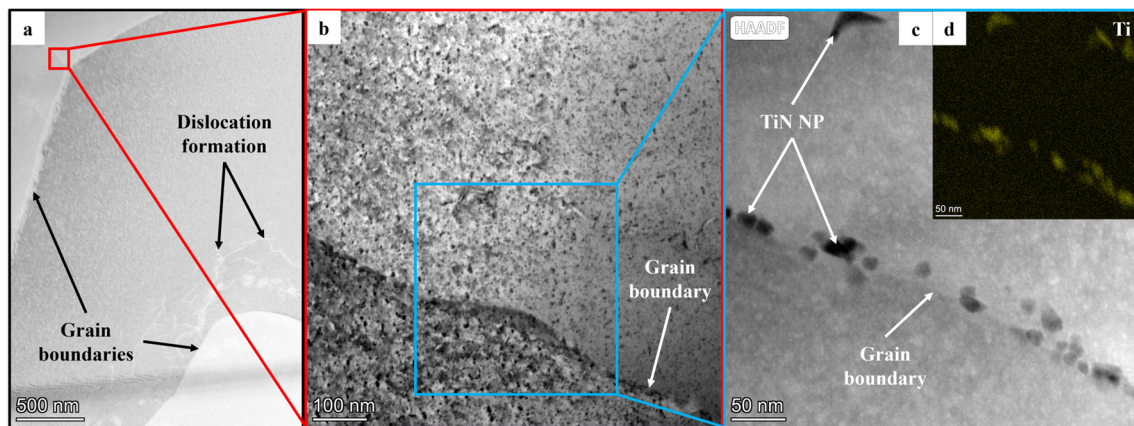


**Figure 8.** Post-FBR particle STEM characterization revealing (a) occasional dislocation accumulation within grains, (b) magnification of GB area, (c,d) dark field and Ti-EDS-mapping of GB rich in TiN nanoparticles.

### 3.2.3. Powder Cu Segregation and Nanoparticle Formation Mechanism

It is remarkable that nanoparticles in both the pre- and the post-FBR states primarily accumulated along surface and internal grain boundaries rather than inside the respective grains. Also, as discussed, Cu tends to segregate, meaning that the majority of Cu is present along GB, while simultaneously, the larger proportion of Ni can be found within the grains. Still, Alloy 400 forms an fcc solid solution of Cu and Ni [1,2]. Therefore, in order to generate a deeper understanding of the various formation mechanisms occurring during gas atomization and FBR, a sequence of solidification during atomization is proposed in Figure 9, and a mechanism for the increased NP quantity in post-FBR powders is suggested in Figure 10. The first sequence is split up into the four points of time  $t_0$  (actual temperature  $T_0$  being higher than the melting temperature of titanium  $T_{m,Ti}$ ),  $t_1$  ( $T_1$  being in between

$T_{m,Ti}$  and the melting temperature of nickel  $T_{m,Ni}$ ,  $t_2$  ( $T_2$  being in between  $T_{m,Ni}$  and the melting temperature of copper  $T_{m,Cu}$ ), and  $t_3$  ( $T_3$  being below  $T_{m,Cu}$ ). As nitrogen reveals a boiling point of  $-196^\circ\text{C}$ , it is considered gaseous throughout the whole cooling procedure, apart from the portion that forms a compound with titanium as TiN. The remaining N may thus move freely throughout the solid solution fcc structure. At  $t_0$ , Ti, Ni, and Cu are in the liquid phase, forming the melt. Hence, no crystal structure is present, and all atoms flow freely. As the temperature drops to  $T_1$  and thus exceeds the Ti solidification temperature, TiN starts forming. Due to the marginal quantity of N in the atomization atmosphere (Ar pressured system), only a small proportion of the Ti added to the alloy would react to TiN. The reason for the segregation behavior can instead be traced back to the significantly different solidification temperatures of Cu ( $1085^\circ\text{C}$ ) and Ni ( $1455^\circ\text{C}$ ) [70–72]. As a result, during the solid solution nucleation of the NiCu system (cf.  $T_2$ ), grain cores, where nucleation originates, experience a higher intensity in Ni than in Cu. Also, the leftover Ti not forming TiN now starts forming part of the solid solution. In between  $T_2$  and  $T_3$ , a remarkable portion of Ni is already in the solid state, while the main part of Cu is still in the liquid phase of the melt. Therefore, the Cu-rich melt is being “pushed” by the steadily growing Ni-rich grains until encountering an opposite grain. In the same manner, TiN NPs flow with the melt towards the future GB area. Here, the remaining Cu not enclosed in the grain cores yet would then solidify into the preferred fcc solid solution ( $T_3$ ). As a result, after complete cooling below the melting temperature of Cu ( $T_{m,Cu}$ ), grain boundary near regions are rich in Cu atoms as part of the solid solution (with Ni and Ti also being present at GB but to a clearly smaller extent). The TiN NPs are now incorporated into the alloy along its grain boundaries. Also, when  $T_3$  is reached, no more melt is present, and the whole alloy system is in the solid state. It is worth mentioning that due to the high cooling rates described previously [57–61], the proposed sequence of Figure 9 takes place extremely fast, and thus, the phase transformation does not take place in an equilibrium state [73–75]. Therefore, the proposed mechanism must be considered a simplified visualization.

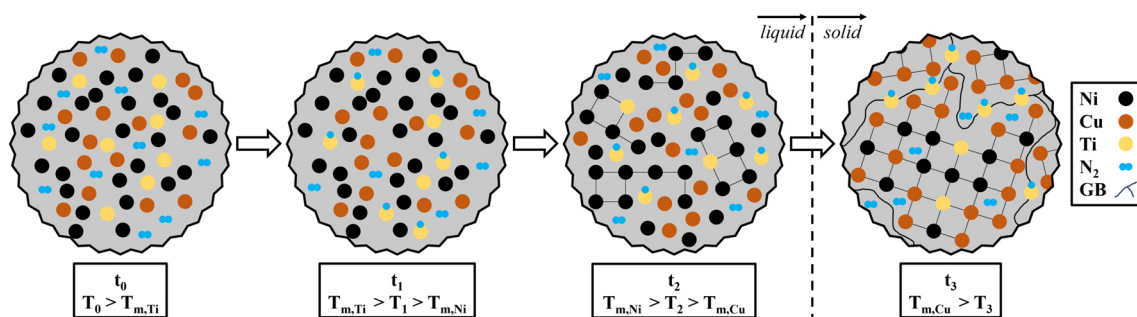


**Figure 9.** Pre-FBR: a proposed mechanism for the emergence of NP GB accumulation and Cu segregation over time, depending on the liquid–solid phase transition temperatures of the respective elements.

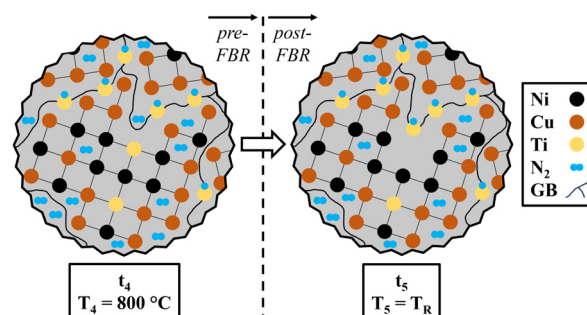


**Figure 10.** Post-FBR: a proposed mechanism for the increase of TiN NP quantity.

Considering the FBR exposure, a new temperature  $T_4$  is set to 800 °C inside the reactor. As the melting point of Alloy 400 is considerably higher, this process takes place in the solid state only. Hence, the microstructure of  $t_4$  can be compared to the one of  $t_3$ , revealing a higher N fraction (cf. Figure 10). As the process is carried out over 4 h at an elevated temperature, a share of the Ti being embedded in the solid solution would now react with the N gas flow. Enabled by diffusion processes, nitrogen is transported along grain boundaries inside the powder, and Ti near these GB leaves its place in the fcc structure to accumulate on the grain boundaries as TiN (cf.  $t_5$ ,  $T_R$  = room temperature). As a result of the FBR process and the low additional surface energy for precipitate formation on GB, the NP fraction is raised, as documented before.

### 3.3. LPBF Parameter Optimization and Part Characterization

#### 3.3.1. Laser Powder Bed Fusion Optimization

As the intermediate pre-FBR powder (modified in chemical composition, non-modified via FBR yet) already revealed a formation of TiN nanoparticles, its printability and the resulting NP formation in parts were considered. Hence, an LPBF parameter optimization of one iteration, consisting of 24 parameter sets, was carried out in order to gain a deeper understanding of defects occurring during 3D printing and the micro-/nanostructure formation. The parameter sets varied in laser power (7–95 W), scanning speed (100–1150 mm/s), and hatch distance (60–80 µm). Amongst these, 85 W, 1100 mm/s, and 70 µm showed a maximum density of 99.5%, as illustrated in Figure 11 (left). Occasional keyhole defects occurred, especially in the edge areas of the part, being attributed to local beam acceleration and the resulting heat accumulation [76–78]. Porosity is always detrimental to the mechanical properties of the part. Still, small pores below ~50 µm would not result in a massive decline in mechanical performance, as it is rather dependent on microstructural properties [79–81]. The achieved level of 0.5% porosity can thus be accepted while still leaving room for improvement during the final parameter optimization of the FBR-modified alloy, which was split up into two iterations, resulting in 41 parameter combinations. Laser power varied from 35 to 135 W, scanning speed from 700 to 1300 mm/s, and hatch distance from 30 to 70 µm. By applying a parameter set of 115 W, 900 mm/s, and 60 µm, a maximum density of 99.87% could be reached (Figure 11 (right)), again revealing most of the residual porosity in border areas. In contrast to the pre-FBR part, the inner side of the density cube barely showed porosity, which contributes considerably to the density increase of nearly 0.4%. Also, the average size of keyhole porosity was significantly smaller (pre-FBR: ~150 µm, post-FBR: ~70 µm). It is thus assumed that the post-FBR process is better adjusted during all phases of the laser travel (constant speed, acceleration, deceleration, and turning) [78,82]. The newly found post-FBR parameter set was used for LPBF manufacturing of all test specimens, as presented in the following sections.

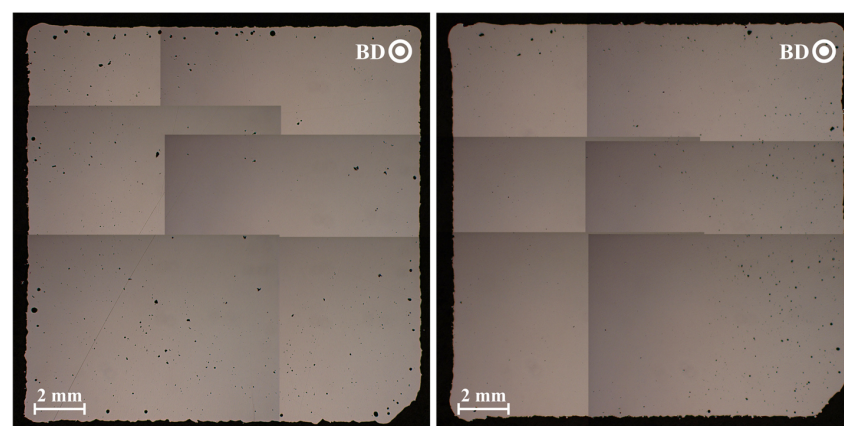


**Figure 11.** Cross-sections of pre-FBR (left) and post-FBR (right) density cubes perpendicular to their build directions.



### 3.3.2. Pre- and Post-FBR Part EBSD Characterization

LPBF-built parts were further analyzed by application of EBSD. The pre-FBR characterization is illustrated in Figure 12, and the post-FBR one in Figure 13. Considering the EBSD mappings (Figures 12a and 13a), a considerable difference becomes present; even though examined under the same magnification, the pre-FBR part revealed a considerably less-ordered grain structure, consisting of a high number of different grain sizes that originated from the respective LPBF process. Thus, besides the previously reported density increase for the post-FBR parts, the grain evolution also occurs more structured, allowing for a smoother LPBF process. The tendency of grains stacking on top of each other and the resulting growth of columns along the build direction, as a function of the directed heat propagation during LPBF, was more apparent [83,84]. Also, the grain diameter was affected, as the post-FBR parts revealed a mean value of  $7.44\ \mu\text{m}$  in contrast to  $5.20\ \mu\text{m}$  for the pre-FBR ones, while both modifications reveal a max. of  $\sim 80\ \mu\text{m}$  in grain size. While small grain sizes in LPBF parts are generally beneficial for mechanical performance according to Hall–Petch, porosity is detrimental [1,40,85–87]. Thus, as the mean grain diameter in post-FBR parts was only  $\sim 2\ \mu\text{m}$  coarser than in pre-FBR ones while simultaneously revealing a very high density of  $\sim 99.9\%$ , the microstructure in post-FBR parts was favored. Moreover, high dislocation density and low texture are improving mechanical properties, both being the case for the post-FBR state [88,89]. The difference in texture can mainly be correlated with the circumstance that considerably more nanoparticles were present in the post-FBR component than in the pre-FBR one (cf. 3.3.3.). Thus, grain nucleation may occur on these high temperature stable NPs in a controlled manner during the liquid–solid transition, whereas the absence of TiN leads to randomly distributed and directed grains. The lower density mentioned for pre-FBR parts and, thus, the reduced adjustment of process parameters also contributed to this texture formation. Comparing dislocation mappings in both Figures 12b and 13b, the post-FBR material revealed considerably fewer grain boundaries (black) than the pre-FBR one, as no such high number of small-sized grains was present. At once, the post-FBR microstructure revealed a profound dislocation density (green), preferably as geometrically necessary dislocations forming along grain boundaries and to a lesser extent as statistically stored dislocations (SSD) within grain cores [89]. For the pre-FBR version, a GND mean of  $4.73 \times 10^{14}/\text{m}^2$  was detected, which was a significant improvement to the  $3.58 \times 10^{14}/\text{m}^2$  being present in the in situ atomized material [9]. However, the post-FBR material resulted in an even slightly higher GND mean value of  $4.86 \times 10^{14}/\text{m}^2$ . Evaluating the respective (inverse) pole figures (IPF/PF) of both modifications (Figures 12c and 13c), several randomly dispersed textures can be stated for the pre-FBR alloy. The {100}, {110}, and {111} PFs did not indicate a clearly preferred texture, while several textures were observed as per the IPF for the build direction X [111] and within the Y/Z layer [101]/[111]. In contrast, the PFs in Figure 13c show a uniform distribution around the [001] center. Moreover, only little texture can be reported throughout the IPF, with a single preference for [001] along X (build direction), revealing a low standardized maximum of 1.79. As reported by Zhao et al. [88], a weakly pronounced texture is beneficial for both an improvement in mechanical properties and a decrease in anisotropy and, thus, desired.

### 3.3.3. Pre- and Post-FBR Part EDS Characterization

In terms of attainable density, GND, and texture, it can be stated from the above results that the post-FBR alloy (the final state of the applied modification route) revealed a higher potential for improving the properties of the part than the pre-FBR one. However, it has to be clarified whether the nanoparticle share in the final version is also higher than in the intermediate one, and thus, an improved strengthening of a final component can be ensured. Nanostructures of both the pre- and the post-FBR parts were analyzed by utilization of STEM. Figure 14a illustrates the pre-FBR part microstructure. It becomes apparent that, in contrast to the powders, the material is now organized in a micro-dendritic cell nanostructure. Evoked by the very high cooling rates during LPBF of up to  $10^6\ \text{K/s}$ , such

cell structures and high dislocation formation are frequently documented, particularities for additively manufactured parts, significantly contributing to an enhanced mechanical performance [82,90–94]. Even though hard to detect and to a small extent of only 0.12%, TiN nanoparticles were found throughout the cells, pinning and curving the dislocations (Figure 14 a–c). Such low NP shares in additively manufactured components may already contribute to its performance in a sufficient manner as documented by, e.g., Doñate-Buendia et al. (0.08%  $\text{Y}_2\text{O}_3$ ) [66], Smith et al. (0.6%  $\text{Y}_2\text{O}_3$ ) [33], and Dai et al. (0.26%  $\text{Y}_2\text{O}_3$ ) [30]. However, considerably higher proportions of up to 7.0% are stated as well in the literature, leading to a substantial improvement in mechanical properties [8,30,38,95]. Hence, increasing the strengthening NP share considerably is generally desired. The size of these NPs resulting from shielding gas atomization are in the range of 50–100 nm, as was the case for the pre-FBR powders as well (and for the in situ manufactured parts) [9]. Hence, these NPs can again be described as coarse and monomodal (no finer NPs below 50 nm are present in the pre-FBR state).

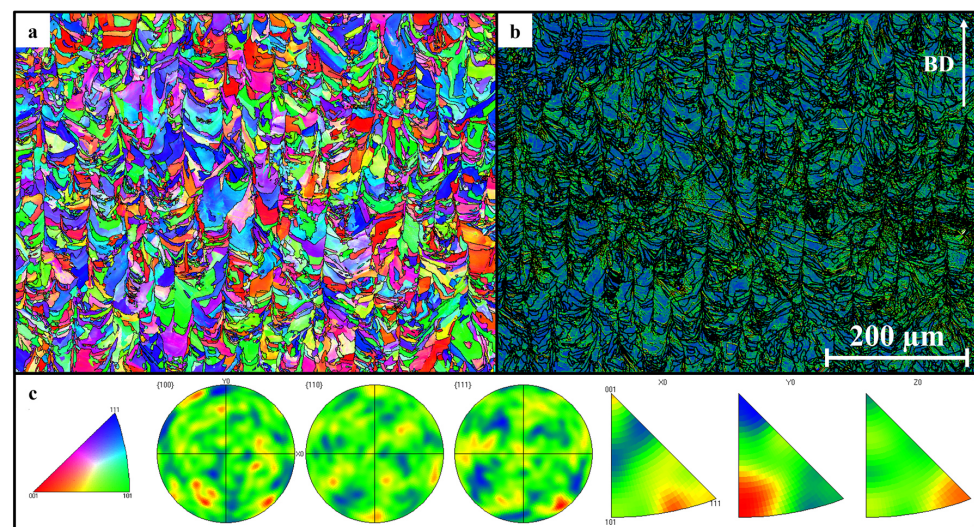


**Figure 12.** Pre-FBR part EBSD characterization revealing (a) X-EBSD mapping in build direction, (b) GND distribution map of (a), (c) color code triangle of (a), and resulting pole figures and inverse pole figures for X (=build direction)/Y/Z.

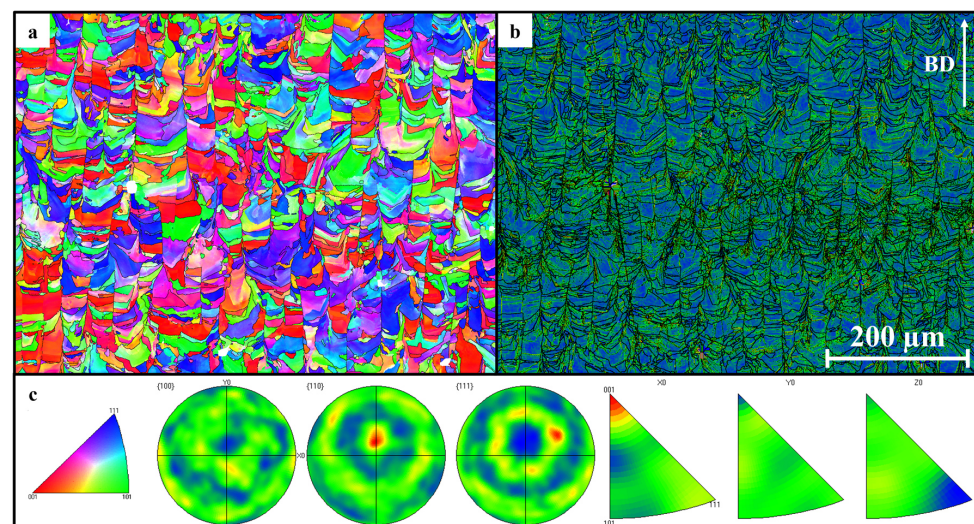


**Figure 13.** Post-FBR part EBSD characterization revealing (a) X-EBSD mapping in build direction, (b) GND distribution map of (a), (c) color code triangle of (a), and resulting pole figures and inverse pole figures for X (=build direction)/Y/Z.



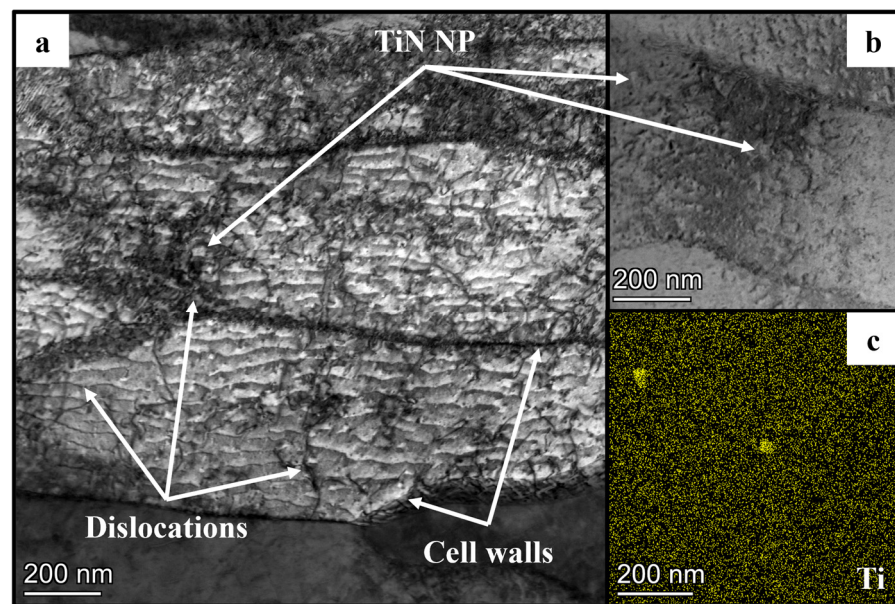


**Figure 14.** Pre-FBR part STEM-EDS characterization revealing (a) a cellular nanostructure, (b) occasional presence of TiN NPs, and (c) accompanying Ti-EDS mapping of (b).

The post-treatment of powders via the fluidized bed reactor increased the NP share in a considerable manner. As displayed in Figure 15a,b, elongated cells were found to be rich in both dislocations and TiN nanoparticles. The NP proportion was 6.53%, which not only represents a significant improvement to the pre-FBR material but also in the in situ processed alloy, which revealed a TiN share of 3.88% only [9]. As mentioned, such proportions are expected to result in enhanced mechanical performance [8,38,95]. A minor portion of NPs can be found within cell cores (i.e., not along their walls), being attached to dislocations, which was also found for the pre-FBR material (Figure 15c,d). However, the great majority of TiN in the post-FBR part primarily aligned along cell walls, as is typical for dispersion-strengthened, LPBF-manufactured components [31,96]. The underlying principle can be explained as per the suggested mechanism for the emergence of NP accumulation in powders (cf. Figure 9), with the difference of accumulation occurring on cell walls instead of grain boundaries because no cell walls were present in the powders. Interestingly, besides plenty of TiN nanoparticles, alumina nanoparticles also formed to a very low extent (Figure 15e,f). They can be clearly differentiated from the cuboidal TiN particles as they appear completely spherical and are not present in the same place. These particles resulted from the reaction  $4 \text{ Al} + 3 \text{ O}_2 \rightarrow 2 \text{ Al}_2\text{O}_3$  occurring in the melt pool between elemental Al as part of Alloy 400 and the remaining atmospheric oxygen in the shielding gas-pressured LPBF building chamber. As the portion of  $\text{Al}_2\text{O}_3$  is relatively low, and the precipitates are not spread homogeneously over the microstructure, they are not considered to contribute highly to the dispersion-strengthening effect. However, Figure 15g illustrates the interaction of alumina with dislocations; dislocations are hindered in their expansion by the alumina and bulge around the nanoparticles. This bending effect becomes even more present with the nanosized TiN particles (Figure 15h). The NPs are located at the “upper” end of the dislocations, meaning that they can be considered the origin for cutting the dislocation chain into the many small sections. The size of a single TiN NP is hard to measure but was determined with approx. 10 nm in diameter (as already detected in the post-FBR powders, cf. Figure 8). As in the powders, these fine NPs were not the only manifestation of titanium nitride; there also existed noticeable coarser TiN particles with an average diameter of ~50–100 nm, which is equivalent to a factor of at least 5 times the diameter of the finer particles. However, these coarser particles did not occur frequently throughout the microstructure of the post-FBR parts, but still, a bimodal nanoparticle formation was found [8,65,66]. In Figure 15i, such a particle of 200 nm edge

length is illustrated, and it can be observed that there is a high dislocation accumulation at its edges. As a result, dislocation pinning occurs on both fine and coarse nanoparticles, and thus, both TiN NP types contribute to the dispersion strengthening effect, leading to enhanced mechanical properties.

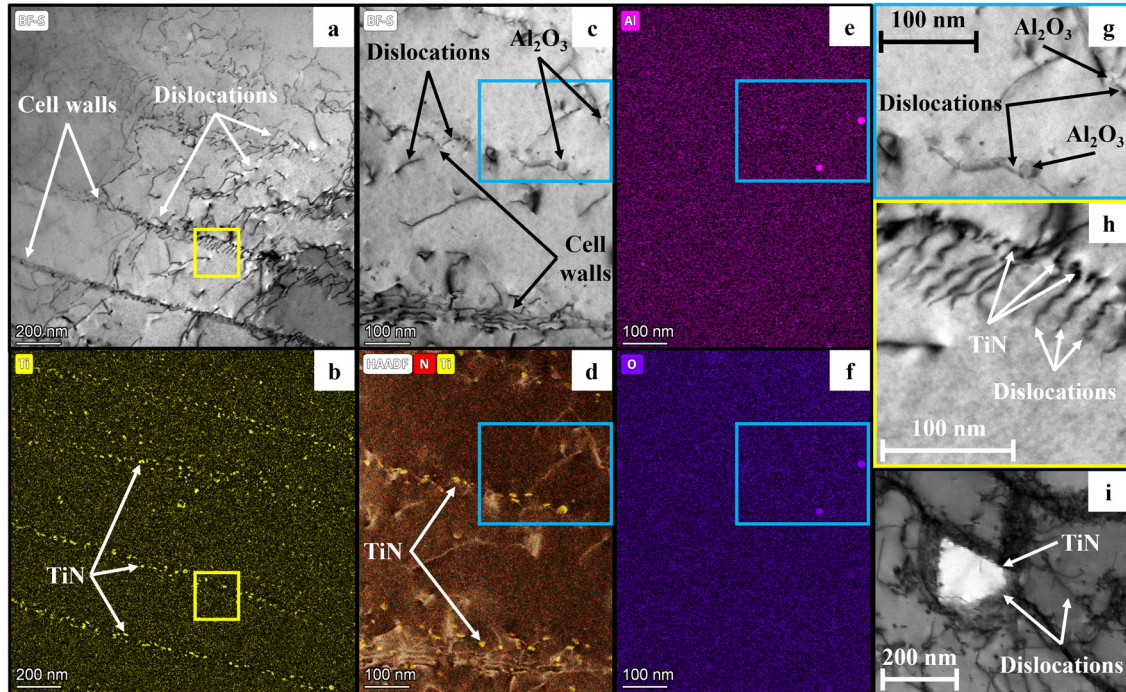


**Figure 15.** Post-FBR part of STEM-EDS characterization revealing (a) a pronounced formation of cell walls and dislocations, (b) accompanying Ti-EDS mapping of (a), (c) a magnified cell wall area, (d–f) accompanying Ti-N-/Al-/O-EDS mappings of (c), (g) a magnification of (c) illustrating  $\text{Al}_2\text{O}_3$  dislocation interaction, (h) a magnification of (a) illustrating TiN dislocation interaction of fine TiN NP, and (i) TiN dislocation interaction of a coarse TiN NP.

Pronounced Cu-GB segregation behavior was detected for both the pre-FBR (cf. Figure 4) and the post-FBR (cf. Figure 7) powders. However, such intense chemical splitting of elements Cu on cell walls and Ni within cell cores was not detected for the parts. As per Figure 16a, the micro-dendritic nanostructure described previously became apparent in another form of appearance, not as elongated cells but as smaller spherical and cuboidal cells for a post-FBR part. This was due to the strongly varying solidification direction on the nanoscale; multiple orientations eventually evolved during dynamic melt pool solidification and thus, depending on the area investigated, cells may appear as cellular, elongated, or a mixture of both [92,97]. Considering the accompanying Cu-/Ni-EDS mappings in Figure 16b,c, the Cu segregation behavior of Alloy 400 previously described for the powders (cf. Figure 7c,d) could be redetected in parts as well. However, the intensity of Cu on cell walls was considerably weaker than in powders, and Cu could be detected all over the cells in clear manifestation. Hence, the segregation behavior in LPBF-built parts was highly less-pronounced, which could be correlated with two main differences in comparison to gas atomization. Firstly, the cooling rates were even higher during LPBF than in atomization (up to  $10^6$  K/s, which equals approximately two orders of magnitude more) [82,90,98]. This led to even less time available for segregation to occur, which is why a high proportion of the elemental Cu was not found solely at cell walls but rather remained inside the homogeneous solid solution during rapid crystallization [99]. In other words, the liquid–solid phase transition of the NiCu system occurred nearly instantly so that the Cu-rich melt was not “pushed” towards the cell walls to such a high extent as was suggested for the GB in powders (cf. Figure 9). Moreover, as already



documented for the gas atomization process, the non-equilibrium solidification behavior during LPBF was even more pronounced [73–75,98–100]. Secondly, the iterative nature of the melting and solidification sequence during LPBF, occurring over several layers, led to the formation of a heat-affected zone [98,101–103]. This zone eventually reduced the segregation manifestation as a heat-induced diffusion was activated, and thus, Cu could reallocate to the solid solution [104–106]. Hence, in summary, when processing Cu segregation-rich powder via LPBF, the considerable decline in segregations in printed parts is dependent on both (i) the high cooling rates, resulting in little time for segregation to occur in the first place, and (ii) the heat affected zone, leading to a further decrease of the already low level of segregations.

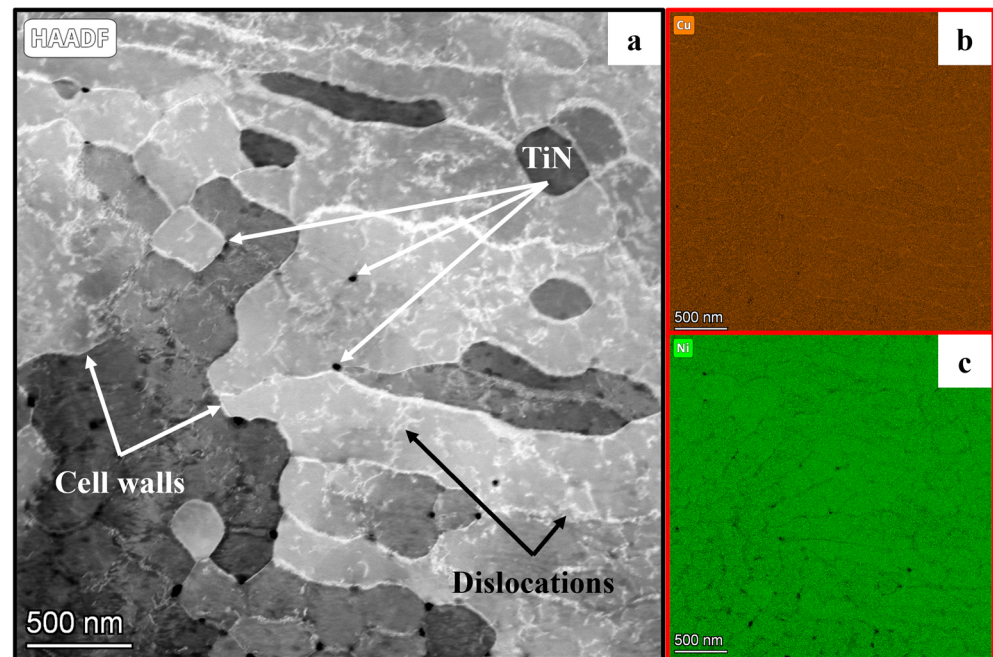


**Figure 16.** Post-FBR part STEM-EDS characterization revealing (a) a pronounced interaction of cell walls, dislocations, and coarse TiN particles and (b,c) accompanying Cu-/Ni-EDS mapping of (a).

### 3.3.4. Part Melt Pool Formation Mechanism

Based on the microstructural properties of the post-FBR material identified above, an underlying concept for the melt pool formation mechanism was elaborated (Figure 17). Throughout the literature, various approaches for nanoparticle formation throughout the additively manufactured microstructure are demonstrated as a result of an NP-containing powder feedstock or due to reactivity of the melt pool alloying elements with the build chamber atmosphere [10,11,31,33,36]. In this work, a combination of both was the case. As illustrated, the post-FBR powder feedstock was enriched in fine and coarse TiN NPs (cf. Figures 7 and 8). As these powders became molten from the laser and thus experienced a solid–liquid phase transformation, the high-temperature-stable nanoparticles stayed in their original form. However, besides the other alloying elements of Alloy 400, titanium and aluminum atoms from the solid solution of the powders could then flow freely within the melt pool. Especially on the melt pool surface (red highlighted area) as well as within the melt pool, triggered by Marangoni convection [31,36,107], these atoms could then interact with the remaining oxygen and nitrogen of the shielding gas-pressured build chamber. As per  $4 \text{ Al} + 3 \text{ O}_2 \rightarrow 2 \text{ Al}_2\text{O}_3$  and  $2 \text{ Ti} + \text{N}_2 \rightarrow 2 \text{ TiN}$ , both molecules, alumina and TiN, began forming. They both deposited on grain boundaries and cell walls during cooling to a columnar microstructure. It is important to mention that alumina was not present in the powders, which is why its formation could be clearly traced back to the LPBF process only. However, TiN was present in the powders already (fine and coarse NPs) and did form

again during LPBF, as the share of fine TiN NPs was significantly increased. This led to the assumption that the TiN formation mechanism can be split up into three stages throughout the whole VIGA-FBR-LPBF process route:

- Primary formation stage:  
Coarse  $\alpha$ -TiN resulting from the atomization process ( $\hat{=}$  pre-FBR powder state)
- Secondary formation stage:  
Fine  $\beta$ -TiN resulting from the FBR exposure ( $\hat{=}$  post-FBR powder state)
- Tertiary formation stage:  
Increase in TiN (=remaining  $\alpha/\beta$ -TiN from powders +  $\gamma$ -TiN formation within melt pool) resulting from the LPBF process ( $\hat{=}$  post-FBR part state)

Still, even though three formation stages were introduced, the nature of TiN within the post-FBR material can be characterized as bimodal (the distinction between fine and coarse particles). For the  $\text{Al}_2\text{O}_3$  formation mechanism, only one stage can be denoted:

- Primary formation stage:  
Comparably coarse  $\alpha$ - $\text{Al}_2\text{O}_3$  resulting from the LPBF process ( $\hat{=}$  post-FBR part state)

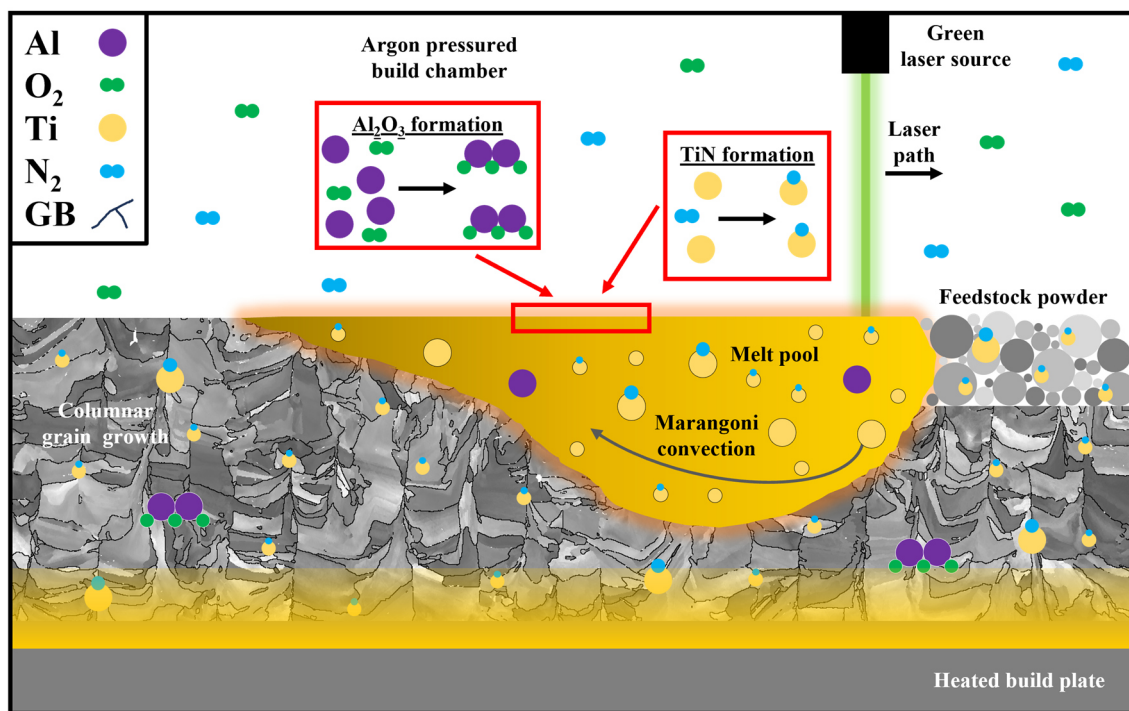


**Figure 17.** Proposed mechanism for melt pool interaction and microstructure formation during LPBF.

As documented by the EBSD mapping (cf. Figure 13) as well as visualized by STEM characterization (cf. Figures 15 and 16), multiple orientations of single grains exist throughout the microstructure. As a result, the appearance of single cells within a respective grain varies strongly from the cells of another grain (Figure 18); grains I. and III. revealed round cells, while grains II. and IV. showed elongated cells (Figure 18a). The difference in orientation can be further studied for the highlighted area (Figure 18b) and the underlying cell formations (Figure 18c). Cell walls rich in dislocations are present for both grains III. and IV. However, it seems like grain III. revealed significantly more dislocations (see green circle). The reason is that dislocations primarily accumulate along cell walls, as discussed before. Hence, with the orientation of cells present in grain IV. and the resulting lower amount of cell walls visible in this cross-section, the number of dislocations visible was lower as well (see purple circle). Dislocations could be found within cells as well but to a much lower extent, which was due to segregations on cell walls being beneficial for dislocation

formation, as stated for powder grain boundaries before [69]. However, it needs to be addressed that during STEM, the grain boundary and cell wall visibility conditions (g.b, where g is the diffraction vector and b is the Burgers vector) must be met. Thus, reduced visibility of dislocations is influenced by the diffraction pattern and not solely dependent on grain orientations. Still, it can be concluded that the number of dislocations is homogenous throughout the nanostructure and only appears to be heterogeneous due to the steadily varying cell growth directions from one grain to another.

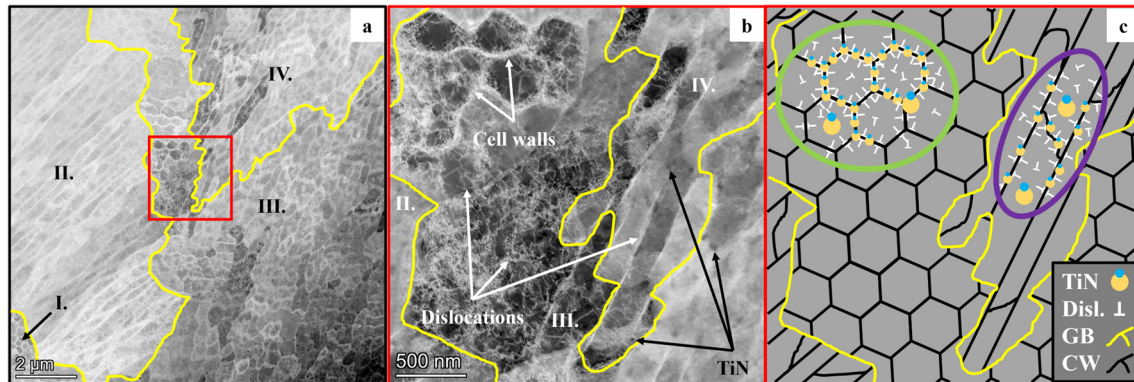


**Figure 18.** Post-FBR part STEM characterization indicating (a) grain formation and underlying cellular structure, (b) a magnification of (a) highlighting pronounced cell wall–dislocation interaction, and (c) corresponding proposed mechanism for nanostructure formation during LPBF as per (b).

### 3.4. Post-FBR Testing

As the pre-FBR powder and part characterization revealed (i) a lower maximum attainable density, (ii) a lower presence of strengthening NPs, (iii) a lower dislocation density, and (iv) a more pronounced texture than the post-FBR ones, only the final state of this modification route, the post-FBR ex situ alloy, was further investigated during mechanical testing. Here, a direct comparison to the GARS in situ processed material [9] was drawn in order to quantify specific drawbacks and improvements achieved via the newly developed FBR processing routine.

#### 3.4.1. Hardness and Tensile Testing

In terms of hardness, the post-FBR nitridation approach led to a mean value of 202 HV10. The nitridation gas atomization reaction synthesis procedure instead enabled the production of parts revealing a slightly higher hardness of 207 HV10 on average. This difference of ~5 HV10 can be accepted if further mechanical properties show an improvement for the FBR material. This was the case for the tensile properties;  $\sigma$  and  $\epsilon$  were enhanced in comparison to the in situ version (Figure 19 (left)). As can be seen, the ultimate tensile strength for the post-FBR material was comparable to the GARS material for RT and 400 °C. However, at higher temperatures, the new alloy performed slightly better. A clear improvement compared to unmodified LPBF-processed Alloy 400 became apparent as well. These conclusions also applied to the yield strength. Elongation and contraction from RT to 750 °C are displayed in Figure 19 (right). At the breaking point, the ex situ material revealed the highest elongation for all elevated temperatures of potential application. Again, a considerable advantage over the unmodified version can be stated. Therefore, among the three different material states, FBR conditioning allowed for a superior alloy system in terms of both strength and elongation. The contraction revealed a varying behavior for the modified versions and the unmodified one; at RT and 400 °C, both modified alloys showed a comparably high contraction, but the unmodified did not. From 550 °C on, they all revealed marginal contraction only. Hence, a ductile to brittle transition for the modified parts in the region of 400 °C can be stated, while the unmodified LPBF geometry showed a rather brittle failure mode throughout the whole temperature range tested. The change of failure



mechanism from ductile to brittle can be correlated with decreasing grain size, which is also seen in NiCu alloys at elevated temperatures [72,108]. However, the mean grain diameters did not vary significantly, which is why an effect of the dislocations must be considered. Indeed, the higher the dislocation density, the harder it gets for a single dislocation to move freely throughout the nanostructure, which ultimately causes an increase in strength and a decrease in the ductility of the material [109–111]. Hence, a pronounced dislocation density is the reason for brittle material failure, especially at elevated temperatures up to 750 °C, where increased movement activity is present. Furthermore, the brittle behavior of the unmodified material even at RT is rather caused by a higher level of porosity in contrast to the modified material. Voids and near-grain boundary oxides may cause such brittle failure initiation [37,112]. Figure 20 provides an overview of the exact sequence of the tensile tests for the post-FBR material. The maximum reached UTS that attained elongation at a break for all five temperatures applied can be determined as per:

- RT: 624.4 MPa and 22.5%
- 400 °C: 577.2 MPa and 20.7%
- 550 °C: 457.4 MPa and 13.1%
- 650 °C: 321.8 MPa and 4.5%
- 750 °C: 237.4 MPa and 4.0%

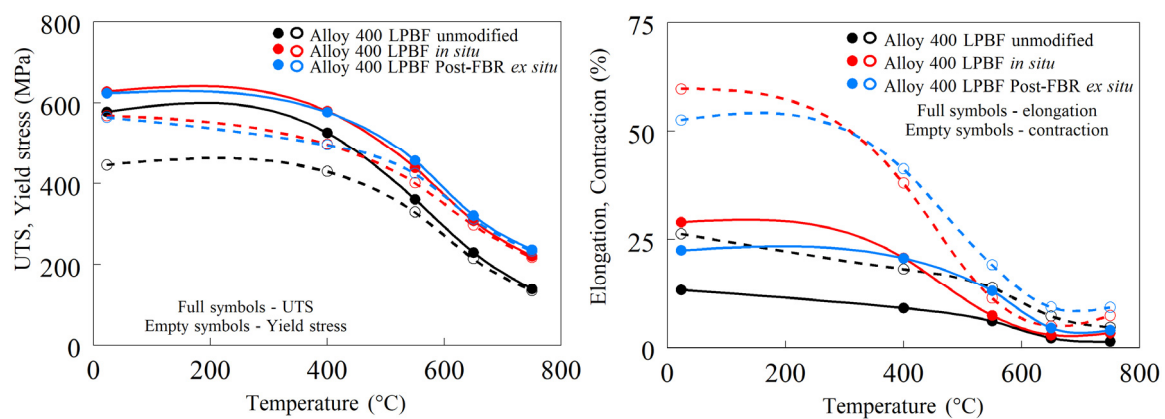


**Figure 19.** Tensile properties of unmodified reference material, in situ GARS-processed material, and ex situ FBR-processed material.

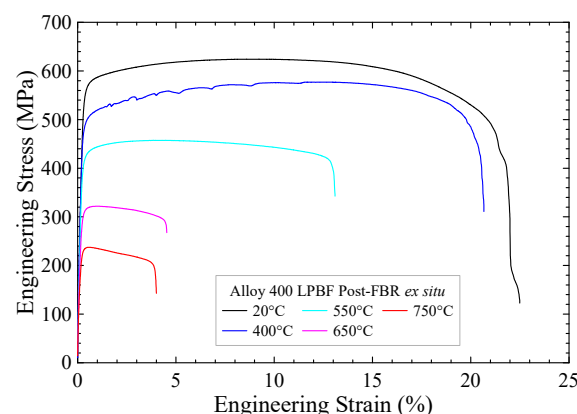


**Figure 20.** Stress vs. strain diagram of ex situ FBR processed material in the temperature range of RT–750 °C.

A clear positive shift in tensile properties can thus be denoted for the ex situ modification, especially at higher temperatures, where the offset in UTS to unmodified material is more pronounced than at lower temperatures.

### 3.4.2. Creep and Fatigue Testing

Creep and fatigue experiments were carried out at 650 °C as a potential application temperature of the alloy system. Checked against unmodified and in situ material, Figure 21 (left) illustrates the creep properties of the ex situ alloy in time to rupture  $t_r$  for several  $\sigma$  stresses applied. A precise comparison was made for 50, 75, and 100 MPa, and a definite hierarchy became apparent: the newly developed post-FBR material exhibited clearly superior creep properties to the GARS test specimens and the unmodified ones. For instance, at 75 MPa, the ex situ modification endured ~300 h during creep testing, whereas the in situ one failed after ~85 h, with the standard material even breaking at a very low  $t_r$  of just 8 h. Thus, the TiN dispersion strengthening effect caused an increase of several orders of magnitude, being linked to the dislocation pinning on nanoparticles [26]. Moreover, not only the values achieved were higher but also the gradients of the connecting lines were flatter, meaning that at higher stresses, the modified materials performed even better than with lower stresses anyway. Ultimately, even though the ex situ modification possessed small grain sizes, which were also linked to multiple grain nucleation on the TiN present in the melt pool, the strengthening achieved via these nanoparticles equaled the creep strengthening loss due to grain refinement [27,68,95]. For the same applied temperature of 650 °C, Figure 21 (right) displays the fatigue results in endured number of cycles  $N_f$  for several applied stresses  $\sigma_a$ . At first glance, the gradation from ex situ to in situ to unmodified LPBF material can be noted. As the modified versions performed better, a comparison could only be carried out at stresses of 150 and 175 MPa. At the higher stress level, the standard variant of the material did not even reach 2000 cycles. The GARS modification instead showed good fatigue properties of 80,000 cycles until failure, which marks a tremendous advancement already. However, the material designed by FBR throughout this study reached nearly 600,000 cycles. Therefore, similar to creep results, the post-FBR ex situ material showed excellent fatigue properties, not only outperforming the unmodified variant (300x improvement) but also the GARS one (7.5x improvement) due to nanoparticle presence on cell walls [31,113]. In conclusion, considering tensile, creep, and fatigue properties, the newly generated post-FBR ex situ modification marks a significant advancement in the material development of Alloy 400. The reason for the post-FBR material performing clearly better in terms of fatigue and creep during tensile testing, only revealing a slight improvement in comparison to the other two versions, is mainly due to the Orowan mechanism. The pinning of dislocations along the nanoparticles is much more pronounced during the long-term experiments of fatigue and creep. Tensile testing, in turn, occurs instantly, leaving significantly less space for a pronounced dispersoid–dislocation interaction (e.g., pinning of dislocations). This effect even intensifies with rising temperatures [7,31–35].

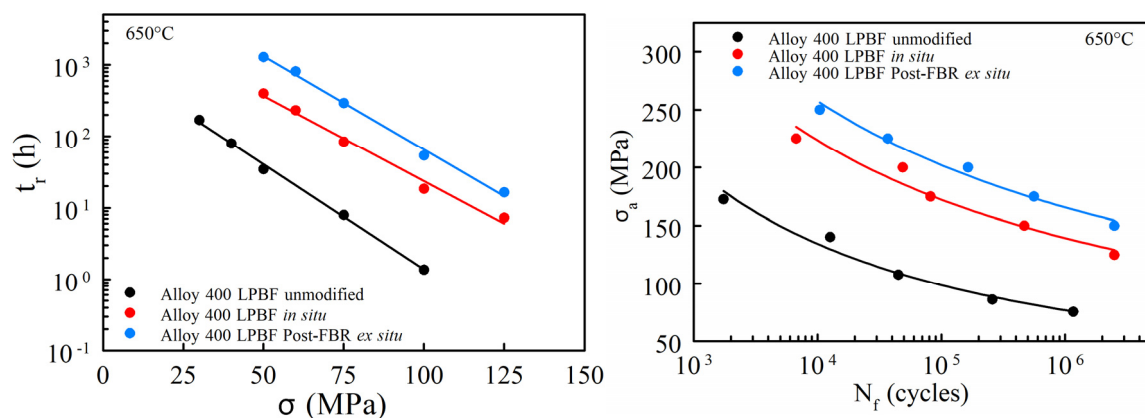


**Figure 21.** Creep (left) and fatigue (right) properties of unmodified reference, in situ GARS, and ex situ FBR material.

### 3.4.3. Thermal Diffusivity

The thermal diffusivity results given in Figure 22 draw a comparison between the different LPBF modifications of Alloy 400 throughout the whole temperature range. They show a clear trend of an increased thermal diffusivity with rising temperature [114]. While there is nearly no difference at low temperatures, a slight difference is observed for the slope of the “Alloy 400 LPBF unmodified” from 300 °C on. The difference is only marginal and can be correlated to the absence of nanoparticles. Apart from that, there are no significant deviations. This indicates that the FBR modification of powders, and thus, the final formation of nanoparticles on cell walls of parts, did not substantially alter the heat transport properties of the material in comparison to unmodified LPBF material (this conclusion is similar for the GARS routine). The results are considered a desirable outcome, as the mechanical properties were successfully improved, as shown previously, while simultaneously, a drawback in heat propagation was avoided, as required for heat exchangers as a potential final application [114–116].

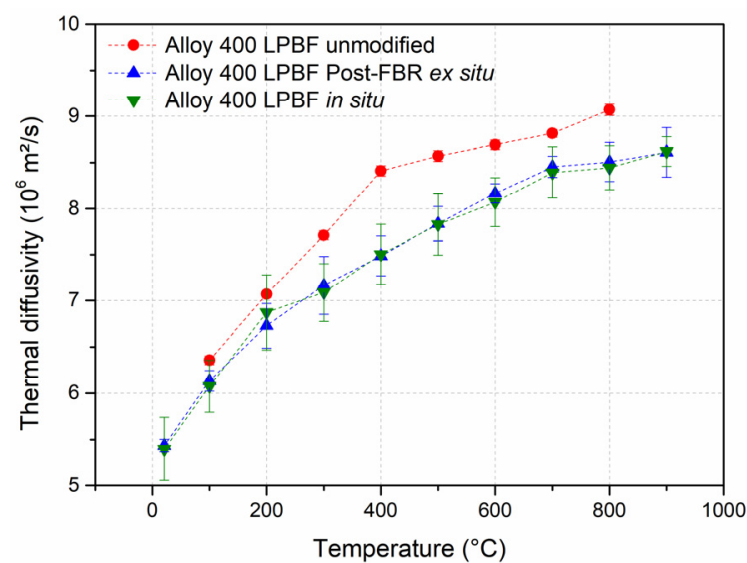


**Figure 22.** Thermal diffusivity for various modifications of Alloy 400 over temperature.

## 4. Conclusions

This work elaborated a new approach for a dispersion-strengthened Alloy 400 material system. Processing of shielding gas atomized powders in a fluidized bed reactor, where the particles were set to a nitrogen stream over time and temperature, resulted in a TiN-enriched powder feedstock for LPBF. In-depth characterization at both the micro- and nanoscale was carried out for both powders and parts resulting from this conditioning method, split up into a pre-FBR and a post-FBR fraction. This enabled specific improvements that resulted directly from the fluidized bed reactor process. Formation mechanisms for nanoparticle nucleation, segregation behavior, and cellular evolution of the nanostructure during melt pool solidification were provided and accompanied by mechanical testing of the components produced. Throughout the whole study, specific peculiarities of this *ex situ* approach were elaborated and set in comparison to the previously introduced *in situ* GARS variant [9]. Altogether, Table 2 summarizes the pre- and post-FBR results of this work and sets them in relation with the *in situ* material.

**Table 2.** Comparison between both process routes, the GARS in situ and the FBR ex situ nitridation approach for Alloy 400.

	In Situ Nitridation [9]	Pre-FBR Ex Situ Nitridation [This Work, Sections 3.1 and 3.3]	Post-FBR Ex Situ Nitridation [This Work, Sections 3.2–3.4]
Atomization type	GARS (nitrogen) CCA	Shielding gas (argon) CCA	-
Post treatment	-	-	FBR (nitrogen)
Targeted NP in powder	TiN	None	TiN
Detected NP in powder	TiN	TiN	TiN
Appearance form	Monomodal	Monomodal	Bimodal
Powder-TiN-NP diameter in [nm]	Fine: - Coarse: ~50–100	Fine: - Coarse: ~50–100	Fine: ~10 Coarse: ~50–100
NP share in powder in [%]	Surface: 0.12 Inside: 0.13	Surface: 0.96 Inside: 0.22	Surface: 1.80 Inside: 0.88
Bulk density in [g/cm <sup>3</sup> ]	4.62	4.3	4.7
Flowability in [s/50 g]	14.0	14.5	15.2
Particle size distribution in [d <sub>10</sub> /d <sub>50</sub> /d <sub>90</sub> ; µm]	17.3/30.7/51.5	21.3/37.9/58.1	20.2/38.8/59.8
Targeted NP in LPBF part	TiN	None	TiN
Detected NP in LPBF part	TiN, Al <sub>2</sub> O <sub>3</sub>	TiN, Al <sub>2</sub> O <sub>3</sub>	TiN, Al <sub>2</sub> O <sub>3</sub>
Appearance form	Monomodal	Monomodal	Bimodal
Part-TiN-NP diameter in [nm]	Fine: - Coarse: ~50–100	Fine: - Coarse: ~50–100	Fine: ~10 Coarse: ~50–100
NP share in part in [%]	3.88	0.12	6.53
Mean grain diameter in [µm]	6.78	5.20	7.44
GND density in [10 <sup>14</sup> /m <sup>2</sup> ]	3.58	4.73	4.86
Hardness in [HV10]	207.4	178.8	202.0
Tensile properties	Enhanced $\sigma$ and $\epsilon$ to unmodified material	-	Enhanced $\sigma$ and $\epsilon$ to in situ version
Creep properties	Longer $t_R$ to unmodified material	-	Longer $t_R$ to in situ version
Fatigue properties	Higher $N_f$ to unmodified material	-	Higher $N_f$ to in situ version
Thermal diffusivity	$\hat{=}$ ex situ	-	$\hat{=}$ in situ

Ultimately, and in accordance with the above-listed results, it can be concluded that a new, superior Alloy 400 system was generated via the application of the fluidized bed reactor.

**Author Contributions:** Conceptualization, J.-P.R., U.K. and K.J.; methodology, J.-P.R.; software, J.-P.R., I.Š. and M.G.; validation, J.-P.R.; formal analysis, J.-P.R. and G.B.; investigation, J.-P.R., I.Š., M.G., A.D. and G.B.; resources, F.P., U.K. and K.J.; data curation, J.-P.R., I.Š., M.G., A.D. and G.B.; writing—original draft preparation, J.-P.R.; writing—review and editing, J.-P.R., I.Š., F.P., U.K. and K.J.; visualization, J.-P.R., I.Š., M.G. and G.B.; supervision, J.-P.R., I.Š., G.B., F.P., U.K. and K.J.; project administration, F.P., U.K. and K.J.; funding acquisition, F.P., U.K. and K.J. All authors have read and agreed to the published version of the manuscript.

**Funding:** This research was funded by the European Union’s Horizon 2020 research and innovation program, grant number 958192.

**Data Availability Statement:** Dataset available on request from the authors.

**Acknowledgments:** The authors would like to acknowledge QuesTek Europe AB for providing the Ti-modified alloy composition.

**Conflicts of Interest:** The authors declare no conflicts of interest. The funders had no role in the design of the study; in the collection, analyses, or interpretation of data; in the writing of the manuscript; or in the decision to publish the results.

## References

1. Raffeis, I.; Adjei-Kyeremeh, F.; Vroomen, U.; Westhoff, E.; Bremen, S.; Hohoi, A.; Bührig-Polaczek, A. Qualification of a Ni–Cu Alloy for the Laser Powder Bed Fusion Process (LPBF): Its Microstructure and Mechanical Properties. *Appl. Sci.* **2020**, *10*, 3401. [CrossRef]
2. Shoemaker, L.E.; Smith, G.D. A century of monel metal: 1906–2006. *JOM* **2006**, *58*, 22–26. [CrossRef]
3. Special Metals Corporation. High-Performance Alloys for Resistance to Aqueous Corrosion 2000. Available online: <https://www.specialmetals.com/documents/aqueous-corrosion-handbook.pdf> (accessed on 18 August 2024).
4. Dutta, R.S. Corrosion aspects of Ni–Cr–Fe based and Ni–Cu based steam generator tube materials. *J. Nucl. Mater.* **2009**, *393*, 343–349. [CrossRef]
5. Küçük, Y.; Döleker, K.M.; Gök, M.S.; Dal, S.; Altınay, Y.; Erdoğan, A. Microstructure, hardness and high temperature wear characteristics of boronized Monel 400. *Surf. Coat. Technol.* **2022**, *436*, 128277. [CrossRef]
6. Jahns, K.; Ulrich, A.S.; Schlereth, C.; Reiff, L.; Krupp, U.; Galetz, M.C. The Effect of Cu Content and Surface Finish on the Metal Dusting Resistance of Additively Manufactured NiCu Alloys. *Oxid. Met.* **2021**, *96*, 241–256. [CrossRef]
7. Martin, J.H.; Yahata, B.D.; Hundley, J.M.; Mayer, J.A.; Schaedler, T.A.; Pollock, T.M. 3D printing of high-strength aluminium alloys. *Nature* **2017**, *549*, 365–369. [CrossRef]
8. Ma, S.; Shang, Z.; Shang, A.; Zhang, P.; Tang, C.; Huang, Y.; Leung, C.L.A.; Lee, P.D.; Zhang, X.; Wang, X. Additive manufacturing enabled synergetic strengthening of bimodal reinforcing particles for aluminum matrix composites. *Addit. Manuf.* **2023**, *70*, 103543. [CrossRef]
9. Roth, J.-P.; Šulák, I.; Chlup, Z.; Fischer-Bühner, J.; Krupp, U.; Jahns, K. The dispersion-strengthening effect of TiN evoked by in situ nitridation of NiCu-based Alloy 400 during gas atomization for laser powder bed fusion. *Mater. Sci. Eng. A* **2024**, *893*, 146129. [CrossRef]
10. Horn, T.; Rock, C.; Kaoumi, D.; Anderson, I.; White, E.; Prost, T.; Rieken, J.; Saptarshi, S.; Schoell, R.; DeJong, M.; et al. Laser powder bed fusion additive manufacturing of oxide dispersion strengthened steel using gas atomized reaction synthesis powder. *Mater. Des.* **2022**, *216*, 110574. [CrossRef]
11. Saptarshi, S.; deJong, M.; Rock, C.; Anderson, I.; Napolitano, R.; Forrester, J.; Lapidus, S.; Kaoumi, D.; Horn, T. Laser Powder Bed Fusion of ODS 14YWT from Gas Atomization Reaction Synthesis Precursor Powders. *JOM* **2022**, *74*, 3303–3315. [CrossRef]
12. Zhang, D.; Darsell, J.T.; Wang, J.; Ma, X.; Grant, G.J.; Anderson, I.E.; Rieken, J.R.; Edwards, D.J.; Setyawan, W.; Horn, T.J.; et al. No ball milling needed: Alternative ODS steel manufacturing with gas atomization reaction synthesis (GARS) and friction-based processing. *J. Nucl. Mater.* **2022**, *566*, 153768. [CrossRef]
13. Anderson, I.E.; Foley, J.C. Determining the role of surfaces and interfaces in the powder metallurgy processing of aluminum alloy powders. *Surf. Interface Anal.* **2001**, *31*, 599–608. [CrossRef]
14. Pereira, T.; Kennedy, J.V.; Potgieter, J. A comparison of traditional manufacturing vs additive manufacturing, the best method for the job. *Procedia Manuf.* **2019**, *30*, 11–18. [CrossRef]
15. Pérez, M.; Carou, D.; Rubio, E.M.; Teti, R. Current advances in additive manufacturing. *Procedia CIRP* **2020**, *88*, 439–444. [CrossRef]
16. Gibson, I.; Rosen, D.W.; Stucker, B. (Eds.) *Additive Manufacturing Technologies: 3D Printing, Rapid Prototyping, and Direct Digital Manufacturing*; Springer: New York, NY, USA, 2016; ISBN 978-3-030-56127-7.
17. Guth, S.; Babinský, T.; Antusch, S.; Klein, A.; Kuntz, D.; Šulák, I. Creep–Fatigue Interaction of Inconel 718 Manufactured by Electron Beam Melting. *Adv. Eng. Mater.* **2023**, *25*, 2300294. [CrossRef]
18. Šulák, I.; Babinský, T.; Chlupová, A.; Milovanović, A.; Náhlík, L. Effect of building direction and heat treatment on mechanical properties of Inconel 939 prepared by additive manufacturing. *J. Mech. Sci. Technol.* **2023**, *37*, 1071–1076. [CrossRef]
19. Handal, R. An implementation framework for additive manufacturing in supply chains. *JOSCM* **2017**, *10*, 18–31. [CrossRef]
20. Hopkinson, N.; Dicknes, P. Analysis of rapid manufacturing—Using layer manufacturing processes for production. *Proc. Inst. Mech. Eng. Part C J. Mech. Eng. Sci.* **2003**, *217*, 31–39. [CrossRef]
21. Safaei, K.; Abedi, H.; Nematollahi, M.; Kordizadeh, F.; Dabbaghi, H.; Bayati, P.; Javanbakht, R.; Jahadakbar, A.; Elahinia, M.; Poorganji, B. Additive Manufacturing of NiTi Shape Memory Alloy for Biomedical Applications: Review of the LPBF Process Ecosystem. *JOM* **2021**, *73*, 3771–3786. [CrossRef]
22. Cao, L.; Li, J.; Hu, J.; Liu, H.; Wu, Y.; Zhou, Q. Optimization of surface roughness and dimensional accuracy in LPBF additive manufacturing. *Opt. Laser Technol.* **2021**, *142*, 107246. [CrossRef]
23. Sanchez, S.; Smith, P.; Xu, Z.; Gaspard, G.; Hyde, C.J.; Wits, W.W.; Ashcroft, I.A.; Chen, H.; Clare, A.T. Powder Bed Fusion of nickel-based superalloys: A review. *Int. J. Mach. Tools Manuf.* **2021**, *165*, 103729. [CrossRef]



24. Tian, Z.; Zhang, C.; Wang, D.; Liu, W.; Fang, X.; Wellmann, D.; Zhao, Y.; Tian, Y. A Review on Laser Powder Bed Fusion of Inconel 625 Nickel-Based Alloy. *Appl. Sci.* **2020**, *10*, 81. [\[CrossRef\]](#)
25. Pollock, T.M.; Clarke, A.J.; Babu, S.S. Design and Tailoring of Alloys for Additive Manufacturing. *Met. Mater. Trans. A* **2020**, *51*, 6000–6019. [\[CrossRef\]](#)
26. Boes, J.; Röttger, A.; Becker, L.; Theisen, W. Processing of gas-nitrided AISI 316L steel powder by laser powder bed fusion—Microstructure and properties. *Addit. Manuf.* **2019**, *30*, 100836. [\[CrossRef\]](#)
27. Hadraba, H.; Chlup, Z.; Dlouhy, A.; Dobes, F.; Roupčova, P.; Vilemova, M.; Matejicek, J. Oxide dispersion strengthened CoCrFeNiMn high-entropy alloy. *Mater. Sci. Eng. A* **2017**, *689*, 252–256. [\[CrossRef\]](#)
28. Li, B.; Qian, B.; Xu, Y.; Liu, Z.; Zhang, J.; Xuan, F. Additive manufacturing of ultrafine-grained austenitic stainless steel matrix composite via vanadium carbide reinforcement addition and selective laser melting: Formation mechanism and strengthening effect. *Mater. Sci. Eng. A* **2019**, *745*, 495–508. [\[CrossRef\]](#)
29. Li, W.; Yang, Y.; Liu, J.; Zhou, Y.; Li, M.; Wen, S.; Wei, Q.; Yan, C.; Shi, Y. Enhanced nanohardness and new insights into texture evolution and phase transformation of TiAl/TiB 2 in-situ metal matrix composites prepared via selective laser melting. *Acta Mater.* **2017**, *136*, 90–104. [\[CrossRef\]](#)
30. Dai, S.; Zhu, J.; Yan, X.; Wu, S.; Liu, Y.; Gao, X.; Fraser, H.; Hodgson, P.; Zhu, Y.; Heilmaier, M.; et al. Unique Ytria Nanoparticle Strengthening in an Inconel 718 Superalloy Fabricated by Additive Manufacturing. *Adv. Mater. Technol.* **2024**, *9*, 2301421. [\[CrossRef\]](#)
31. Xu, R.; Geng, Z.; Wu, Y.; Chen, C.; Ni, M.; Li, D.; Zhang, T.; Huang, H.; Liu, F.; Li, R.; et al. Microstructure and mechanical properties of in-situ oxide-dispersion-strengthened NiCrFeY alloy produced by laser powder bed fusion. *Adv. Powder Mater.* **2022**, *1*, 100056. [\[CrossRef\]](#)
32. Smith, T.M.; Kantzos, C.A.; Zarkevich, N.A.; Harder, B.J.; Heczko, M.; Gradl, P.R.; Thompson, A.C.; Mills, M.J.; Gabb, T.P.; Lawson, J.W. A 3D printable alloy designed for extreme environments. *Nature* **2023**, *617*, 513–518. [\[CrossRef\]](#)
33. Smith, T.M.; Thompson, A.C.; Gabb, T.P.; Bowman, C.L.; Kantzos, C.A. Efficient production of a high-performance dispersion strengthened, multi-principal element alloy. *Sci. Rep.* **2020**, *10*, 9663. [\[CrossRef\]](#) [\[PubMed\]](#)
34. Yu, L.; Lu, Z.; Xian, J.; Chen, X.; Peng, S.; Li, X.; Li, H. Effects of Al content on microstructure and tensile properties of Ni-based ODS superalloys. *J. Alloys Compd.* **2023**, *941*, 168965. [\[CrossRef\]](#)
35. Jang, J.; Kim, T.K.; Han, C.H.; Min, H.-K.; Jeong, S.-H.; Kim, D.H. A Preliminary Development and Characterization of Ni-based ODS Alloys. *Procedia Eng.* **2013**, *55*, 284–288. [\[CrossRef\]](#)
36. Mirzababaei, S.; Ghayoor, M.; Doyle, R.P.; Pasebani, S. In-situ manufacturing of ODS FeCrAlY alloy via laser powder bed fusion. *Mater. Lett.* **2021**, *284*, 129046. [\[CrossRef\]](#)
37. Ramakrishnan, T.; Espiritu, E.R.; Kwon, S.; Keshavarz, M.K.; Muniz-Lerma, J.A.; Gauvin, R.; Brochu, M. Laser powder bed fusion additive manufacturing of molybdenum using a nitrogen build atmosphere. *Int. J. Refract. Met. Hard Mater.* **2024**, *119*, 106555. [\[CrossRef\]](#)
38. Chen, P.; Yang, C.; Li, S.; Attallah, M.M.; Yan, M. In-situ alloyed, oxide-dispersion-strengthened CoCrFeMnNi high entropy alloy fabricated via laser powder bed fusion. *Mater. Des.* **2020**, *194*, 108966. [\[CrossRef\]](#)
39. Tjong, S.C. Novel Nanoparticle-Reinforced Metal Matrix Composites with Enhanced Mechanical Properties. *Adv. Eng. Mater.* **2007**, *9*, 639–652. [\[CrossRef\]](#)
40. Šulák, I.; Chlupová, A.; Záležák, T.; Kuběna, I.; Roth, J.-P.; Jahns, K.; Krupp, U.; Kruml, T. High-temperature Fatigue and Creep Performance of Additively Manufactured NiCu-based Alloy. *Procedia Struct. Integr.* **2024**, *52*, 143–153. [\[CrossRef\]](#)
41. Narayana Samy, V.P.; Brasche, F.; Šulák, I.; Verma, B.; Nowak, B.; Chlup, Z.; Záležák, T.; Schleifenbaum, J.H.; Krupp, U.; Haase, C. The influence of microstructural heterogeneities on high-temperature mechanical properties of additively manufactured  $\gamma'$ -forming Ni-based alloys. *Addit. Manuf.* **2024**, *88*, 104267. [\[CrossRef\]](#)
42. Meltzer, R.L.; Fiorini, Y.R.; Horstman, R.T.; Moore, I.C.; Batik, A.L.; Hostinsky, T.; Čadek, J. A Constant Tensile Stress Creep Testing Machine. *J. Test. Eval.* **1976**, *4*, 26. [\[CrossRef\]](#)
43. Rettenmayr, M. Melting and remelting phenomena. *Int. Mater. Rev.* **2009**, *54*, 1–17. [\[CrossRef\]](#)
44. Qi, H.; Zhou, X.; Li, J.; Hu, Y.; Xu, L. Performance Testing and Rapid Solidification Behavior of Stainless Steel Powders Prepared by Gas Atomization. *Materials* **2021**, *14*, 5188. [\[CrossRef\]](#) [\[PubMed\]](#)
45. Gao, C.; Xiao, Z.; Zou, H.; Liu, Z.; Chen, J.; Li, S.; Zhang, D. Characterization of spherical AlSi10Mg powder produced by double-nozzle gas atomization using different parameters. *Trans. Nonferrous Met. Soc. China* **2019**, *29*, 374–384. [\[CrossRef\]](#)
46. Priyadarshi, A.; Bin Shahrani, S.; Choma, T.; Zrodowski, L.; Qin, L.; Leung, C.L.A.; Clark, S.J.; Fezzaa, K.; Mi, J.; Lee, P.D.; et al. New insights into the mechanism of ultrasonic atomization for the production of metal powders in additive manufacturing. *Addit. Manuf.* **2024**, *83*, 104033. [\[CrossRef\]](#)
47. Pellicer, E.; Varea, A.; Sivaraman, K.M.; Pané, S.; Suriñach, S.; Baró, M.D.; Nogués, J.; Nelson, B.J.; Sort, J. Grain boundary segregation and interdiffusion effects in nickel-copper alloys: An effective means to improve the thermal stability of nanocrystalline nickel. *ACS Appl. Mater. Interfaces* **2011**, *3*, 2265–2274. [\[CrossRef\]](#)
48. Naghash, A.R.; Etsell, T.H.; Xu, S. XRD and XPS Study of Cu–Ni Interactions on Reduced Copper–Nickel–Aluminum Oxide Solid Solution Catalysts. *Chem. Mater.* **2006**, *18*, 2480–2488. [\[CrossRef\]](#)
49. Erdélyi, Z.; Girardeaux, C.; Tókei, Z.; Beke, D.L.; Cserhádi, C.; Rolland, A. Investigation of the interplay of nickel dissolution and copper segregation in Ni/Cu(111) system. *Surf. Sci.* **2002**, *496*, 129–140. [\[CrossRef\]](#)

50. Guler, U.; Suslov, S.; Kildishev, A.V.; Boltasseva, A.; Shalae, V.M. Colloidal Plasmonic Titanium Nitride Nanoparticles: Properties and Applications. *Nanophotonics* **2015**, *4*, 269–276. [\[CrossRef\]](#)
51. Clatworthy, E.B.; Yick, S.; Murdock, A.T.; Allison, M.C.; Bendavid, A.; Masters, A.F.; Maschmeyer, T. Enhanced Photocatalytic Hydrogen Evolution with TiO<sub>2</sub>–TiN Nanoparticle Composites. *J. Phys. Chem. C* **2019**, *123*, 3740–3749. [\[CrossRef\]](#)
52. Alvarez Barragan, A.; Ilawe, N.V.; Zhong, L.; Wong, B.M.; Mangolini, L. A Non-Thermal Plasma Route to Plasmonic TiN Nanoparticles. *J. Phys. Chem. C* **2017**, *121*, 2316–2322. [\[CrossRef\]](#)
53. Tavares, J.; Coulombe, S.; Meunier, J.-L. Synthesis of cubic-structured monocrystalline titanium nitride nanoparticles by means of a dual plasma process. *J. Phys. D Appl. Phys.* **2009**, *42*, 102001. [\[CrossRef\]](#)
54. Chen, G.; Zhao, S.Y.; Tan, P.; Wang, J.; Xiang, C.S.; Tang, H.P. A comparative study of Ti-6Al-4V powders for additive manufacturing by gas atomization, plasma rotating electrode process and plasma atomization. *Powder Technol.* **2018**, *333*, 38–46. [\[CrossRef\]](#)
55. Yodoshi, N.; Endo, T.; Masahashi, N. Evaluation of Porosity in Gas-Atomized Powder by Synchrotron X-ray CT and Investigation of the Effect of Gas Species. *Mater. Trans.* **2021**, *62*, 1549–1555. [\[CrossRef\]](#)
56. Ruan, G.; Liu, C.; Qu, H.; Guo, C.; Li, G.; Li, X.; Zhu, Q. A comparative study on laser powder bed fusion of IN718 powders produced by gas atomization and plasma rotating electrode process. *Mater. Sci. Eng. A* **2022**, *850*, 143589. [\[CrossRef\]](#)
57. Liu, T.; Leazer, J.D.; Menon, S.K.; Brewer, L.N. Microstructural analysis of gas atomized Al-Cu alloy feedstock powders for cold spray deposition. *Surf. Coat. Technol.* **2018**, *350*, 621–632. [\[CrossRef\]](#)
58. Schwenck, D.; Ellendt, N.; Fischer-Bühner, J.; Hofmann, P.; Uhlenwinkel, V. A novel convergent–divergent annular nozzle design for close-coupled atomisation. *Powder Metall.* **2017**, *60*, 198–207. [\[CrossRef\]](#)
59. Mullis, A.M.; Farrell, L.; Cochrane, R.F.; Adkins, N.J. Estimation of Cooling Rates During Close-Coupled Gas Atomization Using Secondary Dendrite Arm Spacing Measurement. *Met. Mater. Trans. B* **2013**, *44*, 992–999. [\[CrossRef\]](#)
60. Ciftci, N.; Ellendt, N.; Coulthard, G.; Soares Barreto, E.; Mädler, L.; Uhlenwinkel, V. Novel Cooling Rate Correlations in Molten Metal Gas Atomization. *Met. Mater. Trans. B* **2019**, *50*, 666–677. [\[CrossRef\]](#)
61. Soares Barreto, E.; Frey, M.; Wegner, J.; Jose, A.; Neuber, N.; Busch, R.; Kleszczynski, S.; Mädler, L.; Uhlenwinkel, V. Properties of gas-atomized Cu-Ti-based metallic glass powders for additive manufacturing. *Mater. Des.* **2022**, *215*, 110519. [\[CrossRef\]](#)
62. Mani, C.; Karthikeyan, R.; Kannan, S. Electrochemical Impedance Analysis on Cryogenically Treated Dissimilar Metal Welding of 316L Stainless Steel and Monel 400 Alloy Using GTAW. *Metals* **2019**, *9*, 1088. [\[CrossRef\]](#)
63. Kostryzhev, A.G.; Marenych, O.O.; Pan, Z.; Li, H.; van Duin, S. Strengthening mechanisms in Monel K500 alloyed with Al and Ti. *J. Mater. Sci.* **2023**, *58*, 4150–4164. [\[CrossRef\]](#)
64. Tian, Y.T.; Li, Y.; Xia, L.; Man, T.H. Research on New Technology of Metal Powder-Plate Composite Rolling. *Int. Conf. Adv. Mater. Eng. Mater.* **2020**, *861*, 41–45. [\[CrossRef\]](#)
65. Wei, P.; Chen, Z.; Zhang, S.; Li, B.; Han, J.; Lu, B. Microstructure and mechanical properties of graphene and nano-zirconia reinforced AlSi10Mg composite fabricated by laser powder bed fusion. *Mater. Sci. Eng. A* **2023**, *864*, 144574. [\[CrossRef\]](#)
66. Doñate-Buendia, C.; Kürnsteiner, P.; Stern, F.; Wilms, M.B.; Streubel, R.; Kusoglu, I.M.; Tenkamp, J.; Bruder, E.; Pirch, N.; Barcikowski, S.; et al. Microstructure formation and mechanical properties of ODS steels built by laser additive manufacturing of nanoparticle coated iron-chromium powders. *Acta Mater.* **2021**, *206*, 116566. [\[CrossRef\]](#)
67. Zhang, Z.; Chen, D.L. Contribution of Orowan strengthening effect in particulate-reinforced metal matrix nanocomposites. *Mater. Sci. Eng. A* **2008**, *483–484*, 148–152. [\[CrossRef\]](#)
68. Kang, Y.; Han, Q.; Zhao, X.; Cai, M. Influence of nanoparticle reinforcements on the strengthening mechanisms of an ultrafine-grained dual phase steel containing titanium. *Mater. Des.* **2013**, *44*, 331–339. [\[CrossRef\]](#)
69. Zou, L.; Yang, C.; Lei, Y.; Zakharov, D.; Wiezorek, J.M.K.; Su, D.; Yin, Q.; Li, J.; Liu, Z.; Stach, E.A.; et al. Dislocation nucleation facilitated by atomic segregation. *Nat. Mater.* **2018**, *17*, 56–63. [\[CrossRef\]](#)
70. Marenych, O.O.; Ding, D.; Pan, Z.; Kostryzhev, A.G.; Li, H.; van Duin, S. Effect of chemical composition on microstructure, strength and wear resistance of wire deposited Ni-Cu alloys. *Addit. Manuf.* **2018**, *24*, 30–36. [\[CrossRef\]](#)
71. Kannan, A.R.; Kumar, S.M.; Pramod, R.; Shanmugam, N.S.; Vishnukumar, M.; Channabasavanna, S.G. Microstructure and corrosion resistance of Ni-Cu alloy fabricated through wire arc additive manufacturing. *Mater. Lett.* **2022**, *308*, 131262. [\[CrossRef\]](#)
72. Marenych, O.; Kostryzhev, A. Strengthening Mechanisms in Nickel-Copper Alloys: A Review. *Metals* **2020**, *10*, 1358. [\[CrossRef\]](#)
73. Ting, J.; Peretti, M.W.; Eisen, W.B. The effect of wake-closure phenomenon on gas atomization performance. *Mater. Sci. Eng. A* **2002**, *326*, 110–121. [\[CrossRef\]](#)
74. Vedovato, G.; Zambon, A.; Ramous, E. A simplified model for gas atomization. *Mater. Sci. Eng. A* **2001**, *304–306*, 235–239. [\[CrossRef\]](#)
75. Tournet, D.; Reinhart, G.; Gandin, C.-A.; Iles, G.N.; Dahlborg, U.; Calvo-Dahlborg, M.; Bao, C.M. Gas atomization of Al-Ni powders: Solidification modeling and neutron diffraction analysis. *Acta Mater.* **2011**, *59*, 6658–6669. [\[CrossRef\]](#)
76. Ertay, D.S.; Ma, H.; Vlasea, M. *Correlative Beam Path and Pore Defect Space Analysis for Modulated Powder Bed Laser Fusion Process*; Solid Freeform Fabrication Symposium, University of Texas at Austin: Austin, TX, USA, 2018.
77. Ulbricht, A.; Mohr, G.; Altenburg, S.J.; Oster, S.; Maierhofer, C.; Bruno, G. Can Potential Defects in LPBF Be Healed from the Laser Exposure of Subsequent Layers? A Quantitative Study. *Metals* **2021**, *11*, 1012. [\[CrossRef\]](#)

78. Hojjatzadeh, S.M.H.; Parab, N.D.; Guo, Q.; Qu, M.; Xiong, L.; Zhao, C.; Escano, L.I.; Fezzaa, K.; Everhart, W.; Sun, T.; et al. Direct observation of pore formation mechanisms during LPBF additive manufacturing process and high energy density laser welding. *Int. J. Mach. Tools Manuf.* **2020**, *153*, 103555. [\[CrossRef\]](#)
79. Kan, W.H.; Chiu, L.N.S.; Lim, C.V.S.; Zhu, Y.; Tian, Y.; Jiang, D.; Huang, A. A critical review on the effects of process-induced porosity on the mechanical properties of alloys fabricated by laser powder bed fusion. *J. Mater. Sci.* **2022**, *57*, 9818–9865. [\[CrossRef\]](#)
80. Kan, W.H.; Gao, M.; Zhang, X.; Liang, E.; Chiu, N.S.L.; Lim, C.V.S.; Huang, A. The influence of porosity on Ti-6Al-4V parts fabricated by laser powder bed fusion in the pursuit of process efficiency. *Int. J. Adv. Manuf. Technol.* **2022**, *119*, 5417–5438. [\[CrossRef\]](#)
81. Voisin, T.; Calta, N.P.; Khairallah, S.A.; Forien, J.-B.; Balogh, L.; Cunningham, R.W.; Rollett, A.D.; Wang, Y.M. Defects-dictated tensile properties of selective laser melted Ti-6Al-4V. *Mater. Des.* **2018**, *158*, 113–126. [\[CrossRef\]](#)
82. Huang, Y.; Fleming, T.G.; Clark, S.J.; Marussi, S.; Fezzaa, K.; Thiyaalingam, J.; Leung, C.L.A.; Lee, P.D. Keyhole fluctuation and pore formation mechanisms during laser powder bed fusion additive manufacturing. *Nat. Commun.* **2022**, *13*, 1170. [\[CrossRef\]](#)
83. Li, C.; White, R.; Fang, X.Y.; Weaver, M.; Guo, Y.B. Microstructure evolution characteristics of Inconel 625 alloy from selective laser melting to heat treatment. *Mater. Sci. Eng. A* **2017**, *705*, 20–31. [\[CrossRef\]](#)
84. Pilz, S.; Gustmann, T.; Günther, F.; Zimmermann, M.; Kühn, U.; Gebert, A. Controlling the Young's modulus of a  $\beta$ -type Ti-Nb alloy via strong texturing by LPBF. *Mater. Des.* **2022**, *216*, 110516. [\[CrossRef\]](#)
85. Avateffazeli, M.; Carrion, P.E.; Shachi-Amirkhiz, B.; Pirgazi, H.; Mohammadi, M.; Shamsaei, N.; Haghshenas, M. Correlation between tensile properties, microstructure, and processing routes of an Al-Cu-Mg-Ag-TiB<sub>2</sub> (A205) alloy: Additive manufacturing and casting. *Mater. Sci. Eng. A* **2022**, *841*, 142989. [\[CrossRef\]](#)
86. Krakhmalev, P.; Fredriksson, G.; Svensson, K.; Yadroitsev, I.; Yadroitsava, I.; Thuvander, M.; Peng, R. Microstructure, Solidification Texture, and Thermal Stability of 316 L Stainless Steel Manufactured by Laser Powder Bed Fusion. *Metals* **2018**, *8*, 643. [\[CrossRef\]](#)
87. Cordero, Z.C.; Knight, B.E.; Schuh, C.A. Six decades of the Hall–Petch effect—A survey of grain-size strengthening studies on pure metals. *Int. Mater. Rev.* **2016**, *61*, 495–512. [\[CrossRef\]](#)
88. Zhao, Y.; Ma, T.; Gao, Z.; Feng, Y.; Li, C.; Guo, Q.; Ma, Z.; Liu, Y. Significant reduction of grain size and texture intensity in laser powder bed fusion fabricated nickel-based superalloy by increasing constitutional supercooling. *Compos. Part B Eng.* **2023**, *266*, 111040. [\[CrossRef\]](#)
89. Muránsky, O.; Balogh, L.; Tran, M.; Hamelin, C.J.; Park, J.-S.; Daymond, M.R. On the measurement of dislocations and dislocation substructures using EBSD and HRSD techniques. *Acta Mater.* **2019**, *175*, 297–313. [\[CrossRef\]](#)
90. Smith, J.; Xiong, W.; Yan, W.; Lin, S.; Cheng, P.; Kafka, O.L.; Wagner, G.J.; Cao, J.; Liu, W.K. Linking process, structure, property, and performance for metal-based additive manufacturing: Computational approaches with experimental support. *Comput. Mech.* **2016**, *57*, 583–610. [\[CrossRef\]](#)
91. Zhang, X.X.; Andrä, H.; Harjo, S.; Gong, W.; Kawasaki, T.; Lutz, A.; Lahres, M. Quantifying internal strains, stresses, and dislocation density in additively manufactured AlSi10Mg during loading-unloading-reloading deformation. *Mater. Des.* **2021**, *198*, 109339. [\[CrossRef\]](#)
92. Voisin, T.; Forien, J.-B.; Perron, A.; Aubry, S.; Bertin, N.; Samanta, A.; Baker, A.; Wang, Y.M. New insights on cellular structures strengthening mechanisms and thermal stability of an austenitic stainless steel fabricated by laser powder-bed-fusion. *Acta Mater.* **2021**, *203*, 116476. [\[CrossRef\]](#)
93. Kong, D.; Dong, C.; Wei, S.; Ni, X.; Zhang, L.; Li, R.; Wang, L.; Man, C.; Li, X. About metastable cellular structure in additively manufactured austenitic stainless steels. *Addit. Manuf.* **2021**, *38*, 101804. [\[CrossRef\]](#)
94. Bertsch, K.M.; Meric de Bellefon, G.; Kuehl, B.; Thoma, D.J. Origin of dislocation structures in an additively manufactured austenitic stainless steel 316L. *Acta Mater.* **2020**, *199*, 19–33. [\[CrossRef\]](#)
95. Gao, C.; Wang, Z.; Xiao, Z.; You, D.; Wong, K.; Akbarzadeh, A.H. Selective laser melting of TiN nanoparticle-reinforced AlSi10Mg composite: Microstructural, interfacial, and mechanical properties. *J. Mater. Process. Technol.* **2020**, *281*, 116618. [\[CrossRef\]](#)
96. Jena, A.; Atabay, S.E.; Gontcharov, A.; Lowden, P.; Brochu, M. Laser powder bed fusion of a new high gamma prime Ni-based superalloy with improved weldability. *Mater. Des.* **2021**, *208*, 109895. [\[CrossRef\]](#)
97. Huang, Z.; Zhai, Z.; Lin, W.; Chang, H.; Wu, Y.; Yang, R.; Zhang, Z. On the orientation dependent microstructure and mechanical behavior of Hastelloy X superalloy fabricated by laser powder bed fusion. *Mater. Sci. Eng. A* **2022**, *844*, 143208. [\[CrossRef\]](#)
98. Qin, H.; Dong, Q.; Fallah, V.; Daymond, M.R. Rapid Solidification and Non-equilibrium Phase Constitution in Laser Powder Bed Fusion (LPBF) of AlSi10Mg Alloy: Analysis of Nano-precipitates, Eutectic Phases, and Hardness Evolution. *Met. Mater. Trans. A* **2020**, *51*, 448–466. [\[CrossRef\]](#)
99. Li, J.; Cheng, T.; Liu, Y.; Yang, Y.; Li, W.; Wei, Q. Simultaneously enhanced strength and ductility of Cu-15Ni-8Sn alloy with periodic heterogeneous microstructures fabricated by laser powder bed fusion. *Addit. Manuf.* **2022**, *54*, 102726. [\[CrossRef\]](#)
100. Song, Z.; Gao, S.; Wang, Z.; Lan, L.; Hou, J.; He, B. Effects of non-equilibrium microstructures on microstructure evolution and mechanical properties of laser powder bed fusion IN625 Ni-based superalloy during long-term thermal exposure at 700 °C and 750 °C. *Mater. Sci. Eng. A* **2022**, *856*, 143883. [\[CrossRef\]](#)
101. Jodi, D.E.; Kitashima, T.; Singh, A.; Watanabe, M. High-temperature microstructural stability of pure Ni fabricated by laser powder bed fusion using Gaussian and flat-top beam profiles. *Mater. Charact.* **2023**, *200*, 112897. [\[CrossRef\]](#)

102. Bassini, E.; Sivo, A.; Martelli, P.A.; Rajczak, E.; Marchese, G.; Calignano, F.; Biamino, S.; Ugues, D. Effects of the solution and first aging treatment applied to as-built and post-HIP CM247 produced via laser powder bed fusion (LPBF). *J. Alloys Compd.* **2022**, *905*, 164213. [\[CrossRef\]](#)
103. Hatakeyama, T.; Sawada, K.; Suzuki, M.; Watanabe, M. Microstructure development of modified 9Cr-1Mo steel during laser powder bed fusion and heat treatment. *Addit. Manuf.* **2023**, *61*, 103350. [\[CrossRef\]](#)
104. Jiang, R.; Mostafaei, A.; Wu, Z.; Choi, A.; Guan, P.-W.; Chmielus, M.; Rollett, A.D. Effect of heat treatment on microstructural evolution and hardness homogeneity in laser powder bed fusion of alloy 718. *Addit. Manuf.* **2020**, *35*, 101282. [\[CrossRef\]](#)
105. Okugawa, M.; Saito, K.; Yoshima, H.; Sawaizumi, K.; Nomoto, S.; Watanabe, M.; Nakano, T.; Koizumi, Y. Solute segregation in a rapidly solidified Hastelloy-X Ni-based superalloy during laser powder bed fusion investigated by phase-field and computational thermal-fluid dynamics simulations. *Addit. Manuf.* **2024**, *84*, 104079. [\[CrossRef\]](#)
106. Seede, R.; Zhang, B.; Whitt, A.; Picak, S.; Gibbons, S.; Flater, P.; Elwany, A.; Arroyave, R.; Karaman, I. Effect of heat treatments on the microstructure and mechanical properties of an ultra-high strength martensitic steel fabricated via laser powder bed fusion additive manufacturing. *Addit. Manuf.* **2021**, *47*, 102255. [\[CrossRef\]](#)
107. Gu, D.; Zhang, H.; Dai, D.; Xia, M.; Hong, C.; Poprawe, R. Laser additive manufacturing of nano-TiC reinforced Ni-based nanocomposites with tailored microstructure and performance. *Compos. Part B Eng.* **2019**, *163*, 585–597. [\[CrossRef\]](#)
108. Marenych, O.O.; Kostryzhev, A.G.; Pan, Z.; Li, H.; van Duin, S. Comparative effect of Mn/Ti solute atoms and TiC/Ni<sub>3</sub>(Al,Ti) nano-particles on work hardening behaviour in Ni Cu alloys fabricated by wire arc additive manufacturing. *Mater. Sci. Eng. A* **2019**, *753*, 262–275. [\[CrossRef\]](#)
109. Mukhopadhyay, A.; Urkude, D.K.; Mukhopadhyay, G. Effect of Cold Work on Hydrogen Embrittlement of Monel-400. *J. Fail. Anal. Preven.* **2024**, *24*, 279–290. [\[CrossRef\]](#)
110. Janardhan, G.; Kishore, K.; Dutta, K.; Mukhopadhyay, G. Tensile and fatigue behavior of resistance spot-welded HSLA steel sheets: Effect of pre-strain in association with dislocation density. *Mater. Sci. Eng. A* **2020**, *793*, 139796. [\[CrossRef\]](#)
111. Jeong, W.C. Effect of prestrain on aging and bake hardening of cold-rolled, continuously annealed steel sheets. *Met. Mater. Trans. A* **1998**, *29*, 463–467. [\[CrossRef\]](#)
112. Smith, B.A.; Laursen, C.M.; Bartanus, J.; Carroll, J.D.; Pataky, G.J. The Interplay of Geometric Defects and Porosity on the Mechanical Behavior of Additively Manufactured Components. *Exp. Mech.* **2021**, *61*, 685–698. [\[CrossRef\]](#)
113. Yin, D.; Liu, H.; Chen, Y.; Yi, D.; Wang, B.; Wang, B.; Shen, F.; Fu, S.; Tang, C.; Pan, S. Effect of grain size on fatigue-crack growth in 2524 aluminium alloy. *Int. J. Fatigue* **2016**, *84*, 9–16. [\[CrossRef\]](#)
114. Boissonnet, G.; Boulesteix, C.; Bonnet, G.; Balmain, J.; Pedraza, F. Thermal Transport Properties of New Coatings on Steels for Supercritical Steam Power Plants. *Oxid. Met.* **2017**, *88*, 191–202. [\[CrossRef\]](#)
115. Boissonnet, G.; Bonnet, G.; Pasquet, A.; Bourhila, N.; Pedraza, F. Evolution of thermal insulation of plasma-sprayed thermal barrier coating systems with exposure to high temperature. *J. Eur. Ceram. Soc.* **2019**, *39*, 2111–2121. [\[CrossRef\]](#)
116. Boissonnet, G.; Bonnet, G.; Pedraza, F. Thermo-Physical Properties of HR3C and P92 Steels at High-Temperature. *J. Mater. Appl.* **2019**, *8*, 59–64. [\[CrossRef\]](#)

**Disclaimer/Publisher's Note:** The statements, opinions and data contained in all publications are solely those of the individual author(s) and contributor(s) and not of MDPI and/or the editor(s). MDPI and/or the editor(s) disclaim responsibility for any injury to people or property resulting from any ideas, methods, instructions or products referred to in the content.

# Chapter 8

APPENDIX



**8.1 Comparison of  
Microstructure and Properties  
of Nickel-Copper Alloy  
Prepared by Casting and  
Laser Powder Bed Fusion  
Process**

Alice Chlupová, Ivo Šulák, Ivo Kuběna,  
Tomáš Kruml, **Jan-Philipp Roth**, Katrin  
Jahns

Materials Science Forum 1082 (2023)  
171–176

DOI 10.4028/p-884q32

Reference [4]

## Comparison of Microstructure and Properties of Nickel-Copper Alloy Prepared by Casting and Laser Powder Bed Fusion Process

Alice Chlupová<sup>1,a\*</sup>, Ivo Šulák<sup>1,b</sup>, Ivo Kuběna<sup>1,c</sup>, Tomáš Kruml<sup>1,d</sup>,  
Jan-Philipp Roth<sup>2,e</sup> and Katrin Jahns<sup>2,3,f</sup>

<sup>1</sup>Institute of Physics of Materials, The Czech Academy of Sciences, Žitkova 22, 616 00 Brno, Czech Republic

<sup>2</sup>Laboratory for Materials Design and Structural Integrity, Osnabrück University of Applied Sciences, Albrechtstr. 30, 49076 Osnabrück, Germany

<sup>3</sup>Steel Institute IEHK, RWTH Aachen University, Intzestraße 1, 52072 Aachen, Germany

<sup>a\*</sup>chlupova@ipm.cz, <sup>b</sup>sulak@ipm.cz, <sup>c</sup>kubena@ipm.cz, <sup>d</sup>kruml@ipm.cz, <sup>e</sup>j.roth@hs-osnabrueck.de, <sup>f</sup>katrin.jahns@iehk.rwth-aachen.de

**Keywords:** nickel-copper alloy; microstructure; tensile properties; fractography; casting; laser powder bed fusion.

**Abstract.** Nickel-copper alloys are commonly used in highly corrosive conditions where strength is required. Typical applications are in the marine sector, petrochemical industry, or energy facilities such as chemical tubes, pumps, heat exchangers and superheated steam systems. This paper compares the microstructure and mechanical properties of a cast alloy with a 3D printed alloy processed via a laser powder bed fusion (LPBF) technique. Small cylindrical specimens were used for tensile tests at room temperature (RT) and elevated temperatures up to 750 °C in air. The tensile stress-strain response was determined for both types of materials. At RT, LPBF material has a higher yield strength and ultimate tensile strength than a cast alloy. At elevated temperatures, the strength of both variants is comparable. However, the fracture elongation of the LPBF material is significantly lower over the entire range of investigated temperatures. Fracture surfaces and polished sections parallel to the specimen axis were investigated to compare the microstructure and damage mechanisms of the nickel-copper alloy 400 prepared by conventional casting and via LPBF.

### Introduction

Nickel-copper-based alloys contain usually from 52 to 67 % nickel. The high variability of alloying elements gives rise to materials with a wide range of properties. Alloy 400 (material number 2.4360) is a single phase alloy strengthened by Mn, Si, Fe and C [1]. Alloy 400 is stronger than pure nickel; its high toughness is maintained over a considerable range of temperatures. It also has good ductility and thermal conductivity. It has excellent mechanical properties at subzero temperatures without a ductile-to-brittle transition. It exhibits relatively low hardness between 115 and 250 HV which excludes this material from applications exposed to adhesive wear, erosion, or cavitation. Alloy 400 offers exceptional resistance to corrosion by many aggressive agents, i.e. hydrofluoric, sulfuric and hydrochloric acids and rapidly flowing seawater. It is commonly used in highly corrosive conditions in applications where strength is needed as pumps in marine engineering, heat exchangers and condenser tubes in the chemical industry and superheated steam systems in power applications [2, 3].

Additive manufacturing (AM) has developed significantly in recent years. It can be used not only for the improvement of functionality and weight reduction of complex-shape components that are difficult to produce by conventional machining but also for maintenance and repair operations [4]. With the evolvement of AM and a price reduction for 3D printers, the possibilities to create functional end-use components not only from plastics but also from metals have been expanded [5]. As additive manufacturing becomes more feasible, there is a growing need to increase knowledge of the microstructure and associated mechanical properties of 3D printed metallic materials. Laser powder bed fusion (LPBF) is an AM process where a laser is used as a heat source to fuse powder feedstock

to create a 3D object [4]. Lasers are widely used in metal processing due to their ability to deliver high power focused in a precise spot and quickly heat the material. This feature makes the laser a perfect device for obtaining specific properties in metals due to microstructural modification. Moreover, another advantage can be seen in changes in chemical composition if additional material is supplied to the molten pool, e.g. oxides to obtain the ODS version of the material [6].

The work is aimed to compare the microstructure and fracture mode of the Alloy 400 prepared either conventionally by casting or unconventionally by the LPBF method. The effect of microstructure on mechanical properties and appearance of the fracture under mechanical loading was monitored and discussed in terms of material production way.

## Experiment

The chemical composition of the Alloy 400 alloy according to DIN 17743 is listed in Table 1. Two types of materials were studied, i.e. cast and prepared by LPBF. Microstructural analysis was performed on the cross-sectional metallographic samples prepared by grinding with SiC papers and polishing with silica suspensions. Both cast and LPBF materials were characterized by scanning electron microscopy (SEM) using TESCAN LYRA 3 XMU FEG/SEM x FIB. Grain size and orientation were characterized using electron backscatter diffraction (EBSD). The EBSD data were acquired using an Oxford Symmetry EBSD detector with an Aztec control system. To determine the mechanical properties of the two types of Alloy 400, cylindrical specimens with a gauge length of 9 mm and diameter of 3 mm were used. Specimens were machined at IPM; the specimen axis for the LPBF variant was perpendicular to the building direction. Tensile tests were performed until a complete fracture using a universal test system (Instron 8862) with an electromechanical actuator at a cross-head displacement rate of 1 mm/min. The morphology of the fracture surfaces was observed using SEM to analyse the failure mechanisms.

Table 1 Chemical composition of Alloy 400 [wt. %]

Cu	Fe	Mn	Si	Al	C	Ni
28 – 34	1.0 – 2.5	2.0 max	0.5 max	0.5 max	0.15 max	63 min

## Results and Discussion

The microstructure of Alloy 400 prepared by two different methods, i.e. conventional casting and LPBF is presented in Fig. 1. The microstructure of the cast variant is composed of equiaxed grains with the presence of twins typical for cast material (Fig. 1a). The grain orientation map in the Z direction is shown in Fig. 1b and it revealed the random grain orientation. The microstructure of LPBF material is composed of cells / melting pools typical for materials prepared by this type of AM (Fig. 1c). The material exhibits preferential  $\langle 110 \rangle$  orientation in the building direction and random orientation in the perpendicular directions (see Fig. 1d).

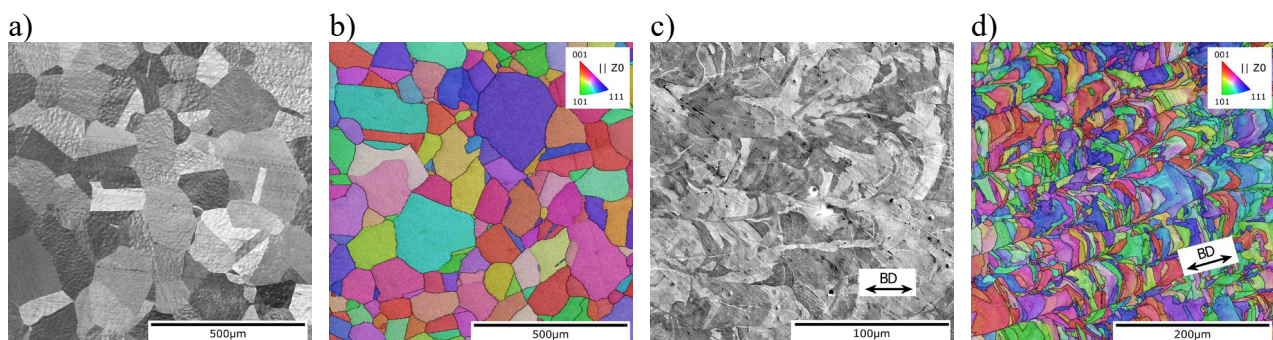


Fig. 1 SEM micrographs and EBSD maps for the cast (a,b) and LPBF variant (c,d) of Alloy 400.

Contrary to the conventionally prepared material, no twins were detected. The average grain size of both material variants as obtained from EBSD data post-processing is: cast =  $63 \pm 49 \mu\text{m}$  (excluding twin boundaries), LPBF =  $16 \pm 11 \mu\text{m}$ . The density of the LPBF variant was evaluated from metallographic sections to 99.5 %.

Tensile properties were evaluated up to  $750^\circ\text{C}$  and results are plotted in Fig. 2. For comparable temperatures, higher values of yield and ultimate tensile strength exhibited the LPBF variant of Alloy 400, nevertheless, the plasticity decreased. These results are supported by the findings of Raffels [7]. The higher strength can be ascribed to the significant refinement of the microstructure. However, contrary to the result in [7] the fracture elongation is lower, which can be explained by the presence of defects in the LPBF variant of material as was confirmed by fractography analysis.

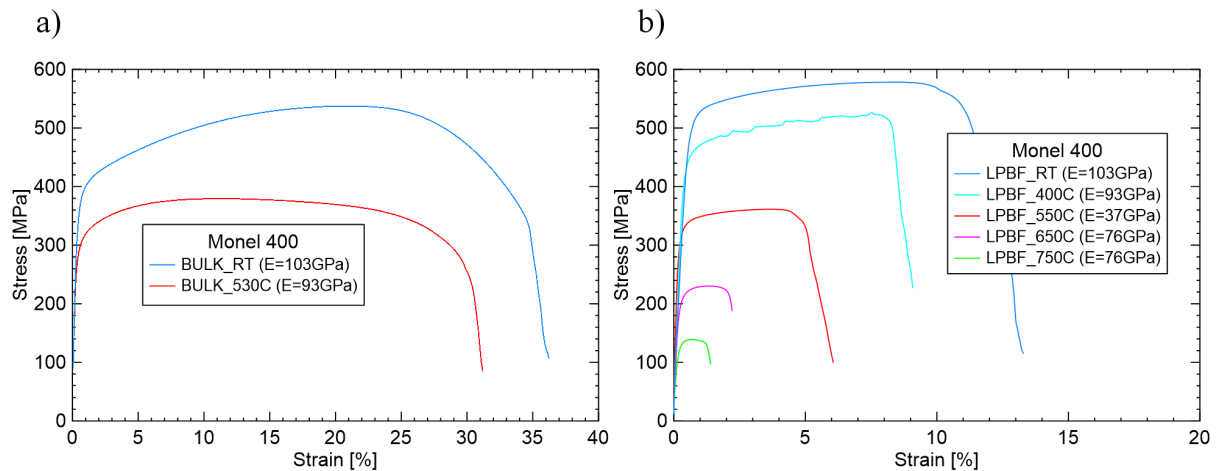


Fig. 2 Tensile properties: cast (a) and LPBF variant (b) of Alloy 400 at different temperatures.

Fracture surfaces of the specimens tested at two temperatures were selected for fractographical observation (Fig. 3). Initial visual investigation revealed high plasticity accompanied by strong necking in the case of cast material. The fracture surface was rough with significant height differences. In comparison with that, fracture surfaces of specimens prepared by LPBF exhibited small height differences, i.e. the fracture surface was relatively flat and part of the fracture consisted of pores arranged in rows. The lower plasticity was confirmed by weak necking of specimens before fracture, nevertheless, the dimples typically associated with ductile fracture were observed at higher magnification.

Results of detailed observation of typical patterns present on a fracture surface of the tensile specimen of cast variant tested at RT are shown in Fig. 4. The micrograph in Fig 4a shows typical ductile dimples. In Fig. 4b, there are wrinkles present on the cylindrical part of gauge length resulting from strong plastic deformation in the area of necking. Similar features were observed for a cast specimen tested at  $530^\circ\text{C}$  where slightly smaller ductile dimples were observed and additional features in the form of oxide layer were present.

Analogically to the cast specimen, the thorough analysis of typical fractography patterns on the fractured specimen from LPBF material was performed and results for the specimen tested at RT are shown in Fig. 5. In comparison with the cast variant, the necking is weak and the whole fracture surface exhibits quite low height differences (see overview in Fig. 5a). The fracture surface consists of mainly two patterns: bands of large pores (keyholes) arranged in rows (see Fig. 5b) and a slightly dimpled surface (see Fig. 5c). The cylindrical part of the LPBF specimen shows a flat surface. It is important to note that the surface was post-processed and it does not show an outer surface processed by LPBF. Similar features on the fracture surface were observed in the case of the LPBF specimen tested at  $550^\circ\text{C}$ . Except for ductile dimples and the bands of keyhole porosity also the occasional presence of „cleavage-like“ facets was observed. It confirms the lower plasticity in comparison with the specimen tested at RT (see the plot in Fig. 2b where fracture elongation decreases from 13 % at RT to 6 % at  $550^\circ\text{C}$ ).

The formation of internal defects depends strongly on the applied processing conditions and set up parameters so they can be seen as a particular process fingerprint. Different pore sizes, shapes, and distributions result in different stress concentrations and stimulate the initiation and propagation of cracks differently. No casting defects were observed on the fracture surface of cast specimens of Alloy 400, nevertheless, the LPBF variant of material exhibited the occurrence of printing defects. In [8], a comprehensive description of the formation of pores during the LPBF process was published concerning process parameters such as laser power, distance of melt pools, powder layer thickness, scanning speed, scanning strategy, powder properties, inert gas, etc. and three types of defects were described: 1) lack-of-fusion defects (LOF), 2) gas porosity and 3) balling.

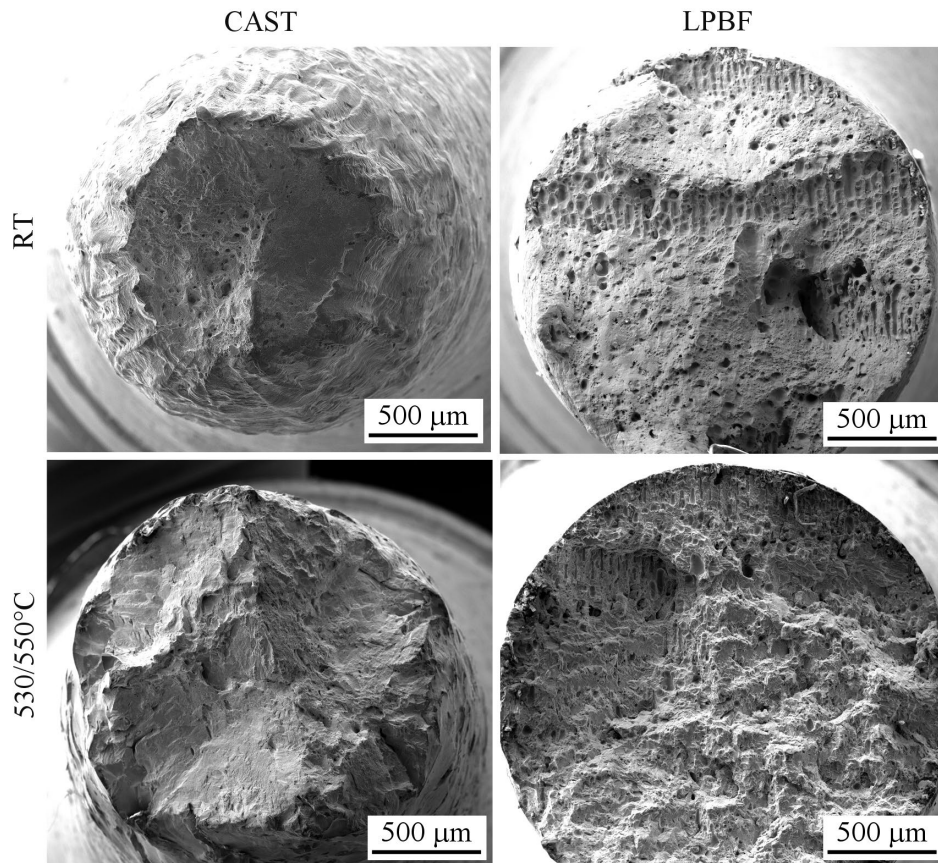


Fig. 3 Micrographs of fracture surfaces of tensile specimens for the cast (left) and LPBF variant (right) of Alloy 400 at RT (up) and elevated temperature 530/550 °C (down).

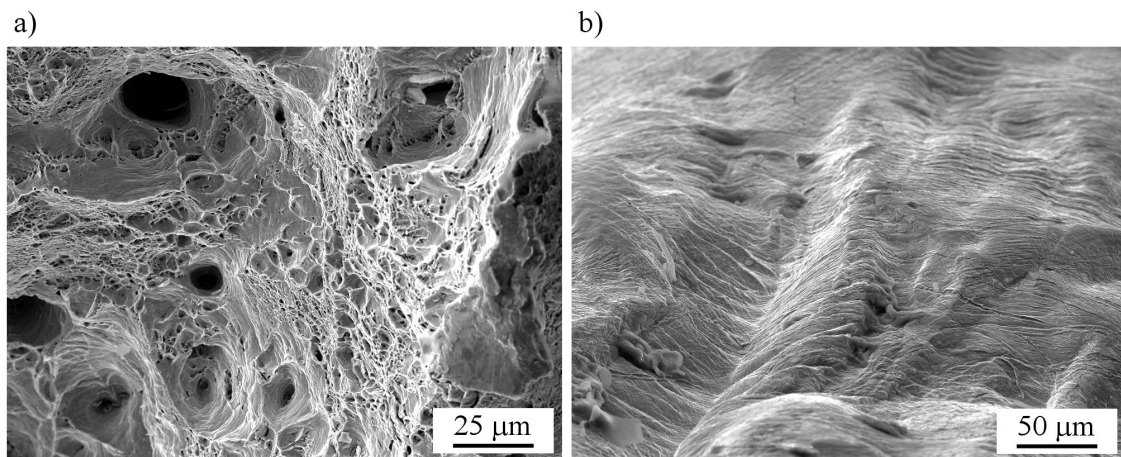


Fig. 4 Detail of fracture surface of tensile specimens for the cast variant at RT. Typical ductile dimples on fracture surface (a) and wrinkles on the cylindrical part of specimen resulting from strong plastic deformation in the area of necking (b).



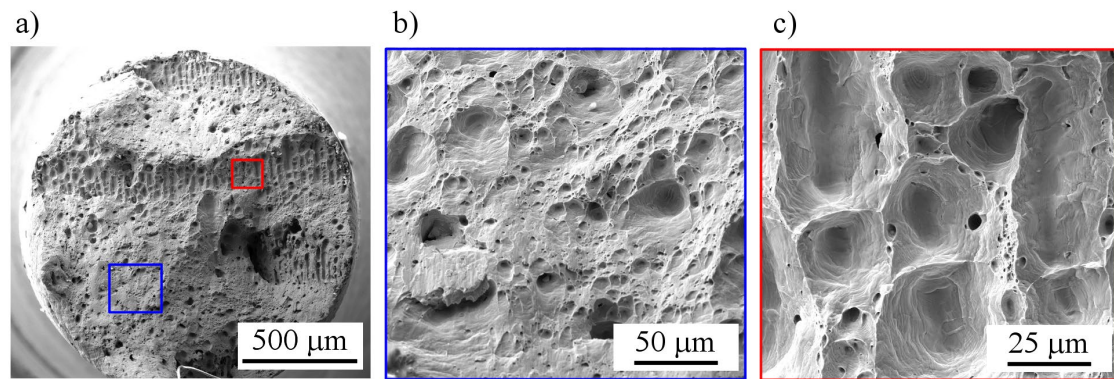


Fig. 5 Detail of fracture surface of tensile specimens for LPBF variant at RT. Overview of fracture surface (a) ductile dimples (b) and details of gas porosity (c).

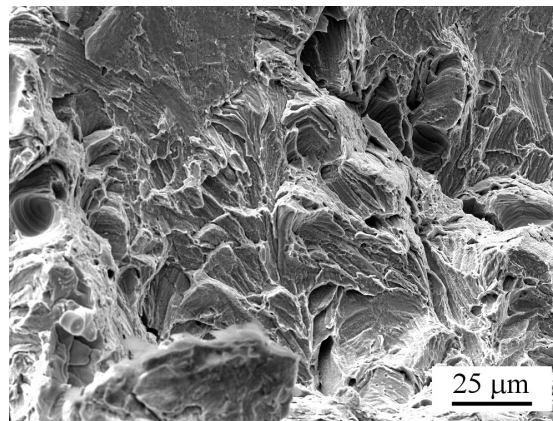


Fig. 6 Detail „cleavage-like“ facets on the fracture surface of tensile specimens for LPBF variant tested at 550 °C.

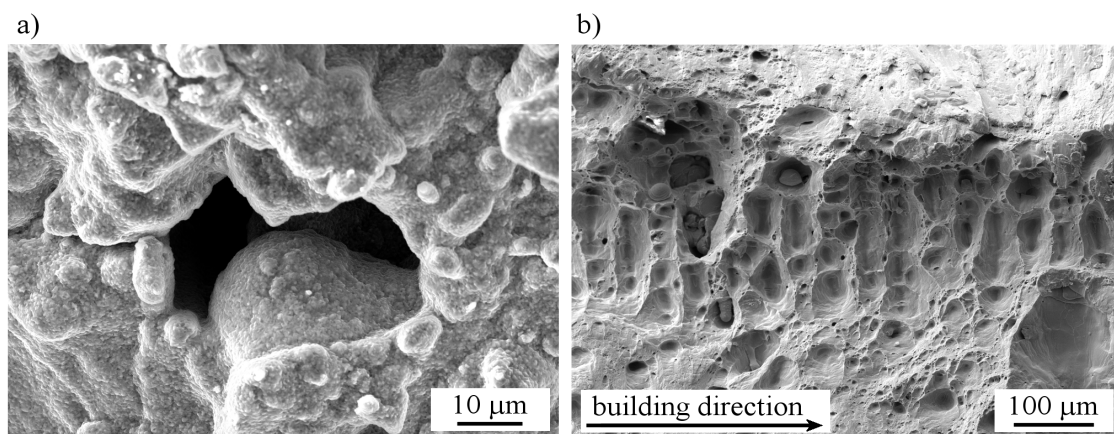


Fig. 7 Defects present in LPBF variant of material: lack-of-fusion pores (a), and keyholes (b).

The occasional presence of LOF was found with small and randomly located defects (see Fig. 7a). LOF defects are related mainly to the lack of the overlap of melt pools respectively laser scan tracks. These defects show highly irregular shapes often partially filled with unmolten powder particles. The balling which is affected by poor wettability was not observed in this work. The most often case of defects in LPBF specimens was spherical gas porosity arranged typically into rows (see Fig. 7b). Generally, the gas porosity can be divided according to the size of pores. Small pores are typically related to the presence of the hydrogen that was bound in the moisture on the surface of the powder particles. Large pores arranged typically in rows in the scanning direction are called keyholes. Keyhole porosity occurs when the power density of the laser beam is high enough to cause metal evaporation. The vapour cavities are locked in the root of the overheated melt pool by solidified

material above it. Keyhole porosity can be distinguished by its usually spherical or elliptical shape elongated in the direction perpendicular to the building direction (see arrow indicating the building direction in Fig. 7b).

## Conclusions

Two material variants of Alloy 400 were exposed to the tensile loading at RT and elevated temperatures. Initial microstructure of both cast and LPBF specimens was observed and fractography analysis of fractured specimens was performed. The investigation has resulted in the following conclusions:

- 1) The LPBF variant shows an increase in yield and ultimate strength but a decrease in plasticity compared to the cast material.
- 2) The presence of defects (LOF and keyholes) in the LPBF parts results in lowering mechanical properties, especially fracture elongation. Typical and often observed keyhole porosity exhibited elliptical shape, whereas occasionally present lack-of-fusion pores were irregularly shaped. Despite the defects present in the LPBF material which significantly reduce the mechanical properties, very interesting results were achieved.
- 3) The distribution and type of defects present in LPBF material can provide information about the process conditions. Adjustment of printing parameters will lead to improvement of microstructure quality with a positive effect on the mechanical properties of LPBF material.

## Acknowledgement

The authors would like to acknowledge the support of the research project from the European Union's Horizon 2020 research and innovation programme under grant agreement No 958192.

Alice Chlupová would like to acknowledge the support of publication by H2020-WIDESPREAD-2018-03 under grant agreement No. 857124, the Twinning project on the Structural Integrity and Reliability of Advanced Materials obtained through additive Manufacturing (SIRAMM).

## References

- [1] O. Marenych, A. Kostryzhev, C. Shen, Z. Pan, H. Li, S. van Duin, Precipitation Strengthening in Ni–Cu Alloys Fabricated Using Wire Arc Additive Manufacturing Technology, *Metals* 9 (1) (2019) 105.
- [2] Monel 400. (<https://www.hpalloy.com/Alloys/descriptions/MONEL400>).
- [3] O. Marenych, A. Kostryzhev, Strengthening mechanisms in nickel-copper alloys: A review, *Metals* 10 (10) (2020) 1358.
- [4] K. S. Prakash, T. Nancharaih, V. V. S. Rao, Additive Manufacturing Techniques in Manufacturing -An Overview, *Materials Today: Proceedings* 5 (2, Part 1) (2018) 3873-3882.
- [5] I. Šulák; T. Babinský; A. Chlupová; A. Milovanović; L. Náhlík, Effect of building direction and heat treatment on mechanical properties of Inconel 939 prepared by additive manufacturing, *Journal of Mechanical Science and Technology* (2022) (accepted for publication)
- [6] Y. Shi, Z. Lu, L. Yu, R. Xie, Y. Ren, G. Yang, Microstructure and tensile properties of Zr-containing ODS-FeCrAl alloy fabricated by laser additive manufacturing, *Materials Science and Engineering: A* 774 (2020) 138937.
- [7] I. Raffeis, F. Adjei-Kyeremeh, U. Vroomen, E. Westhoff, S. Bremen, A. Hohoi, A. Bührig-Polaczek, Qualification of a Ni–Cu Alloy for the Laser Powder Bed Fusion Process (LPBF): Its Microstructure and Mechanical Properties, *Applied Sciences* 10 (10) (2020) 3401.
- [8] N. Nudelis, P. Mayr, A Novel Classification Method for Pores in Laser Powder Bed Fusion, *Metals* 11 (12) (2021) 1912.

## 8.2 High-temperature Fatigue and Creep Performance of Additively Manufactured NiCu-based Alloy

Ivo Šulák, Alice Chlupová, Tomáš Záležák, Ivo Kuběna, **Jan-Philipp Roth**, Katrin Jahns, Ulrich Krupp, Tomáš Kruml

Procedia Structural Integrity 52 (2024) 143–153

DOI 10.1016/j.prostr.2023.12.015

Reference [5]

## Fracture, Damage and Structural Health Monitoring

High-temperature Fatigue and Creep Performance of Additively  
Manufactured NiCu-based AlloyIvo Šulák<sup>a\*</sup>, Alice Chlupová<sup>a</sup>, Tomáš Záležák<sup>a</sup>, Ivo Kuběna<sup>a</sup>, Jan-Philipp Roth<sup>b</sup>,  
Katrín Jahns<sup>b</sup>, Ulrich Krupp<sup>c</sup>, Tomáš Kruml<sup>a</sup><sup>a</sup>*Institute of Physics of Materials, Czech Academy of Sciences, Žitkova 22, 616 00 Brno, Czech Republic*<sup>b</sup>*Faculty of Engineering and Computer Science, Osnabrück University of Applied Sciences, Albrechtstr. 30, 49076 Osnabrück, Germany*<sup>c</sup>*Steel Institute IEHK, RWTH Aachen University, Intzestraße 1, 52072 Aachen, Germany*

---

**Abstract**

NiCu-based alloys are frequently employed as a key material for heat exchangers and superheated steam systems where the emphasis is put on the resistance against metal dusting and corrosion in harsh environments and, at the same time, excellent mechanical properties at elevated temperatures. The present contribution delivers the experimental results on high-temperature fatigue and creep performance of additively manufactured NiCu-based Alloy 400 and compares it with conventionally produced material. The fatigue tests were performed in symmetrical force control loading in laboratory air at elevated temperatures. Standard constant stress uniaxial creep tests were carried out up to the rupture at applied stresses ranging from 30 to 150 MPa and temperatures between 600–880 °C in a protective argon atmosphere. Results indicate inferior fatigue and creep properties of additively manufactured Alloy 400. This detrimental effect of the manufacturing process on mechanical properties can be caused by several factors, including the orientation of the building direction relative to the loading direction, strong texture in <011> direction, and also by the presence of defects revealed by means of scanning electron microscopy on fracture surfaces of additively manufactured materials.

© 2023 The Authors. Published by Elsevier B.V.

This is an open access article under the CC BY-NC-ND license (<https://creativecommons.org/licenses/by-nc-nd/4.0>)

Peer-review under responsibility of Professor Ferri Aliabadi

**Keywords:** Additive manufacturing, Alloy 400, fatigue lifetime, creep behaviour, electron microscopy

---

**1. Introduction**

The laser powder bed fusion (LPBF) process is one of the additive manufacturing technologies used for the 3D printing of metals. It emerged as a disruptive technology with reduced manufacturing steps and minimum processing

---

\* Corresponding author. Tel.: 420-532-290-343.

E-mail address: [sulak@ipm.cz](mailto:sulak@ipm.cz)

waste, and become an important consideration for Industry 4.0. The advantages of the LPBF process in high-tech industries include component complexity with new features and designs that are impossible to produce using traditional manufacturing tools. However, the LPBF process is also inextricably connected with printing defects like internal cracks, gas porosity, un-melted particles, etc., that can affect the mechanical properties (Chlupová et al., 2023; Du Plessis et al., 2020; Hosseini and Popovich, 2019; Liu et al., 2022; Šulák et al., 2023).

NiCu-based alloys are due to their chemical composition predestined for application, where high resistance to aggressive environments is required (Jahns et al., 2021). One of the representatives of NiCu-based alloys is Alloy 400, which belongs to the Monel family with relatively low cost and high corrosion resistance. Its typical deployment is in gas and liquid pipelines in power facilities, impellers in the marine sector, pump shafts in offshore platforms, heat exchangers for combustion engines, and the chemical conversion of CO<sub>2</sub> and hydrogen. In these applications, components are exposed to vibrations, considerable thermal gradients and centrifugal forces, which result in different degradation mechanisms like high-temperature fatigue and creep (Devendranath Ramkumar et al., 2012). Since this alloy is ductile and easy to machine, the production process was mainly carried out in conventional ways. Only recently, there has been a demand for complex geometries that cannot be produced except by additive technologies. This brings not only new opportunities in component and microstructural design but also challenges in terms of mechanical and chemical properties (Chlupová et al., 2023; Jahns et al., 2021).

This work is a comparative study of the microstructure and high-temperature fatigue and creep properties of conventionally produced NiCu-based Alloy 400 and its LPBF counterpart. S-N curves, creep lifetime curves, creep deformation curves, and creep activation energies for both material variants were obtained in the temperature range of 400–880 °C. The effect of grain size, texture, fracture mode and defects on fatigue and creep properties is presented and discussed in terms of the respective material manufacturing process.

## Nomenclature

$\dot{\epsilon}$	creep rate (-)
$\sigma$	applied creep stress (MPa)
$n$	creep stress exponent (-)
$A$	creep calibration constant (-)
EBS	electron backscatter diffraction
LPBF	laser powder bed fusion
$N_f$	number of cycles to fracture (-)
$Q$	activation energy (kJ.mol <sup>-1</sup> )
$R$	gas constant (J.K <sup>-1</sup> .mol <sup>-1</sup> )
SEM	scanning electron microscope
$T$	temperature (K)
TEM	transmission electron microscope

## 2. Experimental

### 2.1. Material

The material under investigation was Alloy 400 manufactured by the LPBF technique. The LPBF blocks for creep (one piece) and fatigue (two pieces) experiments with dimensions shown in Fig. 1 were fabricated at Osnabrück University of Applied Sciences using an EOS M290 machine. The machine operates a green laser system with a wavelength of 532 nm (85 W were applied) and enables a pre-heating of the build plate (80 °C was used in this study). All blocks were manufactured under argon atmosphere and by application of a layer height of 20 µm. As scanning speed, 1050 mm/s was chosen, and the hatch distance amounted to 50 µm. No heat treatment was applied. The density of the LPBF Alloy 400 was evaluated from metallographic sections to 99.5 % (Chlupová et al., 2023). To compare LPBF material properties, the creep and fatigue specimens were manufactured also from conventionally produced (hot extruded) material supplied by KME Germany GmbH. In this study, hot extruded material is nominated as “bulk”.



The chemical composition of Alloy 400 as determined by an energy dispersive x-ray (EDX) microanalysis is listed in Tab. 1.

Table 1. The chemical composition of Alloy 400 (in wt. %).

	C	Si	Mn	Al	Fe	Cu	Ni
Bulk	0.1	0.2	0.9	0.1	1.8	33.3	Bal.
LPBF	0.1	0.2	1.1	0.1	1.6	31.9	Bal.

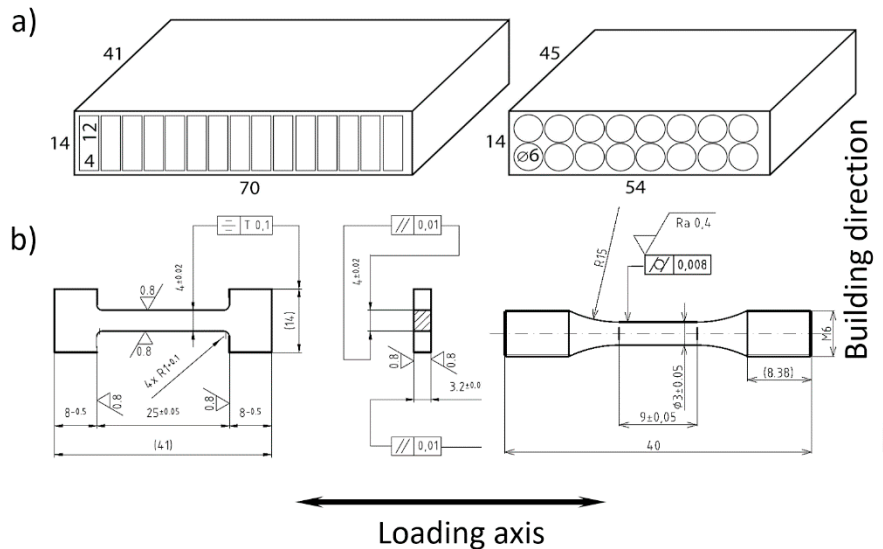


Fig. 1. a) The schematic illustration of blocks produced via the LPBF process for creep (left) and fatigue (right) experiments; b) the drawing of creep (left) and fatigue (right) specimens.

## 2.2. Observation

Detailed microstructural investigation and fractographic observation of features specific for fatigue and creep loading of bulk and LPBF Alloy 400 were performed using a Tescan Lyra 3 XMU scanning electron microscope (SEM) equipped with a Symmetry electron backscatter diffraction (EBSD) detector and an Oxford XMax 80 EDX spectrometer. Analysis of the internal dislocation structure of both materials was carried out in a Thermo Scientific™ Talos F200i transmission electron microscope (TEM). TEM foils were prepared by a standard procedure consisting of spark cutting, mechanical polishing, and 3 mm disc cutting. Final electrolytic polishing was carried out at a temperature of -5 °C and voltage of 20 V in a solution of acetic acid and perchloric acid.

## 2.3. High-temperature fatigue and creep experiments

Stress-controlled high-temperature fatigue experiments were performed on cylindrical specimens with gauge length and diameter of 9 and 3 mm, respectively. A symmetrical push-pull cycling with a loading frequency of 5Hz was done using a servo-hydraulic testing machine MTS 810 equipped with a three-zone resistance furnace. The temperature was monitored and controlled by four K-type thermocouples attached to the surface of the specimens. Experiments were carried out at 400 °C, 550 °C, 650 °C, and 750 °C.

The creep tests were performed using self-designed creep machines developed in the IPM in the 1970s (Dobes et al., 1986; Hostinsky and Cadek, 1976). The machines have a lever construction, where a creep specimen is mounted into grips connected to a hook on the top end attached to the loading lever, and to a fixed hook on the bottom end. The opposite part of the lever is loaded with a constant weight. The loading is applied on a cam located on the lever, which

automatically adjusts the applied force. Thus a constant stress is applied upon the specimen. The displacement is measured by a half-bridge induction coil sensor connected to a measuring amplifier. The induction sensor provides a measuring range of  $\pm 10$  mm. The grips are placed in a furnace with a Eurotherm 2416 electronic regulation with a controlling Ni-Cr or Pt-Rh thermocouple situated close to the specimen gauge length. The creep tests were carried out in tension in a protective argon atmosphere in the temperature range of 600–880 °C and in the stress range of 30–150 MPa.

### 3. Results and discussion

#### 3.1. Microstructure

The microstructure of bulk and LPBF Alloy 400 is presented in Fig. 2. At first glance, the differences in the microstructure brought about by different production methods are apparent. In the case of bulk Alloy 400, the equiaxed grains with the presence of twins (Fig. 2a) can be seen. No preferential orientation was identified (EBSD map in Fig. 2b). An average grain size of  $(63.3 \pm 49.1)$   $\mu\text{m}$  was established using an equivalent circle diameter from EBSD data. The grain size distribution histogram can be seen in Fig. 2c. The microstructure of LPBF Alloy 400 is typical with comparably finer grains with an average grain size of  $(14.7 \pm 10.1)$   $\mu\text{m}$ . The grains are preferentially orientated along the  $\{011\}$  direction (Fig. 2f) in the building direction (Chlupová et al., 2023). The microstructure exhibits a so-called honeycomb structure with melt-pools going through several grains (Fig. 2e). The dislocation arrangement as revealed by TEM (Fig. 2d and Fig. 2h) is also different for both material batches. In the bulk material, we can observe relatively low dislocation density with dislocations arranged in bands along the  $\{111\}$  planes (Fig. 2d). However, in the case of LPBF Alloy 400, a cell-like structure with dislocations densely allocated to the cell walls and relatively clean centre is formed (Fig. 2h), which is a typical manifestation of 3D printed materials (Liu et al., 2022), where multiple reflows create significant strain fields that in some ways resemble thermomechanical loading (Babinský et al., 2023).

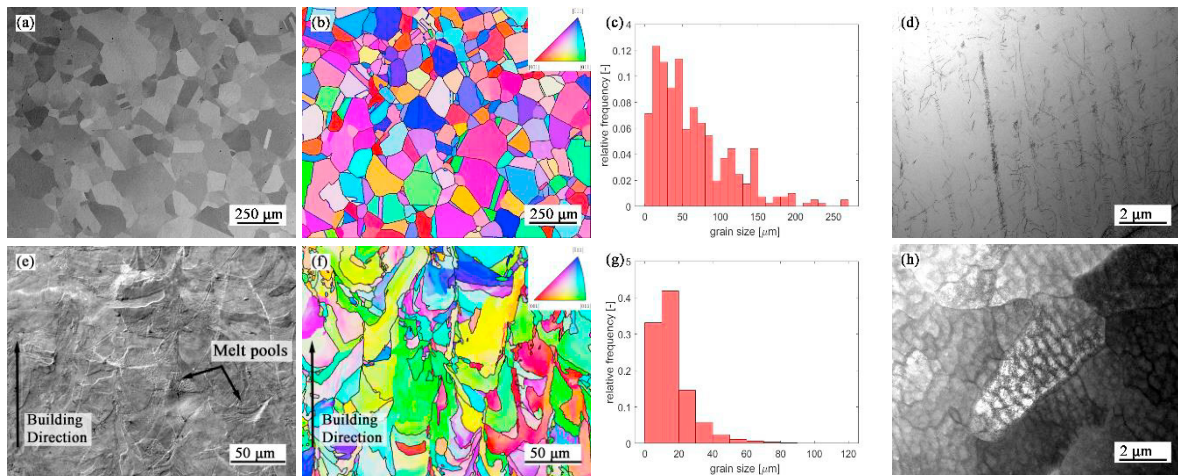


Fig. 2. The microstructure and grain size distribution of Alloy 400 a)-d) bulk; e)-h) LPBF.

#### 3.2. Fatigue

The S-N curves for both bulk and LPBF Alloy 400 are displayed in Fig. 3 in the representation of stress amplitude versus the number of cycles to failure. Due to the limited amount of material (especially the LPBF variant), only a few fatigue tests were performed at each temperature (each point corresponds to one experiment). However, even with this limitation, the results are representative. Two regions with different behaviour can be observed. As can be seen, from the S-N curves, the fatigue life of LPBF Alloy 400 is comparable with bulk Alloy 400 at 400 °C and 550 °C. However, a significant drop in the fatigue life of LPBF Alloy 400 compared to bulk Alloy 400 occurs when fatigue loading is applied at 650 °C and 750 °C. The explanation for this behaviour can be seen in both the grain size and the

mechanism of fatigue crack propagation at different temperatures. At temperatures up to 550 °C, fatigue crack propagation is transgranular via a striation mechanism (Fig. 4a-d and Fig. 5a-d). In this case, the finer-grained structure typical of LPBF Alloy 400 is preferable for the mechanical properties as there is a significant increase in strength characteristics (Armstrong, 1970). Fine-grained materials generally exhibit considerably better fatigue properties (Fintová et al., 2021, 2020; Fintová and Kunz, 2015). In this case, however, the positive effect of grain size is counterbalanced by the detrimental impacts of LPBF defects like keyholes, gas porosity or lack of fusion (Du Plessis et al., 2020), as can be seen from fracture surfaces in Fig. 5. The fatigue crack propagation mechanism changes with increasing temperature. At 650 °C and 750 °C, fatigue crack propagates predominantly along grain boundaries (intergranularly), which leads to faster fatigue crack propagation and thus to a reduction in fatigue life (Eckmann and Schweizer, 2017; Šulák et al., 2022). Since the number of grain boundaries is inversely proportional to the grain size, it can be assumed, that the fatigue crack growth rate is higher for fine-grained material (LPBF Alloy 400) than for coarse-grained material (bulk) (Fintová et al., 2017). Therefore, in conjunction with a number of LPBF defects, a significant decrease in the lifetime of LPBF Alloy 400 can be observed with increasing temperature. The association between fatigue crack propagation direction and printing strategy (orientation of keyhole defects) was not observed.

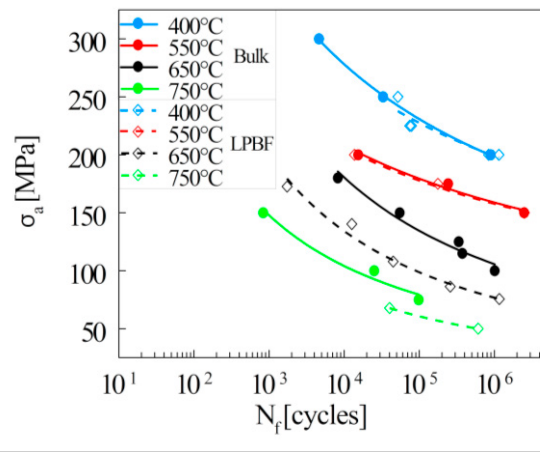


Fig. 3. S-N curves of bulk and LPBF alloy 400 tested in the temperature range of 400-750 °C (full symbols and lines – bulk; empty symbols and dash lines – LPBF).

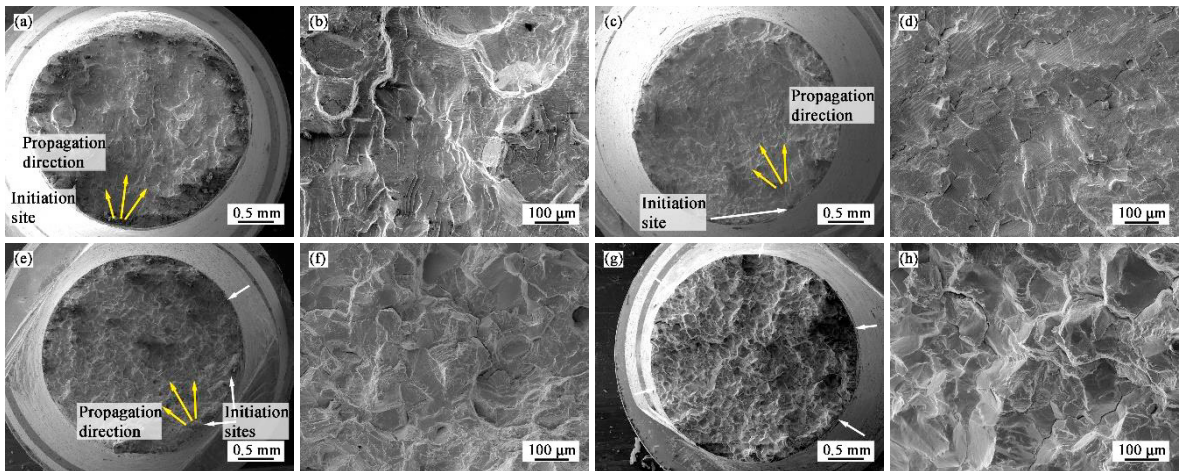


Fig. 4. Representative fracture surface of bulk Alloy 400 fatigued at a), b) 400 °C; c), d) 550 °C; e), f) 650 °C; g), h) 750 °C.



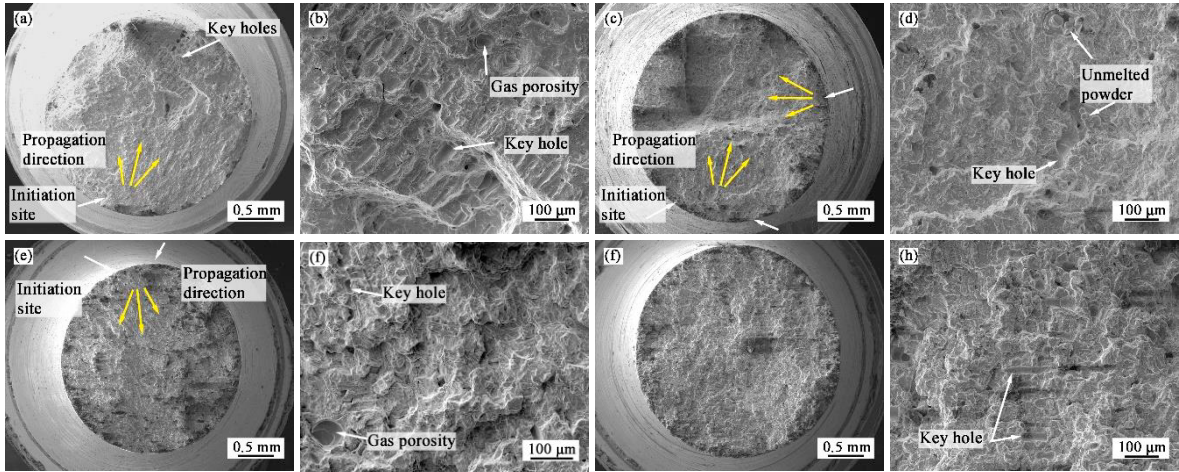


Fig. 5. Representative fracture surface of LPBF Alloy 400 fatigued at a), b) 400 °C; c), d) 550 °C; e), f) 650 °C; g), h) 750 °C.

### 3.3. Creep

At first, a series of tests at  $(830 \pm 50)$  °C and constant applied stresses between 50 and 100 MPa on bulk Alloy 400 were carried out. The creep curves are summarized in Fig. 6. The results show typical creep curves with a primary stage where the creep rate gradually decreases, a secondary stage with steady-state creep with strain rates between  $10^{-5} \text{ s}^{-1}$  and  $10^{-3} \text{ s}^{-1}$  and short tertiary stage ending with fracture. The true strains achieved span from 14 % (100 MPa) to 27 % (50 MPa), whereas the time to fracture spans from 2 minutes (100 MPa) to 7 hours (50 MPa).

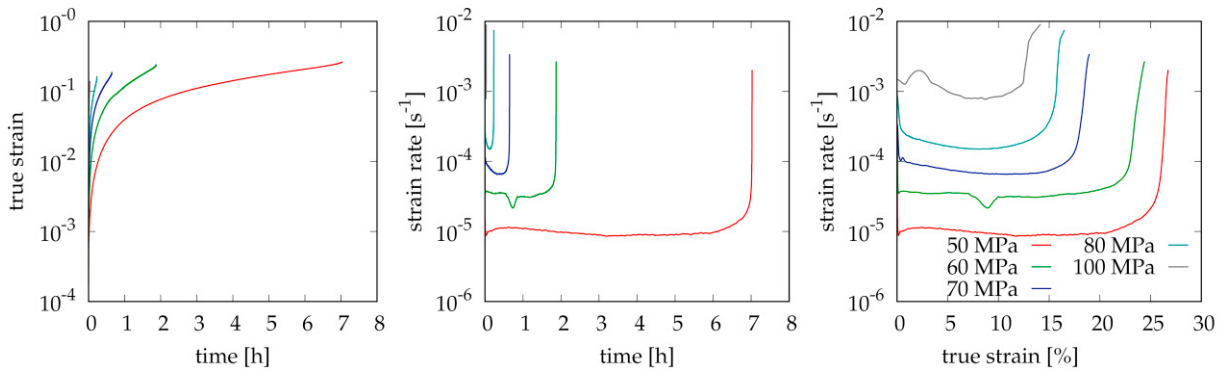


Fig. 6. Creep curves for Alloy 400 bulk at 50-100 MPa and 830 °C.

Two more tests were done with applied stress of 80 MPa at 780 and 880 °C and one more at 60 MPa and 880 °C. These have been used to calculate the activation energy. The steady creep rate can be modelled as:

$$\dot{\epsilon} = A\sigma^n \exp\left(-\frac{Q}{RT}\right) \quad (1)$$

where  $\dot{\epsilon}$  is the creep rate,  $A$  is a calibration constant,  $\sigma$  is the applied stress,  $n$  is the stress exponent,  $Q$  is the activation energy,  $R$  is a gas constant, and  $T$  is the temperature in Kelvin. The  $\sigma^n$  term corresponds to Norton's law (Kassner and Pérez-Prado, 2004; Norton, 1929) and the exponential term represents Arrhenius's law (Čadek, 1988).

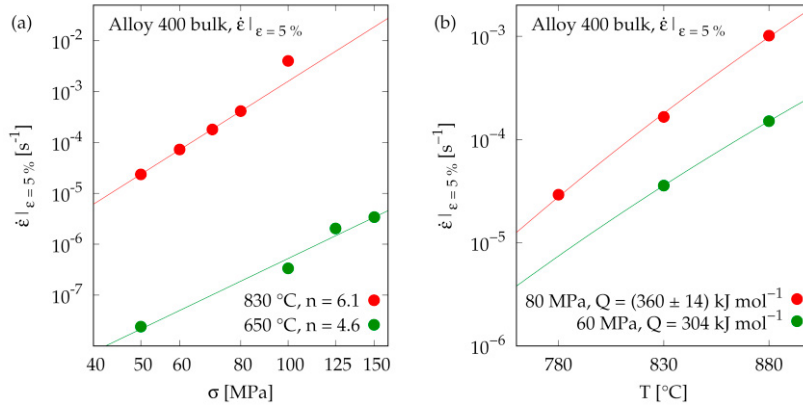


Fig. 7. a) Stress exponents for bulk Alloy 400 at 830 °C and 650 °C; b) Activation energies for bulk Alloy 400 crept at 80 MPa and 60 MPa. The strain rates are taken at the true strain of 5 %.

The five tests at 830 °C give a stress exponent  $n = 6.1$  (Fig. 7a), whereas the tests at constant stresses of 60 MPa and 80 MPa give activation energies of 304 kJ mol<sup>-1</sup> and 360 kJ mol<sup>-1</sup>, respectively (Fig. 7b). These data have been obtained from the strain rates at 5 % true strain. Because the strain rates in the first batch highly surpass the values plausible for practical applications, the remaining tests have been carried out at  $(650 \pm 50)$  °C. The results for five tests at 650 °C with applied stresses from 50 to 150 MPa show significantly lower steady-state creep rates between  $10^{-8}$  s<sup>-1</sup> and  $10^{-5}$  s<sup>-1</sup>, see Fig. 8. The tests with lower applied stresses (50 and 75 MPa) also show a sharp minimum in the strain rate during the primary stage. The tertiary phase quickly ends with fracture.

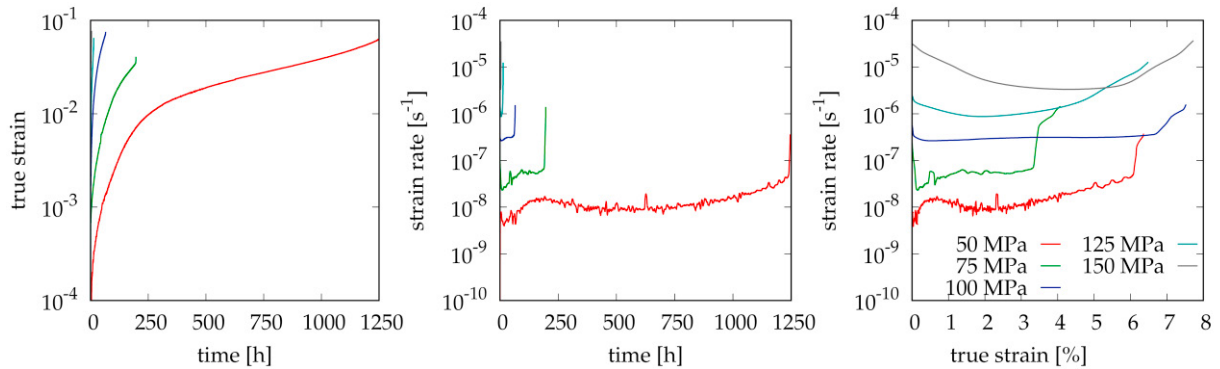


Fig. 8. Creep curves for bulk Alloy 400 at 50-150 MPa and 650 °C.

The true strains achieved span from 4 % (75 MPa) to 8 % (150 MPa). Apart from the tests at higher temperatures, the true strain achieved tends to increase with the applied stress. Also, the time to fracture is longer, from 4 hours for 150 MPa to 196 hours for 75 MPa and 1245 hours for 50 MPa. The stress exponent  $n = 4.6$  is slightly lower (Fig. 7) than for higher temperatures. Strain rates at 5 % true strain were used. For strain rates at 2 % true strain, the stress exponent for the bulk Alloy 400 is  $n = 5.7$  (Fig. 9a). Two more tests at 600 and 700 °C and a constant applied stress of 125 MPa allowed to obtain the activation energy – 380 kJ mol<sup>-1</sup> (Fig. 9b). These data have been obtained from the strain rates at 2 % true strain.



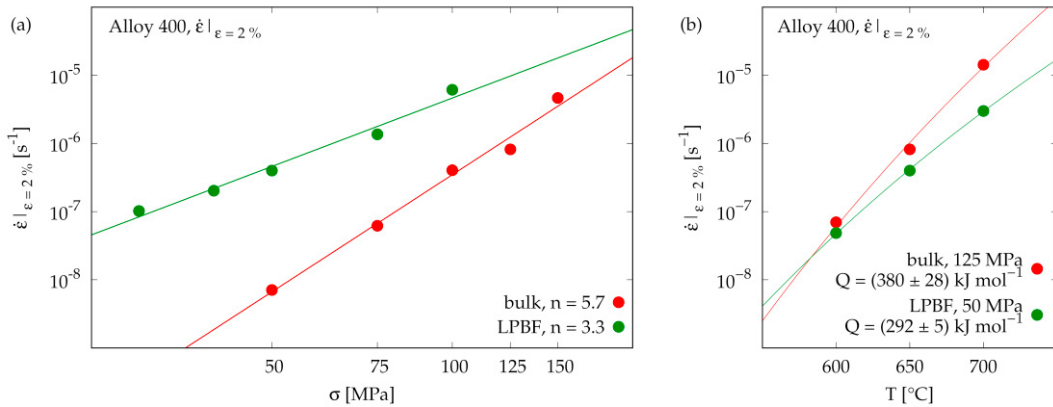


Fig. 9. a) Stress exponents for bulk and LPBF Alloy 400 at 650 °C; b) Activation energies for bulk Alloy 400 bulk crept at 125 MPa and LPBF Alloy 400 crept at 50 MPa. The strain rates are taken at the true strain of 2 %.

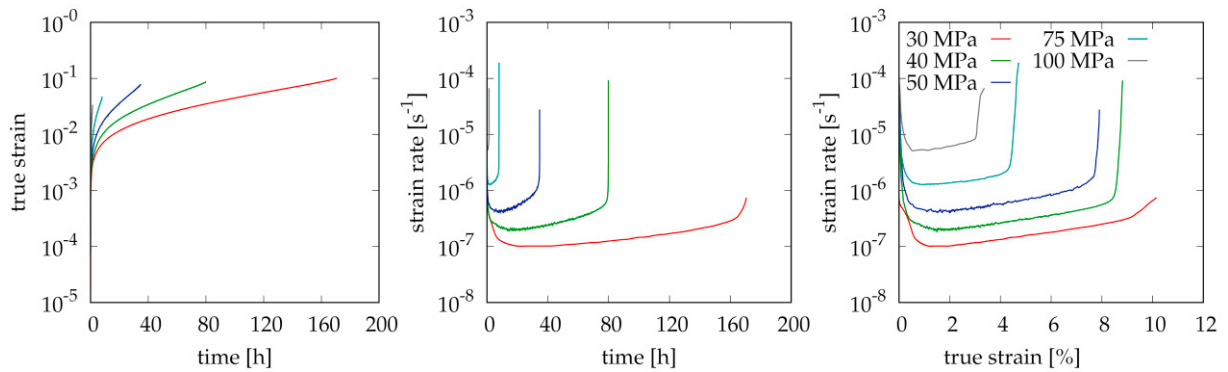


Fig. 10. Creep curves for LPBF Alloy 400 at 30-100 MPa and 650 °C.

The LPBF Alloy 400 has been tested only at  $(650 \pm 50) ^\circ\text{C}$  because the samples were available after the decision to follow on with lower temperatures. The tests followed the same pattern as for the bulk material – five tests at 650 °C for the stress exponent and two more at 600 °C and 700 °C for the activation energy.

The creep curves for the LPBF Alloy 400 are shown in Fig. 10. The steady-state creep rates are in the range from  $10^{-7} \text{ s}^{-1}$  and  $10^{-5} \text{ s}^{-1}$ , which are higher than for the bulk, and the applied stresses fall between 30 and 100 MPa. The time to fracture is shorter – from 82 minutes (100 MPa) to 170 hours (30 MPa). Also, the achieved true strain is somewhat smaller, from 3.3 % (100 MPa) to 10 % (30 MPa). The LPBF Alloy 400 thus shows significantly worse creep properties in comparison with the bulk material. The stress exponent for the LPBF Alloy 400 is  $n = 3.3$  (Fig. 9a) which is considerably lower than for the bulk Alloy 400.

In Fig. 11, the bulk and the LPBF Alloy 400 at 650 °C and 100 MPa are compared. Noticeable is also the achieved true strain, which is smaller for the LPBF Alloy 400. The activation energy  $292 \text{ kJ mol}^{-1}$  has been obtained from the tests at 50 MPa (Fig. 6) and is based on the strain rates at 2 % true strain.

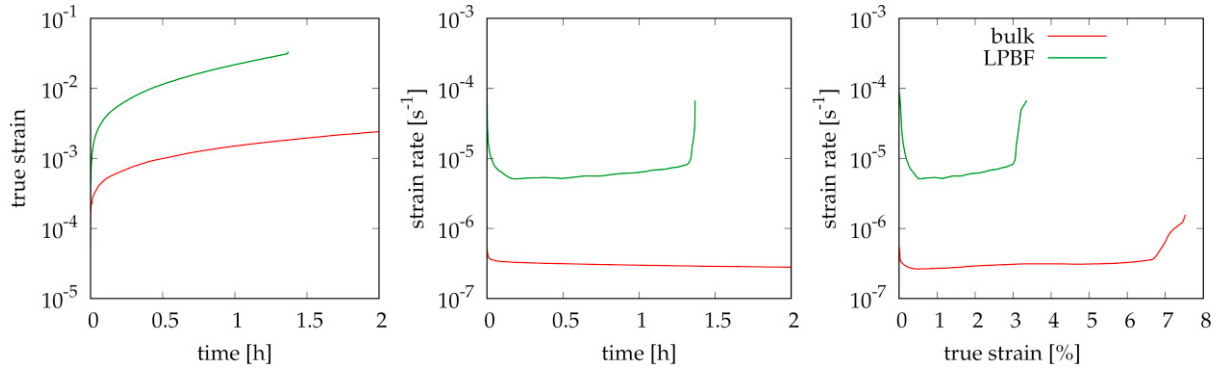


Fig. 11. The comparison of creep curves for bulk and LPBF Alloy 400, both crept at 100 MPa and 650 °C.

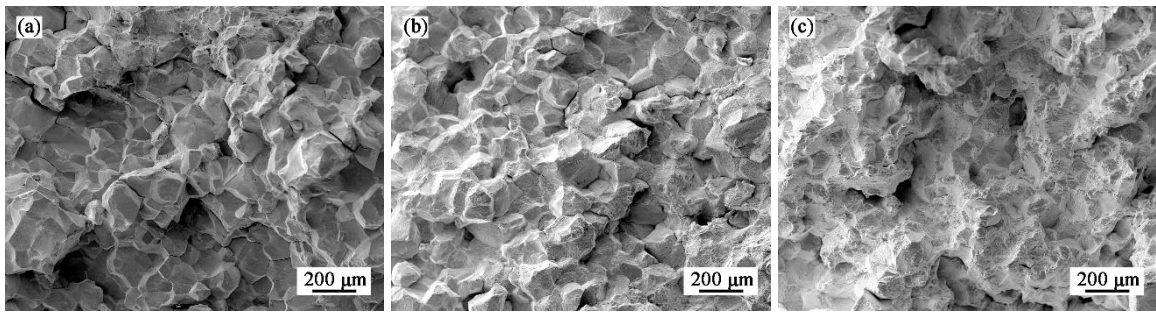


Fig. 12. Representative fracture surface of bulk Alloy 400 crept at a) 600°C; b) 650 °C; c) 700 °C.

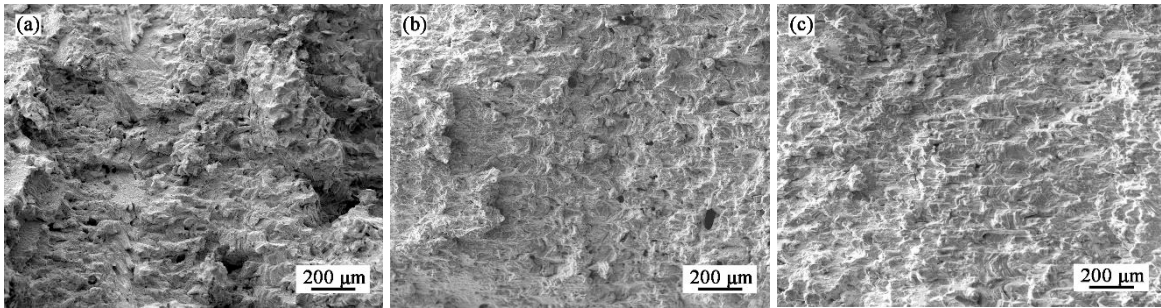


Fig. 13: Representative fracture surface of LPBF Alloy 400 crept at a) 600°C; b) 650 °C; c) 700 °C.

The creep results of the bulk and LPBF Alloy 400 differ significantly. Particularly, the steady strain rates for the bulk material are lower and the true strain achieved is higher than for the LPBF Alloy 400 (see Fig. 11). This can be partially explained by the grain size difference. The bulk material consists of coarse grains with a mean grain size of about 63  $\mu\text{m}$ , whereas the LPBF Alloy 400 has an approximately four times smaller value of mean grain size ( $\approx 14 \mu\text{m}$ ). Although the smaller grain size might improve the strength and creep properties of the material (Čadek, 1988), the LPBF Alloy 400 contains a significant amount of manufacturing defects (as can be seen from fracture surfaces) (Chlupová et al., 2023). These defects have a detrimental effect on the creep properties, as the voids, gas porosity and keyholes facilitate the crack initiation. The SEM micrographs in Fig. 12 and Fig. 13 indicate that the creep tests of both bulk and LPBF Alloy 400 terminate in intergranular fracture. However, it is also possible to observe several defects on the fracture surfaces of LPBF Alloy 400, which accelerated the fracture. The inferior creep properties of the LPBF Alloy 400 are also indicated by the stress exponent. While the bulk material crept at 650 °C has  $n = 5.7$ , the

LPBF material has  $n = 3.3$ , which indicates lower creep strength. The stress exponents of bulk Alloy material do not match either typical values for solid solutions ( $n = 3$ ) or pure metals ( $n = 5$ ) (Čadek, 1988). However, for the LPBF Alloy 400 value ( $n = 3.3$  – Fig. 9a) is close to solid solutions values. The activation energies for all creep results are of the same order. However, it can be seen that the value of the activation energy increases with the applied stress (Figs. 7b and 9b). For lower applied stresses, processes along grain boundaries become more important because these processes have lower activation energies.

#### 4. Conclusions

Experimental investigation of the high-temperature fatigue and creep behaviour of conventionally and additively manufactured NiCu-based alloy via laser powder bed fusion technique allows for the following conclusions:

- 1) The LPBF process for this alloy is still not optimal and needs to be improved to reduce the number of defects that have a detrimental effect on mechanical properties.
- 2) Finer-grained structure compensated for the negative effect of LPBF defects on fatigue life up to 550 °C. Above this temperature, the fatigue crack propagation mechanism changes from transgranular to intergranular, which entails a significant drop in the fatigue life of the LPBF Alloy 400 compared to the bulk Alloy 400.
- 3) LPBF Alloy 400 shows inferior creep properties in the whole range of tested temperatures and stresses. The steady strain rates for the bulk Alloy 400 are lower, and the true strain achieved is higher than for the LPBF Alloy 400.

#### Acknowledgements

The financial support from European Union's Horizon 2020 Research and Innovation Programme under grant agreement No 958192 is acknowledged.

#### References

- Armstrong, R.W., 1970. The influence of polycrystal grain size on several mechanical properties of materials. *Metallurgical and Materials Transactions* 1, 1169–1176. <https://doi.org/10.1007/BF02900227>
- Babinský, T., Šulák, I., Kuběna, I., Man, J., Weiser, A., Švábenská, E., Englert, L., Guth, S., 2023. Thermomechanical fatigue of additively manufactured 316L stainless steel. *Materials Science and Engineering: A* 869, 144831. <https://doi.org/10.1016/j.msea.2023.144831>
- Čadek, J., 1988. Creep in Metallic Materials, Materials science monographs. Elsevier.
- Chlupová, A., Šulák, I., Kuběna, I., Kruml, T., Roth, J.P., Jahns, K., 2023. Comparison of Microstructure and Properties of Nickel-Copper Alloy Prepared by Casting and Laser Powder Bed Fusion Process. *MSF* 1082, 171–176. <https://doi.org/10.4028/p-884q32>
- Devendranath Ramkumar, K., Arivazhagan, N., Narayanan, S., 2012. Effect of filler materials on the performance of gas tungsten arc welded AISI 304 and Monel 400. *Materials & Design* 40, 70–79. <https://doi.org/10.1016/j.matdes.2012.03.024>
- Dobes, F., Zverina, O., Čadek, J., 1986. LOADING SYSTEM FOR CREEP TESTS AT CONSTANT COMPRESSIVE STRESS. *Metallic Materials* (English translation of Kovove Materialy) (Cambridge, Engl) 24, 293–298.
- Du Plessis, A., Yadroitsava, I., Yadroitsev, I., 2020. Effects of defects on mechanical properties in metal additive manufacturing: A review focusing on X-ray tomography insights. *Materials & Design* 187, 108385. <https://doi.org/10.1016/j.matdes.2019.108385>
- Eckmann, S., Schweizer, C., 2017. Characterization of fatigue crack growth, damage mechanisms and damage evolution of the nickel-based superalloys MAR-M247 CC (HIP) and CM-247 LC under thermomechanical fatigue loading using in situ optical microscopy. *International Journal of Fatigue* 99, 235–241. <https://doi.org/10.1016/j.ijfatigue.2017.01.015>
- Fintová, S., Arzaghi, M., Kuběna, I., Kunz, L., Sarrazin-Baudoux, Ch., 2017. Fatigue crack propagation in UFG Ti grade 4 processed by severe plastic deformation. *International Journal of Fatigue* 98, 187–194. <https://doi.org/10.1016/j.ijfatigue.2017.01.028>
- Fintová, S., Dlhý, P., Mertová, K., Chlup, Z., Duchek, M., Procházka, R., Hutař, P., 2021. Fatigue properties of UFG Ti grade 2 dental implant vs. conventionally tested smooth specimens. *Journal of the Mechanical Behavior of Biomedical Materials* 123, 104715. <https://doi.org/10.1016/j.jmbbm.2021.104715>
- Fintová, S., Kuběna, I., Palán, J., Mertová, K., Duchek, M., Hutař, P., Pastorek, F., Kunz, L., 2020. Influence of sandblasting and acid etching on fatigue properties of ultra-fine grained Ti grade 4 for dental implants. *Journal of the Mechanical Behavior of Biomedical Materials* 111, 104016. <https://doi.org/10.1016/j.jmbbm.2020.104016>
- Fintová, S., Kunz, L., 2015. Fatigue properties of magnesium alloy AZ91 processed by severe plastic deformation. *Journal of the Mechanical Behavior of Biomedical Materials* 42, 219–228. <https://doi.org/10.1016/j.jmbbm.2014.11.019>
- Hosseini, E., Popovich, V.A., 2019. A review of mechanical properties of additively manufactured Inconel 718. *Additive Manufacturing* 30, 100877. <https://doi.org/10.1016/j.addma.2019.100877>

- Hostinsky, T., Cadek, J., 1976. CONSTANT TENSILE STRESS CREEP TESTING MACHINE. *Journal of Testing and Evaluation* 4, 26–28. <https://doi.org/10.1520/jte10503j>
- Jahns, K., Ulrich, A.S., Schlereth, C., Reiff, L., Krupp, U., Galetz, M.C., 2021. The Effect of Cu Content and Surface Finish on the Metal Dusting Resistance of Additively Manufactured NiCu Alloys. *Oxid Met* 96, 241–256. <https://doi.org/10.1007/s11085-021-10037-8>
- Kassner, M.E., Pérez-Prado, M.T., 2004. Fundamentals of Creep in Metals and Alloys, Fundamentals of Creep in Metals and Alloys. <https://doi.org/10.1016/B978-0-08-043637-1.X5000-5>
- Liu, Z., Zhao, D., Wang, P., Yan, M., Yang, C., Chen, Z., Lu, J., Lu, Z., 2022. Additive manufacturing of metals: Microstructure evolution and multistage control. *Journal of Materials Science & Technology* 100, 224–236. <https://doi.org/10.1016/j.jmst.2021.06.011>
- Norton, F.H., 1929. *The Creep of Steel at High Temperatures*, Bulletin. McGraw-Hill book Company, Incorporated.
- Šulák, I., Babinský, T., Chlupová, A., Milovanović, A., Náhlík, L., 2023. Effect of building direction and heat treatment on mechanical properties of Inconel 939 prepared by additive manufacturing. *Journal of Mechanical Science and Technology* 37, 1071–1076. <https://doi.org/10.1007/s12206-022-2101-7>
- Šulák, I., Obrtlík, K., Babinský, T., Guth, S., 2022. The low cycle fatigue behaviour of MAR-M247 superalloy under different strain rates and cycle shapes at 750 °C. *International Journal of Fatigue* 164, 107133. <https://doi.org/10.1016/j.ijfatigue.2022.107133>

### **8.3 Nanoparticle-Modification of NiCu-Based Alloy 400 for Laser Powder Bed Fusion**

**Jan-Philipp Roth**, Ivo Šulák, Zdeněk Chlup, Jörg Fischer-Bühner, Ulrich Krupp, Katrin Jahns

Solid Freeform Fabrication 2023:  
Proceedings of the 34th Annual  
International Solid Freeform Fabrication  
Symposium – An Additive  
Manufacturing Conference (2023)  
574–575, Austin, Texas, USA

Reference [6]



## NANOPARTICLE-MODIFICATION OF NICU-BASED ALLOY 400 FOR LASER POWDER BED FUSION

J.-P. Roth<sup>1</sup>, I. Šulák<sup>2</sup>, Z. Chlup<sup>2</sup>, J. Fischer-Bühner<sup>3</sup>, U. Krupp<sup>4</sup>, K. Jahns<sup>1</sup>

<sup>1</sup> Faculty of Engineering and Computer Science, Osnabrück University for Applied Sciences,  
49076 Osnabrück, Germany

<sup>2</sup> Institute of Physics of Materials, Czech Academy of Sciences,  
61600 Brno, Czech Republic

<sup>3</sup> INDUTHERM Gießtechnologie GmbH,  
75045 Walzbachtal, Germany

<sup>4</sup> Steel Institute IEHK, RWTH Aachen University,  
52072 Aachen, Germany

### Long Abstract

NiCu-based Alloy 400 is a material being frequently used in corrosive environments wherefore it is applied in several industries like the maritime sector or chemical processing [1]. Numerous functional parts made of this alloy, like heat exchangers or liquid-carrying tubes for instance, may withstand harsh environments to a certain extend but still, at high temperatures and especially in carbon-rich atmospheres, component failure occurs due to poor metal dusting and creep resistance [2–5]. Reinforcing the base alloy system with nanoparticles using gas atomization and subsequent laser powder bed fusion (LPBF) can counteract such material failure [6]. Hence, in this work, titanium was added to Alloy 400 and atomized under nitrogen atmosphere in order to cause TiN nanoparticle formation in the microstructure of printed components.

Nitrogen atomization of the present alloy resulted in spherical, flowable powder with a particle size distribution approx. in between 15 and 53  $\mu\text{m}$ , being considered usable for additive manufacturing. Surface and cross section analysis of powder particles with scanning and scanning transmission electron microscopy (SEM, STEM) revealed the presence of TiN on the nanoscale. Grains, consisting of dislocation-enriched cells, showed Cu segregations on both, grain and cell boundaries as commonly known for NiCu alloys [7]. As a nanoparticle formation was achieved in powders, these were further applied to the LPBF process.

A parameter study varying in laser power, hatch distance and scanning speed was performed. Throughout this, a parameter set leading to a density of  $\sim 99.8\%$  was achieved. Test specimens showed multiple layers of scanning tracks resulting from a rotating scanning geometry. Also, no dominant texture could be determined for grains being oriented in build direction. STEM characterization of LPBF parts revealed a higher quantity of TiN nanoparticles than in powders. Also, the dislocation density on cell walls was higher than in single particles. Besides Cu segregations, there were also found Ti segregations in the microstructure. In very low quantity, occasional AlO nanoparticles could be verified as well, not being expected to have any notable effect on mechanical properties.

Ti-enriched Alloy 400 showed the highest engineering strength while still demonstrating an acceptable engineering strain of nearly 30 %. Conventional material had better strain properties but could not reach the ultimate tensile strength of the newly generated LPBF material, which exceeded 600 MPa. Standard LPBF Alloy 400 did by far show the worst strain properties and comparable strength as in conventional material. Considering creep performance, the NiCu-based

alloy strengthened with TiN nanoparticles and the conventionally fabricated part exhibited nearly similar properties, again being significantly more resistant to mechanical load than the unmodified LPBF version. With an approx. ten times longer time to fracture at elevated temperature, the material developed in this study is considered a promising candidate in withstanding the above-described demanding environments.

### **Acknowledgements**

This work has received funding from the European Union's Horizon 2020 research and innovation program under grant agreement No 958192 which is gratefully acknowledged.

### **References**

- [1] Special Metals Corporation, 2005. Monel alloy 400, Publication number SMC-053.
- [2] T.M. Smith, R.R. Unocic, H. Deutchman, M.J. Mills, Creep deformation mechanism mapping in nickel base disk superalloys, *Materials at High Temperatures* 33 (2016) 372–383. <https://doi.org/10.1080/09603409.2016.1180858>.
- [3] C. Geers, Inhibition of coking and metal dusting on conventional alloys by using a nickel-tin intermetallic coating. PhD thesis (2013).
- [4] L.E. Shoemaker, G.D. Smith, A century of monel metal: 1906–2006, *JOM* 58 (2006) 22–26. <https://doi.org/10.1007/s11837-006-0077-x>.
- [5] R.K. Devendranath, N. Arivazhagan, S. Narayanan, M. Narayanan, A. Mondody, R. Kashyap, Development of Defect Free Monel 400 Welds for Marine Application, *AMR* 383-390 (2011) 4693–4696. <https://doi.org/10.4028/www.scientific.net/AMR.383-390.4693>.
- [6] C. Doñate-Buendía, F. Frömel, M.B. Wilms, R. Streubel, J. Tenkamp, T. Hupfeld, M. Nachev, E. Gökce, A. Weisheit, S. Barcikowski, F. Walther, J.H. Schleifenbaum, B. Gökce, Oxide dispersion-strengthened alloys generated by laser metal deposition of laser-generated nanoparticle-metal powder composites, *Materials & Design* 154 (2018) 360–369. <https://doi.org/10.1016/j.matdes.2018.05.044>.
- [7] Z. Erdélyi, C. Girardeaux, Z. Tókei, D.L. Beke, C. Cserháti, A. Rolland, Investigation of the interplay of nickel dissolution and copper segregation in Ni/Cu(111) system, *Surface Science* 496 (2002) 129–140. [https://doi.org/10.1016/S0039-6028\(01\)01571-0](https://doi.org/10.1016/S0039-6028(01)01571-0).

*The end.*